The University Of Sheffield.

Computational Models of Dopamine Diffusion and Receptor Binding in the Striatum

Lars Hunger

A thesis submitted in partial fulfilment of the requirements for the degree of Doctor of Philosophy

The University of Sheffield

Faculty of Science

Department of Psychology

June 2019

Abstract

The neuromodulator dopamine (DA) has complex effects on the activity of striatal neurons by changing their excitability and strength of synaptic inputs in the context of motor control, action-selection, reinforcement learning, and addiction. DA is volume transmitted, it leaves the synaptic cleft and diffuses through the extracellular space in the striatum. The spatial and temporal distribution of DA created by this diffusion have not been extensively studied yet. In this thesis a computational model based on diffusion in a porous medium was developed to study the spatiotemporal distribution of DA in the striatum. During the development of the model a second interesting problem was identified: DA receptors have slow kinetics. Due to these slow kinetics the DA receptors do not directly follow the DA concentration, but can integrate over longer timespans. Taking into account realistic kinetics it is shown that the different DA receptors do not have markedly different responses to different timescales of DA signals. The full model incorporates inhomogenous DA uptake, DA axonal tree morphologies, detailed receptor kinetics and spike trains based on rat cell recording. The thesis shows that spatiotemporal DA maps of a healthy striatum are highly variable in space and time but the death of dopaminergic axons, as seen in Parkinsons Disease, reduces the variability of the DA maps and makes them more homogenous. Furthermore, the DA receptor maps are shown to be correlated to anatomical features, synaptic positions and locations of reduced local DA uptake, and therefore have a component that is stable in time. The code of the full model has been made available at `https://bitbucket.org/Narur/dope-amine/src/`, so that others may also find out that dopamine is a dope amine.

Acknowledgements

I would like to express my sincere thanks to my supervisors Dr. Robert Schmidt and Dr. Arvind Kumar for their guidance encouragement and friendship. I would also like to thank my friends thanks in Innsbruck, Sheffield and Freiburg for keeping me sane during the process of writing this work. I would also like to thank my parents for their continuing support, even though I am moving farther and farther away from them. Special thanks go to my lovely wife Amy for supporting me in this quest even though it meant a time of separation which felt like an eternity.

Contents

Preamble

After some internal debate I decided that in my Thesis, presented here, “I” will be used whenever the text speaks about decisions I made. “We” will be used in the text when decisions or conclusions have been made in a collaborative fashion, and when I give explanations, proofs or derivations, It will also be the default tone of voice.

Chapter 1

Introduction: Dopamine in the Striatum of the Basal Ganglia

The Basal Ganglia are a set of subcortical nuclei, that includes the striatum, globus pallidus, subthalamic nucleus (STN) and the substantia nigra, so named for its dark color. Of special interest for this work are the striatum, one of the the principal input structures of the Basal Ganglia, and the subtantia nigra pars compacta, which sends dopaminergic projections towards the striatum. The principal neurons of the striatum are medium spiny neurons (MSN) (Kemp and Powell, 1971), which are a special form of GABA-ergic i.e. inhibitory neurons. The Basal ganglia is involved in the action selection of motor behavior (Redgrave et al., 1999; Hikosaka et al., 2000) . On of the first models of basal ganglia function proposed a separation of pathways starting from the striatum into a direct and an indirect pathway, based on anatomical separation (Albin et al., 1989). In this model the direct pathway projects to the Substantia Nigra pars reticulata and the Globus Pallidus interna, while the projections of the indirect pathway end up in the Globus Pallidus externa. The direct pathway is named that way since it directly projects to striatal output structures which in turn send inhibitory projections to the thalamus, suppressing movement. The direct pathway promotes movement, since activation of the direct pathway inhibits the neurons in the output nuclei that suppress movement. The opposing, indirect pathway, suppresses movement, by inhibiting the globus pallidus externa which in turn inhibits the STN which excites the striatal output structures and therefore suppresses movement. For this reason these pathways are also often called Go and No-Go pathways. An interesting feature of this model is that the anatomically distinct neurons of the different pathways have also physiological differences. One of the most interesting differences is that the neurons of the different pathways express different dopamine receptors (Gerfen et al., 1990; Le Moine and Bloch, 1995). These DA receptors are generally classified as D1 and D2 type receptors. In turn the different MSN types are called D1-MSN and D2-MSN. It should be noted that D1 type receptors are a family containing the D1 and D5 receptors, and D2 type receptors are a family containing D2, D3, D4 receptors. However generally the D1 and D2 receptors themselves are

most numerous. These receptor types also have diametrically opposed effects on the MSNs. Activation of D1 receptors tends to make MSNs more excitable while activation of D2 receptors tends to make MSNs less excitable (Gerfen and Wilson, 1996; Surmeier et al., 2007; Gerfen and Surmeier, 2011). Since they are both DA receptors, that means that in the model different levels of DA lead to a bias either towards the direct, Go, circuit or towards the indirect, No-Go, circuit. In the model that means that DA plays an important role in action selection by biasing the Basal Ganglia either towards action taking or action suppression. The model is also able to successfully explain the bradykinesia of Parkinsons disease (PD). One of the clinical signs of PD is the death of dopaminergic neurons in the Substantia nigra pars compacta (Jellinger, 2002). During PD the amount of dopaminergic neurons innervating the striatum reduces. In the model it is assumed that this leads to a reduction in DA concentration in the striatum, biasing the system towards the No-Go pathway which leads to trouble initiating movement. Sadly, the model turned out to be not entirely correct, the organization and function of the Basal Ganglia is more complicated than initially assumed (Redgrave et al., 2010; Calabresi et al., 2014; Nelson and Kreitzer, 2014). However the interesting problem of the separation of MSNs into distinct classes with different DA receptors and their modulation through DA remains. In this work I am less interested about the specific makeup of the Basal Ganglia circuits, and more about how the MSNs in the striatum are modulated through DA.

1.1 Dopamine

DA modulates the function of the striatum, however this modulation it is not as straightforward as I implied above. I made it look like the function of DA simply changes the excitability of MSNs, however that was an oversimplification. DA has complex effects on the activity of striatal neurons and seems to have a myriad of functions within the Basal ganglia. On a physiological level it changes their excitability (Day et al., 2008), depending on the type of DA receptors (D1 or D2) the MSNs posess, and can change the strength of synaptic inputs (Reynolds et al., 2001; Reynolds and Wickens, 2002). These seemingly simple physiological effects lead to its diverse roles in motor control (Syed et al., 2016), action-selection (Redgrave et al., 2010), reinforcement learning (Schultz, 2007), motivation (Phillips et al., 2008) and addiction (Everitt and Robbins, 2005). However what the exact mechanism of DA in all these roles is remains a matter of debate.

DA usually is being implicated with a motivational function, however the specifics of this relation are complex and sometimes difficult to unravel. It is also generally referred to as the reward system, but exactly what this means with relation to reinforcement and motivation is hard to pin down (Salamone and Correa, 2012). In popular literature it is often stated that DA codes for "pleasure" or "liking", possibly because of its role in reward processing. However it has been established that "liking" and "wanting" are neurobiologically dissociable, meaning they do not have to coincide. Furthermore experiments indicate that DA does not code for "liking", but infers a motivational "wanting" component referred to as incentive salience (Berridge and Robinson, 1998;

Berridge, 2007).

Dopaminergic neurons fire in a way that is consistent with them acting as a reward prediction error (RPE) (Schultz, 1998), meaning they fire when an unpredicted reward is presented and show reduced firing when a predicted reward is not delivered. This RPE type firing has been shown to be causally linked to cue reward type learning by showing that stimulation of dopaminergic neurons at the time of reward delivery cancels blocking (Steinberg et al., 2013). This learning role of the DA system fits well with its function in modifying synaptic strengths. The RPE responses have not just been detected in the firing of dopaminergic neurons, but have also been directly measured in the DA concentration (Hamid et al., 2016). However they are superimposed on a ramping DA signal that seems to increase with the approach to a goal, which is believed to be more motivational in nature (Hamid et al., 2016).

DA also plays a role in Action selection believed to be facilitated by the different effects of the D1 and D2 receptors on the excitability of MSNs (Redgrave et al., 2010). This role in action selection was first proposed due to the motor symptoms observed in PD. PD first presents clinically as a loss of dopaminergic neurons in the Substantia nigra pars compacta, which is believed to change dopaminergic signaling which in turn leads to the motor-symptoms. However, that role in action selection is more complicated than initially imagined in the simple Go, No-Go pathway model mentioned above. One theory is that DA influences if behaviour is executed in a goal-directed or habitual fashion (Redgrave et al., 2010). The disruption of the DA system during PD leads, in this model, to a an overreliance on behaviour executed in the goal-directed mode.

On top of that DA also plays an important role in drug addiction since a number of drugs of abuse, e.g. cocaine, directly influence the DA system and therefore bypass the normal adaptive processes related to normal rewards(Di Chiara and Bassareo, 2007). This change of the DA concentration seems to interfere with the normal motivational and learning function of DA. Addiction seems to consist of two parts: First, context independent e.g. compensatory adaption processes like altered presynaptic release. Second context dependent e.g. conditioned responses to drug related stimuli (Berke and Hyman, 2000). The context dependent part of addiction can be seen as a type of learning gone wrong activating a compulsive stimulus response behavior which could indicate a mismatch between the goal directed and habitual execution of behaviors.

To complicate matters the differing functions of DA are assumed to happen on differing timescales (Niv et al., 2007) as does the striatal DA concentration ([DA]) (Schultz, 2007). Fast, abrupt increases in [DA] lasting for $\approx 1 - 3s$ result from phasic bursts in DA neurons (Roitman et al., 2004), which signal reward-related information (Schultz, 2007; Grace et al., 2007). Slightly slower [DA] ramps occur when rats approach a goal location (Howe et al., 2013) or perform a reinforcement learning task (Hamid et al., 2016). Finally, slow tonic spontaneous firing of DA neurons controls the baseline [DA] and may change on a timescale of minutes or longer (Grace et al., 2007). However, if these fast and slow changes in [DA] actually represent distinct signalling modes has recently been called into question (Berke, 2018).

On top of all this DA is distinct from other neurotransmitters like GABA and Glutamate in that it is volume transmitted (Cragg and Rice, 2004; Rice

and Cragg, 2008). It does not just get released at a presynaptic element and acts by activating the postsynaptic receptors, rather it can leave the synaptic cleft (Garris et al., 1994) and distribute in space, activating receptors not only on the postsynaptic element but farther away. This is corroborated by finding DA receptors predominantly at extrasynaptic locations (Hersch et al., 1995; Sesack et al., 1994). Furthermore, Dopamine transporters (DAT), that remove DA from the extracellular space (ECS) of the striatum are found in extrasynaptic locations (Nirenberg et al., 1996). The efflux of glutamate out of its synapses is largely limited by the high density of glutamate transporters close to the synapses (Lehre and Danbolt, 1998). However the density of DAT is much lower (Garris et al., 1994) and DAT are removing DA at a lower rate than the glutamate transporters, further strengthening the case for volume transmission of DA. Volume transmission leads to DA not only having a time-component, but also a spatial component. This spatio-temporal distribution of DA could be quite complicated but has not been studied extensively. Often it is even implicitly assumed that the DA concentration only has a time-component, and no microscopic spatial structure (e.g. Schultz 2002). Presumably since experimental results usually did not allow for a spatial resolution $< 10\mu m$ (Kelly and Wightman, 1986).

What should also be kept in mind when thinking about the DA system in the Basal Ganglia, is that the studies performed use very different experimental techniques. Some studies measure neural activity of dopaminergic neurons directly (Schultz, 1998), while others measure DA concentrations (Hamid et al., 2016; Floresco et al., 2003). Some techniques measure DA concentration directly (Floresco et al., 2003) while others measure changes relative to a reference (Hamid et al., 2016). In principle all these measurements should be related, however how exactly they fit together is not always straightforward. Some features e.g. the DA ramps, can be seen in DA concentration measurements, while seemingly not having a counterpart in the neural activity of dopaminergic neurons. Furthermore, depending on the utilized technique the interpretation of seemingly similar measurements can be quite different e.g. a value signal measured with FCSV could masquerade as an RPE type signal (Berke, 2018).

All in all DA has a lot of functions that are related, however the exact nature of this relation is currently still under debate. DA acts on different timescales that may or may not represent distinct signalling modes. It interacts with two different main receptor types D1 and D2 which have opposing effects on the neurons that express them. Additionally it is volume transmitted which leads to a spatial component of the DA signal the significance of which is largely unclear. On top of that studies of the DA system utilize a lot of different experimental techniques sometimes giving conflicting results whose connection is unclear. In summary the DA system still poses a lot of open questions on which a good model could shed some light.

1.2 Theory and Modelling

This thesis is an almost exclusively theoretical work concerned with mathematical and computational modeling. What is the purpose of such a a work? First,

this thesis is not a big data work. It seems like there is an increasing sentiment that more data in combination with machine learning (sometimes also called artificial intelligence) will solve all the problems in neuroscience and other fields. However I don't believe this sentiment. Of course machine learning will find its place in the toolkit of any (neuro-)scientist and it is a powerful tool, however I believe it will not solve as many problems as promised. Essentially, I think, these new methods are very effective in finding correlations, together with large datasets they will be able to find a lot of correlations. However as the old adage goes "correlation does not mean causation". Without knowing why phenomena are correlated we cannot reach a full understanding of the underlying system. One task of theory and modelling is finding the mechanisms of correlations. That means that one goal of theoretical work is not necessarily hypothesis testing, but rather hypothesis generation, which in the eyes of at least one of my colleagues makes it unscientific. I would like to stress that this is different from finding a correlation in the data. Finding the correlations is akin to the question "Is there a connection?" while finding the mechanism answers the question "Why is there a connection?". The generated hypothesis can then subsequently be tested, however these tests might not be in the realm of theory anymore.

Hypothesis generation is not the only goal of theory. Theory and modeling have another purpose: assembly of information. Taking pieces of knowledge and trying to assemble them into a model which, hopefully, functions as expected. However if it doesn't than one of the mechanisms in the model is likely to be wrong. The goal of the modeler is then to figure out which part does not fit. This type of theoretical work is more closely related to hypothesis testing, and therefore in the eyes of my colleague "real science".

These two aspects of modeling work cannot always be disentangled, usually building a model aims to do both. It tests if the parts of the model fit together, and if they do can predict behavior that has not been measured yet. A functioning model is a powerful tool, since we have full control over all aspects of it, and can quickly and cheaply do e.g. pharmacological modifications and can predict what their outcome should be. At this point I also believe we can say we have a decent grasp of the system that is being modeled, to paraphrase Donald Knuth: "Science is what we understand well enough to explain to a computer."

1.3 Model goals, hopes and dreams

The DA system presents a fruitful landscape for extensive modelling since there are still a lot of open questions and unexplored connections between different experimental approaches. However, I had to choose a focus for what kind of model I wanted to design. After reviewing the literature I decided to design a model focused on the volume transmission aspect of DA, an aspect I believe has been largely neglected in past studies. There have been successful attempts on simulating volume transmission (Dreyer et al., 2010; Dreyer and Hounsgaard, 2012), however usually the focus of these studies was not investigating the spatial structure of the DA concentration in detail but on the averaged DA timelines that are generated. There seems to be the general opinion that the DA concentration in the striatum can be seen as a monolithical value i.e. it can be seen as a bath that has the same value independent on location and only changes with respect to time. Investigating if this is true was the first goal for this model.

The model was designed to study the spatio-temporal distribution of DA in the striatum, to see if there is a spatial structure, or if the general view that the DA concentration can be seen as a constant value in space holds. Additionally I aimed to address the question how DA interacts with its receptors. Here again the focus was on the spatial distribution of receptor activation as an extension of the spatial distribution of DA. If there is a spatial structure in the DA or DA receptor activation then theories of higher order function, like learning and motor control, should be cognizant of it since the MSNs leading to this higher order function will, through there receptors, see a signal that is not only dependent on time but also on there position in the striatum.

The model simulates the DA diffusion and receptor interaction in the striatum while trying to be as biologically realistic as possible. The attempt to make the model as biologically realistic as possible is used here to get the best possible results, but also as a test of consistency between models of higher order function and the known low level details of the DA system. The model is kept as realistic as possible in places where it is hard to estimate the exact effect of the modeled details, however approximations are used when it is easy to argue that the effects will be small e.g. the incorporation of unspecific uptake. As a secondary goal the model also aims to create a connection between different experimental approaches, specifically dopaminergic neuron firing and direct DA concentration measurements.

The model presented in this work can be seen, as a sort of bottom up approach for the understanding of DA function. In this capacity it does not directly address high order function as such, however I believe that an incomplete understanding of these low order processes will seriously hamper the understanding of higher order function.

1.4 Thesis Outline

In this thesis I aim to present the computational model of DA diffusion in the striatum I developed during my PhD studies.

In **Chapter 2** I will present a short overview about the basic theory of diffusion, and diffusion in porous media which will be the theoretical foundation of the computational model.

Chapter 3 will give a short overview about numerical models that can be used to solve the diffusion equation, with source terms. I will introduce some common pitfalls and explain the numerical method I used in the work presented here. Furthermore I will show that the code I developed solves the diffusion equation correctly.

Chapter 4 introduces the model I developed to generate synthetic axons, which in turn are used to introduce inhomogeneous uptake and realistic synaptic positioning into the diffusion model. This chapter also explains the generation of spiketrains for the dopaminergic neurons.

In **Chapter 5** I will introduce the receptor activation model that is based on realistic receptor kinetics that I developed, at first, to provide realistic source

and sink-terms for the diffusion model. However, the implications of DA receptors having kinetics that are not instantaneous are quite broad and will be discussed in this chapter. The work from this chapter has also already been uploaded to biorxiv `https://doi.org/10.1101/444984` .

Chapter 6 Will show the results of the simulations done with the full model. Mainly showing that the DA landscape is very inhomogeneous, and that the anatomy, synaptic positions and uptake distribution, has an important impact on the DA receptor activation maps.

Chapter 7 will provide a short discussion of the findings of this work.

Chapter 2

Introduction: Modelling Dopamine Diffusion

The main part of my thesis treats diffusion of dopamine (DA) in the striatum. Why am I interested in the diffusion of DA? After all, most models of neural networks do not explicitly treat diffusion to explain the effects of excitatory or inhibitory neurons. The difference between these neural network models and DA neuromodulation is that, in contrast to other neurotransmitters, DA does not only act on the postsynaptic element but can leave the synaptic cleft and distribute in the vicinity of the release site (Cragg and Rice, 2004; Arbuthnott and Wickens, 2007; Liu et al., 2018). This is commonly known as volume transmission. How this extrasynaptic DA distributes in the surrounding extracellular space (ECS) is governed by diffusive processes. An implicit assumption in this work is that their is no bulk flow in the ECS. In other words I assume that the extracellular medium does not flow inside the striatum. In this chapter I will give some background on the basics of diffusion and the derivation of the diffusion equation. Although I will refer to DA as the diffusing molecules the derivations presented in this Chapter are not specific for DA and also apply, with different parameters, to other volume transmitted molecules in the brain.

2.1 Diffusion basics: Microscopic random walk

First we look at how molecules diffuse in a solution, in our case DA molecules in water. Of course I did not originally come up with these arguments. The original, and more thorough, derivations can be found in Einstein (1905) and Von Smoluchowski (1906). One form or another of these derivations can be found in any physics textbook treating diffusion e.g. (Feynman et al., 1965).

To help with the derivation I will reduce the problem to its simplest form, and will only treat a one dimensional case. Diffusion is the result of Brownian motion, which can be described as a random walk. Molecules in a solution travel in a straight line and will change direction when they collide with another molecule. The, in liquids, typically quite short average distance that they travel unimpeded is called the mean-free path l. Our first simplifying assumptions are that all the dopamine molecules move with the same speed, the average molecule speed v, and collide after traveling a distance l, the mean free path. Between

collision the time $\tau = l/v$ passes. After each collision the particles moves into a new randomly chosen direction. There is no preferred direction so all directions have the same probability. With these assumptions, how does a large number of molecules, in one dimension, spread with increasing time? Initially, at $t = 0$, we place all the molecules at position $x = 0$. We define the mean position after n time-steps as

$$\langle x(n) \rangle = \frac{1}{N} \sum_{0}^{N} x_i(n) \tag{2.1}$$

with $x_i(n)$ the position of the i-th molecule after n steps. After n steps the position of a molecule is given by

$$x(n) = x(n-1) \pm l \tag{2.2}$$

the position after $n-1$ steps plus the movement in the last step. Then the mean position after n steps, combining **Eq. 2.1** and **Eq. 2.2** is

$$\langle x(n) \rangle = \frac{1}{N} \sum_{0}^{N} x_i(n-1) \pm l = \frac{1}{N} \sum_{0}^{N} x_i(n-1) = \langle x(n-1) \rangle \,. \tag{2.3}$$

In the model case, steps in each direction have the same probability, so the $\pm l$ term averages to 0. The mean position of the molecules after n steps is the mean position after $n-1$ steps. We can apply this finding iteratively and find $\langle x(n) \rangle = \langle x(0) \rangle$, the mean position after n steps is the mean position of the initial distribution. In other words, the molecules spread symetrically around their initial position. How far do the particles spread? To quantify how far the molecules travel with respect to the number of steps we choose the mean-square displacement as our measure. It is defined as

$$\left\langle x^2(n) \right\rangle = \frac{1}{N} \sum_{0}^{N} x_i(n)^2 \tag{2.4}$$

since the square of a number cannot be negative, the average displacement must be larger than zero. Now we use **Eq. 2.2** to calculate the mean square displacement after n steps

$$\left\langle x^2(n) \right\rangle = \frac{1}{N} \sum_{0}^{N} x_i^2(n-1) \pm 2l \cdot x_i(n-1) + l^2 = \left\langle x^2(n-1) \right\rangle + l^2. \tag{2.5}$$

As before, the term that contains $\pm l$ averages to 0. The mean square displacement after n steps is the mean square displacement after $n-1$ steps plus l^2. Again we can apply the solution iteratively, and we find that $\left\langle x^2(n) \right\rangle = nl^2$. The mean square displacement is proportional to the number of steps. The number of steps in a time t is $n = t/\tau$. So the mean square displacement as a function of time becomes

$$\left\langle x^2(t) \right\rangle = \left(\frac{t}{\tau} \right) l^2 = \left(\frac{l^2}{\tau} \right) t = 2Dt \tag{2.6}$$

where in the last step, we defined a diffusion coefficient as

$$D = l^2/2\tau. \tag{2.7}$$

Eq. 2.6 shows that the mean displacement from the origin $\sqrt{\langle x^2(t)\rangle} = \sqrt{2Dt}$, grows with $\sqrt{t}$. Which means that molecules travel quickly over short distances, but take a long time to diffuse long distances. We can intuitively understand this phenomenon: the movement of the molecules is random so they are unlikely to travel in the same direction for a large number of consecutive steps which is required for a large displacement.

We defined the diffusion constant above to be dependent on l and τ. D generally depends on the diffusing molecule and the medium of diffusion, since different molecules will have different sizes, and therefore different mean free paths l in the medium. Furthermore, for a given temperature different molecules will have different mean velocities v since temperature is a measure for the mean kinetic energy of the molecules, and kinetic energy depends on mass. In turn the diffusion coefficient is also dependent on temperature since a higher temperature will lead to higher mean velocities v.

Our approach easily extends to three dimensions. For this we require the random walk to happen in each given direction. Assuming that the walks in x, y and z direction are independent of each other we get $\langle x^2\rangle = \langle y^2\rangle = \langle z^2\rangle = 2Dt$. We know that in three dimensions the squared distance to the origin is $r^2 = x^2 + y^2 + z^2$, so we get

$$\langle r^2\rangle = 6Dt. \tag{2.8}$$

The displacement grows faster in higher dimensions.

Above we restricted movement to a lattice. However the same arguments can be used to get results for a random walk in arbitrary directions when e.g. in 2 dimensions we let the movement be in a random direction given by the angle θ. We will still describe the location of the molecules in cartesian coordinates (x,y). The position in the x direction after n steps will then be $x(n) = x(n-1)+cos(\theta)l$, which since the full circle average of the cosine is 0, will be equal to the above result. The same is true for the y-coordinate $y(n) = y(n-1) + sin(\theta)l$. In the case of three-dimensional diffusion we have to add another angle to the movement direction but the same argument still holds.

2.2 Diffusion basics: Fick's Laws

The description given in the previous chapter allows us to calculate the displacement of molecules with time. However, it would be infeasible to calculate the changes of a distribution of DA in a volume by tracking all the dopamine molecules. What we require is a description that allows us to track how the distribution of DA in a volume changes in time due to diffusive processes. In this chapter I will try to use the microscopic description to arrive at such a evolution equation.

For this derivation we will stick with the random walk model for the molecules in solution. Again a form of this derivation can be found in any physics textbook that deals with diffusion (e.g. Feynman et al. (1965)). All calculations are treated as if movement of the molecules only happens along the x direction,

allowing us to treat the problem as a one dimensional problem, however the argument is easily extendable to two, three or more dimensions. First we look at the net flux of particles across a surface A. In the example we start with two adjacent volumes that have a number of number of molecules $N(x)$ to the left of surface A and $N(x+h)$ to the right of the same surface A, as illustrated in **Fig. 2.1**. Initially the volumes are separated by a barrier so that there can be no particle exchange between the two segments. At time t the barrier is removed so that a particle exchange can happen. What is the flux of particles across the surface A in the short time interval Δt after the barrier has been removed?

The molecules are moving around in random directions with speed v in the solution. Since there is no preferred direction half of the molecules will move to the left, and the other half will move to the right. The number of molecules moving from the left to the right segment during the short time interval Δt is then $\frac{N(x)}{2}$.

So the flux, the amount of particles flowing through a unit area per unit of time across the surface A to the right, is

$$j_R = \frac{1}{2}\frac{N(x)}{A\Delta t} \tag{2.9}$$

while the flux to the left is

$$j_L = -\frac{1}{2}\frac{N(x+h)}{A\Delta t}. \tag{2.10}$$

We define the flux j_L as negative since the flux is oriented to the right. The net flux across the surface A is simply the sum of both fluxes:

$$j = j_R + j_L = \frac{1}{2}\left[\frac{N(x)}{A\Delta t} - \frac{N(x+h)}{A\Delta t}\right]. \tag{2.11}$$

After expanding the fraction with h^2 and rearranging we end up with:

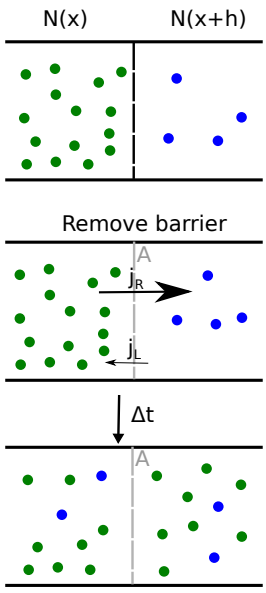

Figure 2.1: The diffusive flux points from regions with high concentration to regions with low concentration.

$$j = \frac{h^2}{2\Delta t}\left[\frac{N(x)}{Ah^2} - \frac{N(x+h)}{Ah^2}\right]. \tag{2.12}$$

Concentration is defined as particles per unit volume, so we can substitute

$$C(x) = \frac{N(x)}{Ah}. \tag{2.13}$$

Furthermore, we define the prefactor

$$D = \frac{h^2}{2\Delta t} \tag{2.14}$$

We will see below why it is prudent to call this prefactor D. So we are left with

$$j = D\left[\frac{C(x)}{h} - \frac{C(x+h)}{h}\right]. \tag{2.15}$$

When taking the limit of h being infinitesimally small the right hand side becomes a spatial derivative leading to

$$j = -D\frac{\partial C}{\partial x} \tag{2.16}$$

which is commonly known as Fick's first law, named after Adolf Fick who first proposed and empirically verified the law (Fick, 1855). The additional minus sign originates from the definition of the derivative. **Eq.2.16** shows that the molecule flux is proportional to the derivative of the concentration of the diffusing molecules and, due to the negative sign, points from regions of high concentration to regions of low concentration.

In **Eq. 2.14** we defined the proportionality factor D. We stated in **Section 2.1** that the molecules in the solution perform a random walk with a step size l and a mean velocity v. Then the distance traveled h in a time Δt will be, $h = v\Delta t$. We can replace Δt with the mean time between collisions $\tau = l/v$ and are left with $l = h = v\tau$. Substituting $l = h$ and $\Delta t = \tau$ into **Eq. 2.14** we arrive at

$$D = \frac{l^2}{2\tau} \tag{2.17}$$

the diffusion coefficient as defined in **Section 2.1**. Hence why we called it D here as well.

The arguments presented here also hold for multiple dimensions. Extending Fick's first law to three dimensions requires replacing the derivative in **Eq. 2.16** by the three dimensional nabla operator $\nabla = (\frac{\partial}{\partial x}, \frac{\partial}{\partial y}, \frac{\partial}{\partial z})$. Then Fick's first law in three dimensions reads

$$\vec{j} = -D\nabla C \tag{2.18}$$

with $\vec{j}$ the vector of diffusion.

Fick's first law allows us to calculate the diffusive flux for a given concentration distribution. It does not describe the changes in a given concentration distribution directly, however we can use the fluxes to calculate the evolution, due to diffusion, of a given concentration distribution in time. **Eq. 2.16** tells us where DA flows to if we have a concentration gradient. If there are no sources or sinks of dopamine in the domain, the only changes of the dopamine concentration at a location x are due to the diffusion flux. This is commonly known as the continuity equation (in the surface integral form):

$$\frac{\partial C}{\partial t} + \oiint_{S(V)} \vec{j} \cdot dS = 0 \tag{2.19}$$

where S is the surface enclosing the volume in which C is measured. **Eq. 2.19** means that the changes of the concentration $\frac{\partial C}{\partial t}$ are caused by the diffusive flux $\vec{j}$ through the surface of the volume V in which C is measured. The change in concentration is exactly the amount of diffusive flux out of or into the volume since the right hand side is zero (no sources or sinks). In short, no DA is

created or destroyed by diffusion. We can utilize the divergence theorem to rewrite **Eq. 2.19** as a differential equation

$$\frac{\partial C}{\partial t} + \nabla \cdot \vec{j} = 0. \tag{2.20}$$

which can be interpreted as: the change in concentration $\frac{\partial C}{\partial t}$ is caused by the sources of diffusive flux. We already know the value of the diffusive flux, so we can substitute **Eq. 2.18** into **Eq. 2.20** and arrive at

$$\frac{\partial C}{\partial t} - D(\nabla \cdot \nabla)C = 0, \tag{2.21}$$

where we implicitly assumed that D is a constant that does not depend on the location in the test volume. $(\nabla \cdot \nabla)$ is also known as the Laplace operator which is usually denoted by $\triangle$ or ∇^2 and is the sum of all unmixed second derivatives in cartesian coordinates. So after rearranging we find the diffusion equation in a homogeneous medium without sources or sinks (Fick, 1855)

$$\frac{\partial C}{\partial t} = D\nabla^2 C, \tag{2.22}$$

which is also referred to as Fick's second law. **Eq. 2.22** allows us to evaluate the changes in DA concentration, purely from the current concentration landscape. That means if we have a given concentration distribution, we can integrate it in time and find the concentration landscape at later points in time.

2.3 Diffusion in a porous medium

The equations derived in **Section 2.2** are valid for the diffusion of DA in water. However the brain is not just the ECS but is also full of cells, blood vessels and other obstacles to free diffusion. We can treat diffusion in he the brain like the diffusion in a porous two-phase medium (e.g. Nicholson 2001). The phases in this context are the ECS as the first phase and the cells and other obstacles as the second phase.

The common approach for treating porous media is by defining a volume over which the concentration of the diffusing substance, in our case DA, is averaged (Whitaker, 1985). This averaging volume should be small enough to have local meaning since if it is too large , e.g. half of the striatal volume, local concentration fluctuations will be smoothed out. However the dimension of the averaging volume should be larger than the mean pore diameter (Whitaker, 1969) so that strong, small scale, fluctuations within a pore are smoothed out and we don't have to treat those local inhomogeneities. This is directly related to the size of the phenomenon to be studied. I am not studying the microdiffusion within the interstitial space, I am interested in the DA concentration distribution in a volume of the striatum in the $\approx 100\mu m$ scale. At this scale the volume averaging approach has the advantage that we do not have to explicitly treat the geometry of the two phases, i.e. we do not have to know the precise geometry of the cell-ECS boundary. Below we will also see that, when treating the diffusion with this approach, the precise geometry of the cell-ECS boundary does not matter for the diffusive processes.

As said above, we want to choose an averaging volume larger than the mean pore diameter. What is the mean pore diameter in the brain? I decided that the average size of the interstitial spaces would be a good estimate for the mean pore diameter d. The size of the interstitial spaces is around $d = 0.05\mu m$ (Nicholson and Phillips, 1981; Syková and Nicholson, 2008) so our minimum averaging size should be at least an order of magnitude larger, around $1\mu m$. The averaging volume will be called V, however it will contain sub-volumes of both phases so that the volume of the ECS, denoted by V_0 within the averaging volume will $V_0 < V$. The parameter describing the ratio

$$\alpha = \frac{V_0}{V} \tag{2.23}$$

is called the volume fraction, and is usually taken to be around 0.15 to 0.2 in the brain (Lei et al., 2017).

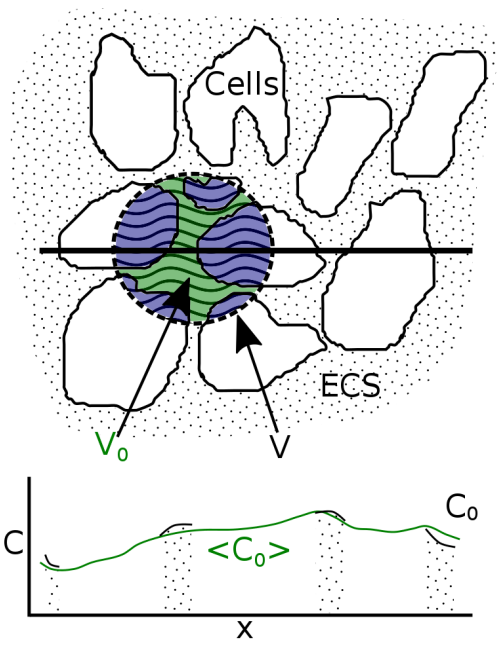

Figure 2.2: Sketch of diffusion in a porous medium. The averaging volume V is moved through the domain along the black line, to find a spatially averaged continuous value $\langle C_0 \rangle$ for the discontinuous distribution of C_0. The volumes shown are the averaging volume V and the ECS volume within the averaging volume $V_0 = \alpha V$. The non-averaged concentration in the ECS C_0 only exists on discontinuous areas of the tissue volume, whereas the spatially averaged value $\langle C_0 \rangle$ has a continuous value on the whole domain.

The concentration of the diffusing substance in the ECS is C_0, but before the spatial averaging its value is discontinuous because we do not have values of C_0 inside the second phase, the intracellular space. We move the averaging volume across the whole domain and assign the spatially averaged concentration to the position of the centroid of this averaging volume leaving us with a smoothed representation of the concentration of the diffusing substance in the ECS (see **Fig. 2.2**). We use an averaging procedure for any variable ϕ (Whitaker, 1969; Gray and Lee, 1977):

$$\langle \phi \rangle = \frac{1}{V} \int_{V_0} \phi \; d^3x \tag{2.24}$$

with the assumption that $\phi = 0$ outside of V_0. That does not mean that there can be no dopamine inside the non-diffusing phase (in this case the neurons and glia cells). It simply means that we do not take intracellular dopamine into account, for the diffusion model. DA uptake and release will be treated purely as sources and sinks of dopamine (see below).

We can use the averaging procedure to develop the diffusion equation for a porous medium. To do this we apply the averaging procedure **Eq. 2.24** to Fick's first law **Eq. 2.18** under the assumption that D is a constant:

$$\left\langle \vec{j} \right\rangle = -D \left\langle \nabla C_0 \right\rangle . \tag{2.25}$$

The spatial average of the gradient ∇C_0 is not straightforward and leads to (Gray and Lee, 1977):

$$\langle \nabla C_0 \rangle = \nabla \langle C_0 \rangle + \frac{1}{V} \int_A C_0 \vec{n} \, d^2x. \tag{2.26}$$

This averaging complicates the equation with another integral over the surface A, which is the interface between the ECS and the intracellular space. In the integral $\vec{n}$ (the vector normal to the surface A) points away from the ECS into the cells. The interpretation of this integral is not straightforward. However (Lehner, 1979) showed that the function that relates $\langle \nabla C_0 \rangle$ to $\nabla \langle C_0 \rangle$ must be a linear transformation of the form

$$\langle \nabla C_0 \rangle = \boldsymbol{K} \nabla \langle C_0 \rangle , \tag{2.27}$$

which leaves us with Fick's first law in a porous medium

$$\left\langle \vec{j} \right\rangle = -D^* \nabla \langle C_0 \rangle = -D\boldsymbol{K} \nabla \langle C_0 \rangle \tag{2.28}$$

here $D^* = D\boldsymbol{K}$ is the effective diffusion coefficient in the medium. $\boldsymbol{K}$ is a rank 2 tensor describing the ease of diffusion through the tissue. In a free medium $\boldsymbol{K} = \boldsymbol{I}$ (where $\boldsymbol{I}$ is the identity matrix) since there is no interface of the two phases, which leads to the surface integral in **Eq. 2.26** to be zero (since the area $A = 0$), so that $\langle \nabla C_0 \rangle = \nabla \langle C_0 \rangle$. That means we recover Fick's law for a free medium, if there is no second phase, a nice sanity check. What is the meaning of $\boldsymbol{K}$ in the porous medium? $\boldsymbol{K}$ contains the information how the velocity of diffusion depends on direction in the given medium. Specifically $\boldsymbol{K}$ can be identified with the reciprocal of a parameter known as tortuosity (λ) of the medium. In an isotropic medium $\boldsymbol{K}$ becomes a scalar since the diffusivity does not depend on direction. So for an isotropic porous medium we can write

$$D^* = \frac{D}{\lambda^2}, \tag{2.29}$$

where the square is by convention and related to how tortuosity is defined in neuroscience. Usually $\lambda > 1$, so $D^* < D$, meaning that diffusion in a porous medium like the brain is typically slower than in a free medium. This slowdown is due to an increase in path length between two points caused by obstacles in the porous medium. In short, the diffusing molecules have to bypass the cells in the brain, which increases the length of the shortest path connecting two points. However it is not possible to calculate the modified diffusion tensor from first principles directly, but direct measurements for the modified diffusion coefficient in the rat striatum exist (see Nicholson 2001).

What happens if the medium is non-isotropic? An anisotropic medium can lead to anisotropic diffusion, e.g. if the domain contains an axonal bundle. In

such a bundle, there will be less obstacles to diffusion along the axons than perpendicular to them, leading to a higher diffusivity along the main fiber direction than perpendicular to it. This is commonly used in a technique called diffusion-tensor imaging to map the fiber orientation of bundles (Jones and Leemans, 2011). The general definition of the diffusion tensor in three dimensions is:

$$D^* = \begin{pmatrix} D_{xx} & D_{xy} & D_{xz} \\ D_{yx} & D_{yy} & D_{yz} \\ D_{zx} & D_{zy} & D_{zz} \end{pmatrix} \tag{2.30}$$

with the diagonal elements D_{xx}, D_{yy}, D_{zz} describing the diffusivity along the cardinal directions of the (cartesian) coordinate system, and the off-diagonal elements describing correlations between movements along each pair of the cardinal components. D^* has to be symmetric, since the diffusivity in the e.g. $x \to y$ direction should be the same as the in the $y \to x$ direction. Altough D^* can describe general anisotropic diffusion, it does so with respect to the coordinate system used. That means that the direction of fastest diffusion does not have to align with any of the cardinal directions, e.g. if an axonal bundle lies along the $x = y = z$ the direction of fastest diffusion would not be along any of the cardinal directions. In this case D^* will have off-diagonal elements that are non-zero. In the model I treat the rat striatum as an isotropic medium, with one diffusion coefficient as described above. However the model code I wrote to solve the diffusion equation can treat anisotropic diffusion as long as the anisotropy can be described with a diffusion ellipsoid. This description assumes that the anisotropy of the diffusion is oriented in a way so that the direction of highest diffusivity aligns with one of the cardinal directions of the coordinate system. In such a case there will be no off-diagonal elements of D^* making the numerical solution more efficient and a lot easier. However that is not a serious limitation since the orientation of the coordinate system of the model can be chosen freely and it is possible to transform a general D^* into the corresponding D^* described by a diffusion ellipsoid. This is equivalent to changing the coordinate system in which D^* has been measured. This change of coordinate system can be performed by calculating the eigen-decomposition of D^*. The orthogonal eigenvectors will then be the cardinal directions of our new coordinate system. The eigenvectors will be orthogonal since D^* is symmetric. The diffusion coefficient along each direction will be given by the corresponding eigenvalues $(\lambda_1, \lambda_2, \lambda_3)$. It is convention to order the eigenvalues from largest to smallest. The diffusion tensor in the new form is then

$$D^*_{ellipse} = \begin{pmatrix} \lambda_1 & 0 & 0 \\ 0 & \lambda_2 & 0 \\ 0 & 0 & \lambda_3 \end{pmatrix}. \tag{2.31}$$

So if we want to treat anisotropic diffusion in our model, we will have to align the direction of highest diffusivity with the coordinate system of our simulation domain so that we can replace D_1, D_2, D_3 in **Eq. 3.70** with $\lambda_1, \lambda_2, \Lambda_3$ (see **Section 3.4**).

We already derived Fick's first law for the porous medium. However like in the free diffusion case, we want an equation that we can use to evolve the concentration of the neurotransmitter in the porous medium in time. As in the

free diffusion case we apply the continuity equation **Eq. 2.20**, however this time we have to apply spatial averaging before we continue

$$\left\langle \frac{\partial C_0}{\partial t} \right\rangle + \left\langle \nabla \cdot \vec{j} \right\rangle = 0 \tag{2.32}$$

(we assume again that there are no sources or sinks of neurotransmitter). The averaging theorem leaves us with

$$\left\langle \nabla \cdot \vec{j} \right\rangle = \nabla \cdot \left\langle \vec{j} \right\rangle + \frac{1}{V} \int_A \vec{j} \cdot \vec{n} \; d^2x \tag{2.33}$$

This time the surface integral has a more straightforward interpretation. It describes the diffusive flux through the cell membranes. If the cell membranes are impermeable to dopamine diffusion i.e. $\vec{j} \cdot \vec{n} = 0$ then the surface integral is zero too, leading us to conclude that for such a model

$$\left\langle \nabla \cdot \vec{j} \right\rangle = \nabla \cdot \left\langle \vec{j} \right\rangle . \tag{2.34}$$

In case of of a permeable membrane with a flux that is proportional to the gradient across the membrane, with a proportionality coefficient k (as expected from diffusion) we get

$$\vec{j} \cdot \vec{n} = k(C_0 - C_{in}) \tag{2.35}$$

where C_{in} is the concentration of DA inside the cell phase (which we will set to 0 since we do not treat DA in the cells). This formulation leads to a sink term which will be treated below.

We still need to find the value for the spatially averaged time derivative in **Eq. 2.32**. We use a second spatial averaging theorem from Gray and Lee (1977), in which the additional surface integral term depends on the velocity with which the phase interface is moving. For the timescales of the model the neurons and glia cells in the brain should be stationary, meaning this velocity is zero, which leads to

$$\left\langle \frac{\partial C_0}{\partial t} \right\rangle = \frac{\partial \left\langle C_0 \right\rangle}{\partial t}. \tag{2.36}$$

In our model we are interested in the concentration of the neurotransmitter in the ECS, Till now the value $\langle C_0 \rangle$ is still using the spatial averaging over the whole tissue, as shown in **Eq. 2.24**; to calculate the concentration in the ECS, we have to divide by V_0, the volume of the ECS phase, instead of V the volume of the tissue. We can use the volume fraction α defined in **Eq. 2.23** to transform between values, of any variable ϕ, with respect to the ECS volume and the full tissue volume:

$$\langle \phi \rangle_0 = \frac{\langle \phi \rangle}{\alpha} \tag{2.37}$$

where $\langle \phi \rangle_0$ is the value of the variable that refers to the ECS.

Combining **Eq. 2.28** with **Eq. 2.34** and substituting the result together with **Eq. 2.36** into **Eq. 2.34** and transforming to the ECS volume with **Eq. 2.37** afterwards leads to:

$$\frac{\partial \left\langle C_0 \right\rangle_0}{\partial t} = D^* \nabla^2 \left\langle C_0 \right\rangle_0 \tag{2.38}$$

the diffusion equation for a spatially averaged neurotransmitter in a porous medium (since α appears on both sides we can remove it). When we compare

Eq. 2.38 with **Eq. 2.22**, we can see that they are analogous i.e. they have the same functional form. That means we can describe the diffusion in the ECS by free diffusion and concentration C with a diffusion tensor D^*. Where C describes the volume averaged concentration in the ECS, without us having to explicitly go through the spatial averaging step. So the main change from the free diffusion equation to the porous medium equation is the change from D to D^*. That is analogous to stating that diffusion in a porous medium macroscopically behaves like diffusion in a free medium, but with a (generally) smaller diffusion coefficient. So as long as we assume our averaging volume to be large enough solving the modified diffusion equations is equivalent of solving a full two phase model and spatially averaging afterwards. Due to this equivalence we will substitute $C = \langle C_0 \rangle_0$, and in all following equations C will refer to the spatially averaged concentration in the ECS, so the equation we will need to solve in **Chapter 3** is

$$\frac{\partial C}{\partial t} = D^* \nabla^2 C \tag{2.39}$$

2.4 Sinks and sources

In the previous section we showed that diffusion in a porous medium behaves like diffusion in a free medium with a different diffusion tensor. However, we were only looking at an equation that evolved a given neurotransmitter concentration distribution in time. We used the continuity equation **Eq. 2.20** to derive the evolution equation while assuming that there are no sources or sinks of DA so that the amount of neurotransmitter in the system is constant. In the model there will be sources of dopamine due to spiking and processes that remove DA from the system, e.g. removal of DA through the DA transporter (DAT), which will be called sinks. Here I will quickly discuss the modes of uptake and release of dopamine and will deal with the specifics of firing patterns, geometry and spike trains in **Chapter 4**.

2.4.1 Sources

How is spiking release treated in the model? Any source of dopamine contributes on the right hand side of **Eq. 2.32** with its source density $\langle q(x) \rangle / \alpha$. The source density relates to the amount of released neurotransmitter

$$\int_U q \; d^3x = \int_U \langle q \rangle \, d^3x = Q \tag{2.40}$$

where Q is the amount of neurotransmitter, in *mol*, in the released vesicle and U is the full simulation domain. Naturally the spatial averaging should not change the amount of neurotransmitter released so that the integral over q and $\langle q \rangle$ are equal. Of course the contents of a vesicle are not released uniformly in the whole simulation domain. I model a release event by releasing the entire content of a vesicle into the ECS instantaneous (which in the context of the numerical solution means $t_{release} < \Delta t$) and at a single location. Such a point source release will be smeared out in space by the spatial averaging, but Nicholson and Phillips (1981) showed that the error due to this smearing is negligible, so we can replace the spatial averaged point source $\langle q \rangle$ with q. Furthermore,

since we will solve the diffusion equation numerically on a discretized grid, the exact representation of a point source will not be possible anyway (see **Chapter 3**). Instead the source be averaged over the discretization volume (the spatial resolution of the simulation, which can be different from the spatial averaging V). This leads to the diffusion equation with a source term:

$$\frac{C}{\partial t} = D^* \nabla^2 C + \frac{q}{\alpha}. \tag{2.41}$$

Where we will add a DA concentration of $q = Q/V_{voxel}$ at the locations and times where a release event is happening.

Is it reasonable to represent point sources in this discretized manner? From microscopic diffusion theory we know that the mean travel distance of a molecule in three dimensions is

$$r^2 = 6Dt \tag{2.42}$$

so we can rearrange and get an estimate for the time in which the average molecule has traveled a distance r

$$t = \frac{r^2}{6D^*}. \tag{2.43}$$

So if we substitute r with the distance from the center to the corners of a cubical calculation cell of size Δx, $r = \sqrt{3}\Delta x$ and use a typical Δx of the simulations ($1\mu m$) we get travel times of $t < 1ms$. Dopamine released as a point source travels through the whole cell in less time than a typical timestep ($\Delta t = 1ms$), so we can conclude that the assumption that the released dopamine distributes in the calculation cell in a timestep is reasonable.
Where and when quantal release is going to happen in the model is governed by axonal geometry, active site positioning and the spiketrains of the dopaminergic neurons which I will treat in detail in **Chapter 4**.

Theoretically another source of dopamine is given by the unbinding from dopamine receptors. The relative importance of this source term depends largely on the kinetics of the receptors. However this topic requires a more extended treatment that will be given below and **Chapter 5**.

2.4.2 Sinks

With only sources of DA and no removal eventually the whole simulation domain would fill with an arbitrarily high DA concentration. Of course that doesn't happen since there are processes that remove DA. In the model we consider two forms of uptake. Linear unspecific uptake through the cell membranes which is quite slow, and specific, much faster, uptake of DA through the dopamine transporters (DAT).

The linear removal term models unspecific uptake through the cell membrane. Assuming that the cell membranes are not fully impermeable to dopamine so that we have to consider the flux across the ECS-ICS interface in the model. Nicholson (2001) showed that volume averaging for a flux of the form shown in **Eq. 2.35** leads to an uptake term

$$\frac{\partial C}{\partial t} = -k\sigma C = -k^{'} C \tag{2.44}$$

where σ is the volume average over the surface area over which the diffusive flux across the phases takes place. Like in the case of D^* the parameter $k^{'}$ can be derived from experiments and is 0.007^{-1} (Rice and Cragg, 2008). For this linear uptake model I treat $C_{in} = 0$, for simplicity. This treatment can be motivated by the assumptions that the intracellular compartment is large with respect to the extracellular one so that the local concentration behind the cell-membrane is low and there is some process that binds DA molecules removing them from the diffusion balance. Of course there can be other linear processes that remove dopamine from the ECS, e.g. enzymatic destruction of DA in the ECS. Adding any of these processes just requires a modification of the removal rate $k^{'}$. However to keep the model simple I choose to ignore them. As it stands the linear unspecific removal, is a quite slow process. For a DA concentration of $C_0 = 20nM$ the removal rate is going to be $\partial C/\partial t = 0.14nM/s$.

In addition of the linear removal term, there is specific, much faster, uptake of dopamine through the dopamine transporters. This uptake follows Michaelis Menten kinetics (see e.g. Nicholson 1995):

$$\frac{\partial C}{\partial t} = -\frac{1}{\alpha}\left(\frac{V_{max}C}{K_m + C}\right). \tag{2.45}$$

For this mechanism dopamine binds to the dopamine transporter (DAT) and is transported into the cell after binding. The processes are the same as for the receptor binding in **Chapter 5**. Implicitly it is assumed that the binding to the transporter is fast with respect to the dopamine fluctuations, so that a chemical equilibrium is reached. Under this assumption the fraction f of DAT that is bound to dopamine can be estimated with the help of the dissociation constant, here called K_m

$$f = \frac{C}{K_m + C} \tag{2.46}$$

which only differs from the uptake rate by the maximum uptake rate $V_{max} = [DAT]^{max}k_T$ which is a combination of the amount of DAT in the ECS and the rate with which DAT transports dopamine into the cell (k_T). This means that the maximum uptake rate is reached when all DAT are occupied and are transporting dopamine into the cell. Since individual DATs should have the same transport rate k_T (being the same molecule and all), V_{max} scales directly with the concentration of transporters in the ECS, which we will use in **Sec. 4** to calculate the V_{max} for inhomogeneous uptake. I will give the uptake constant V_{max} in units of μMs^{-1} with respect to the volume of the tissue V (dividing by α will then give the value for the ECS). This value is usually given between 0.6 μMs^{-1} to 1.0 μMs^{-1} (Nicholson, 1995; Wightman et al., 1988). With this V_{max} the removal rate at e.g. 20 nm dopamine would be around $\partial C/\partial t = 340.0\ nMs^{-1}$ which is orders of magnitude faster than the uptake due to diffusion through the cell membrane.

Even though in the striatum the uptake depends primarily on DAT (Morón et al., 2002), there are other processes that remove dopamine from the ECS. Dopamine is also taken up by serotonergic transporters (Berger and Glowinski, 1978) or ,in areas with low levels of DAT, norephinephrine transporters (Morón et al., 2002). We ignore uptake through serotonergic transporters since they

have a very low affinity for dopamine ($K_m = 78\ \mu M$; Larsen et al., 2011). However uptake through the serotonergic transporters could be comparatively more important in a Parkinsonian case when the amount of DAT declines with the amount of dopaminergic neurons (see **Chapter 4**).

Another sink of dopamine is given by the binding of dopamine to its receptors. As for the source term due to receptor binding the relative importance of this sink term depends largely on the kinetics of the receptors. However this topic requires a more extended treatment that will be given below and in **Sec. 5**.

2.4.3 Diffusion with sinks and sources and reaction terms

Finally we can combine the diffusion equation in a porous medium with source terms **Eq. 2.41** with the sink terms from **Eq. 2.45** and **Eq. 2.44** to arrive at

$$\frac{\partial C}{\partial t} = D^* \nabla^2 C + \frac{q}{\alpha} - k^{'} C - \frac{1}{\alpha}\left(\frac{V_{max} C}{K_m + C}\right) \tag{2.47}$$

which can be used to calculate the DA concentration map, over time, from a given initial map.
During the work on this project I also decided to implement interaction of dopamine with its receptors. Which is extensively discussed in Chapter **Chapter 5**. Here it should just be noted that when DA binds or unbinds from its receptors it is added or subtracted from the free DA in the ECS, the diffusing DA. If the binding and unbinding is fast it will have an influence on the diffusion processes by changing the available DA concentration in the ECS. I assume that receptors are not freely diffusing through the ECS but are locked in place in the cell membrane. So for the receptor component the diffusion coefficient is set to $D_{recp} = 0$. Instead of just solving the diffusion equation, we will now have to solve a system of equations for each spatial location

$$\begin{aligned} \frac{\partial C_{DA}}{\partial t} = D^* \nabla^2 C_{DA} + \frac{q}{\alpha} - k^{'} C_{DA} - \frac{1}{\alpha}\left(\frac{V_{max} C_{DA}}{K_m + C_{DA}}\right) \\ - k_{on}^{D1} C_{DA} C_{D1} + k_{off}^{D1} C_{DA-D1} \end{aligned} \tag{2.48}$$

$$\frac{\partial C_{DA-D1}}{\partial t} = k_{on}^{D1} C_{DA} C_{D1} - k_{off}^{D1} C_{DA-D1} \tag{2.49}$$

where C_{DA} is the DA concentration, C_{DA-D1} the concentration of D1 receptor bound to DA and C_{D1} the concentration of free D1 receptor. The amount of free receptor and bound receptor are linked by the equation $C_{D1}^{max} = C_{D1} + C_{DA-D1}$ where C_{D1}^{max} is the total concentration of receptors. The system shown here just treats one receptor type. More receptors add another equation but with different parameters. Binding to the receptor removes the DA from the ECS acting as a sink term for DA while unbinding returns DA to the ECS.

These equations do not have an analytical solution, so that **Chapter 3** will show which numerical methods I used to solve them.

Chapter 3

Introduction: Numerical Methods

In this chapter I will introduce numerical methods that can be used to solve parabolic partial differential equations like the the diffusion equation for a porous medium with source and sink terms that we derived in **Chapter 2**:

$$\frac{\partial C}{\partial t} = D^* \nabla^2 C + \frac{q}{\alpha} - k^{'} C - \frac{1}{\alpha}\left(\frac{V_{max} C}{K_m + C}\right). \tag{3.1}$$

There is a analytical solution to **Eq. 3.1** for a steady state, spherically symmetric problem with $k^{'} = 0$ (Simpson and Ellery, 2012). However we want to study the time evolution of the DA distribution, so calculating the steady state solution will not be sufficient. Furthermore, the distribution of DA in the model will not be spherically symmetric at all times. Since there is no analytical solution for the general case I am going to use a numerical method to solve **Eq. 3.1**. In this chapter I will give an overview over the considerations that were made while choosing the numerical method for solving **Eq. 3.1** and give some detail on how the chosen method influenced the setup of the model. I will motivate the use of a finite difference method (FDM) and describe how to construct such a method. Furthermore I will present considerations about stability and noise dampening of such FDM methods. I will describe how to expand FDM to more than one dimension, and introduce the precise method I am utilizing. I will also shortly talk about iteration, which is necessary for incorporating sink terms. I will also explain what kind of boundary conditions are implemented in the model.

3.1 Finite Difference Methods

3.1.1 Why a Finite Difference Method (FDM)?

In the model **Eq. 3.1** is solved by a high order FDM described in Gu et al. (2003). What is a FDM and why did I choose one for my solver? There are a number of different methods for solving partial differential equations like **Eq. 3.1**. The most common ones are Finite Element Methods (FEM), Finite

Volume Methods (FVM) and FDM. In all of this schemes the simulation domain is discretized, that means the value of the quantities to be calculated are only evaluated on a discrete set of points. This is done to transform differential equations into algebraic equations that can be solved by a computer. In the case of FEM schemes, the operators themselves are discretized by an appropriate method, e.g. a galerkin method (Ern and Guermond, 2013). However since this process is quite complicated and unfamiliar to me I decided against using a FEM. In FVM the idea is to draw a small volume around each point on which the field is to be evaluated, the changes of the value are then due to the flux through the surface of the drawn volume. FVM methods are conceptually closer to the surface integral formulation of the continuity equation **Eq. 2.19** than to the differential version shown in **Eq. 2.20** (see **Section 2.2**). As such FVM methods have the advantage of being automatically conservative, beause fluxes out of one volume have to be equal to the same flux entering a neighboring volume. Since evaluating a flux through a surface is fairly straightforward, FVM methods can easily deal with grids that have non uniform cell shapes and therefore are well suited to model volumes with arbitrary boundaries. FVM methods are also well suited for dealing with parameter discontinuities (e.g. changing diffusion coefficient D) when the cell boundaries are aligned with the discontinuity. However even though FVM have these advantages I decided use a FDM for solving **Eq. 3.1**. Why? FDM schemes work directly with the equation to be solved. The idea is to replace the derivatives in the presented equation by an algebraic equation that gives an approximation of these derivatives. That can be a quite tedious and complicated task if the given grid is non-uniform. However we can choose the shape of the domain we want to solve **Eq. 3.1** on. We do not treat the biological geometry explicitly as explained in **Section 2.3** so the shape of our domain is largely left to our devices. So we can choose a cubic domain, and divide this domain into uniform cubic cells so that the discretization is easy within the framework of an FDM. Furthermore, we do not expect there to be large abrupt changes in the diffusion constant D so the problem that FDM might have with discontinuities is of no concern for our model. Since we can choose a uniform grid and we do not expect discontinuities FVM and FDM perform equally well in our case (Botte et al., 2000). When employing higher order methods FDM codes on a uniform grid can even be more accurate (Hoffmann and Chiang, 2000). FDM methods are simple in their formulation and have no disadvantages that apply to our problem. So I decided to use an FDM method for discretizing the simulation domain, and solving **Eq. 3.1**.
Because of this choice our domain for the simulation of diffusion will be a cube with uniform cubical voxels with a given side-length h.

3.1.2 Finite Differences

In a FDM we want to replace the derivatives in the equation with algebraic approximations to these derivatives. For illustrative purposes I will show some examples on a one-dimensional diffusion equation with a source term q (see **Section 2.2**)

$$\frac{\partial C}{\partial t} = D\frac{\partial^2 C}{\partial x^2} + q. \tag{3.2}$$

Before replacing the derivatives with their algebraic equivalents we need to discretize the space. We will use a uniform one dimensional grid, that means

we are replacing the domain [0,L] with a set of grid points

$$x_i = ih, i = 1, ..., N_x \tag{3.3}$$

furthermore we call C_i^n the function on the grid that gives $C(x_i, t_n)$, where t_n is the n-th timestep. If we require that **Eq. 3.2** is fulfilled on the discrete grid points we arrive at

$$\frac{\partial C(x_i, t_n)}{\partial t} = D\frac{\partial^2}{\partial x^2}C(x_i, t_n) + q(x_i, t_n). \tag{3.4}$$

We still have the derivatives in the equation, which we would like to replace with algebraic expressions that approximate the derivatives. To come up with these expressions we will utilize the Taylor series (see e.g. Bronstein et al. 2004), a series expansion that allows us to estimate the value of a function $f(x)$ at point $x + h$ from the value of the function at point x under the assumption that f is smooth

$$f(x+h) = f(x) + \frac{h}{1!}\frac{\partial f(x)}{\partial x} + \frac{h^2}{2!}\frac{\partial^2 f(x)}{\partial x^2} + ... = \sum_{i=0}^{\infty}\frac{h^i}{i!}\frac{\partial^i f(x)}{\partial x^i}. \tag{3.5}$$

Now we can use Taylor series to calculate an estimate of C_{i+1}^n on the uniform grid

$$C_{i+1}^n = C_i^n + h\frac{\partial C_i^n}{\partial x} + \frac{h^2}{2!}\frac{\partial^2 C_i^n}{\partial x^2} + O(h^3) \tag{3.6}$$

where $O(h^3)$ denotes a leading term "of order" h^3 and h is the spatial resolution. This can now be easily rearranged (while silently dropping the n superscript denoting time) to an algebraic expression for the first derivative

$$\frac{\partial C_i}{\partial x} = \frac{C_{i+1} - C_i}{h} - \frac{h}{2!}\frac{\partial^2 C_i}{\partial x^2} + O(h^2) = \frac{\Delta_x^+ C_i}{h} + O(h) \tag{3.7}$$

where $\Delta_x^+ = C_{i+1} - C_i$ denotes the first forward difference operator in the x direction. We can see that the term we dropped is of order h. That means the error of our approximation, also called the truncation error, behaves linear in h. Doubling the resolution, and correspondingly halving $h = 0.5h$ will halve the truncation error of the approximation of the first derivative. We can apply the same reasoning for defining the forward difference operator in time, which we will call Δ_t^+.

Eq. 3.2 contains a second derivative in space, so we will also need an algebraic expression for this second derivative. We can write another Taylor series

$$C_{i+2} = C_i + 2h\frac{\partial C_i}{\partial x} + \frac{(2h)^2}{2!}\frac{\partial^2 C_i}{\partial x^2} + \frac{(2h)^3}{3!}\frac{\partial^3 C_i}{\partial x^3} + ... \tag{3.8}$$

which we can combine with **Eq. 3.6** in such a way that the $\partial C_i/\partial x$ term vanishes to get

$$\frac{\partial^2 C_i}{\partial x^2} = \frac{C_{i+2} - 2C_{i+1} + C_i}{h^2} - h\frac{\partial^3 C_i}{\partial x^3} + ... = \frac{\Delta_x^{2+}}{h^2} + O(h) \tag{3.9}$$

with Δ_x^{2+} the second forward difference in the x direction. Now we have an algebraic expression for the second derivative which again has a leading error

of order $O(h)$. However, we also require an extra point, C_{i+2}, to calculate this derivative. Generally adding one more points adds another $O(h)$ to the next derivative. So we can write

$$\frac{\partial^n C_i}{\partial x^n} = \frac{\Delta_x^{n+}}{h^n} + O(h) \tag{3.10}$$

where the forward differences can be applied recursively as

$$\Delta_x^{n+} C_i = \Delta_x^{+}(\Delta_x^{n-1+} C_i). \tag{3.11}$$

Similar to these forward differences, there are also backwards differences, denoted by Δ_x^-, defined in an analogous way but starting with

$$C_{i-1} = C_i - h\frac{\partial C_i}{\partial x} + \frac{h^2}{2!}\frac{\partial^2 C_i}{\partial x^2} + ... \tag{3.12}$$

instead.

Having an error that is first order in the spatial resolution is not necessarily the best case, since doubling the resolution only halves the truncation errors. It is possible to increase the order of the error term for the approximation in the forward and backward difference schemes by adding more points. We can combine **Eq. 3.6** with **Eq. 3.8** weighted by a factor A, and arrive at

$$C_{i+1}+AC_{i+2} = (1+A)C_i+(1+2A)h\frac{\partial C_i}{\partial x}+(1+4A)\frac{h^2}{2!}\frac{\partial^2 C_i}{\partial x^2}+(1+8A)\frac{h^3}{3!}\frac{\partial^3 C_i}{\partial x^3}+... \tag{3.13}$$

Now what we want is to remove the second order error term before we rearrange. We have to choose $A = 1/4$ so that the $O(h^2)$ term vanishes in **Eq. 3.13**. Then we can rearrange again and get a $O(h^2)$ estimate for the first derivative, using the forward difference operator

$$\frac{\partial C_i}{\partial x} = \frac{-C_{i+2} + 4C_{i+1} - 3C_i}{2h} - \frac{h^2}{3!}\frac{\partial^3 C_i}{\partial x^3} + O(h^3). \tag{3.14}$$

With the leading error term being $O(h^2)$ doubling the resolution reduces the approximation error to $1/4$. Higher order forward difference operators can be constructed in an analogous manner by adding more points and removing ever higher order terms. However these higher order operators require more and more points, which complicates treating boundaries considerably. Furthermore, calculating the estimates of the derivatives becomes progressively more computationally expensive since the amount of operations required to calculate one estimate also grows with the number of points involved. The higher order backward difference operators can be constructed in an analogous manner.

There is another trick to increase the order of the approximation of the derivative without adding any more points. We can combine the forward and backward difference operator by simply adding them and defining a new operator

$$\Delta_x^+ + \Delta_x^- = C_{i+1} - C_{i-1} = \delta C_i \tag{3.15}$$

the central difference operator. By looking at **Eq. 3.6** and **Eq. 3.12** we can see that the term of $O(h)$ is removed by the combination and we are left with an

approximation of the derivative that is $O(h^2)$

$$\frac{\partial C_i}{\partial x} = \frac{\delta C_i}{2h} + O(h^2). \tag{3.16}$$

Again higher order operators can be generated by adding more points, however the approximation with the central difference operator (**Eq. 3.15**) has a truncation error of one order higher then the forward or backward difference operator when using the same amount of points. Generally it is advantageous to use higher order operators since they make the calculated estimates more accurate, however this advantage always has to be balanced against the increased computational costs and possible boundary problems.

3.1.3 Solvers

With the help of the finite difference operators we can now rewrite the diffusion equation **Eq. 3.2**, a partial differential equation, as an algebraic equation whose solution will give an approximate result of the original solution. However, this can be achieved by using different (e.g forward difference, backward difference) operators, giving rise to different numerical schemes. I will present the a few simple numerical schemes and their problems to introduce some possible problems and to show what we are looking for in a numerical method. These considerations can also be found in works about FDM or general numerical methods, e.g. Langtangen (2013a); Press et al. (1988).

Explicit (Forward) Euler

For the most intuitive numerical scheme, called the forward Euler scheme, we use the central difference operators in space, and the forward difference operator in time to replace the derivatives in **Eq. 3.2** leading to

$$\Delta_t^+ C = D\delta_x\delta_x C + q. \tag{3.17}$$

Writing out all the operators (and this time not dropping the time superscript) leaves us with

$$\frac{C_i^{n+1} - C_i^n}{\Delta t} = D\frac{C_{i+1}^n - 2C_i^n + C_{i-1}^n}{h^2} + q_i^n \tag{3.18}$$

an algebraic equation that approximates the original differential equation. Looking at **Eq. 3.18** we notice that we can assume, when starting with some initial conditions, that we know all quantities C^n the values at the current timepoint. The only unknown quantity, is C_i^{n+1}, the concentration one step into the future. We can rearrange to solve for C_i^{n+1}

$$C_i^{n+1} = C_i^n + D\frac{\Delta t}{h^2}(C_{i+1}^n - 2C_i^n + C_{i-1}^n) + \Delta t \cdot q_i^n \tag{3.19}$$

which is commonly known as the Euler forward scheme. We will also define the dimensionless parameter $\nu = D\frac{\Delta t}{h^2}$, also known as the Fourier number. Which will turn out to be an important parameter for the stability behavior of the method. Now we can use **Eq. 3.19** to start from given initial conditions and evolve them through time indefinitely. However when attempting this we also realize that we will require a set of points outside of the domain, in which we

want to calculate our solution. For example, to calculate C_1^{n+1} we will require a point at C_0^n. These points are known as boundary conditions since they are at the boundary of the domain, and in this example we will choose them to be $C(0) = C(L) = 0$ at all points in time t.

To test the validity of the Euler forward scheme we can simulate an example, in this case a discontinuous step, and see how it develops in time. All parameters are in arbitrary units. In the example we choose the spatial resolution $h = 0.01$, the diffusion coefficient $D = 0.1$ and adjust the time resolution Δt so that we arrive at the desired ν. The initial conditions for this example are a step of size 1.0 that extends from $x = 0.4$ to $x = 0.6$.

In **Fig. 3.1** it is clear that the parameter we called ν is of critical importance for the validity of the solution. For $\nu = 0.25$ the solution gives a smooth solution, however for $\nu = 0.5$ we see a sawtooth shaped noise on top of the solution. The scheme leads to unrealistic growing solutions for $\nu > 0.5$. Why is that?

The explicit euler scheme, is unstable for values of $\nu > 0.5$. Even though for $\nu = 0.5$ the solution does not have an unrealistic growth behavior, we can see that the solution is not smooth. The reason for this is the high frequency noise that is present in the discontinuous initial conditions. The Euler forward scheme does not suppress high frequency noise, so that initial noise remains as a saw-tooth pattern in the solution. One reason for this stability problem is that we calculate the change of C by extrapolating the rate of change of C with the help of the current values of C. With longer timesteps the error of th this extrapolation grows, which leads to unwanted behavior. Generally all explicit patterns have these stability problems. So even if we would increase the order of this scheme we would still have to retain a timestep, small enough to prevent the solution from showing unrealistic growth. Is there a pattern that does not have these stability problems?

Implicit (Backward) Euler

We can choose not to extrapolate from the current timestep. If we use the backward temporal difference operator Δ_t^- instead of the forward temporal difference operator in **Eq. 3.2** we arrive at

$$\Delta_t^- C = D\delta_x\delta_x C + q \tag{3.20}$$

which is very similar to **Eq. 3.17** except for the backwards finite difference operator. So we are left with the algebraic equation

$$\frac{C_i^n - C_i^{n-1}}{\Delta t} = D\frac{C_{i+1}^n - 2C_i^n + C_{i-1}^n}{h^2} + q_i^n. \tag{3.21}$$

for which we assume that we know all values at timestep $t = n - 1$ and we are looking for all values at $t = n$. We can rearrange like we did above, again substituting $\nu = D\frac{\Delta t}{h^2}$ and arrive at

$$C_i^n - \nu(C_{i+1}^n - 2C_i^n + C_{i-1}^n) = C_i^{n-1} + \Delta t \cdot q_i^n \tag{3.22}$$

which can be further rearranged to

$$(1 + 2\nu)C_i^n - \nu C_{i+1}^n - \nu C_{i-1}^n = C_i^{n-1} + \Delta t \cdot q_i^n. \tag{3.23}$$

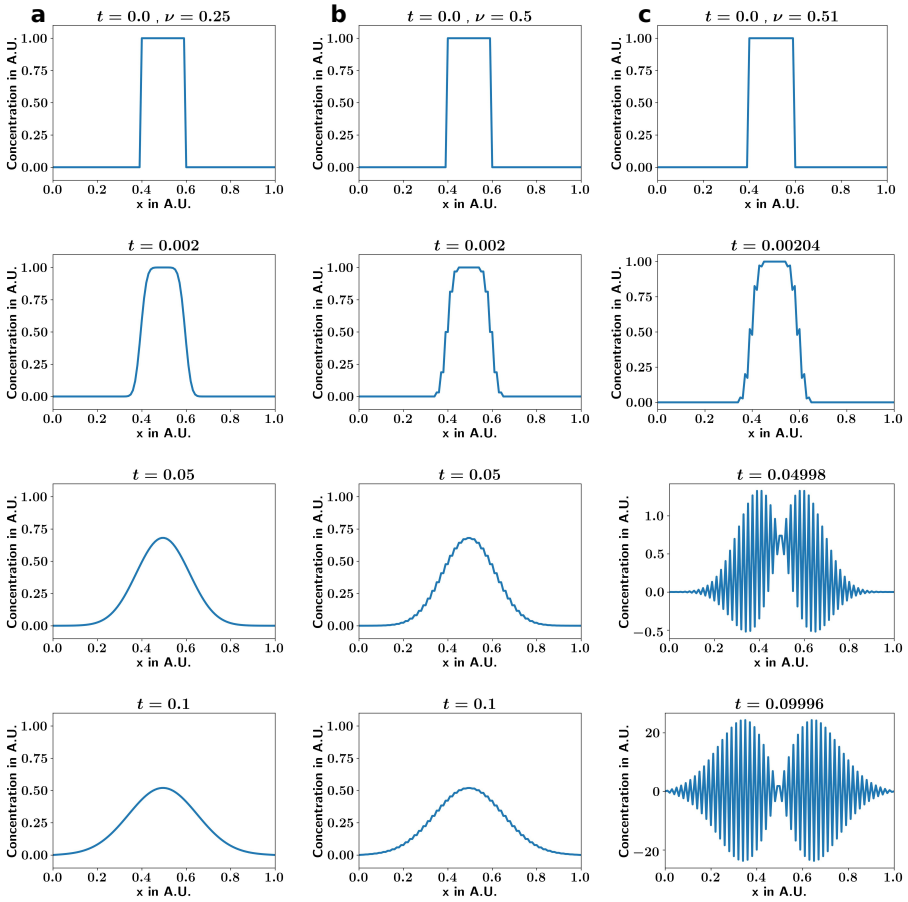

Figure 3.1: Solving the one dimensional diffusion equation with the Euler forward method. Each panel shows an example for the initial conditions given at the top. The solution is has no obvious problems for $\nu = 0.25$ (a). Even though the solution seems to distribute as expected from a diffusion problem for $\nu = 0.5$, there is sawtooth noise visible on top of the solution (b).The forward Euler solution becomes unstable for $\nu > 0.5$ (c) showing unrealistic growth in the solution.

However, this is not an explicit formula for calculating the new timestep, since the value C_i^n is coupled to the value at neighboring cells. Instead of an explicit solution formula **Eq. 3.23** describes a system of equations that needs to be solved in its entirety to arrive at a solution C^n at all spatial locations. To work further with the system of algebraic equations in **Eq. 3.23** we will write it in its matrix form

$$A\vec{x} = \vec{b} \tag{3.24}$$

with matrix A, the vector of known values $\vec{b}$ and the solution to be computed $\vec{x}$. The system of equations resulting from **Eq. 3.23** can be written as the matrix A:

$$A = \begin{pmatrix} A_{0,0} & A_{0,1} & 0 & \cdots & \cdots & \cdots & 0 \\ -\nu & 1+2\nu & -\nu & & & & \vdots \\ 0 & -\nu & 1+2\nu & -\nu & & & \vdots \\ \vdots & \ddots & \ddots & \ddots & \ddots & & \vdots \\ \vdots & & & -\nu & 1+2\nu & -\nu & 0 \\ \vdots & & & & -\nu & 1+2\nu & -\nu \\ 0 & \cdots & \cdots & \cdots & 0 & A_{N,N-1} & A_{N,N} \end{pmatrix} \tag{3.25}$$

the vector $\vec{b}$ containing the values of the current timestep

$$\vec{b} = \begin{pmatrix} C_0^{n-1} \\ C_1^{n-1} \\ \vdots \\ \vdots \\ C_{N-1}^{n-1} \\ C_N^{n-1} \end{pmatrix} \tag{3.26}$$

and the vector $\vec{x}$ containing the solution to be computed

$$\vec{x} = \begin{pmatrix} C_0^{n} \\ C_1^{n} \\ \vdots \\ \vdots \\ C_{N-1}^{n} \\ C_N^{n} \end{pmatrix}. \tag{3.27}$$

Where $N = N_x$ is the number of gridpoints and values at the boundaries are given by the boundary conditions

$$C_0^{n-1} = C(0) \qquad C_N^{n-1} = C(L). \tag{3.28}$$

It is not instantly clear from **Eq. 3.23** what the terms in the first and last row of A should be. These terms describe the interaction of the solution with the chosen boundaries. In our example we have explicit boundary conditions so the values at the boundaries are $C(0) = C(L) = 0$. We have to fill the

solution, as is, in the first and last row. That means $A_{0,0} = A_{N,N} = 1$ and $A_{0,1} = A_{N,N-1} = 0$, so that the first equation of the system $Ax = b$ will read

$$A_{0,0}C_0^n + A_{0,1}C_1^{n-1} = C_0^n = C(0). \tag{3.29}$$

Now we have a finished matrix version of **Eq. 3.23**. To advance a timestep we have to solve **Eq. 3.24** once, which requires significantly more operations than the explicit version shown above. Matrix A does not change with time, so we can use the same matrix in all timesteps. We can use Gaussian elimination to find the solution to **Eq. 3.24**. However this method requires $O(n^3)$ arithmetic operations (Fang and Havas, 1997), where n is the number of unknowns. So for a system with double the size we would require 8 times as many operations, making this method too computationally expensive for any system of reasonable size. However, this problem can be fixed. When we look at the matrix A, we can see that the matrix is largely empty, i.e. A is a so called sparse matrix. Furthermore, A only has entries on the main diagonal and its two neighboring diagonals, a property that is commonly called tri-diagonal. For these type of matrices an efficient algorithm, the Thomas-algorithm, exists (Thomas, 1949), which can solve our problem in $O(n)$ operations. This enables us to solve systems of a realistic size in a reasonable time.

Again we can test our solution, and will do so for different parameters of ν (see **Fig. 3.2**). Independent of the parameter ν the solutions are all smooth. There are no physically unrealistic instabilities for $\nu > 0.5$ as observed in the explicit method. Furthermore, we also do not see the sawtooth noise we saw at $\nu = 0.5$ for the explicit method. The implicit Euler method is unconditionally stable, and suppresses high frequency noise. So even for high ν it leads to a smooth solution. This scheme already has noticeable advantages over the Euler forward scheme, however we would still like to improve on the truncation error behavior.

Crank Nichsolson Scheme

Both of the methods shown above use the central difference operator δ_x in space. So that both of these methods are second order $O(h^2)$ in space. (Here we use the O-notation with respect to the truncation error, meaning that havling the timestep will reduce the truncation error by $0.5^2 = 0.25$, a factor of 4.) However for the time evolution they either use the forward or backward difference operator in time. Both of these operators have a truncation error of $O(\Delta t)$. So both methods are first order in time.

Here we will show a method that is also second order in time, first proposed in Crank and Nicolson (1947). The easiest way to increase the order of the truncation error in time would be using a central difference operator in time. However, for the time derivation this is not straightforward. Since replacing the first time derivative with the central difference operator $\delta_t = C^{n+1} - C^{n-1}$ removes the value we would want to solve C^n from the formula. However we can use a trick to get a type of central difference operator for the timestep too. This trick contains of solving our algebraic problem on all the spatial grid points, but requiring the solution in time between the timesteps, at $t = n + 0.5\Delta t$ leading to

$$\delta_t C(x, t + 0.5\Delta t) = D\delta_x\delta_x C(x, t + 0.5\Delta t) + q(x, t + 0.5\Delta t). \tag{3.30}$$

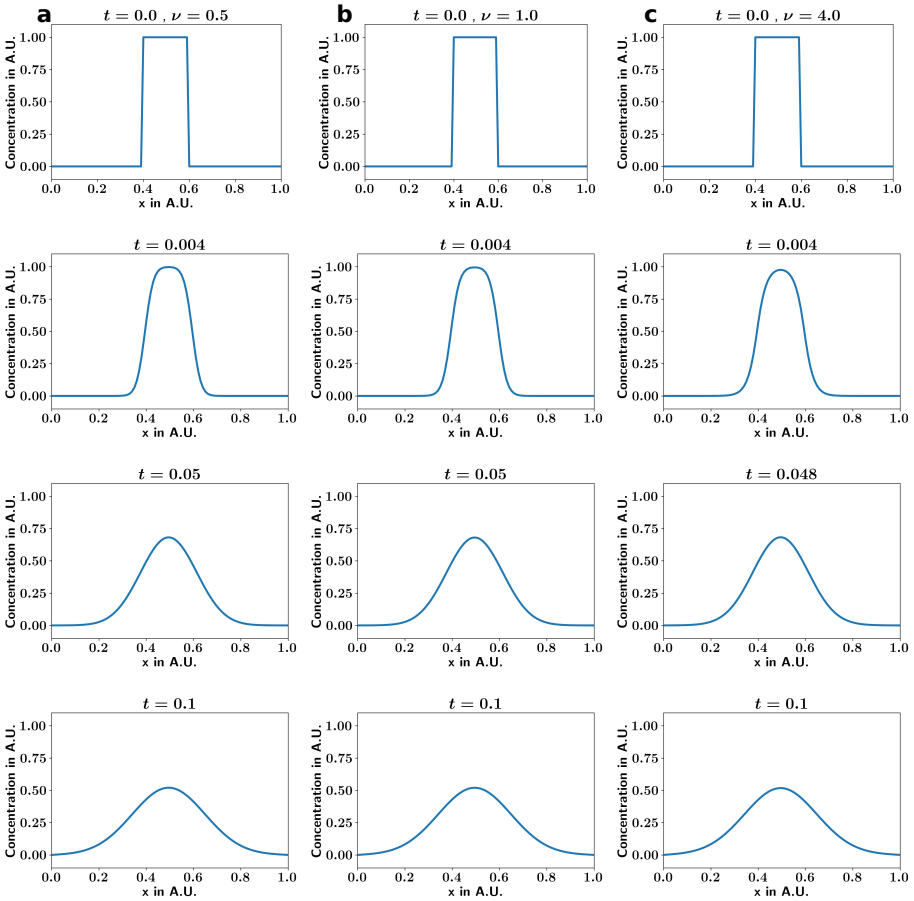

Figure 3.2: Solving the one dimensional diffusion equation with the Euler backward method. Each panel shows an example for the initial conditions given at the top. Independent of ν the solution behaves well and shows no obvious numerical problems. The Euler backward method is unconditionally stable.

Here we chose the virtual timestep to be $0.5\Delta t$ for the central difference on the left hand side, so that we can write the algebraic equation as

$$\frac{C_i^{n+1} - C_i^n}{2(0.5\Delta t)} = D\frac{C_{i+1}^{n+\frac{1}{2}} - 2C_i^{n+\frac{1}{2}} + C_{i-1}^{n+\frac{1}{2}}}{2h^2} + q_i^{n+\frac{1}{2}}. \tag{3.31}$$

On the left hand side we now only have values aligned with the timegrid, but on the right hand side we require the values at times between the current and next timestep. Usually we do not calculate this value. However, we can replace this value by the arithmetic mean of the current timestep and the timestep to be calculated

$$C_i^{n+\frac{1}{2}} = 0.5(C_i^{n+1} + C_i^n) \tag{3.32}$$

which we can substitute into **Eq. 3.31**. That leaves us with an expression not unlike the one resulting in the implicit method (**Eq. 3.23**)

$$(1+\nu)C_i^{n+1} - \frac{\nu}{2}C_{i+1}^{n+1} - \frac{\nu}{2}C_{i-1}^{n+1} = \frac{\nu}{2}(C_{i+1}^n - 2C_i^n + C_{i-1}^n) + \frac{1}{2}(q_i^{n+1} + q_i^n). \tag{3.33}$$

Again we can write a matrix equation, this time with the matrix

$$A = \begin{pmatrix} A_{0,0} & A_{0,1} & 0 & \cdots & \cdots & \cdots & 0 \\ -\frac{1}{2}\nu & 1+\nu & -\frac{1}{2}\nu & & & & \vdots \\ 0 & -\frac{1}{2}\nu & 1+\nu & -\frac{1}{2}\nu & & & \vdots \\ \vdots & \ddots & \ddots & \ddots & \ddots & & \vdots \\ \vdots & & & -\frac{1}{2}\nu & 1+\nu & -\frac{1}{2}\nu & 0 \\ \vdots & & & & -\frac{1}{2}\nu & 1+\nu & -\frac{1}{2}\nu \\ 0 & \cdots & \cdots & \cdots & 0 & A_{N,N-1} & A_{N,N} \end{pmatrix} \tag{3.34}$$

which looks very similar to **Eq. 3.25**. It also contains the same factors $A_{0,0} = A_{N,N} = 1$ and $A_{0,1} = A_{N,N-1} = 0$ when using the same boundaries as above. The vector b then evaluates to

$$b = \begin{pmatrix} C(0) \\ (1-\nu)C_1^n + \frac{\nu}{2}(C_2^n + C_0^n) + \frac{1}{2}(q_1^{n+1} + q_1^n) \\ \vdots \\ \vdots \\ (1-\nu)C_{N-1}^n + \frac{\nu}{2}(C_N^n + C_{N-2}^n) + \frac{1}{2}(q_{N-1}^{n+1} + q_{N-1}^n) \\ C(L) \end{pmatrix}. \tag{3.35}$$

Since the matrix A is tridiagonal again, we can use the Thomas algorithm again to solve this system.

As in the previous cases we can test the solution for different values of ν (**Fig. 3.3**). The solution does not become unstable for large ν, but we see artifacts in the solutions with large ν that only vanish slowly over a couple of timesteps (**Fig. 3.4**). We can see that after the initial timestep artifacts persist. These artifacts are a common problem with the straightforward Crank Nicholson scheme, which tends to show non-physical oscillations for larger values

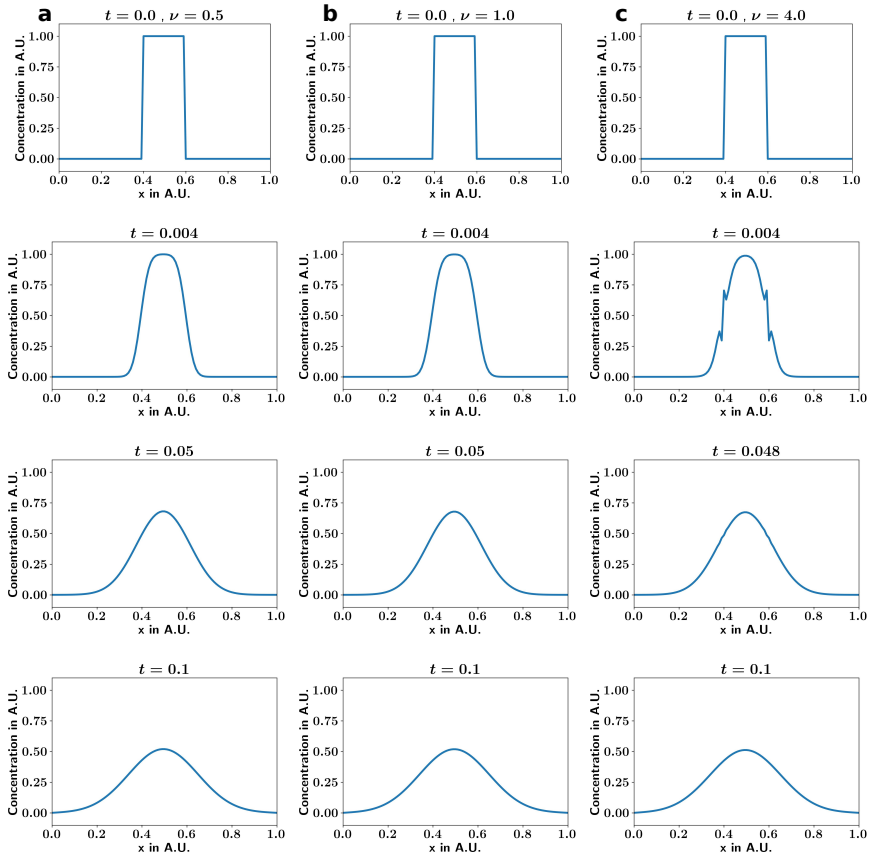

Figure 3.3: Solving the one dimensional diffusion equation with Crank-Nicholson method. Each panel shows an example for the initial conditions given at the top. The Crank-Nicholson does not become unstable for large ν but shows spurious oscillations for large ν (c).

of ν. However the Crank Nicholson scheme has the advantage that it has a truncation error of $O(\Delta t^2)$. So it is second order in time. We will not reproduce the calculation for the truncation error here, but it can be found in Langtangen (2013b). The Crank Nicholson method is second order in time, but unsuitable for use with larger ν since these produce artifacts in the solution.

3.1.4 Stability, Noise Suppression and other Errors

In the previous section we found, by utilizing numerical experiments, that the forward Euler method becomes unstable for values of $\nu > 0.5$, while the backwards Euler method experiences no such instabilities. We also found that the Crank-Nichsolson method does not become unstable, but shows oscillations for large values of ν. However we do not want to perform a numerical experiment for all possible numerical schemes, we would rather like a systematic way to check the stability of these numerical schemes (at least in the case without non-linear terms). This systematic way of testing the stability of FDM used to solve

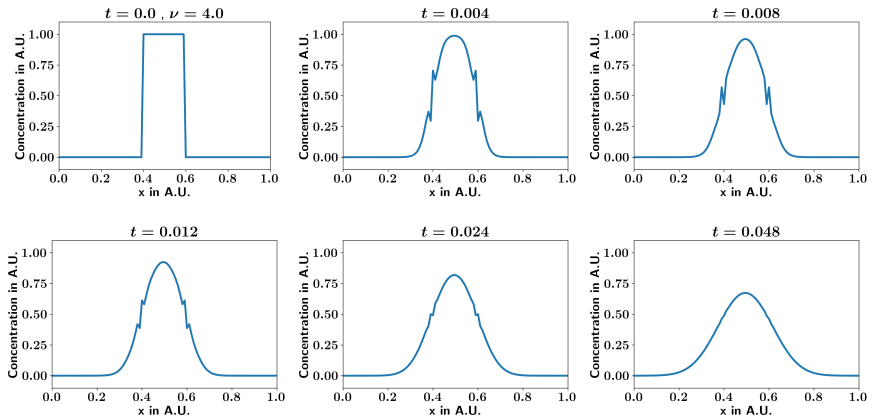

Figure 3.4: Solving the one dimensional diffusion equation with Crank-Nicholson method. The Oscillations in the Crank Nicholson scheme persist for quite a few timesteps ($\nu = 4.0$).

linear partial differential equations is generally known as von Neumann stability analysis, and was first described in Crank and Nicolson (1947) and was later treated in more detail in Charney et al. (1950).
Here I will quickly go through the steps of this method and also discuss the results of the numerical experiments presented before in the light of stability analysis. In our example we solve the one dimensional diffusion equation, here without sources

$$\frac{\partial C}{\partial t} = D\frac{\partial^2 C}{\partial x^2}. \tag{3.36}$$

We start with the definition of the error of our solution as

$$\epsilon_i^n = N_i^n - C_i^n \tag{3.37}$$

where N_i^n denotes the numerical solution to the problem and C_i^n the excact solution to the discretized problem. Since C_i^n is exact, the error term has to fulfill the discretized equation too, otherwise N_i^n would not be a solution of the scheme. If we find a solution for the discretized version of **Eq. 3.36** this solution will also be a solution for the error term e_i^n which can be understood by rearranging **Eq. 3.37**. That means any conclusion about the numerical solution will also be applicable to the error term. To find this solution we start with an analytical solution for **Eq. 3.36** under the assumption that the domain is infinitely sized (or the boundaries are periodic). A usefull Ansatz is given by

$$C(x,t) = Qe^{-at}e^{-ikx} \tag{3.38}$$

where the amplitude Q and the wavenumber $k = 2\pi/\lambda$ can be chosen arbitrarily (with λ the wavelength of the wave). Substituting **Eq. 3.38** into **Eq. 3.36** gives the constraint that

$$a = -Dk^2 \tag{3.39}$$

and with this constraint, **Eq. 3.38** solves the one dimensional diffusion equation without sources. Since all wave numbers k lead to solutions of **Eq. 3.36** linear

combinations of **Eq. 3.38** will also be solutions. That means that a general solution can be written as

$$C(x,t) = \sum_{k=-\infty}^{\infty} a_k e^{-Dk^2 t} e^{ikx} \tag{3.40}$$

which is a superposition of an infinite number of wave solutions, commonly also recognized as a Fourier transform. One thing that can be gleamed from the analytical solution is that the amplitude of all wavenumbers is suppressed in time by the $e^{-Dk^2 t}$ term. That means that high wavenumbers, associated with fast oscillations in space, are damped faster than oscillations with smaller wavenumbers. This is a characteristic of the diffusion equation. Diffusion smooths the solution by damping high frequency oscillations.

What does that mean for our numerical schemes? We can analyze our numerical schemes by using a discretized version of the solution, and see how it evolves timestep by timestep. The analytical solution on the discrete points of our grid is

$$C_j^n = e^{-Dk^2 n\Delta t} e^{-ikjh} = A^n e^{-ikjh} \tag{3.41}$$

where we replaced the spatial index i with j to not have it confused with the imaginary number $i = \sqrt{-1}$ and choose the amplitude factor Q to be 1 for convenience. We also combined the damping factor up to this point t into one amplitude term A^n. The damping factor tells us how an oscillation with wavenumber k grows in amplitude over n timesteps which can be used to test the stability behavior of a solution.

Euler Forward

To analyze the stability of the numerical solution we want to know what the amplification factor of one timestep $A^1 = A$ is. If the amplification factor A is larger than one, than the solution will grow in every timestep, which will lead to unrealistic exponential growth of this solution.

For this we have to insert **Eq. 3.41** into the discretized version of **Eq. 3.36** for the numerical scheme we are interested in. For example for the Euler forward scheme we substitute **Eq. 3.41** into **Eq. 3.18** and are left with

$$e^{ikjh}[\Delta_t^+ A] = A^n D[\delta_x \delta_x e^{ikjh}] \tag{3.42}$$

where we can pull the exponential term in front of the time-difference operator since it has no time terms, and the A^n in front of the central difference operator in space since it has no space-terms. After applying the difference operators we arrive at the left hand side

$$e^{ikjh} \frac{A^{n+1} - A^n}{\Delta t} = A^n e^{ikjh} \frac{A-1}{\Delta t} \tag{3.43}$$

while the right hand side leaves us with

$$A^n D(e^{ik(j+1)h} - 2e^{ikjh} + e^{ik(j-1)h}) = A^n \frac{D}{h^2} e^{ijkh}(e^{-ikh} + e^{ikh} - 2). \tag{3.44}$$

when we combine both parts again and divide by A^n and e^{ikjh} we arrive at

$$\begin{aligned}\frac{A-1}{\Delta t} =& \frac{D}{h^2}(e^{-ikh} + e^{ikh} - 2) && (3.45)\\ =& 2\frac{D}{h^2}(cos(kh) - 1) && (3.46)\\ =& -4\frac{D}{h^2}sin^2\left(\frac{kh}{2}\right) && (3.47)\end{aligned}$$

where we used the identities $2cos(kh) = e^{-ikh} + e^{ikh}$ and $-2sin^2(kh/2) = cos(kh) - 1$. Now we can replace $\nu = \frac{\Delta t D}{h^2}$ and solve for A, the amplification factor in one timestep

$$A = 1 - 4\nu sin^2\left(\frac{kh}{2}\right). \tag{3.48}$$

So what does that mean? When is a solution stable? If $|A| > 1$ the solution grows in every timestep. That means we get exponential growth of the amplitude in time. Of course that is behavior that we do not want since it will make the solution unstable as seen in the $\nu = 0.51$ case of **Fig. 3.2**. So for stability we require $|A| < 1$. In **Eq. 3.48** we see that $A \geq 1$, but A can assume values of $A < -1$, so for all stable parameters it is required that

$$4\nu sin^2\left(\frac{kh}{2}\right) \leq 2. \tag{3.49}$$

We know that

$$sin^2\left(\frac{kh}{2}\right) \leq 1. \tag{3.50}$$

So for the worst case we set **Eq. 3.50** to 1 and get the stability criterion

$$\nu \leq \frac{1}{2}. \tag{3.51}$$

As observed in **Fig. 3.2** the Euler forward scheme becomes unstable for $\nu > 0.5$. The Euler forward scheme is only conditionally stable. However already for $\nu = 0.5$ we can see problems when **Eq. 3.50** is 1. For this combination the solution does not decay in time and the oscillations are not damped. **Eq. 3.50** becomes one if $kh/2 = \pi/2$, so when we substitute our definition for $k = 2\pi/\lambda$ and solve for lambda we get $\lambda = 2h$. Therefore the shortest possible wavelength does not decay for $\nu = 0.5$. This unrealistic, since in the analytical solution short wavelengths are suppressed strongest. This is especially troubling if the initial conditions, or source terms, are discontinuous and add artificial high frequency terms to the solution, since these will not decay. That means for the euler forward scheme $\nu < 0.5$ should be chosen.
The stability criterions for the Euler backward and Crank Nicholson scheme can be derived in the same way, by substituting **Eq. 3.41** into the appropriate algebraic version of the diffusion equation. I will not show all the (tedious) steps here but rather will just present the results.

Euler Backward

Performing the stability analysis for the Euler backward scheme leaves us with an amplification factor of

$$A = \frac{1}{1 + 4\nu sin^2\left(\frac{kh}{2}\right)} \tag{3.52}$$

for which $|A| < 1$ is always true. That means that the Euler backward scheme is unconditionally stable.

Crank Nicholson

The stability analysis for the Crank Nicholson scheme gives an amplification factor of

$$A = \frac{1 - 2\nu sin^2\left(\frac{kh}{2}\right)}{1 + 2\nu sin^2\left(\frac{kh}{2}\right)}. \tag{3.53}$$

This amplification factor stays $|A| \leq 1$ for all values for ν. However if $1 - 2\nu sin^2(kh/2) < 0$ the solution flips sign on every timestep, which will lead to artifacts in the form of artificial oscillations (as shown in **Fig. 3.4**). That means the Crank Nicholson scheme is unconditionally stable, but to avoid numerical oscillations $\nu < 0.5$ is required.
Stability analysis is not restricted to one dimension, or just the numerical schemes presented here. It is a quite general method that can be used for all finite difference schemes, as long as their are no non-linear terms. Since we said above that the errors of the numerical solution have to fulfill the same discrete difference equation as the analytical solution, we can also conclude that errors are dampened with time if the amplification factor $|A| < 1$.

Numerical Diffusiom

One thing to keep in mind for FDM, FVM, and generally all methods that operate on a grid is a phenomenon called numerical diffusion (Andersson et al., 2011). This phenomenon describes an increased diffusivity along the grid lines, which can be easily understood when we picture a spherical area of high DA concentration on the grid. In the real system the diffusion coefficient will be the same in all directions, meaning diffusion will have the same speed independent of reaction. However in the discretized model there is only a limited amount of directions the material can be transported in, where transport will be fastest along the grid directions, and slower along diagonals in space. This effect is more prominent in lower order methods, but is not abolished by high-order methods, since it is a consequence of the discretization. When looking at explicit schemes this effect becomes more obvious, e.g. for a 2D first order Euler scheme it is clear that in one timestep there can be no flow along the diagonals, since the calculation of the new concentration in a cell only depends on the neighboring cells. That means for a flow along the diagonals it needs at least two timesteps (since the cell on the diagonal is adjacent to the neighbors of the cell where the flow originates). However that also means that the diffusion along the grid directions is faster, since the equation approximates the flow out of the cell to an accuracy within the truncation error. This effect is weaker in implicit and high

order methods, since implicit methods link the whole domain together (through the system of equations to be solved) and higher order methods generally have smaller errors, suggesting a high order implicit method for our model.

Conclusion

So what do we conclude from these results? Our numerical method should be unconditionally stable, and should not experience unrealistic oscillations. Since DA is delivered to the system from point sources the method should dampen high frequency oscillations that may be caused by such a delivery mode. This is not an artificial consideration, since diffusion itself suppresses high frequency oscillations so the chosen method should reflect that. Implicit solvers, which are often noise dampening, are commonly used to solve the diffusion equation in reaction diffusion systems (Ruuth, 1995). Sometimes implicit methods are not used in computational fluid dynamics because they dampen strong discontinuities, like e.g. shockfronts. However this feature is desirable in our case in which we only solve diffusion, but not bulk flows, and there are no shockfronts. We choose a high order method to reduce numerical errors as much as possible since it has been shown that first order methods, even for sufficiently reduced timesteps, can produce results that are plausible but incorrect (Ruuth, 1995).

3.2 Boundary Conditions

So far we assumed that the boundary conditions of our problems are known. We knew the value of the solution at the boundaries, these type of boundary conditions are commonly called Dirichlet type boundaries. However, for our simulations of DA diffusion in the brain these types of boundaries are impractical, since problems arise when we have to decide what value the boundaries should have. This is always a problem when boundary conditions are not defined by the problem itself. If we set the boundaries to a fixed concentration, it will distort the behavior within the domain. For example if we set the boundaries to $C_{DA} = 0$, they will act as a sink of DA, since the diffusive flux will always point outwards at the boundaries. Furthermore, since we do not know the common DA concentration a priori choosing any fixed concentration at the boundaries will always pull the system towards that boundary value.

This can be easily understood if we picture an"empty" ($C_{DA} = 0$ in the full volume) simulation domain, with non-zero boundaries. For these boundaries the diffusive flux will point inwards, and the domain will flood with DA from the boundaries inwards. Another type of possible boundaries would be reflective boundaries, where all flux across the boundary is reflected back into the domain. However, those type of boundaries would also lead to pronounced boundary effects since the DA could not flow across the boundary. Release events close to boundaries, e.g. in a corner of the simulation domain, would have a different time-concentration profiles than release events in the center of the domain.

To avoid these unrealistic and problematic effects I use periodic boundaries where if the diffusive flux crosses a boundary, it enters the domain again on the opposite site. So if it flows out to the left, it flows back in from the right side of the domain. Of course at first glance that seems like an unrealistic topology for diffusion in the brain. But with periodic boundaries we act as if we embed

the simulation domain in a much larger system where the neighboring domain behaves similarly to our domain. Sometimes there will be a diffusive flux across the boundary, which will be similar to the flux that flows out of the simulated domain into the neighboring domains. We close the system as a torus so that all boundaries have a realistic inflow and outflow rate of DA. As an added benefit it will make the analysis of the resulting data easier with respect to Fourier-transformations (see **Section 6.1.5**).

So, how do we implement periodic boundaries in our model? For periodic boundaries the last point in the domain is a neighbor to the first point. So e.g. for the implicit Euler scheme we have to change the matrix A to reflect this new neighborhood

$$A = \begin{pmatrix} 1+2\nu & -\nu & 0 & \cdots & & & -\nu \\ -\nu & 1+2\nu & -\nu & & & & \\ 0 & -\nu & 1+2\nu & -\nu & & & \\ \vdots & \ddots & \ddots & \ddots & \ddots & & \\ & & & -\nu & 1+2\nu & -\nu & 0 \\ & & & & -\nu & 1+2\nu & -\nu \\ -\nu & & & \cdots & 0 & -\nu & 1+2\nu \end{pmatrix}. \quad (3.54)$$

Where we don not need any explicit boundary terms for the vector $\vec{b}$ anymore. We can just solve the system $Ax = b$, and have periodic boundaries in our model. This can easily be done for other numerical schemes too. Periodic boundaries are fairly simple to implement in the matrix equations by just writing the equations under the assumption that the last point in one direction is a neighbor to the first point in the same direction. One problem presents itself though. To efficiently solve the matrix equation we usually want to use the Thomas-algorithm, which only works on tridiagonal matrices. However the matrix for the system with periodic boundaries is no longer tridiagonal. Solving a non-tridiagonal matrix will require a lot more operations, and will make these schemes prohibitively expensive, computation-wise. Luckily we can use a trick to help us (as described in e.g. Teukolsky et al. (1992)). We can use the Sherman-Morrison formula

$$(A + uv^T)^{-1} = A^{-1} - \frac{A^{-1}uv^TA^{-1}}{1 + v^TA^{-1}u} \quad (3.55)$$

to calculate the inverse of the modified matrix $(A+uv^T)^{-1}$. For this calculation we need the inverse of the matrix A, but then we only have to perform a few matrix-vector products. We have to calculate $A^{-1}u$ and v^TA^{-1}, which if we know the inverse of A, are equivalent to matrix multiplications. We also have to calculate $v^TA^{-1}u$ but this is just a matrix vector product since we can reuse previous results. This is useful since we can choose both vectors u and v, so that the matrix A, which we have to inverse, will be tridiagonal. This can be achieved by the choice of

$$u^T = \begin{bmatrix} -(1+2\nu) & 0 \ldots\ldots 0 & -\nu \end{bmatrix} \quad (3.56)$$

and

$$v^T = \begin{bmatrix} 1 & 0 \ldots\ldots 0 & -\frac{\nu}{1+2\nu}. \end{bmatrix} \quad (3.57)$$

We can see that with this choice we can solve a matrix $A^{'}$ so that $A = (A^{'} + uv^T)$, where the modified matrix

$$A^{'} = \begin{pmatrix} A_{0,0} & -\nu & 0 & \cdots & & & & \\ -\nu & 1+2\nu & -\nu & & & & & \\ 0 & -\nu & 1+2\nu & -\nu & & & & \\ \vdots & \ddots & \ddots & \ddots & \ddots & & & \\ & & & -\nu & 1+2\nu & -\nu & 0 & \\ & & & & -\nu & 1+2\nu & -\nu & \\ & & & \cdots & 0 & -\nu & A_{N,N} \end{pmatrix} \tag{3.58}$$

with $A_{0,0} = 2(1 + 2\nu)$ and $A_{N,N} = (1 + 2\nu) + \frac{\nu^2}{1+2\nu}$ is tridiagonal. So we can use the Thomas-algorithm to solve the tridiagonal matrix $A^{'}$ and then use the Sherman-Morrison formula to calculate the solution for the original, non-tridiagonal system. The method outlined here is not limited to the Euler-backward method, or nearly tridiagonal systems but can be used for nearly arbitrary replacements of rows or columns. Furthermore, we can even use a form of the Sherman-Morrison formula if storage of the full inverse matrix $A^{-}1$ is impractical (again see Teukolsky et al. (1992)). For that we can solve

$$(A^{'} + uv)x = b \tag{3.59}$$

with $A^{'}$ and u as defined above. We solve two auxiliary problems

$$A^{'}y = b \quad A'z = u \tag{3.60}$$

and can construct the solution x with the formula

$$x = y - \left[\frac{v \cdot y}{1 + (v \cdot z)}\right] z \tag{3.61}$$

which is just the Sherman Morrison formula without explicitly storing the inverse of matrix A^{-1}. This was also used for the implementation of our diffusion model.

It should also be noted that for the reaction diffusion system with receptors the system to be solved is not tridiagonal, but block tridiagonal. For these kind of problems the Woodsbury Formula replaces the Sherman-Morrison formula, however the application is functionally the same. For more details on this process see (Teukolsky et al., 1992).

3.3 Higher Dimensions

Of course we are not only interested in problems in one dimension. We aim to solve the diffusion equation in the brain, a system that is commonly assumed to have three spatial dimensions. So how do the methods for the one dimensional system translate to higher dimensions? Let us look at the two dimensional diffusion equation

$$\frac{\partial C}{\partial t} = D\left(\frac{\partial^2 C}{\partial x^2} + \frac{\partial^2 C}{\partial y^2}\right) + q. \tag{3.62}$$

If we want to define a two dimensional Crank-Nicholson scheme we follow the same steps as in the Crank-Nicholson parts of **Section 3.1.3**,but this time for both of the spatial dimensions. When replacing all the derivatives with the appropriate finite difference operators we get

$$\begin{aligned}&\delta_t C(x, t + 0.5\Delta t) = \\ &\quad D\left(\delta_x \delta_x C(x, t + 0.5\Delta t) + \delta_x \delta_x C(x, t + 0.5\Delta t)\right) + q(x, t + 0.5\Delta t).\end{aligned} \tag{3.63}$$

which is very similar to **Eq. 3.30**. Applying the difference operators leaves us with

$$\begin{aligned}(1 + 2\nu)C_{i,j}^{n+1} - \frac{\nu}{2}(C_{i+1,j}^{n+1} + C_{i-1,j}^{n+1} + C_{i,j+1}^{n+1} + C_{i,j-1}^{n+1}) = \\ (1 - 2\nu)C_{i,j}^{n} + \frac{\nu}{2}(C_{i+1,j}^{n} + C_{i-1,j}^{n} + C_{i,j+1}^{n} + C_{i,j-1}^{n})\end{aligned} \tag{3.64}$$

which we can transform into a more readable form by using the central difference operators

$$(1 - \frac{\nu}{2}\delta_x^2 - \frac{\nu}{2}\delta_y^2)C_{i,j}^{n+1} = (1 + \frac{\nu}{2}\delta_x^2 + \frac{\nu}{2}\delta_y^2)C_{i,j}^{n}. \tag{3.65}$$

This can be solved straightforward as a matrix problem of the form $Ax = b$, where the vector b should contain all the concentrations of the whole domain e.g.

$$b = \begin{bmatrix} C_{0,0}^n \\ C_{0,1}^n \\ \vdots \\ C_{0,Nx}^n \\ C_{1,0}^n \\ C_{1,1}^n \\ \vdots \\ C_{Nx,Ny}^n. \end{bmatrix} \tag{3.66}$$

However, there is a problem with this solution. Due to the appearance of mixed central differences $\delta_x delta_y$ the matrix A in this problem will not be tridiagonal anymore, since it will link some points to points that are far away in the vector b leading to off diagonal entries. The matrix will be banded, but will have a high bandwidth. Which makes it expensive to solve the matrix directly. One possible solution is splitting the system so that we can solve it in multiple steps, but without having to solve a matrix that is not tridiagonal, a method first proposed for the diffusion equation in Peaceman and Rachford (1955). This is commonly known as operator splitting. In this specific case, where we will try to split the equation along physical dimensions, it is also known as dimensional splitting. To do this we can consider the equation

$$\left(1 - \frac{\nu}{2}\delta_x^2\right)\left(1 - \frac{\nu}{2}\delta_y^2\right)C_{i,j}^{n+1} = \left(1 + \frac{\nu}{2}\delta_x^2\right)\left(1 + \frac{\nu}{2}\delta_y^2\right)C_{i,j}^{n} \tag{3.67}$$

which approximates **Eq. 3.65** reasonably well up to terms quadratic in ν. The error introduced by the splitting procedure is known as the splitting error and

would, in this case, be $O(\Delta t^2)$. What do we get by solving the approximate equation rather than the original one? We can solve **Eq. 3.67** in two steps, by utilizing an intermediate solution C^*

$$\begin{aligned}\left(1-\frac{\nu}{2}\delta_x^2\right)C_{i,j}^* &= \left(1+\frac{\nu}{2}\delta_y^2\right)C_{i,j}^n \\ \left(1-\frac{\nu}{2}\delta_y^2\right)C_{i,j}^{n+1} &= \left(1+\frac{\nu}{2}\delta_x^2\right)C_{i,j}^*.\end{aligned} \tag{3.68}$$

We only have to be careful to evaluate the right-hand side of both steps correctly. Other than in the 1D case, the right hand side now does not have only terms in the direction which the matrix on the left hand side couples together, but also off-axis components. However since we already know the values of the previous timestep, it is straightforward to evaluate these off-axis terms. In other words, we can fill the vector on the right hand side before we solve the system of equations. The advantage is that the matrices on the left hand sides of **Eq. 3.68** are both tridiagonal, and therefore can be solved quite efficiently. Note that, **Eq. 3.68** is not a solution for the whole domain, but has to be solved column by column. Of course one question remains, does **Eq. 3.68** actually solve **Eq. 3.67**? We can show that it does by multiplying the top equation by $1+\frac{\nu}{2}\delta_x^2$ and the bottom equation by $1-\frac{\nu}{2}\delta_x^2$ leading to

$$\begin{aligned}\left(1+\frac{\nu}{2}\delta_x^2\right)\left(1-\frac{\nu}{2}\delta_x^2\right)C_{i,j}^* &= \left(1+\frac{\nu}{2}\delta_x^2\right)\left(1+\frac{\nu}{2}\delta_y^2\right)C_{i,j}^n \\ \left(1-\frac{\nu}{2}\delta_x^2\right)\left(1-\frac{\nu}{2}\delta_y^2\right)C_{i,j}^{n+1} &= \left(1-\frac{\nu}{2}\delta_x^2\right)\left(1+\frac{\nu}{2}\delta_y^2\right)C_{i,j}^*\end{aligned} \tag{3.69}$$

showing the correctness of the splitting scheme.

The method shown here is known as approximate factorization of the finite difference operator and is the operator splitting method that is used in the method we eventually implemented. There are other operator splitting schemes, e.g. the well known alternating difference implicit (ADI) schemes using the method described in Douglas (1962); Chang et al. (1991). One reason to use this approximate factorization splitting scheme over the ADI schemes is that, together with the right finite difference operators, it can fix the oscillation problems of Crank-Nicholson scheme (Lawson and Morris, 1978).

3.4 Choice of Numerical Method

With these considerations in mind, what method did I choose to solve the reaction diffusion equation? For accuracy I want to use a high order method. The method should implicit, or if it is based on the Crank-Nicholson scheme it should fix the problem that this scheme has with oscillations. The scheme should be oscillation damping, since this is a characteristic of the diffusion equation. Also since the source of DA in the system is spiking release, I expect high frequency components on DA injection, since the spiking release will be creating local discontinuities. The method should be computationally fairly cheap to be solved, so preferably a method that uses operator splitting so that I can use efficient algorithms for tridiagonal matrices. What also needs to be considered is the nonlinear uptake term due to Michaelis Menten uptake. Usually non-linear terms are also operator split, and solved iteratively.

With all these constraints I decided to implement the method described in Liao et al. (2002) and Gu et al. (2003). This chapter will be a quick summary of the reasoning in Gu et al. (2003) with some explanations for better understanding and callbacks to previous chapters. The method can be used to solve a system of the form

$$C_t = D_1 \frac{\partial^2 C}{\partial x^2} + D_2 \frac{\partial^2 C}{\partial y^2} + D_3 \frac{\partial^2 C}{\partial z^2} + f(C, x, y, z, t) \tag{3.70}$$

where D_x are diagonal matrices of dimension $n \times n$ and C is a vector of length n. Luckily the system we want to solve (**Eq. 2.47**) is such a system. For the pure diffusion part the dimension will be $n = 1$ since we are only treating DA, but the method can also deal with multiple diffusing and interacting substances, which will be useful for the treatment of DA receptors. We can also assign different diffusion coefficients along each cardinal direction, which enables us to also treat anisotropic diffusion, using the diffusion ellipsoid, as described in **Section 2.3**.

The method is based on a Crank Nicholson method and uses an approximate factorization operator splitting approach together with the pade approximation. This makes it fourth order $O(h^4)$ in space and removes the problems that the Crank Nicholson scheme has with oscillations (Lawson and Morris, 1978; Liao et al., 2002). So how is it constructed? The standard central difference operator for the second derivative δ_x^2 has a second order truncation error. A straightforward way to get a higher order method in space would be to use a higher order central difference operator, constructed by adding more points as described in **Chapter 3.1.2**. A short form to write the $O(h^4)$ central difference operator for the second derivative is

$$(C_{xx})_{ij} = \frac{1}{h^2} \left(1 - \frac{1}{12}\delta_x^2\right) \delta_x^2 C_{ij}. \tag{3.71}$$

However evaluating this high order operator requires five points as opposed to the three points required for the lower order operator. This can be problematic for boundary conditions, but could be solvable with the repeated application of the Sherman-Morrison formula. The problem that is much harder to solve is that a an operator with more points considered, leads to a matrix with higher banwidth (in this case bandwidth 5) which will be more computationally expensive to solve than a simple tri-diagonal matrix. To construct a high order method with a small stencil Gu et al. (2003) the Pade approximant can be used. This approximant often gives better approximations than the Taylor series truncation that we used to construct the finite difference operators before (Baker et al., 1996). The high order compact approximation of the second derivative is then (Adam, 1977)

$$(C_{xx})_{ij} = \frac{1}{h^2} \frac{\delta_x^2}{(1 + \frac{1}{12}\delta_x^2)} C_{ij} \tag{3.72}$$

where C_{xx} is the second derivative along the x-direction. Since δ_x^2 is not applied twice in this approximant its evaluation only requires three points, the point on which we evaluate the derivative and its neighbors. After replacing **Eq. 3.70** with a Crank Nicholson scheme and using the high order compact stencil and

requiring a function term of the form $f(x, y, z, t)$ the system to be solved becomes

$$\begin{aligned} C_{ijk}^{n+1} - C_{ijk}^{n} =& \frac{\nu_x}{2} \frac{\delta_x^2}{1 + (\delta_x^2/12)} (C_{ijk}^{n+1} + C_{ijk}^{n}) \\ &+ \frac{\nu_y}{2} \frac{\delta_y^2}{1 + (\delta_y^2/12)} (C_{ijk}^{n+1} + C_{ijk}^{n}) \\ &+ \frac{\nu_z}{2} \frac{\delta_z^2}{1 + (\delta_z^2/12)} (C_{ijk}^{n+1} + C_{ijk}^{n}) \\ &+ \frac{\Delta t}{2} (f_{ijk}^{n+1} + f_{ijk}^{n}) \end{aligned} \tag{3.73}$$

which is still recognizable as a Crank Nicholson type scheme. Here we choose the factor $\nu_x = \frac{D_x \Delta t}{h_x^2}$ for generality, but for isotropic diffusion ($D = D_x = D_y = D_z$) and the same spatial resolution in all directions ($h = h_x = h_y = h_z$) all factors $\nu = \nu_x = \nu_y = \nu_z$ are the same. However the method can accommodate a rectangular spatial discretization, or non-isotropic diffusion. After rearranging and approximate factorization as shown in **Section 3.3**, we end up with a three step approach (for details see Liao et al. (2002) and Gu et al. (2003))

$$\begin{aligned} &\left(1 + \frac{\delta_x^2}{12} - \frac{\nu_x}{2}\delta_x^2\right) C_{ijk}^{**} = \\ &\quad \left(1 + \frac{\delta_x^2}{12} + \frac{\nu_x}{2}\delta_x^2\right) \left(1 + \frac{\delta_y^2}{12} + \frac{\nu_y}{2}\delta_y^2\right) \left(1 + \frac{\delta_z^2}{12} + \frac{\nu_z}{2}\delta_z^2\right) C_{ijk}^{n} \\ &\quad + \frac{\Delta t}{2} \left(1 + \frac{\delta_x^2}{12}\right) \left(1 + \frac{\delta_y^2}{12}\right) \left(1 + \frac{\delta_z^2}{12}\right) (f_{ijk}^{n+1} + f_{ijk}^{n}), \end{aligned} \tag{3.74}$$

$$\left(1 + \frac{\delta_y^2}{12} - \frac{\nu}{2}\delta_y^2\right) C_{ijk}^{*} = C_{ijk}^{**}, \tag{3.75}$$

$$\left(1 + \frac{\delta_z^2}{12} - \frac{\nu}{2}\delta_z^2\right) C_{ijk}^{n+1} = C_{ijk}^{*} \tag{3.76}$$

which requires us to solve three tri-diagonal systems. Again, like in **Section 3.3** there are terms in all spatial directions on the right hand side of the first step. However, as before, they only depend on C^n we can fill the vector on the right hand side before we solve the first system of equations. Taking into account splitting and truncation errors, this algorithm is fourth order in space and second order in time (for a derivation of the order see Gu et al. 2003). Of course we required $f = f(x, y, z, t)$, however our uptake terms both depend on C and the Michaelis Menten term is even nonlinear. So the method still needs to be modified to accommodate this functional term. In Gu et al. (2003) this is solved by applying a predictor corrector algorithm to solve for an approximation of $f_i^{n+1}jk$ which leads to an iterative scheme. However applying this type of algorithm requires an iteration over all three steps of the method, which is quite inefficient. In Gu et al. (2003) a way to rewrite the algorithm is presented, so that the iteration only has to be performed on the last step of the algorithm, saving a lot of computations. The final version of the algorithm, also

implemented in my simulation code, then becomes

$$\left(I+\frac{\delta_x^2}{12}-\frac{\nu_x}{2}\delta_x^2\right)C_{ijk}^{**}=$$
$$\left(I+\frac{\delta_x^2}{12}+\frac{\nu_x}{2}\delta_x^2\right)\left(I+\frac{\delta_y^2}{12}+\frac{\nu_y}{2}\delta_y^2\right)\left(I+\frac{\delta_z^2}{12}+\frac{\nu_z}{2}\delta_z^2\right)C_{ijk}^{n}$$
$$+\frac{\Delta t}{2}\left(I+\frac{\delta_x^2}{12}+\frac{\nu_x}{2}\delta_x^2\right)\left(I+\frac{\delta_y^2}{12}+\frac{\nu_y}{2}\delta_y^2\right)\left(I+\frac{\delta_z^2}{12}\right)(f_{ijk}^{n}), \tag{3.77}$$

$$\left(I+\frac{\delta_y^2}{12}-\frac{\nu}{2}\delta_y^2\right)C_{ijk}^{*}=C_{ijk}^{**}, \tag{3.78}$$

$$\left(I+\frac{\delta_z^2}{12}-\frac{\nu}{2}\delta_z^2-\frac{\Delta t}{2}\left(I+\frac{\delta_z^2}{12}\right)\boldsymbol{J}_{ijk}^{n}\right)C_{ijk}^{n+1}$$
$$=C_{ijk}^{*}+\frac{\Delta t}{2}\left(I+\frac{\delta_z^2}{12}\right)(f_{ijk}^{n}-\boldsymbol{J}_{ijk}^{n}C_{ijk}^{n}+\Delta t(f_t)_{ijk}^{n}) \tag{3.79}$$

where $\boldsymbol{J}_{ijk}^{n}$ denotes the local Jacobi matrix, which contains the derivatives along all dimensions of the function term. For example for a two-dimensional function linking the concentrations of two molecules

$$f(C^{DA},C^{D1})=\begin{bmatrix}f_1(C^{DA},C^{D1})\\ f_2(C^{DA},C^{D1})\end{bmatrix} \tag{3.80}$$

the Jacobi matrix is

$$J_{ijk}^{n}=\begin{bmatrix}\partial f_1/\partial C^{DA} & \partial f_1/\partial C^{D1}\\ \partial f_2/\partial C^{DA} & \partial f_2/\partial C^{D1}\end{bmatrix}_{ijk}^{n}. \tag{3.81}$$

To solve nonlinear problems with high accuraccy **Eq. 3.79** is solved with Newtons iteration

$$\left(I+\frac{\delta_z^2}{12}-\frac{\nu}{2}\delta_z^2-\frac{\Delta t}{2}\left(I+\frac{\delta_z^2}{12}\right)\boldsymbol{J}_{ijk}^{n+1^{m-1}}\right)C_{ijk}^{n+1^{m}}$$
$$=C_{ijk}^{*}+\frac{\Delta t}{2}\left(I+\frac{\delta_z^2}{12}\right)(f_{ijk}^{n+1^{m-1}}-\boldsymbol{J}_{ijk}^{n+1^{m-1}}C_{ijk}^{n+1^{m-1}}+\Delta t(f_t)_{ijk}^{n}) \tag{3.82}$$

where m denotes the number of the iteration, and $C_{ijk}^{n+1^{0}}=C_{ijk}^{n}$ is used to start the first iteration. This is (nearly) the final algorithm I implemented. In each timestep we can solve **Eq. 3.77** and **Eq. 3.78** once for each "column" in space, so for a cubical domain with N voxels in each dimension we have to solve N^2 columns , of N voxels, for each of the first two steps. The timestep is then finished by iterating **Eq. 3.82** for each column.

In the algorithm I stands for the identity matrix, the matrix version of a one. In the case where we only solve the DA diffusion without any other substances, like DA receptors, all the I in the algorithm can be replaced by ones. In this case the Jacobi matrix also becomes a simple derivative of the functional term, since the uptake term here only explicitly depends on C it is simply $\partial f/\partial C$. It should also be noted that since the uptake term in our model has no explicit

time dependency the f_t term is 0. Gu et al. (2003) also provides a method to implement Dirichlet boundaries into the algorithm. But we will use periodic boundaries, which we will integrate by using the Sherman Morrison formula on equations **Eq. 3.77**, **Eq. 3.78** and **Eq. 3.82**.

The method we up to now is fourth order $O(h^4)$ in space. However since it is based on the Crank Nicholson scheme it is only second order in time $O(\Delta_t^2)$. To make the method also fourth order in time as described in Gu et al. (2003) we use Richardson extrapolation (Richardson et al., 1927), a sequence acceleration method to cancel the $O(\Delta_t^2)$ error term making the method fourth order (since the Crank Nicholson truncation error has no third oder terms). This is a similar idea than for higher order finite difference operators, where lower order terms are summed so that the lower order error term cancels. For the method given here this can be done by calculating

$$C = \frac{4C^{\Delta t/2} - C^{\Delta t}}{3} \tag{3.83}$$

where $C^{\Delta t/2}$ is the solution at $t = t + \Delta t$ calculated with stepsize Δt and $C^{\Delta t/2}$ is the solution $t = t + \Delta t$ calculated with two steps stepsize $\Delta t/2$. That means making the algorithm fourth order in time requires three times as much work as the second order solution. Nevertheless our implementation implements the full scheme.

The matrix problems are all solved with the help of the LAPACK library (Anderson et al., 1999).

3.4.1 Receptor Terms

Eq. 2.47 also contains the interaction between DA and receptors. However the numerical method we chose above is already well suited for dealing with a solution of multiple interacting components. Interacting components are implemented by having C in **Eq. 3.70** as a vector of dimension n and D_x being a a diagonal matrix of corresponding dimensionality. In our case the entries of D_x will be zero for all entries concerning receptors, since the receptors do not diffuse. However the extra components have to be considered for the iteration of the functional term in **Eq. 3.82**. That means that the resulting matrices that need to be solved for the iteration are no longer tridiagonal but block tridiagonal, since an entry C_{ijk} has multiple components. In the implementation I solve the resulting systems of equation with a band-matrix solver. Which is still fairly efficient since the bandwidth of the matrix is usually quite low. Treating the receptors as a full reaction-diffusion system is necesarry if the receptor kinetics are fast enough so that the source/sink terms in the diffusion equation are not negligible. However, if the receptors are slow and the sink terms due to binding are negligible (i.e. when the Michaelis Menten uptake rate is at least an order of magnitude larger than the rate at which DA binds to its receptors) we can treat the DA diffusion independent of the receptor binding. In this we solve the diffusion equation without receptors and calculate the resulting receptor activation by using an explicit fourth order Runge Kutta scheme on the resulting DA timeline. Our tests have shown that in our implementation the runtime for this reduced system is around 5 times shorter than the full solution.

3.4.2 Validation

I tested my implementation of the method presented in this chapter on a few numerical test cases. First I compared the analytical solution for an extended, spherical symmetric, source with linear uptake (Nicholson, 2001) to the solution my implementation produces.

Fig. 3.5 shows the illustrative snapshot of this test at $t = 100ms$. Due to the discretization our source is not really spherically symmetric, but rather a cube of a volume of $8\mu m^3$, the volume of a low resolution ($h = 2\mu m$) voxel. For comparison we chose the same physical initial conditions for the high resolution case, filling 8 of the voxels of size $1\mu m^3$ with the initial concentration of DA. The linear uptake constant in the test case is $k = -1.0s^{-1}$. The solution for the high resolution case is nearly indistinguishable from the analytical solution. After 100ms the maximum error is $e_{max} = 1.3\%$ with an average error of $e_{mean} = 0.3\%$. As expected the lower resolution solution is less accurate and shows larger errors ($e_{max} = 6.3\%, e_{mean} = 1.1\%$). The dopamine distribution along one of the diagonals (z=50, x=y), has a slightly smaller width than the solution along the main diagonals, showing a slight numerical diffusion effect as described above.

I also tested the implementation of periodic boundary conditions by generating initial conditions that have a voxel with higher concentration of dopamine in the center of the domain, in one corner, and in the middle of one domain boundary. The initial conditions, and results after $20ms$ are shown in **Fig. 3.6**. The flow through the boundaries works as expected and creates the same dopamine distribution as the point source in the middle of the domain. In this test there was no uptake.

To test if the interaction between DA, its receptors and Michaelis Menten uptake are simulated correctly I filled the whole domain of size $d = 100\mu m^3$ and resolution $h = 1\mu m$ with a given dopamine concentration $C_{DA} = 500nM$ and let the system evolve for $0.5s$ with $\delta_t = 0.001s$. I then compared the resulting solution with the solution for the reaction and uptake terms calculated with the"odeint" solver from the python package "scipy" (Jones et al., 2001–). In this example we use "scipy" to solve just the reaction and uptake terms, i.e. the solution for one cell, while our code solves the reaction for the whole domain. The solutions should be the same since there is no concentration gradient in our initial conditions, that means there is no diffusive flux between the voxels of our full simulation making the whole domain behave like one giant voxel with only uptake and reaction terms. The solutions were virtually identical, so I conclude that the nonlinear and reaction terms are solved correctly **Fig. 3.7**.

For the simulation I used the following parameters: $V_{max} = 4.0\mu M s^{-1}$, $K_m = 0.21\mu M$, $C^{D1}_{max} = 1.6\mu M$, $C^{D2}_{max} = 0.12\mu M$, $k^{D1}_{on} = 0.5\mu M^{-1}s^{-1}$, $k^{D1}_{on} = 33.3\mu M^{-1}s^{-1}$, $k^{D1}_{off} = 0.83s^{-1}$, $k^{D2}_{off} = 0.83s^{-1}$. Initially the concentration of receptor ligand complex of both receptors is 0.

Our implementation solves reaction and diffusion terms correctly and also handles the periodic boundaries as expected. That means we have a tool that can solve the diffusion and reaction diffusion equation with uptake terms and cross terms describing receptor binding/unbinding accurately on a cubical domain with periodic boundaries.

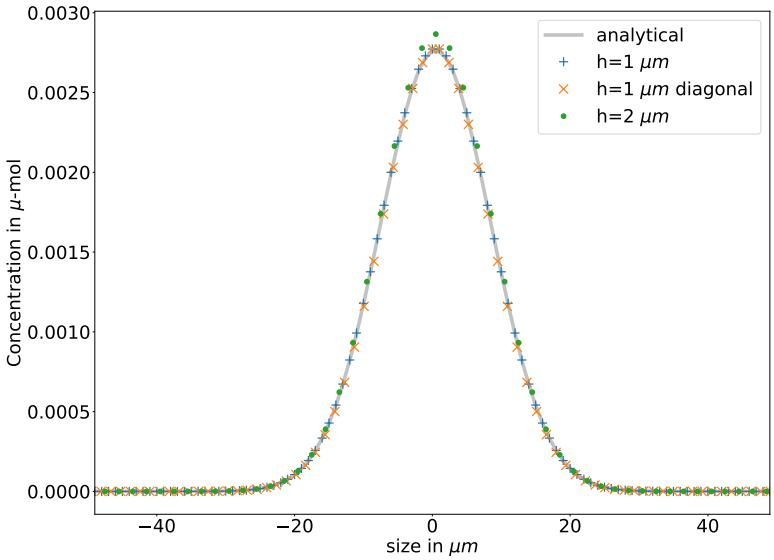

Figure 3.5: Comparison of analytical and numerical solution for an extended source. Shown are the analytical solution to the diffusion of an extended source, and the numerical solutions for resolutions $h = 1\mu m$ and $h = 2\mu m$ after 100 timesteps of length $1ms$, $t = 100ms$. The solution with $h = 1\mu m$ solution is nearly indistinguishable from the analytical solution ($e_{max} = 1.3\%, e_{mean} = 0.3\%$). The $h = 2\mu m$ solution naturally deviates more from the analytical solution, ($e_{max} = 6.3\%, e_{mean} = 1.1\%$). The $h = 1\mu m$ diagonal solution shows the result on a diagonal (x=y). The solution behaves like the $h = 1\mu m$ solution but has a slightly smaller width showing a slight numerical diffusion error.

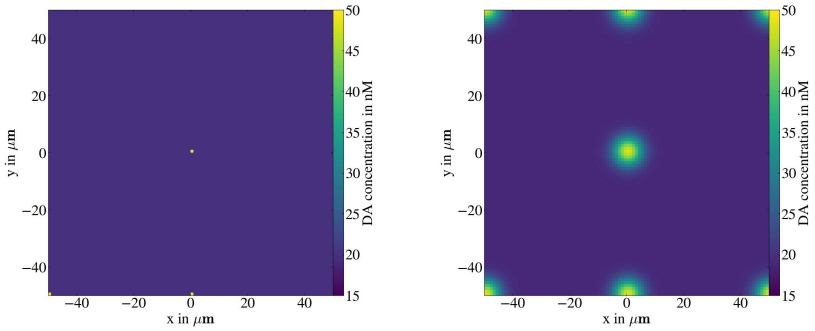

Figure 3.6: Numerical simulation of DA diffusion without uptake for a periodic boundary test-case. The initial conditions have a voxel with high DA in the center off the domain, in the lower left corner of the shown 2D slice, and in the middle of the lower boundary of the 2D slice. The simulated dopamine distribution is shown at $t = 0ms$ (initial) and $t = 20ms$ demonstrating that dopamine at the boundaries flows back in from the opposite sites of the domain. The correct solution for periodic boundaries.

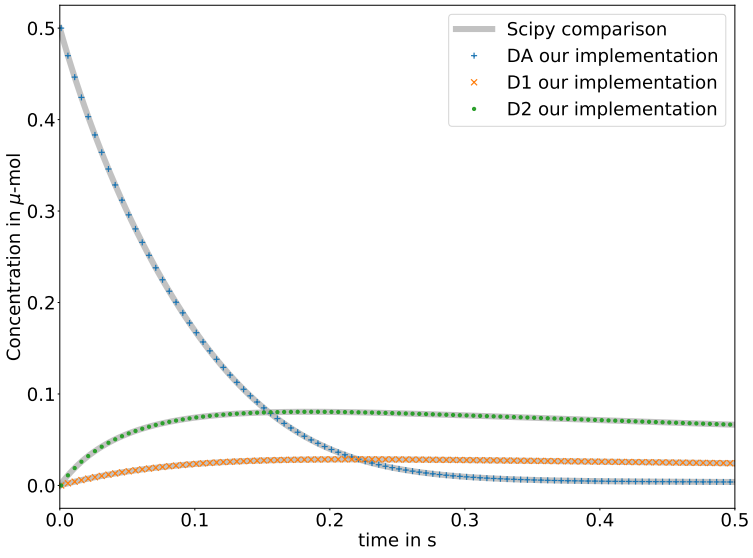

Figure 3.7: Numerical test simulation for the reaction and receptor interaction terms. Shown is the solution calculated with our code for a domain with initial conditions uniformly filled with DA and no bound receptors. Also shown is a comparison solution calculated with the "odeint" solver of the python package "scipy". The solutions agree very well, showing that our diffusion code also solves the nonlinear and reaction parts accurately.

Chapter 4

Preliminaries: Axonal Trees, Uptake and Synaptic Release

I discussed sources and sinks of DA briefly in **Section 2.4**. However, there I only presented a quite abstract treatment of DA sources and sinks, focused on how to incorporate appropriate terms into **Eq. 2.47**. However in this chapter I want to show how to determine the spatial and temporal distribution of sources and sinks in the model.

The only source of DA in my model is spiking release from dopaminergic synapses, even though there are some reports of possible non-spiking DA release e.g. modulated through cholinergic interneurons (Threlfell et al., 2012). This is due to two reasons, firstly because it is unclear how and if the non-spiking release works. How much DA is released, in what relation to acetylcholine? Is all non-spiking release related to cholinergic interneurons? Secondly, I believe that the first iteration of a model should be relatively simple, and the principle source of DA seems to be spiking release from synapses located on dopaminergic axons (Liu et al., 2018).

Sinks of DA are treated in more detail in this chapter too. The focus wil be on the faster, more important uptake, mechanism, Michaelis Menten uptake through the DA transporter (DAT) rather than diffusion through the cell membranes mentioned in **Section 2.4**. Where are these DAT, and therefore the uptake caused by them, located? They seem to be exclusively located on dopaminergic neurons where they can be found on both axonal and dendritic projections (Nirenberg et al., 1996). Dopaminergic neurons projecting to the striatum do not reside in the striatum themselves (Smith and Kieval, 2000; Ungerstedt, 1971; Björklund and Dunnett, 2007), so the DAT on the dendritic projections are of no importance to my model. However, their axons do project to the striatum, where their DAT will act as sinks of DA.

That means the principal sources and sinks of DA in the striatum are located on the axons of dopaminergic neurons. In this chapter I will introduce the model I developed to generate synthethic axonal trees, and how I use them to calculate the uptake distribution and DA release site distribution in the striatum.

The code used to generate the trees can be found at `https://bitbucket.org/Narur/dope-amine/src/` in the Make-Axons-uptake-dist file.

4.1 Growing Axonal Trees

Since both sources and sinks of DA are located on the axonal trees of the dopaminergic neurons, their geometry can be used to calculate local uptake and release of DA. The best source of these axonal geometries would be reconstructions of actual dopaminergic neurons. Dopaminergic neurons in the substantia nigra pars compacta and ventral tegmental area have massive unmyelinated axonal arbors (Pissadaki and Bolam, 2013; Matsuda et al., 2009), which is theorized to make them more susceptible to external stressors, and might be the reason why they degenerate in Parkinson's disease (Pissadaki and Bolam, 2013; Haddad and Nakamura, 2015). Their sheer size makes it quite complicated to reconstruct a large number of them, but do we need a large number to simulate a small cubical striatal volume with a width of $100 - 200\mu m$? The short answer is yes. Not only do dopaminergic neurons have large axonal arbors, there is also considerable overlap of dopaminergic neurons covering the same striatal volume. Generally, it is stated that between 100 and 200 dopaminergic neurons can influence the same striatal neuron (Matsuda et al., 2009; Arbuthnott and Wickens, 2007). Since our simulation volume is much smaller than the extend of dopaminergic axonal arbors ($\approx 1mm^3$; Prensa and Parent 2001; Matsuda et al. 2009), it will also be under the influence of $100 - 200$ dopaminergic neurons. As said before, it is hard to reconstruct a large number of dopaminergic neurons in animal experiments. However there were some successful attempts in reconstructing a few of those neurons (Matsuda et al., 2009). I developed a method that generates synthetic axons by using the reconstructions from Matsuda et al. (2009) and some inference from other neurons as a guideline for how the realistic axons look like.

4.1.1 Topological Axonal Growth

Our model should be as simple as possible, but have the ability to generate axonal trees that are a decent approximation for the axonal trees described in (Matsuda et al., 2009). As a first simplification I will assume that the axon is a binary tree. That means that if an axonal segment branches it will split into exactly two child segments. Splitting into more than two segments is only rarely observed and can be modeled as an aggregation of bifurcations Verwer and Van Pelt (1985, 1990). Therefore it is not considered here. I am using a two step approach. In the first step I generate a topological tree. This topological tree will consist of branches n_i which in turn will be made up of steps with a length Δl. Each branch will have a length $l = k\Delta_l$ attached to it, where $k = 0, 1, 2, ...$ Each branch, except for the very first (root) branch will have a parent, the branch that is connected to it and is closer to the root. Branches can either be terminal (they have no children), or they can end in a branching point, that means that they are the parent to exactly two child-branches. Branches that have the same parent are called siblings. In going with the tree analogy, the outermost branches in the tree, are called leaves.

How do we grow such a tree? We are using a Galton-Watson process like it is described in Binzegger et al. (2004). We grow the tree iteratively from the root upwards. For each iteration of the tree growth each branch, that has not been terminated, has three possible options. It can grow longer increasing its length by Δ_l, with probability p_{el}. It can create a branching point, terminating its own growth process while spawning two child segments, with probability p_{br} and it can simply stop growing with probability p_{st}. Since these are the only options the probabilities have to fulfill the condition

$$p_{br} + p_{el} + p_{st} = 1. \tag{4.1}$$

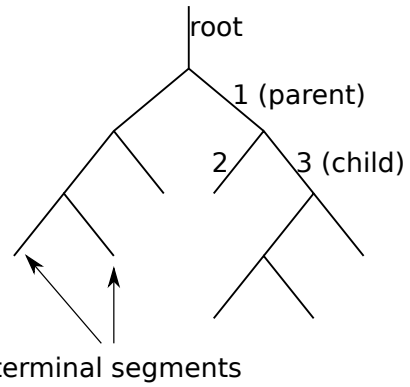

Figure 4.1: Sketch of a binary tree. All branches are connected to the root branch. Branch 1 is the parent to branches 2 and 3, so 2 and 3 are siblings, and children of 1. All outer branches are called leaves.

The exact values of these probabilities are parameters to be chosen in a way that gives us a realistic axonal tree.

When does the tree stop growing? If the probabilities are chosen so that

$$p_{el} + 2p_{br} < 1 \tag{4.2}$$

the trees are self terminating, that means they will eventually stop growing without any explicit stop condition. **Eq. 4.2** means that in each iteration, each branch spawns on average < 1 branches. That means the amount of branches is decaying, so that it will stop growing on its own because all branches are terminal. However our simulations showed that this condition produces quite small trees with far less segments than the ≈ 10000 (Matsuda et al., 2009) segments we are aiming for. Most of the self terminating trees have < 1000 segments. Of course sometimes there can also be exceptionally large trees, however I decided that our axon growing algorithm should not be based on statistical outliers. So in our case we relax this requirement and only keep the requirement from **Eq. 4.1**. However, that means we have to explicitly terminate the tree. This is done by choosing a termination parameter, $N^{max}_{branches}$ that leads to the tree terminating when this number of branches has been crossed. In our tree model we achieve this by tracking the amount of branches on the tree during the growth process, when it crosses $N^{max}_{branches}$ the current iteration over all leaves is still allowed to finish, but for the next iteration we set $p_{br} = 0$ and increase p_{st} accordingly. Then no new branches can be spawned and the tree will terminate leaving us with a tree that has a few more than $N^{max}_{branches}$ branches. In some cases the tree growth can still terminate after only a few segments, to prevent this, we require a minimum amount of branches ≈ 100 to accept a topological tree for farther processing. With this algorithm we can generate topological trees, however we end up with p_{br}, p_{el} and $N^{max}_{branches}$ as our set off parameters for which we have to find sensible estimates. We can use **Eq. 4.1** to find a value for the missing probability reducing the amount of missing parameters by one.

First we look at p_{el}. The probability that a branch has grown to its final number of steps k^{final} is

$$P(k^{final} = k) = (1 - p_{br} + p_{st})^k (p_{br} + p_{st}) = p_{el}^k (1 - p_{el}). \tag{4.3}$$

For the length of a branch it does not matter if it branches or just stops growing, since both processes end the growth process of the branch. From **Eq. 4.3** we see that the number of steps of a branch is described by a geometric distribution (Bronstein et al., 2004). For this distribution the mean the number of steps in a branch is given by $k^{mean} = 1/(1 - p_{el})$, and the mean length of the branches is given by $l = k^{mean}\Delta l$. In this model I chose the length increment $\Delta l = 1\mu m$. Axons in general tend to have very few very small segments (Binzegger et al., 2004), so choosing a very small length increment seems unnecessary and would only increase computational cost of tree generation. Now we can link the parameter p_{el} to the physical parameter of the average branch length, which is given to be $30.9 \pm 21.6\mu m$ (Matsuda et al., 2009). With $\Delta l = 1\mu m$ we choose $p_{el} = 0.9677$ leading to an average branch length of $k^{mean}\Delta l = 31.0 \pm 30.5\mu m$ which matches the experimentally measured branch length. Without much further work we can also decide what the $N^{max}_{branches}$ parameter should be for a given tree, since the total branch length of a (constructed) axonal tree will be given by $l_{total} = N^{max}_{branches} k^{mean}\Delta l$, so for an average tree we choose $N^{max}_{branches} = 17000$ to match the average axonal tree length of around $500,000\mu m$ given in Matsuda et al. (2009). We can choose larger or smaller $N^{max}_{branches}$ to make trees with larger or smaller total branch length. By design, in this growth model, the branch length distribution will always follow a geometric distribution. It seems that the branch length distribution, independent of neuron type, is approximately exponential (Binzegger et al., 2004) which fits well with our tree model since the geometric distribution is the discrete version of the exponential distribution. However, since dopaminergic axons are much larger than most other unmyelinated axons, more research into their branch length distribution would useful to further constrain our growth model. However, the branch length distribution of real axons does have a lack of short ($< 10\mu m$) fibers with respect to the exponential distribution (Binzegger et al., 2004). To keep our model simple we do not address this problem. However depending on what the generated axons are to be used for that might have to be addressed in the future. One possibility to address this problem would be to make p_{el} length dependent, so that it is larger at smaller k.

For the topological tree we still have one parameter to estimate, p_{br}. To estimate this parameter we analyze general axonal trees a little further and have to infer some information from non-dopaminergic axons. However since dopaminergic neurons are quite large, it would be good if the parameter estimation would be based on something that is quite general for multiple (or all) axon types. There are multiple ways to describe the topology of a topological tree. One important concept is the depth of a branch, which is given by the number of branches that have to be traversed to reach the beginning of the root branch (where the root branch itself is counted too). The height of the tree is then given by the maximum depth of all of its branches. Sadly this is not a very helpful measure in our case, since the height of a tree is usually related to the amount of branches in the tree, which is likely to be much larger in dopaminergic neurons than in most other neurons (compare Matsuda et al.

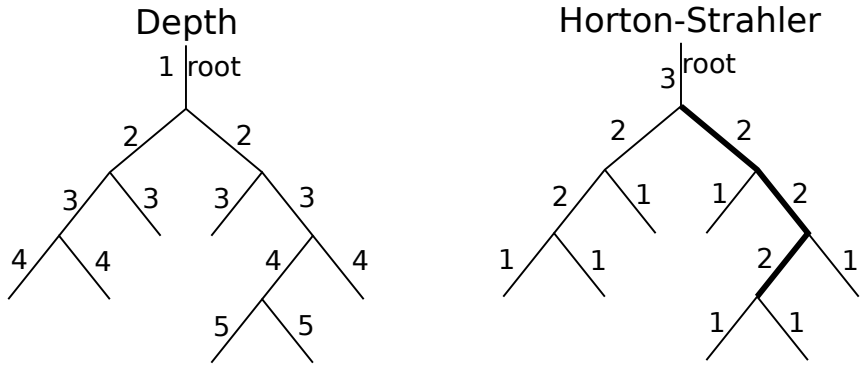

Figure 4.2: Example binary tree annotated with the depth of each branch (left), and the Horton-Strahler number of each branch (right). The Horton-Strahler segments are the maximum chains of branches with the same order. The height of the tree is 5 (the highest depth of any branch), while the Strahler number is 3 (the HS-order of the root)

2009 and Binzegger et al. 2004). However there are other descriptions that can be used e.g. the method proposed in Strahler (1952) that has been used on axonal trees in Binzegger et al. (2004). In this method each branch is assigned a Horton-Strahler number, beginning from the leave branches. In this description all leave branches have order 1. Branches that are not leaves are assigned order $k+1$, if both children have the same order k. However, if the children of a branch have differing order than the branch has order $max(k_l, k_r)$ where k_l and k_r are the orders of the children. In this descriptions multiple connected branches that have the same order k, together form a Horton-Strahler (HS) segment of order k. The root branch is contained in the HS segment with the highest order I called the Strahler number. An example of this is shown in **Fig. 4.2**. The Strahler number is the number of times a tree has to be pruned until the whole tree has been removed. Pruning here refers to the process of removing all end branches, i.e. all HS segments of order 1. Afterwards the HS order of the remaining tree branches is adjusted by subtracting one from each still exisiting HS segment. After pruning the remaining tree for I times the whole tree has been pruned. After $I-1$ pruning steps, only the HS segment containing the root is left. The advantage of this ordering scheme is that it can describe the principal features of branching of any type of binary tree structure with only two numbers (the bifurcation ratio and length ratio, described below) Binzegger et al. (2004). Both of these ratios depend on the Strahl-levels.

The bifurcation ratio of order k, b_k, is the ratio of the number of HS-segments with order k and the number of HS-segments with order $k+1$

$$b_k = \frac{N_k}{N_{k+1}}. \tag{4.4}$$

The bifurcation ratio is always $b_k > 2$. since each higher order HS-segment, spawns at least two lower order HS-segments. However it can be much larger. In our example tree in **Fig. 4.2** the first order bifurcation ration would be $b_k = 3.5$ since there are 7 first order HS-segments, but only 2 second order

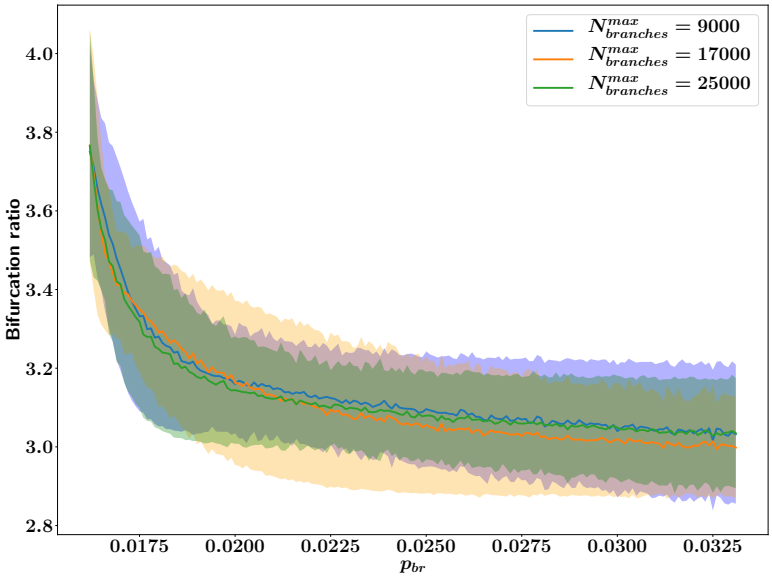

Figure 4.3: The bifurcation index calculated for 1000 trees plotted against the branching probability p_br for different tree sizes. The shaded areas are the 1σ environment of the calculated bifurcation index. It is clear that the bifurcation index is independent of the number of branches on the tree, at least for large trees.

segments. The length ratio is constructed similarly but instead of the number of HS segments, the length of HS-segments enters, so that the length ratio is defined as

$$l_k = \frac{L_k}{L_{k+1}} \tag{4.5}$$

where L_k is the average length of HS-segments of order k. However, here we will not pay a lot of attention to the length ratio, since there does not seem to be a global length ratio that is valid for all axon types. Since we do not know the length ratio for the dopaminergic neurons we can not use it to determine any parameters. However, there is a global bifurcation ratio that is independent of axon type and order of the bifurcation ratio $b = 3.32$ (Binzegger et al., 2004). That means that all axons have a similar bifurcation ratio, possibly related to some common growth mechanism (Binzegger et al., 2004).

For our current problem that means, that we might have a handle on determining p_{br} since it is the parameter that controls the branching behavior of the axonal trees. I performed a parameter search for this parameter by comparing the bifurcation ratio of our simulated trees with this global bifurcation ratio. Since we already know that $p_{el} = 0.9677$ the parameter space to search is fairly small, since **Eq. 4.1** has to be fulfilled. Furthermore we want a tree that is not self-terminating, so $p_{br} > 0.162$. I generated 1000 trees for three different

$N^{max}_{branches} = (9000, 17000, 25000)$ for each parameter $0.0322 > p_{br} > 0.162$ in steps of 0.0001 and calculated the bifurcation index average over all Strahl levels. **Fig. 4.3** shows the results of this parameter search. The bifurcation index is independent off the number of axonal branches. This should be true since all trees have a similar bifurcation index. We chose to use $p_{br} = 0.0192$ so that our our axonal trees have an average bifurcation index $b_{constructed} = 3.19 \pm 0.26$. With all parameters estimated we can now generate topological axonal trees for dopaminergic neurons, with plausible biological parameters. In this tree model, we do not model the initial axonal growth, projecting from the SNc or VTA to the striatum, but only the extensive tree within the striatum. However, this is not a model of how axons grow in reality and should not be taken as such, it is a simple algorithm to generate synthetic axons with empirically fitting parameters.

4.1.2 Making Flat Axons 3D

Now we have a method that creates topological axonal trees. However, in this current form we can not use them for their final task, calculating the location of synapses and DAT in our simulation domain. The trees are still flat, and have no three dimensional structure. In this chapter I will show how the flat, topological trees are turned into 3D structures.

Conceptually this is quite straightforward. We start traversing the tree from the beginning of the root branch. There are three cases we have to treat. First, we have to grow out a segment for the k steps of its given segment length $l = k\Delta x$. This growth will be fairly straight, but occasionally the axon will have a kink and shear out of direction (Katz, 1985b). The second case, a branch has grown out to its final length l and branches into new children. At this point we have to create a branch point with all its related angles, and start growing the new branches following the procedure of case one. The third case is the trivial case in which the branch just stops growing.
How are we traversing the tree? We will make the tree 3D starting from the root growing towards the leaves. After finishing with the root branch, we will create the branch-point and then process all branches of depth 1, growing them out until they terminate or branch again. We continue this for leaves at increasing depth until we have traversed the tree to its full height. This way, we can make sure that the branch points always connect to the new branches of the tree, which would be much harder if we would grow the tree e.g. from the leaves towards the root. After reaching all leaves of the tree, we will have 3D position information for all steps of length Δl in the tree.

Here we will work in cartesian coordinates. A diagram for relevant angles is shown in **Fig. 4.4**. How do we grow out the branches to their full length? Without loss of generality we will start the root at the origin $\vec{x}_0 = (0, 0, 0)$ in direction $\vec{d} = (0, 0, 1)$ and grow it one step into this direction. Now before growing the next step, we check check if the node is shearing out of direction in this step, it does so with probability p_{chdir}, which is a free parameter that will be constrained later. If it does not shear out of direction the branch just keeps growing in the direction $\vec{d}$ and the next segments position starting position will be $\vec{x}_1 = \vec{x}_0 + \Delta l\vec{d}$. However if the branch kinks we have to modify the direction vector $\vec{d}$ appropriately before calculating the starting position of the next

step. We do this in two steps, first we change the direction vector $\vec{d}$ by turning it an angle ϵ around a vector $\vec{d}_{rot}$, in the xy-plane, perpendicular to $\vec{d}$. This may seem arbitrary, however as step two we turn the modified $\vec{d}_{mod}$ around the old direction vector $\vec{d}$ by an angle ϕ that is randomly chosen to be between 0° and 360°. So all arbitrary choices about the rotation axis of the first rotation are meaningless since the second rotation is random and uniformly distributed. The first rotation kinks the growth direction away from the old growth direction, this kink makes the new direction lie anywhere within a cone of opening angle ϵ projected from the old growth direction. The second rotation then randomly chooses one of the directions along the cone. In our model ϵ follows a normal distribution with $\epsilon = 17° \pm 20°$ (Katz, 1985b). This seems to be a fairly uniform value for axons, since in experiments the kinking angle for axons from different species could not be distinguished. Of course it would be beneficial to have more encompassing measurements for dopaminergic neurons, but these measurements seem a reasonable substitute. It should also be noted that the measured values are from 2D cell cultures, so the 3D kinks might look different. However our kinking procedure reconstructs this 2D kink and turns it in space by a random angle. After the kink the next segments position starting position is calculated as $\vec{x}_{i+1} = \vec{x}_i + \Delta l \vec{d}_{new}$, as in the straight growth case. We keep growing the branch step by step, always tracking the direction vector, until the end of the branch is reached.

On reaching a branch point we have to create a branch. Other than for the case of the axon kinking we have to actually generate 2 new branches. First step will be deciding on the branch shape. That means we have to find the appropriate angles, in this case we need the branch opening angle α that describes the angle enclosed between the two new branches, and the angle that the left branch encloses with its parent branch β. Choosing the left angle here is a convention. The branch is fully described with these two angles, since the sum of the three angles on the branch has to be 360° (see **Fig. 4.4**). It seems that axons generally have an opening angle that is normally distributed with a mean between 60° and 90°, and a standard deviation of 30° (Katz, 1985a). So in the model I draw the opening angle α from a normal distribution with $\alpha = 70° \pm 30°$. The angle β is also drawn from a normal distribution with $\beta = 145° \pm 17°$, where the width of the distribution is chosen to match the values in (Katz, 1985a) and the mean is $\beta_{mean} = 180 - \alpha_{mean}/2$ so that the branching does not have a preferred direction. Now with the angles α and β we can perform the branching, in a plane. For this we turn the growth direction leading into the branch point, $\vec{d}$, by an angle θ around a vector $\vec{d}_{rot}$ perpendicular to $\vec{d}$ lying in the xy-plane, analogous to the shearing procedure above. This is done for both the new branches, however each new branch will be assigned a different direction vector. For the left branch the turning angle will be $\theta = 180° - \beta$,

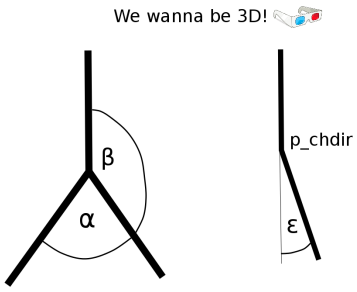

Figure 4.4: Relevant angles on branch points.

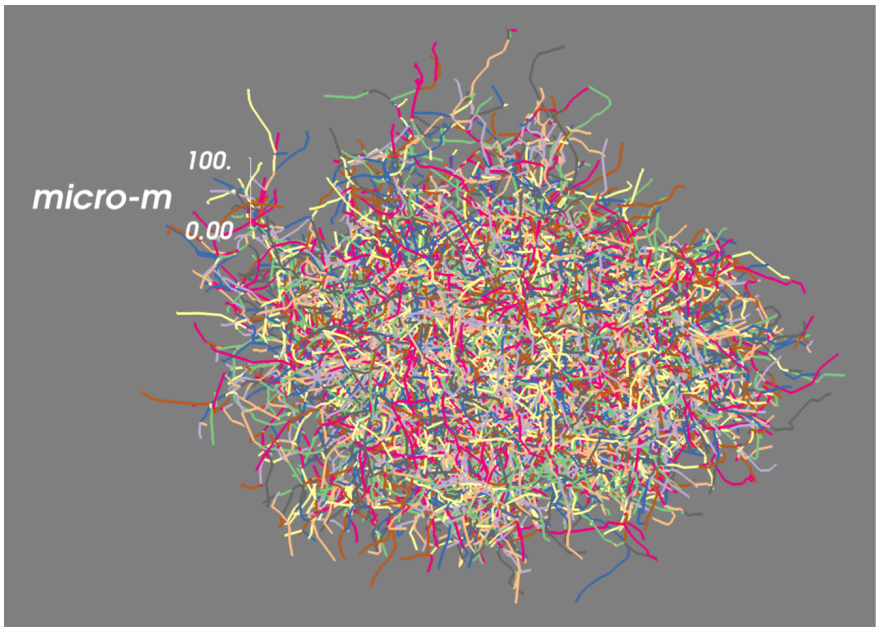

Figure 4.5: An example of a synthethic axonal tree generated with our algorithm. The colors are chosen, so that on each branchpoint at least one of the new branches has a different color.

and for the right branch we will turn by $\theta = \alpha + \beta - 180^{circ}$. After performing the branching in a plane we will turn each of the new direction vectors by the same uniform randomly chosen angle $0° < \phi < 360°$ around the original growth direction, to have the branching be a genuinely 3D process. Again the starting position of the next segment is calculated by $\vec{x}_{i+1} = \vec{x}_i + \Delta l \vec{d}$. In short, when choosing the angles appropriately, branching is just application of the kinking process to each child branch.

After performing the full procedure, from the root to the leaves we are left with a 3D representation of an axonal tree **Fig. 4.5**. It looks similar to real trees (compare Matsuda et al. 2009). By design we also match the branching ratio, branch length distribution and bifurcation ratio of dopaminergic neurons. However, we also want to investigate the size of the axonal tree, and how it depends on parameters. Is the axonal tree covering roughly the right volume? Or do our 3D trees cover a totally different volume than the trees reconstructed in experiments? All the angles are biologically motivated by experiments, however the probability of change in direction p_{chdir} is still a free parameter that we have to constrain.

4.1.3 Validation and Parameter Estimation

What is a good measure to for the volume the created axons enclose? Matsuda et al. (2009) describe the arbors as covering an "oval volume that extends $1.5 - 2.0mm$ rostrocaudally, $0.7 - 1.0mm$ dorsoventrally and $1.0 - 1.5mm$ medi-

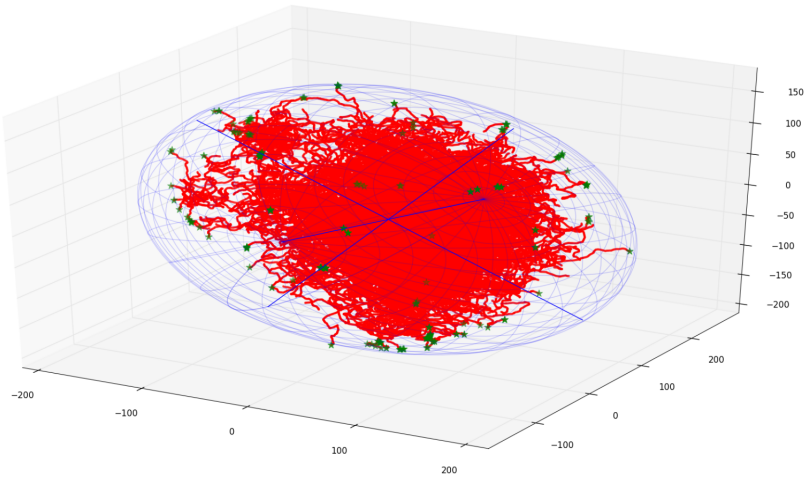

Figure 4.6: An example of an axonal tree with the points of its convex hull (green stars) and its minimum volume enveloping ellipse (MVEE).

olaterally". We want to use a similar measure for the axons we generate, and compare the sizes. For this purpose I will use the minimum volume enveloping ellipsoid (MVEE). That is the smallest ellipsoid that encloses all points of the axonal tree. We can use this directly with the points that describe the endpoints of all branch steps in an axonal tree. However since the number of points is very large (≈ 500000) that is a very slow process. To speed it up, we calculate the convex hull of the point cloud that makes up our axonal tree as a preprocessing step. That means we find the the set of points that describe the volume that contains all other points in the point cloud. That can be done quite quickly. If the enveloping ellipse contains these hull-points it will also contain all other points. This new set of points is much smaller than the full point cloud, so that we can calculate the MVEE in a reasonable time. For these two operations, calculating the convex hull and the MVEE, I use the Computational Geometry Algorithms Library The CGAL Project (2018). **Fig. 4.6** shows an example of an axon with the points of its convex hull marked and circumscribed by its MVEE. We can study the parameters of this ellipse as a proxy for the volume covered by the axon. Mainly, we know the axes lengths of the ellipsoid, so we can compare the dimensions with the values given in Matsuda et al. (2009).

We still need to constrain p_{chdir}, so we have to find out if it has an influence on the size of the enveloping ellipse. For studying single parameters we always create 1000 trees with the standard parameter set, containing the kink angle distribution $\epsilon = 17° \pm 20°$ and the branching angle distribution $\alpha = 70° \pm 30°$. The amount of branches in these standard trees is $N_{branches} = 17000$. For each tree we calculate the MVEE and the length of the three axes describing the ellipsoid and calculate the mean and standard deviation for all three axes. We find that p_{chdir} has a quite pronounced effect on the spanned volume of the created trees **Fig. 4.7**. The lengths of the different axes are more similar in

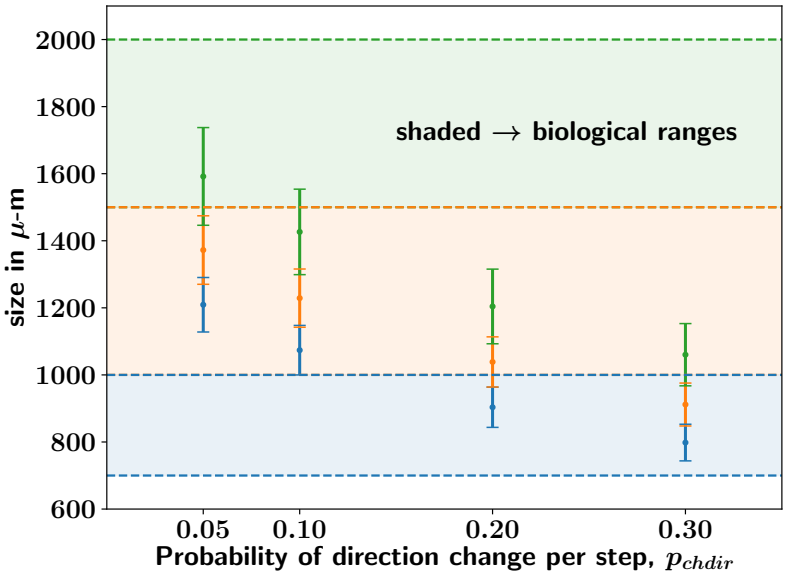

Figure 4.7: The spanned volume of synthetic axonal trees matches experimental values for a probability of direction change per step of $p_{chdir} = 0.1$. Plotted are the average axes lengths, ordered by size, of the MVEE of 1000 3D trees with the same generation parameters but different p_{chdir}. The bars denote one standard deviation. Shaded areas are the biological ranges of the oval volume covered by dopaminergic axons. Colors denote length of the (longest,middle,shortest) axes in order (green,orange,blue). The per step probability for a kink has a strong influence on the spanned volume of the created tree. The generated trees are fairly round, that is the axes length for largest to smallest are not wildly different.

our axons than in the biological ranges given in Matsuda et al. (2009). That means the volume that our axons cover is closer to spherical than for biological axons. This is not too suprising, since we did not put in any mechanism that would force a strong asymetry on the generated axons. However **Fig. 4.7** also shows that for a sensible choice of $p_{chdir} = 0.1$ our axonal trees grow to a similar size as the real axonal trees while being slightly rounder. A reasonable result for the simplicity of the model. We could try to make the axonal trees more asymmetric, but that would make our model more complicated for only little benefit since the data in Matsuda et al. (2009) is based on only a few axonal trees and might therefore suffer from sampling effects. So improving the model would most likely only give the illusion of an accuracy that is not really there. With $p_{chdir} = 0.1$ we now have all the parameters for the generation of the full 3D synthetic axonal trees.

To investigate how inaccuracies in the estimation of the other parameters might influence the spanned volume of the axonal trees I did a small parameter study. This is to make sure that small changes in the given parameters do not

lead to huge changes in the 3D structure of the created trees. First I investigated how the size of the topological tree influences the covered volume, **Fig. 4.8**. There is a tendency for larger trees to cover a slightly larger volume, but it is not very pronounced. The reason for this is probably that after the initial growth of the tree, a lot of the growth processes will not be on the borders of the tree, meaning it will not grow in size, but rather become more densely covered internally. This is conceptually analogous to the displacement of a particle in a random walk. A tree with more branches overall will have more branches at a larger depth, which is analogous to a particle performing more steps in a random walk. Here depth is a proxy for the amount of steps in the walk since it describes how many branches are between the final position of the endpoint of this subbranch and the starting location. However, the average height of a tree does not grow linear with the number of branches. We can calculate the average height of the trees used in this study, by investigating their topological trees. We find that the for the trees with $N_{branches} = 9000$ the average height is 62, while the average height of the trees with $N_{branches} = 25000$ is 72. The average height increases only slowly with the absolute branch number. So in this analogy, larger trees have only a few more steps in the random walk. Furthermore the distance to the starting point only grows with the square root of the number of steps (see **Chapter 2.1**), meaning that the more steps are taken the slower the distance grows. Both of these effects together explain why even trees that have a lot more branches, are not covering a much larger volume **Fig. 4.8**.

I performed experiments with the other parameters, the branching and kinking angles **Fig. 4.9**. I find that the branching angle mean and standard deviation have barely any effect on the covered volume. At least in the parameter space close to our chosen parameters. This is a reassuring result, since it means that the specific choice of the branching angle is of limited importance and the branching angle is experimentally not very well constrained. I find that larger mean kink angles and standard deviations both reduce the size of the covered volume. All these results can be understood in the context of the random walk analogy. The branch points already change the direction vector so strongly that the new direction vector is essentially random. So making the average branch angle larger does not change the system with respect to the maximum displacement. The same is true for the branch angle standard deviation. However larger kink angles, and standard deviations, lead to the branches growing less straight, effectively reducing the step size of the random walk. Reducing the maximum displacement and therefore the covered volume. This also explains why p_{chdir} so strongly influences the size of the covered volume. Since it controls the length of "straight" steps. For $p_{chdir} = 0$ all branching points would be connected by straight segments. So the average random walk step-length would be the average branch length. However this step length is reduced because the connecting branches kink. If they kink stronger the step length is reduced, so the covered volume becomes smaller **Fig. 4.9 c,d**. If they kink more often the step length and therefore the covered volume reduce **Fig. 4.7**.

Generally the axonal growth model worked quite well. All important parameters are well constrained and our synthetic axons match experimentally measured parameters of real axons.

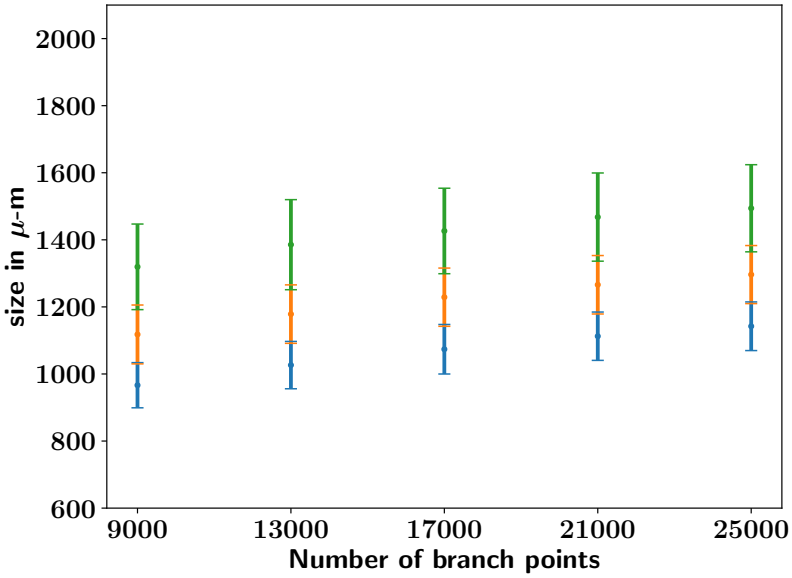

Figure 4.8: The number of branches has only a small influence on the spanned volume of the axonal trees. Plotted are the average axes lengths, ordered by size, of the MVEE of 1000 3D trees with the same generation parameters but a different number of branches on the topological tree. Error bars denote one standard deviation. Larger trees tend to cover a larger volume but the effect is not very pronounced.

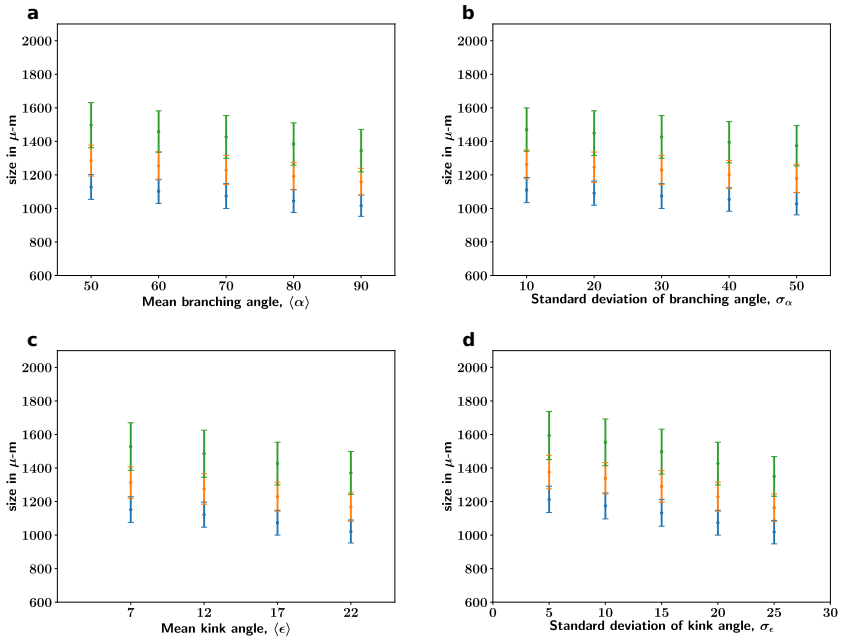

Figure 4.9: Mean branching angle (**a**) and standard deviation of branching angle (**b**) have only very minor influence on the covered volume of the axonal tree. Mean king angle (**c**) and kink angle standard deviation (**d**) have a more noticeable effect. Plotted are the average axes lengths, ordered by size, of the MVEE of 1000 3D trees with the same generation parameters but different mean branching angle (**a**), branching angle standard deviation (**b**), mean king angle (**c**) and kink angle standard deviation (**d**). Error bars denote one standard deviation.

4.2 Inhomogenous Uptake

We generated a set of realistic synthetic axonal trees. So as a next step we have to combine these axons with the numerical diffusion model **Chapter 3**. We already discussed that DAT can only be found on the dopaminergic axons (Nirenberg et al., 1996). Furthermore, DAT can be found all along the dopaminergic axons but is absent from synapses (Hersch et al., 1997). In line with experimental data (Nirenberg et al., 1997) we will model the uptake as if the DAT are uniformly distributed along the axonal length. Hersch et al. (1997) and Nirenberg et al. (1997) find no DAT at synapses. With this distribution of DAT we model the inhomogeneous DA uptake in the striatum by calculating the uptake in each voxel by tracking how much length of axon passes through the voxel. Of course axons have a diameter and therefore an area attached to them. However, since the distribution is modeled as uniform, each length of axon will have the same amount of DAT attached to it and will therefore contribute equally. Therefore, an uptake value V_{max} is assigned to each voxel depending on the length of axon passing through it. The assumption here is that the amount of DAT in a voxel is controlled by the length of axon in that voxel. The amount of DAT is then directly related to the maximum uptake rate V_{max} in this voxel (see **Section 2.3**). However, that means we have to calculate the length of axon passing through each voxel. We already have all the the ingredients, the shape of our domain (cubical, filled with equal sized cubical voxels) and the synthetic axons. We just have to bring them together. For each axon we position the middle of our simulation domain on the center of the MVEE of the axon. Now parts of the axon are within the simulation domain. We can calculate how much of the axon is within each voxel in the simulation domain. This is a conceptually straightforward application of geometry. To ease the complexity of this task I made heavy use of the Computational Geometry Algorithms Library The CGAL Project (2018) again. An example of the result of this process is given in **Fig. 4.10**.

We do this for as many axons as we expect to contribute to our simulation domain (**Fig. 4.11**), which in the simulations for the healthy case will be 100 (Matsuda et al., 2009; Arbuthnott and Wickens, 2007). Here all the axons in our domain will also be centered on our domain. Which again we chose for simplicity. An improvement might be to successively slide the center of the axons MVEE out of the domain with growing axon number. However, since the covered volume of the axon is usually larger than the size of the domain (which is either a cube with side length $100\mu m$ or $200\mu m$) the differences should be small.

Now we have calculated how much axon-length is in each voxel of the simulation domain, but we still need to translate this into a maximum uptake rate V_{max} for each voxel. We do not know what the exact number of DAT is per μm of axon. However, we know that the bulk uptake constant in the striatum is $\approx 5\mu M$ (Nicholson, 1995; Wightman et al., 1988). If we know the average length of axon per voxel, and we assign a fitting $V_{max}/length$ we can calculate V_{max} for each voxel. To find the average length per voxel, we filled 1000 simulation domains with 100 axons with a given number of branches $N_{branches}$ each and calculated the resulting length per voxel for the $100\mu m$ and $200\mu m$ domain size. The average length per voxel, l_{voxel}, depends on the size of the axonal trees. Longer trees lead to a larger length per voxel, since they are denser. In

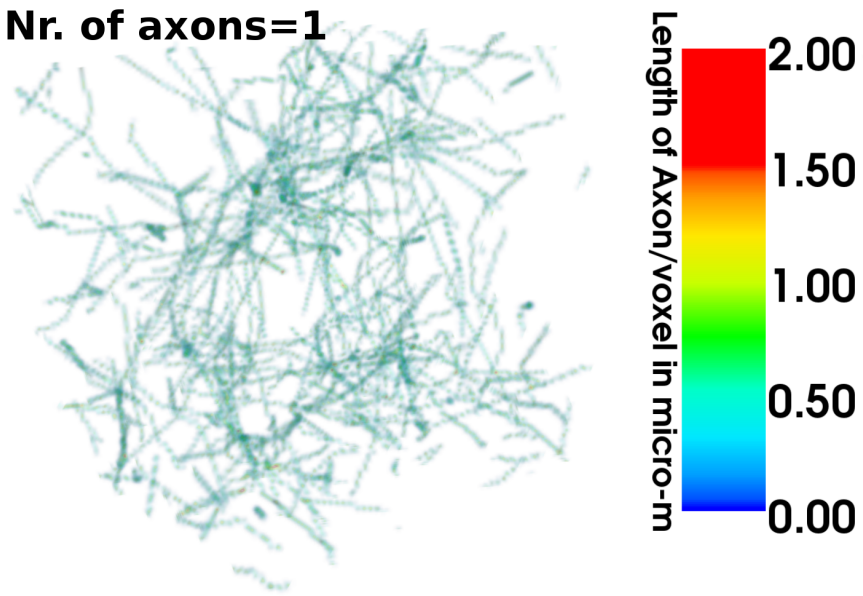

Figure 4.10: Simulation domain with length of axon per voxel after growing one axon through the domain. Transparent areas have no axonal length in them.

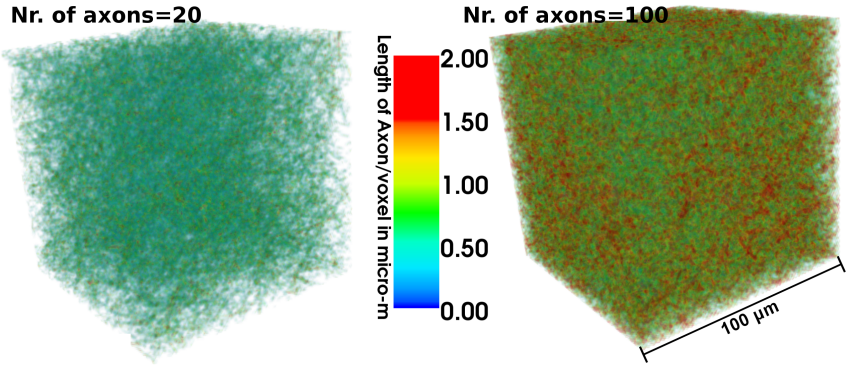

Figure 4.11: Simulation domain with length of axon per voxel after growing 20 and 100 axons through the domain.

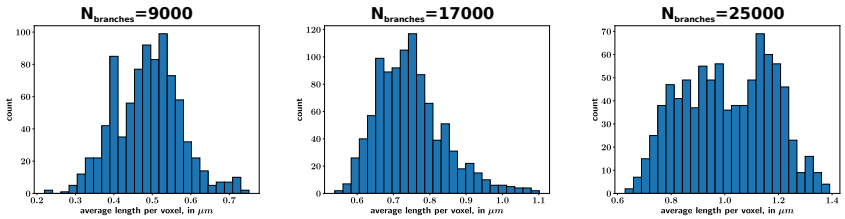

Figure 4.12: Axonal trees with more branches lead to a larger length in voxel. However the largest axonal trees also lead to a broader distribution. Histograms showing the distribution of length per voxel, for 1000 domains each filled with 100 axons with the given number of branches.

return smaller trees lead to smaller lengths per voxel (**Fig. 4.11**). For the final diffusion simulations all the generated axonal tree will have $N_{branches} = 17000$. This way all axons have roughly the average total axonal length. This was chosen since the distribution of $l_{voxel} = length/voxel$ values is already fairly broad even for the same number of branches. Creating trees with different branch numbers would make the distribution even broader, leading to a higher chance that the simulations we run have fairly different maximal uptake values V_{max}. The average length per voxel for the chosen $N_{branches} = 17000$ and the domain with voxel size $1\mu m$ is $l_{voxel} = 0.75\mu m/voxel$. That means that in our simulation $1\mu m$ of axon has to have enough DAT to account for a V_{max} of around $6.7\mu M s^{-1}$. Which we will use to transform the length of axon in each voxel to an uptake constant. Somewhat perplexing is that we find a slightly higher value of length/voxel as expected for the simulation with voxel size $2\mu m$, we find a value of $l_{voxel} = 7.6\mu m/voxel$, whereas we would expect a value closer to $l_{voxel} = 6\mu m voxel^{-1}$ purely from the larger volume of the voxel. The conversion constant is chosen accordingly for the larger simulations. This way of calculating the maximum uptake rate for each voxel means that our simulations will have slightly different global V_{max} depending on their specific length of axon per voxel. However this methodology can be adjusted if necessary to give exactly the same global V_{max} for a set of realizations, simply by adjusting the conversion factor accordingly for each realization.

4.2.1 Inhomogenous Uptake: Validation

Does a domain with inhomogeneous uptake and the same average V_{max} as a flat uptake also produce the same uptake behavior? Generally V_{max} is a linear factor, and should therefore add up linearly. To confirm this I designed a simulation to measure V_{max} and compare the flat uptake case, with the inhomogeneous uptake case.

In this simulation we use a virtual DA sensing electrode with an elliptical cross section as described in Kelly and Wightman (1986). Our virtual electrodes sensing surface is an ellipse with major axis $a = 30\mu m$ and minor axis $b = 10\mu m$, which equals a sensing surface of $235\mu m^2$ (Kelly and Wightman, 1986). For the simulation we fill the whole domain with $10\mu M$ of DA simulate the time-course of the DA concentration with homogeneous uptake, and with 5 different realizations of inhomogeneous uptake. The measurement of the DA

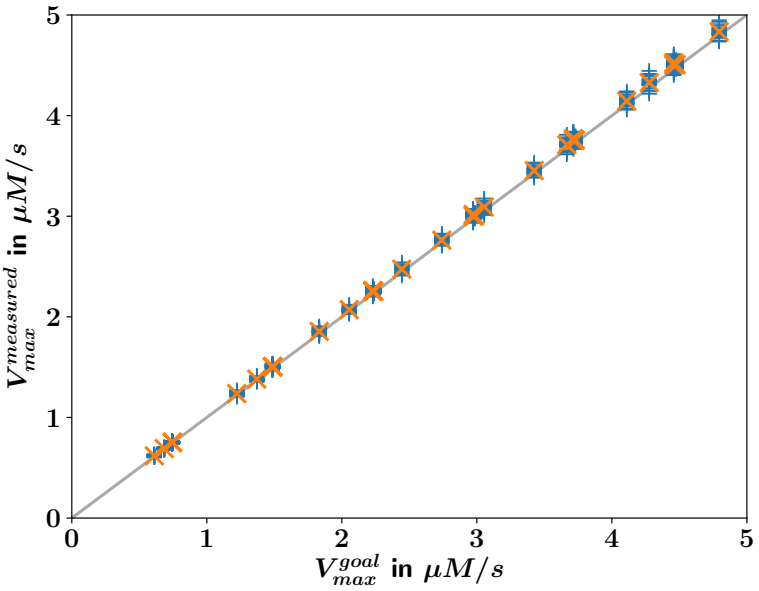

Figure 4.13: The averaged value of V_{max} for an inhomogeneous uptake model equals the uptake of a flat uptake model with the same V_{max}. Plotted are the measured V_{max} for the inhomogeneous uptake case, against the V_{max} calculated by averaging the inhomogeneous V_{max} over the whole domain. The blue crosses, denote the values for individual samples in the domain. The orange x show the average over all sample points in one simulation. The grey line is the line of identity. It is clear that the averaged inhomogeneous V_{max} equals the flat V_{max} values.

concentration is performed by placing our virtual electrode at a randomly chosen location in the simulation domain with a randomly chosen orientation along the major cartesian axes and averaging all the voxels that are inside the elliptical area. The goal here is to measure the DA concentration from a similar sampling area as is done in real experiments for calculating the maximum uptake rate V_{max}. To see if our simulation would give different values of V_{max} in a version of the experiment where the electrodes measurements are error free and there are no adverse effects created by the implantation of the electrode. For the test of V_{max} I initialized the whole domain with a $C_{DA} = 100\mu M$ and let it develop for $4s$. Then I took the measured concentration at the beginning and at the end for each sample and divide by the elapses time to get the V_{max} value. This procedure matches the experimental procedure used in Wightman et al. (1988). In the homogeneous case the bulk removal of DA is equal to V_{max} for high C_{DA}. **Fig. 4.13** shows that inhomogeneous uptake leads to similar bulk removal behavior than homogeneous uptake would. That means if we want to simulate a domain with that has an average uptake of V_{max} we can simply match the average uptake value of our inhomogeneous V_{max}.

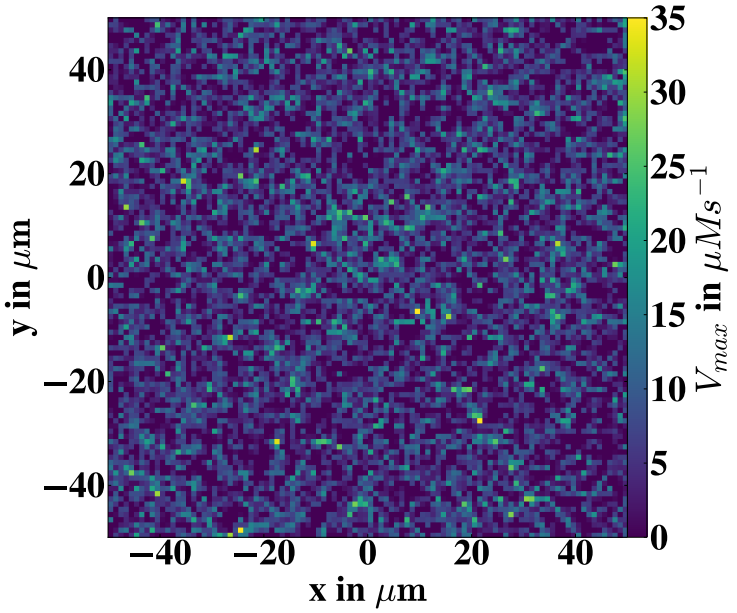

Figure 4.14: 2D slice of the inhomogeneous V_{max} distribution used for the comparison between flat and inhomogeneous uptake used in **Fig. 4.15** and **Fig. 4.16**. The local V_{max} is quite variable, having areas of above $V_{max} > 10\mu Ms^{-1}$ but also areas with nearly no uptake.

4.2.2 Differences Between Homogenous and Inhomogenous Uptake

It is also interesting to know how large the differences are between the inhomogeneous and homogeneous uptake case. To determine these differences I simulated one realization of a striatal cube of size $100\mu m$ with a voxel size of $1\mu m$. For this realization 100 axons were created and grown through the simulation cube. The average length per voxel for this realization was $0.86\mu m$, which results in an average $V_{max} = 5.36\mu Ms^{-1}$ with the V_{max}/l value we calculated before. A slice through the inhomogeneous V_{max} distribution of this realization is shown in **Fig. 4.14**.

The first experiment started with homogeneous initial conditions of $C_{DA} = 30nM$ and was evolved in time without any sources of DA. The results of this experiment are shown in **Fig. 4.15**, for snapshots after $10ms, 30ms$ and $50ms$. As expected C_{DA} declines uniformly in the flat uptake case. In the inhomogeneous case we see a decline of a similar magnitude, fitting with our previous experiments in **Fig. 4.13**. However different to the decline in the flat uptake case, the decline is not fully uniform. In some areas the decline is faster, leading to lower concentrations of C_{DA}, and in others it is slower leading to a higher remaining C_{DA}. **Fig. 4.15** also shows the absolute ($\Delta C = C_{DA}^{flat} - C_{DA}^{inh}$) and relative $\delta C = \Delta C / C_{DA}^{flat}$ difference between the flat and inhomogeneous case.

We chose the convention so that, for residuals and errors, the blue areas show areas where the inhomogeneous case has lower C_{DA} than the flat case. When comparing **Fig. 4.15** with **Fig. 4.14** we can see that the areas of lower C_{DA} in **Fig. 4.15** can be identified with areas of higher V_{max} in **Fig. 4.14**, however this identification is not immediately obvious from **Fig. 4.14** alone. A few features that can be identified are the area of elevated V_{max} in the middle of the frame, that coincides with the depression in C_{DA} at the same location. There is also a chain of elevated V_{max} in the bottom right corner, that can be seen in the residuals, especially at $10ms$. So how large are the differences? The average absolute difference after $50ms$ is $\approx 1.0nM$ which equals a difference of about 10%. The inhomogeneous uptake case shows a noticeable difference, but does this difference remain in a system with dopamine release?

To test this I used the same realization and simulated its DA concentration during periods with ongoing synaptic release, a more realistic scenario. I used 100 resting state spike trains (**Chapter 4.3**), one for each axon, and let the dopaminergic synapses release DA (**Chapter 4.4**). The simulation was run for the flat and inhomogeneous uptake case. I made sure that in both simulations the same set of synapses released DA for each arriving spike, so that I could treat this simulation like the one without DA sources discussed above. The results are shown in **Fig. 4.16**. The distribution in the C_{DA} do not seem qualitatively different, since the instantaneous C_{DA} distribution seems to be dominated by the release events. However, there is a quantitative difference between the flat and inhomogeneous case, that is revealed by the absolute and relative differences. As in the previous experiment the relative difference is $\approx 10\%$. We can also observe that the locations of lower and higher C_{DA} have a fairly stable position even in these simulation snapshots that are seconds apart. This is as expected since the differences in the C_{DA} are due to a quasi anatomical difference in both models. The V_{max} distribution does not change with time. However the V_{max} distribution would differ for a different set of axons, which would be akin to a different animal.

Incorporating inhomogeneous uptake into our simulation makes a quantitative difference to the flat uptake case of about 10%, however there are no immediately obvious qualitative changes.

4.3 Spike Trains

For our model of DA diffusion we require a model of the firing patterns that the dopaminergic neurons, projecting to the Striatum exhibit. The firing patterns are required for a biologically plausible diffusion model. We model our firing patterns according to the firing patterns described in Hyland et al. (2002). Here we describe how the spike trains used in the diffusion model are generated. We will also describe why we chose to model the spike trains as we did. We tried to find a balance between accurately reproducing the firing patterns found in Hyland et al. (2002) and keeping the model simple.

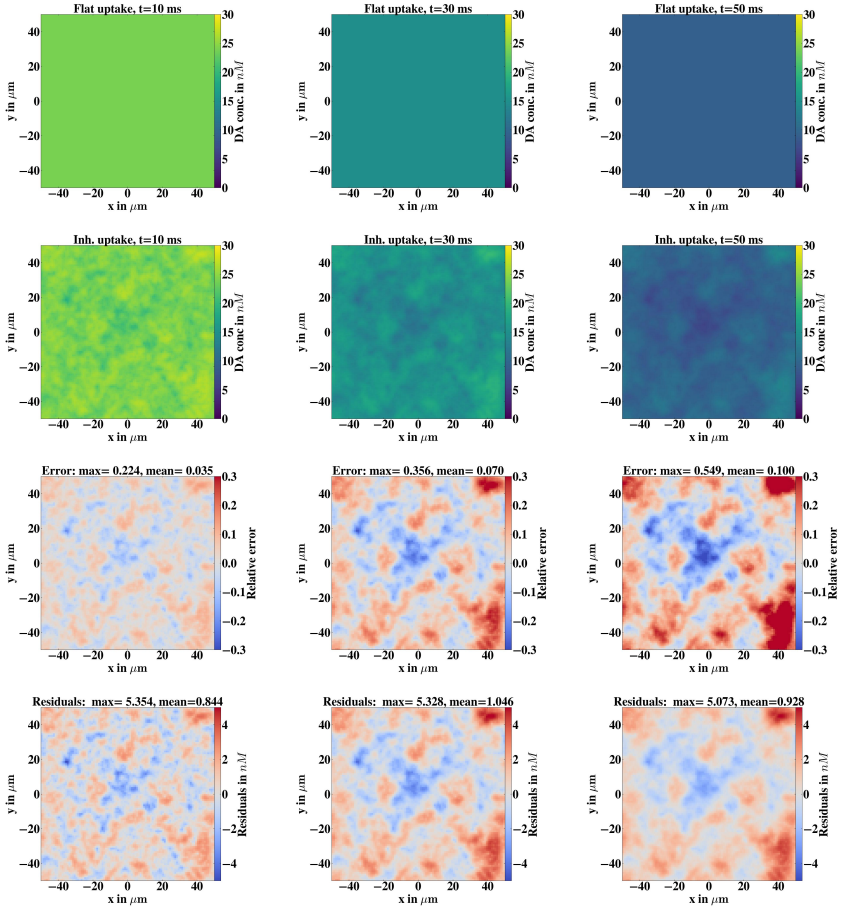

Figure 4.15: Simulations with flat and inhomogeneous uptake distribution differ, by about $1nM$ or $\approx 10\%$ averaged over the domain. Comparison between flat and inhomogeneous uptake. Shown are, from top to bottom, the DA concentration for the flat and inhomogenous uptake case, their relative difference and their absolute difference. Snapshots after $10, 30, 50ms$ are shown from left to right. This simulation started with a uniform $C_{DA} = 30nM$ initial condition.

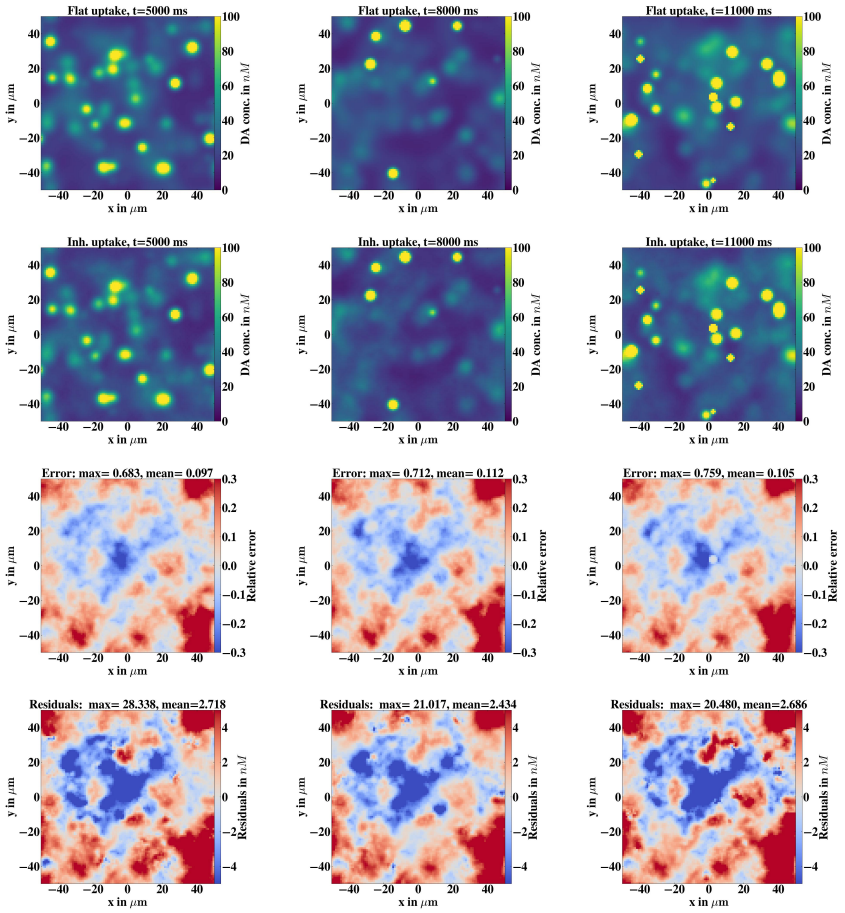

Figure 4.16: Even though there is no qualitative difference between the cases the flat and inhomogeneous case differ, average over the domain, by about $3nM$ equaling $\approx 10\%$. Comparison between flat and inhomogeneous uptake. Shown are, from top to bottom, the DA concentration for the flat and inhomogeneous uptake case, their relative difference and their absolute difference. Snapshots after $5, 8, 11s$ are shown from left to right. In this simulation all axons fire with their resting state firing rate and synapses release DA accordingly. The locations where C_{DA} is lower or higher in the inhomogeneous case are fairly stable in time, since they are primarily due to the, not changing, V_{max} distribution.

4.3.1 Baseline Spike Train Types

Hyland et al. (2002) classifies the baseline firing of dopaminergic neurons along two axes: irregular/regular and high-bursting/low-bursting. Neurons classified as regular firing fire in a clockwork fashion with a relatively constant Inter-Spike interval(ISI). Irregular firing neurons do not exhibit this clockwork firing, but have a broader distribution of ISIs. In Hyland et al. (2002) it is noted that regular-firing cells tend to be nearly exclusively low-bursting. For this reason we model three different spike train types for our neurons. Irregular high-bursting, irregular low-bursting and regular low-bursting. For purposes of simplification, but also to heighten the difference between the different firing patterns we model the low-bursting spike trains without any bursts. We chose the ratios between the different spike train types according to Hyland et al. (2002) with 25% regular firing neurons, 55% irregular firing neurons and 20% (high-)bursting neurons. In the rest of this section I will describe how we model the different spike train types.

Irregular Spike Trains

To model irregular neuronal firing we utilize a gamma-distribution (a generalized version of the exponential distribution, equals an exponential distribution for a shape parameters $k = 1.0$). For one spike train we successively pull ISIs from a gamma distribution with a given shape parameter k and a rate parameter chosen so that the firing rate matches our desired firing rate. When generating a set of spike trains we pull the firing rate from a normal distribution with $f = 4.0 \pm 0.8Hz$. This is not the exact firing rate distribution measured for the irregular firing neurons in Hyland et al. (2002), but we decided to have the same firing rate distribution for irregular and regular firing neurons, to reduce effects based on firing frequency. The shape parameter k is chosen to be 3.0 for all neurons. The resulting CV distribution has a similar mean but is narrower than the measured distribution (our simulation $CV \approx 0.57 \pm 0.01$, Hyland et al. (2002) $CV = 0.66 \pm 0.22$). For these parameters the mean reduced activity time, as calculated in Hyland et al. (2002) is similar to the values measured in hyland ($\approx 160ms$) however the distribution of the reduced activity period is much narrower. Besides these inaccuracies we use this model to keep the spiketrain generation reasonably simple. **Fig.4.17** can be used to compare with Hyland et al. (2002), showing a reasonably similar ISI histogram and autocorrelogram.

Regular Spike Trains

Regular firing is modeled by choosing a mean ISI for the regular firing neuron to match the desired rate $ISI = 1/rate$. The ISIs are then pulled from a normal distribution around the mean ISI with a width chosen to match the desired CV, $\frac{1}{\sigma^2} = CV \cdot 1/rate$. The rates for the regular firing are pulled from a normal distribution with $rate = 4.0 \pm 0.8Hz$ to match the data of Hyland et al. (2002). We choose the CV distribution as $CV = 0.35 \pm 0.15$ which means our regular neurons will be firing more regularly than the measured neurons in Hyland et al. (2002). This is done to increase the effect of the regular firing. The ISI histogram and autocorrelogram of a representative regular spiketrain are shown in **Fig. 4.17**

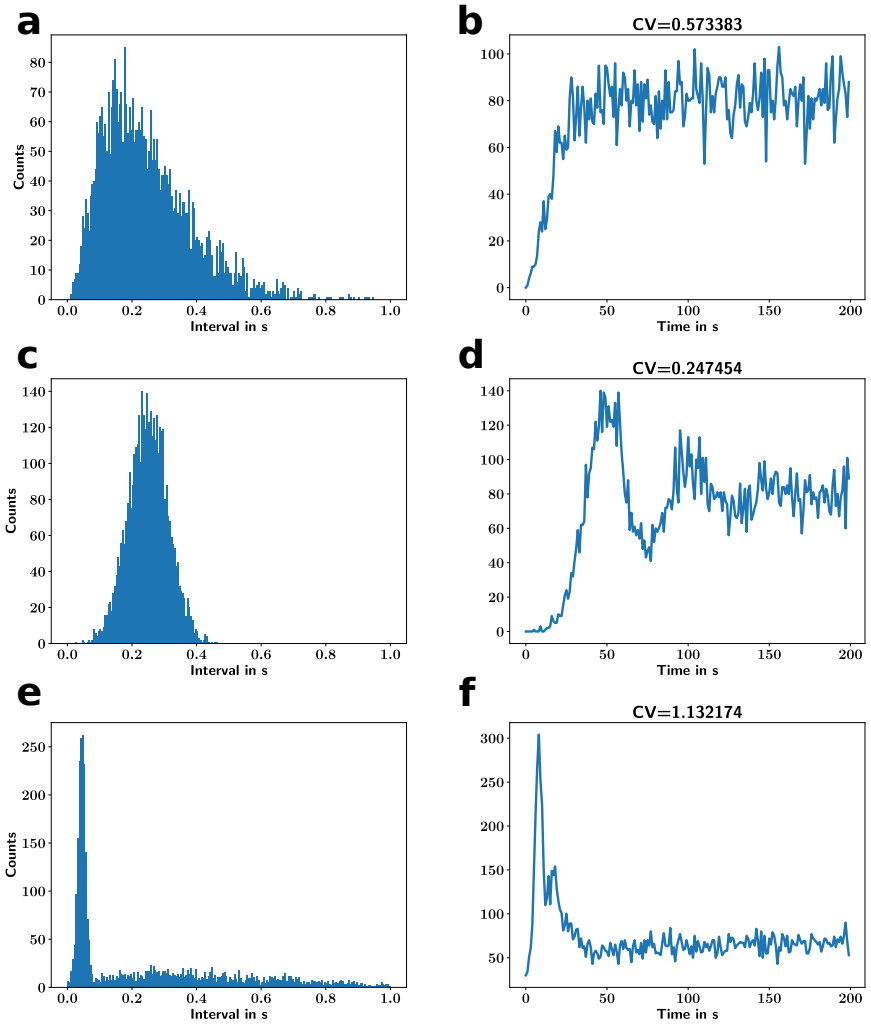

Figure 4.17: The ISI-Histograms and Auto-correlograms of our generated spike trains match with the ISI Histograms and Auto-correlograms of Hyland et al. (2002). Plotted are the ISI Histogram (**a**) and Auto-correlogram (**b**) of a representative irregular spiketrain with $rate = 4.0Hz$ and $k = 3.0$. The ISI Histogram (**c**) and Auto-correlogram (**d**) of a representative regular spiketrain with $rate = 4.0Hz$ and $CV = 0.25$. The ISI Histogram (**e**) and Auto-correlogram (**f**) of a representative high-bursting spiketrain with $rate = 4.0Hz$, $k = 3$, $\lambda = 2.7$ and $rate_{bursts} = 0.82$.

High Bursting Spike Trains

We generate the high bursting spike trains as irregular high bursting spike trains. We start with an irregular spike train with shape parameter $k = 3.0$ and the rate from a normal distribution $rate = 4.0 \pm 0.8$ keeping it comparable to the low-bursting spike trains. However before the irregular spike train is generated as described in **Section 4.3.1** the rate is modified to accommodate the frequent bursts that will will appear in this spike train. For this we reduce the rate so that $rate_{modified} = rate - (rate_{bursts} \cdot Spikes_{burst})$. We then pull the time of the next burst from an exponential distribution depending on the rate of bursts $rate_{bursts} = 0.82 \pm 0.2$ according to Hyland et al. (2002), where we choose the values from the analysis of bursts with at least two spikes. When a burst occurs we pull the number of spikes in the burst from a Poisson distribution with an expected number of spikes of $\lambda = 2.7 \pm 0.5$ as found in Hyland et al. (2002). The intraburst spike interval is generated by making a short regular spike train with an ISI normally distributed around an average $ISI = 1/rate_{intra-burst}$ with width $0.25 * ISI$. When the burst is over the normal irregular firing continues until another burst arrives. This method generates spiketrains with a very similar fraction of spikes in burst to that measured in Hyland et al. (2002). It should be mentioned that the CV for these spiketrains tends to be slightly higher $CV = 1.2 \pm 0.3$ than the CV of the measured spiketrains $CV_{Hyland} = 0.94 \pm 0.22$. The ISI histogram and autocorrelogram of a representative bursting spiketrain are shown in **Fig.4.17**

4.3.2 Reward-Bursting

A burst response, mimicking a reward response is also implemented in our spike train generator. This reward response adds a burst at a given time to a fraction of the spike trains. In the default model the fraction of bursting neurons is chosen to be 0.7, according to fraction of reward-responding neurons in Tobler et al. (2003). This fraction is distributed equally to the baseline fractions. That means that e.g. 70% of the high-bursting, regular and irregular firing neurons are chosen to show a reward burst. The reward bursts are modeled, like the bursts in the high-bursting case, albeit with a higher intra-burst frequency $f_{IB} = 31.3 \pm 8.0Hz$ and a slightly higher number of spikes per burst $\lambda = 3.0 \pm 0.5$ as reported in Hyland et al. (2002) for rewards. To avoid a correlation between the starts of the bursts we jitter the beginning of all events (rewarding or otherwise) by adding a jitter time which is uniformly distributed between 0 and $max_{jittertime}$. The model default is $max_{jittertime} = 100ms$.

4.4 Synapses, Positioning and Release

The created axonal trees are also used to distribute synapses in the simulation domain. The number of synapses on each of the 100 axons is calculated by dividing the length of each given axon in the simulation domain by the mean distance of dopaminergic synapses on one axon, $7.6\mu m$ (Arbuthnott and Wickens, 2007). Then the calculated number of synapses is distributed along each axon, in the simulation cube. For each synapse I randomly choose one of the corresponding axons single step components in the simulation domain and slide the synapse to a random position along this axonal branch step. Repeating this

procedure for all the axons in the domain leaves us with a set of synapses for each axon. As a check we calculate the volume density of synapses in our simulation domain. As we showed above, the average length in voxel, for 100 axons in the simulation domain is $0.75\mu m$ for the domain with voxel size $1\mu m$, and $7.6\mu m$ for the domain with voxel size of $2\mu m$. Each of these domains contains a total of $N_{voxel} = 100^3 = 10^6$ voxels. So the number of synapses in the domain is then

$$N_{synapses} = \frac{l_{voxel} N_{voxel}}{7.6\mu m} \tag{4.6}$$

which gives a number of synapses $N^{100}_{synapses} \approx 10^5$ for the $100\mu m$ domain and $N^{200}_{synapses} \approx 10^6$ for the $200\mu m$ domain. With the volumes of $10^6\mu m^3$ and $8 \cdot 10^6\mu m^3$ we can now calculate the number density ρ_{syn} of synapses in our simulations, when using the generated axonal trees. These number densities are $\rho^{100}_{syn} = 0.1\mu m^3$ and $\rho^{200}_{syn} = 0.125\mu m^3$, which is nearly exactly the biological value of $0.104\mu m^3$ (Arbuthnott and Wickens, 2007). This provides strong evidence for the validity of the axonal growth model because we did not fit any parameters to match this value.

However it should be noted that, since the branches of even one axon have a fairly erratic distribution in the simulation domain (see **Fig. 4.10**), the distribution of the synapses in the domain is not very different than for random synapse placement **Fig. 4.18**.

Release Events

There is still a step missing for the handling of release events. We already have the synaptic positions for each axons, and the spiketrains for each spiketrain. However, we still have to figure out when and how much DA should be released when a spike arrives at a dopaminergic synapse. To keep this simple, we will restrict the release event to a few parameters. We assume that a synapse has a probability p with which it will release a certain amount of DA $Q \pm \sigma_Q$. Q is also called the quantal size. We choose $Q = 3000 \pm 300$, as described in Pothos et al. (1998); Pothos (2002), the same as choosen in Dreyer et al. (2010). Generally the quantal release size is assumed in the order of a few 1000 molecules of DA (Garris et al., 1994; Rooney and Wallace, 2015), however a few measurements with larger quantal sizes also exist (Jaffe et al., 1998). In our model the Quantal release size is a fixed value for one simulation. However it is likely that quantal release size is subject to activity dependent changes (Montague et al., 2004) which we do not incorporate into our model for now the sake of simplicity.

The second question that remains is the probability of release. I did not find any direct measurements of this quantity. However Dreyer et al. (2010) uses the tissue content of dopamine, the quantal release size, the average fraction of the terminal content released per spike, and the total density of release sites to estimate the release probability as $p \approx 6\%$ which Is also used in our model. Again we keep the release probability constant in our simulation. It is known that $D2$ autoreceptors influence the release of DA. A likely candidate for this effect is the release probability (Dreyer and Hounsgaard, 2012). This automodulation is a candidate for a future iteration of the model, since the model can already calculate the receptor activation of the dopamine receptors concurrently to C_{DA}.

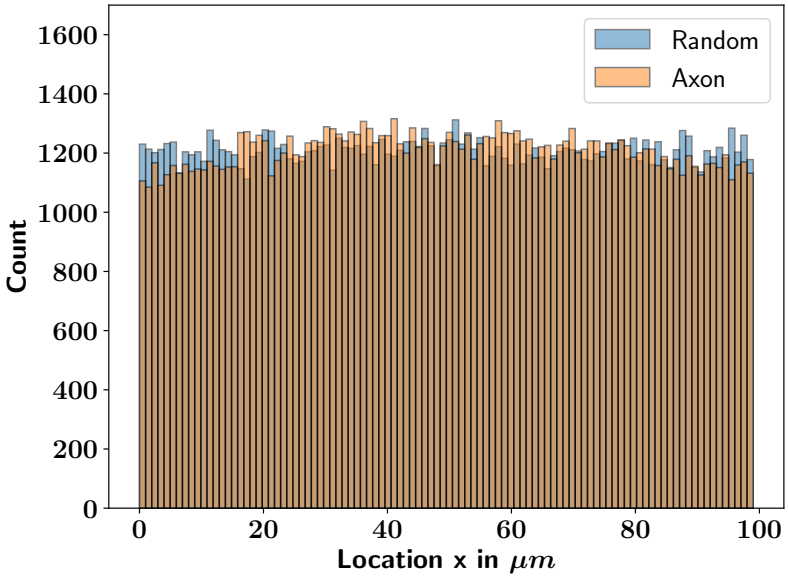

Figure 4.18: Due to the erratic distribution of axon branches in the simulation cube the synapse distribution on the dopaminergic axons are nearly uniformly distributed in space. Histogram of the x-coordinates of all the synapses in a $100\mu m$ simulation cube. For comparison the same histogram for a uniformly random distribution of the x-coordinate is shown. Because of the erratic distribution of the axons in the simulation cube the synapses are nearly uniformly distributed. This also applies for the y and z-axis (data not shown).

4.5 Receptor Distribution

The full model, with the receptor components (see **Sec. 2.4.3** and **Sec. 5**) requires the distribution of DA receptors within the cubic simulation domain. Both types of DA receptors, D1 and D2, are modelled as uniformly distributed in the simulation domain i.e. the concentration of receptors is the same in all locations.

This distribution has been chosen since we do not model single MSNs in our domain and therefore cannot identify receptors with their corresponding MSN. However, the MSNs are homogenously distributed in the striatum, at least at the scale of our model. Furthermore we assume that each MSN of the same type (D1 or D2) has roughly the same amount of receptors on its extracellular membrane. The Combination of the homogenous MSN distribution and the equal amount of receptors on each MSN then leads to the modeled receptor distribution that is independent of location.

Chapter 5

Receptor Kinetics

As mentioned in **Chapter 2.4** the DA diffusion interacts with the DA receptors. Which can be treated as source and sinks terms in the diffusion model. However when researching the appropriate parameters for the kinetics of binding and unbinding, which are required for the system of equations, I found some measurements that indicated that these receptors are binding and unbinding only very slowly. What that means for DA signaling is going to be discussed in this chapter. This chapter is, except for a few changes, a reproduction of the preprint uploaded on biorxiv `https://doi.org/10.1101/444984`. For this reason this chapter comes with its own results and methods section.

The receptor kinetics interact with the diffusion model is through the interaction terms. However the conclusions that can be reached from the starting point of slow receptor kinetics are interesting in their own right. So this chapter will present this reasoning.

In this chapter all values encased in [ ] denote concentrations of the enclosed compound.

5.1 Why are Receptor Kinetics Important?

DA acts on two different main receptor types, D1 and D2. Based on different DA affinities of D1 and D2 receptors (D1R and D2R), it is often assumed that striatal medium spiny neurons (MSN) respond differently to tonic and phasic DA changes, depending on which DA receptor they express predominantly (Dreyer et al., 2010; Surmeier et al., 2007; Grace et al., 2007; Schultz, 2007; Frank and O'Reilly, 2006). According to this "affinity-based" model the low affinity D1Rs (i.e. high dissociation constant $K_D^{D1} = 1.6\mu M$; Richfield et al., 1989) cannot detect tonic changes in [DA] because the fraction of occupied D1Rs is small ($\approx 1\%$) at baseline [DA] ($20nM$), see Methods) and does not change much during tonic, low amplitude [DA] changes. However, D1Rs seem well suited to detect phasic, high amplitude [DA] increases because they saturate at very high [DA]. By contrast, D2Rs have a high affinity (i.e. low dissociation constant $K_D^{D1} = 25nM$; Richfield et al., 1989) leading to $\approx 40\%$ of D2Rs being occupied at baseline [DA] ($20nM$). Due to their high affinity, D2Rs can detect low amplitude, tonic increases/decreases in [DA]. However, as D2Rs saturate at a relatively low $[DA] > 2 \cdot K_D^{D2}$, they seem unable to detect high amplitude,

phasic increases in [DA]. This suggests that D1 and D2 type MSNs differentially encode phasic and tonic changes in [DA] solely because of the different affinities of D1Rs and D2Rs (Schultz, 2007). However, this view is incompatible with recent findings that D2R expressing MSNs can detect phasic changes in [DA] (Yapo et al., 2017; Marcott et al., 2014).

The affinity-based model assumes that the reaction equilibrium is reached instantaneously, whereby the receptor binding affinity can be used to approximate the fraction of receptors bound to DA. However, this assumption holds only if the receptor kinetics are fast with respect to the timescale of the DA signal, which is typically not the case. For instance, D1Rs and D2Rs unbind from DA with a half-life time of $t_{1/2} \approx 80s$ (Burt et al., 1976; Sano et al., 1979; Maeno, 1982; Nishikori et al., 1980), much longer than phasic signals of a few seconds (Robinson et al., 2001; Schultz, 2007; Hamid et al., 2016). Moreover, the fraction of bound receptors might be a misleading measure for the effect of DA signals, since the abundances of D1R and D2R are quite different (see below). Therefore, we developed a model of receptor binding based on the kinetics and abundances of D1Rs and D2Rs to re-evaluate current views on DA signalling in the striatum.

5.2 Receptor Kinetics: Methods and Materials

The receptor kinetics model was implemented in Python. The scripts used to generate the data and figures can be accessed here: `https://bitbucket.org/Narur/abundance_kinetics/src/`.

5.2.1 Kinetics Model

In the instant kinetics model the fraction of occupied D1 and D2 receptors (f_{D1} and f_{D2}) are calculated directly from the concentration of free DA in the extracellular space, $[DA]$, and the dissociation constant K_D:

$$f = \frac{[DA]}{K_D + [DA]}. \tag{5.1}$$

However, the dissociation constant is an equilibrium constant, so it should only be used for calculating the receptor occupancy when the duration of the DA signal is longer than the time needed to reach the equilibrium. As this is typically not the case for phasic DA signals (see main text), we developed a model incorporating slow kinetics.

When DA and one of its receptors are both present in a solution they constantly bind and unbind. During the binding a receptor ligand complex (here called DA−D1 or DA−D2) is formed. We call the receptor ligand complex an occupied DA receptor. Note that although in the following part we provide the equations for D1 receptors, the same equations apply for D2 receptors (with different kinetic parameters). In a solution binding occurs when receptor and ligand meet due to diffusion, with high enough energy and a suitable orientation, described as:

$$\mathrm{DA} + \mathrm{D1} \xrightarrow{\mathrm{k_{on}}} \mathrm{DA{-}D1}. \tag{5.2}$$

Accordingly, unbinding of the complex is denoted as:

$$\mathrm{DA{-}D1} \xrightarrow{\mathrm{k_{off}}} \mathrm{DA} + \mathrm{D1}. \tag{5.3}$$

The kinetics of this binding and unbinding, treated here as first-order reactions, are governed by the rate constants k_{on} and k_{off} that are specific for a receptor ligand pair and temperature dependent. Since both processes are happening simultaneously we can write this as:

$$\mathrm{DA} + \mathrm{D1} \underset{\mathrm{k_{off}}}{\overset{\mathrm{k_{on}}}{\rightleftharpoons}} \mathrm{DA{-}D1}. \tag{5.4}$$

The rate at which the receptor is occupied depends on [DA], the concentration of free receptor [D1] and the binding rate constant k_{on}:

$$\frac{d[\mathrm{DA} - \mathrm{D1}]^{+}}{dt} = k_{\mathrm{on}} \cdot [\mathrm{DA}] \cdot [\mathrm{D1}]. \tag{5.5}$$

The rate at which the receptor-ligand complex unbinds is given by concentration of the complex [DA − D1] and the unbinding rate constant k_{off}:

$$\frac{d[\mathrm{DA} - \mathrm{D1}]^{-}}{dt} = -k_{\mathrm{off}} \cdot [\mathrm{DA} - \mathrm{D1}]. \tag{5.6}$$

The equilibrium is reached when the binding and unbinding rates are equal, so by combining Eq. 5.5 and Eq. 5.6 we obtain:

$$k_{\mathrm{on}} \cdot [\mathrm{DA}] \cdot [\mathrm{D1}] = k_{\mathrm{off}} \cdot [\mathrm{DA} - \mathrm{D1}]. \tag{5.7}$$

At the equilibrium the dissociation constant K_D is defined as:

$$K_D = \frac{[DA] \cdot [D1]}{[DA - D1]} = \frac{k_{off}}{k_{on}}. \tag{5.8}$$

When half of the receptors are occupied, i.e. $[DA{-}D1] = [D1]$, Eq. 5.8 simplifies to $K_D = [DA]$. So at equilibrium, K_D is the ligand concentration at which half of the receptors are occupied.

Importantly, for fast changes in [DA] (i.e. over seconds) it takes some time until the changed binding (Eq. 5.5) and unbinding rates (Eq. 5.6) are balanced, so the new equilibrium will not be reached instantly. The timescale in which equilibrium is reached can be estimated from the half-life time of the bound receptor. The half-life time assumes an exponential decay process as described in Eq. 5.6 and is the time required so that half of the currently bound receptors unbind. If $[DA] = 0$, and there is no more binding, the half life time of the receptors can be calculated from the off-rate by using $t_{1/2} = ln(2)/k_{off}$. Signal durations should be of the same order of magnitude (or longer) than the half-life time in order for the instant kinetics model to be applicable.

We calculated the time course of occupied receptor after an abrupt change in [DA] by integrating the rate equation, given by the sum of Eq. 5.5 and Eq. 5.6:

$$\frac{d[DA - D1]}{dt} = k_{on}[DA][D1] - k_{off}[DA - D1]. \tag{5.9}$$

To integrate Eq. 5.9 we substitute

$$[D1] = [D1^{tot}] - [DA - D1] \tag{5.10}$$

where $[D1^{tot}]$ is the total amount of D1 receptor (bound and unbound to DA) on the cell membranes available for binding to extracellular DA.

To model the effect of phasic changes in [DA] we choose the initial receptor occupancy $[DA - D1](t = 0) = [DA - D1]^0$ and the receptor occupancy for the new equilibrium at time infinity $[DA - D1](t = \infty) = [DA - D1]^\infty$ as the boundary conditions. With these boundary conditions we get an expression for the time evolution of the receptor occupancy under the assumption that binding to the receptor does not significantly change the free [DA]:

$$\begin{aligned}[DA - D1](t) = \\ &([DA - D1]^0 - [DA - D1]^\infty) \cdot e^{-(k_{on}[DA]+k_{off})t} \\ &+ [DA - D1]^\infty.\end{aligned} \tag{5.11}$$

For our slow kinetics model we solved Eq. 5.9 for each receptor type and arbitrary DA timecourses numerically employing a 4th order Runge Kutta solver with a 1 ms time resolution.

We did not take into account the change in [DA] caused by the binding and unbinding to the receptors since the rates at which DA is removed from the system by binding to the receptors is much slower than the rate of DA being removed from the system by uptake through DA transporters. For example the rate at which DA binds to the receptors is:

$$\begin{aligned}\frac{([DA - D1] + [DA - D2])}{dt} = \\ k_{on}^{D1}[DA][D1]+k_{on}^{D2}[DA][D2] \\ = -\frac{[DA]}{dt}.\end{aligned} \tag{5.12}$$

At a DA concentration of $[DA] = 1\mu M$ with a D1 and D2 occupancy of $[DA - D1] \approx 20.0nM$ and $[DA - D2] \approx 40nM$ (the equilibrium values for $[DA] = 20nM$) and $k_{on}^{D1} = 5.2 \cdot 10^{-6} nM^{-1}s^{-1}$, $k_{on}^{D2} = 3.3 \cdot 10^{-4} nM^{-1}s^{-1}$, $[D1] \approx 1600.0nM$, $[D2] \approx 40.0nM$ and $[DA] = 1\mu M$ the rate of DA removal through binding to the receptors is:

$$\frac{[DA]}{dt}^{binding} = -23.6nM/s. \tag{5.13}$$

However, the DA removal rate by Michaelis-Menten uptake through the DA transporters at this concentration would be:

$$\frac{[DA]}{dt}^{uptake} = V_{max}\frac{[DA]}{[DA] + K_m} \tag{5.14}$$

$$= -4.0\frac{\mu M}{s} \cdot \frac{1\mu M}{1\mu M + 0.21\mu M} \tag{5.15}$$

$$= -3.3\frac{\mu M}{s}. \tag{5.16}$$

Where V_{max} is the maximal uptake rate, and K_m the Michaelis-Menten constant describing the $[DA]$ concentration at which uptake is at half the maximum rate. As $\left|\frac{[DA]}{dt}^{uptake}\right| >> \left|\frac{[DA]}{dt}^{binding}\right|$, the DA dynamics are dominated by the uptake process and not by binding to the receptors. Therefore, we neglected the receptor-ligand binding for the DA dynamics in our model. However, for faster DA receptors this effect would become more important.

5.2.2 Receptor Parameters

An important model parameter is the total concentration of the D1 and D2 receptors on the membrane ($[D1]^{tot}$ and $[D2]^{tot}$) that can bind to DA in the extracellular space of the striatum. Our estimate of $[D1]^{tot}$ and $[D2]^{tot}$ is based on radioligand binding studies in the rostral striatum (Richfield et al., 1989, 1987). We use the following equation, in which X is a placeholder for the respective receptor type, to calculate these concentrations.

$$[DX]^{tot} = [DX]^{m} \cdot \frac{\epsilon \cdot f_{DX}^{membrane}}{\alpha \rho_{brain}} \tag{5.17}$$

The experimental measurements provide us with a the number of receptors per unit of protein weight $[D1]^m$ and $[D2]^m$. To transform these measurements into molar concentrations for our simulations, we multiply by the protein content of the wet weight of the rat caudate nucleus ϵ, which is around 12% (Banay-Schwartz et al., 1992). This leaves us with the amount of protein per g of wet weight of the rat brain. Next we divide by the average density of a rat brain which is $\rho_{brain} = 1.05 g/ml$ (DiResta et al., 1990) to find the amount of receptors per unit of volume of the rat striatum. Finally, we divide by the volume fraction α, the fraction of the brain volume that is taken up by the extracellular space in the rat brain, to obtain the receptor concentration of the receptor in the extracellular medium. The procedure ends here for the D1 receptors since there is no evidence that D1 receptors are internalized in the baseline state (Prou et al., 2001). However, a large fraction of the D2 receptors is retained in the endoplasmatic reticulum of the neuron (Prou et al., 2001), reducing the amount of receptors that contribute to the concentration of receptors in the extracellular medium by $f^{membrane}$, the fraction of receptors protruding into the extracellular medium.

In addition to the receptor concentration, the kinetic constants of the receptors are key parameters in our slow kinetics model. In an equilibrium measurement in the canine caudate nucleus the dissociation constant of low affinity DA binding sites, corresponding to D1 receptors (Maeno, 1982), has been measured as $K_d = 1.6 \mu M$ (Sano et al., 1979). However, when calculating K_d (using Eq. 5.8) from the measured kinetic constants (Sano et al., 1979) the value is $K_d^{D1} = 2.6 \mu M$. To be more easily comparable to other simulation works (Dreyer et al., 2010) and direct measurements (Richfield et al., 1989; Sano et al., 1979) we choose $K_d^{D1} = 1.6 \mu M$ in our simulations. For this purpose we modified both the $k_{on}^{D1} = 0.00025 min^{-1} nM^{-1}$ and $k_{off}^{D1} = 0.64 min^{-1}$ rate measured (Sano et al., 1979) by $\approx 25\%$, making $k_{on}^{D1} = 0.0003125 min^{-1} nM^{-1}$ slightly faster and $k_{off}^{D1} = 0.5 min^{-1}$ slightly slower, so that the resulting $K_d^{D1} = 1.6 \mu M$. The kinetic constants have been measured at 30 C and are temperature dependent. In biological reactions a temperature change of 10 C is usually associated with

a change in reaction rate around a factor of 2-3 (Reyes et al., 2008). However, the conclusions of this paper do not change for an increase in reaction rates by a factor of $2-3$ (see **Fig. 5.2**). It should also be noted that the measurement of the commonly referenced K_d (Richfield et al., 1989) have been performed at room temperature.

The kinetic constants for the D2 receptors were obtained from measurements at 37^oC of high affinity DA binding sites (Burt et al., 1976), which correspond to the D2 receptor (Maeno, 1982). The values are $k_{on}^{D2} = 0.02 min^{-1} nM^{-1}$ and $k_{off}^{D2} = 0.5 min^{-1}$, which yields $K_D^{D2} = 25nM$, in line with the values measured in (Richfield et al., 1989). As the off-rate of the D1 and D2 receptors $k_{off}^{D1} = 0.64 min^{-1} nM^{-1}$ and $k_{off}^{D2} = 0.5 min^{-1}$ is quite similar, the difference in $K_D^{D2} = 25nM$ and $K_d^{D1} = 1.5\mu M$ is largely due to differences in the on-rate of the receptors. This is important because the absolute rate of receptor occupancy depends linearly not only on the on-rate, but also on the receptor concentration (see Eq. 5.5), which means that a slower on-rate could be compensated for by a higher number of receptors.

Measured values		
Parameter		Source
$[D1]^m$ in pmol/mg protein	2840	(Richfield et al., 1989)
$[D2]^m$ in pmol/mg protein	696	(Richfield et al., 1989)
ϵ	0.12	(Banay-Schwartz et al., 1992)
α	0.2	(Syková and Nicholson, 2008)
ρ_{brain} in g/ml	1.05	(DiResta et al., 1990)
$f_{D1}^{membrane}$	1.0	(Prou et al., 2001)
$f_{D2}^{membrane}$	0.2	(Prou et al., 2001)
$k_{on}^{D1,orig}$ in $nm^{-1}min^{-1}$	0.00025	(Sano et al., 1979)
$k_{off}^{D1,orig}$ in min^{-1}	0.64	(Sano et al., 1979)
k_{on}^{D2} in $nm^{-1}min^{-1}$	0.02	(Burt et al., 1976)
k_{off}^{D2} in min^{-1}	0.5	(Burt et al., 1976)
Derived Parameters		
Parameter		Source
$[D1]$ in nM	≈ 1600	Eq.(5.17)
$[D2]$ in nM	≈ 80	Eq.(5.17)
$k_{on}^{D1,used}$ in $nm^{-1}min^{-1}$	0.0003125	see Text
$k_{off}^{D1,used}$ in min^{-1}	0.5	see Text

Table 5.1: Receptor parameters

The parameters that we used in the simulations are summarized in Tab. 5.1.

5.2.3 Dopamine Signals

In this model we assumed a baseline [DA] of $[DA]^{tonic} = 20\ nM$ (Dreyer et al., 2010; Dreyer, 2014; Venton et al., 2003; Suaud-Chagny et al., 1992; Borland et al., 2005; Justice Jr, 1993; Atcherley et al., 2015). We modelled changes in [DA] to mimic DA signals observed in experimental studies. We use three types of single pulse DA signals: (long-)burst, burst-pause and ramp.

The burst signal mimics the result of a phasic burst in the activity of DA neurons in the SNc, e.g. in response to reward-predicting cues (Pan et al., 2005). The model burst signal consists of a rapid linear [DA] increase (with an amplitude $\Delta[DA]$ and rise time t_{rise}) and a subsequent return to baseline. The return to baseline is governed by Michaelis Menten kinetics with appropriate parameters for the dorsal striatum $V_{max} = 4.0\ \mu M s^{-1}$ and $K_m = 0.21\ \mu M$ (Bergstrom and Garris, 2003) and the nucleus accumbens $V_{max} = 1.5\ \mu M s^{-1}$ (Dreyer and Hounsgaard, 2013). In our model the removal of DA is assumed to happen without further DA influx into the system (baseline firing resumes when [DA] has returned to its baseline value). Unless stated otherwise, the long-burst signals are used with a $\Delta[DA] = 200\ nM$ and a rise time of $t_{rise} = 0.2\ s$ at $V_{max} = 1.5\ \mu M s^{-1}$, similar to biologically realistic transient signals (Cheer et al., 2007; Robinson et al., 2001; Day et al., 2007).

The burst-pause signal has two components, an initial short, small amplitude burst ($\Delta[DA] = 100\ nM$, $t_{rise} = 0.1\ s$), with the corresponding [DA] return to baseline (as for the long burst above). However, there is a second component in the DA signal, in which [DA] falls below baseline, simulating a pause in DA neuron firing. The length of this firing pause is characterized by the parameter t_{pause}. This burst-pause [DA] signal reflects the DA cell firing pattern consisting of a brief burst followed by a pause in activity (Pan et al., 2008; Schultz, 2016).

The ramp DA signal is characterized by the same parameters as the burst pattern, but with a longer t_{rise}, and a smaller $\Delta[DA]$.

5.2.4 Behavioural Task Simulation

To determine whether DA receptor occupancy can integrate reward signals over minutes, we simulated sequences consisting of 50 trials. Each sequence had a fixed reward probability. The trials contained either a long burst DA signal (mimicking a reward) or a burst-pause DA signal (mimicking no reward) at the beginning of the trial according to the reward probability of the sequence. The inter trial interval was $15 \pm 5s$ (**Fig. 5.7** and **Fig. 5.6**). We choose this highly simplistic scenario to reflect DA signals in a behavioural task in which the animal is rewarded for correct performance. However, here the specifics of the task are not relevant as our model addresses the integration of the DA receptor occupancy over time. Although we chose to use the burst-pause type signal as shown in **Fig. 5.1e** as a non-rewarding event, the difference to a non-signal are minimal after the end of the pause (**Figs. 5.3 and 5.4**). Each sequence started from a baseline receptor occupancy, assuming a break between sequences long enough for the receptors to return to baseline occupancy (around 5 minutes). For the simulations shown in **Fig. 5.4** all trials started exactly 15 s apart.

We simulated all reward probabilities from 0% to 100% in 10% steps. For each reward probability we ran 500 sequences, and calculated the mean receptor occupancy over time (single realisations shown in **Fig. 5.7a, b**). To investigate whether the receptor occupancy distinguished between different reward probabilities we applied a simple classifier to the receptor occupancy timeline.

The classifier was used to compare two different reward probabilities at a time. At each time point it was applied to a pair of receptor occupancies, e.g. one belonging to a 50% and one to a 30% reward probability sequence. The classifier assigned the current receptor occupancy to the higher or lower reward probability depending on which one was closer to the mean (over 500

sequences) receptor occupancy of that reward probability. As we knew the underlying reward probability of each sequence we were able to calculate the true and false positive rates and accuracy for each time point in our set of 500 sequences for both the D1R and D2R (**Fig. 5.6**). The accuracy was calculated based on all time points between 200 and 800s within a sequence to avoid the effect of the initial "swing-in" and post-sequence DA levels returning to baseline.

5.3 Receptor Kinetics: Results and Discussion

To provide a realistic description of receptor kinetics, the binding and unbinding rates that determine the receptor affinity are required. The available experimental measurements indicate that the different D1R and D2R affinities are largely due to different binding rates, while their unbinding rates are similar (Burt et al., 1976; Sano et al., 1979; Maeno, 1982; Richfield et al., 1989). We incorporated these measurements into our slow kinetics model (see **Chapter 5.2**) and investigated the model in a variety of scenarios mimicking DA signals on different timescales.

Firstly, to examine our model at baseline [DA], we investigated receptor binding for a range of affinities (**Fig. 5.1a**), reflecting the range of measured values in different experimental studies (Neve and Neve, 1997). We report the resulting receptor occupancy in terms of the concentration of D1Rs and D2Rs bound to DA (denoted as $[D1-DA]$ and $[D2-DA]$, respectively). Due to the low affinity of D1Rs, slow changes in [DA] only lead to small changes in the fraction of bound D1 receptors. However, there are overall more D1Rs than D2Rs (Richfield et al., 1989), and $\approx 80\%$ of D2Rs are retained in the endoplasmatic reticulum (Prou et al., 2001). Therefore, the concentration of D1Rs in the membrane available to extracellular DA is a lot higher than the concentration of D2Rs (e.g. 20 times more in the nucleus accumbens; Nishikori et al., 1980; Methods). Thus, in our simulation, the actual concentration of bound D1Rs ($[D1-DA] \approx 20nM$) was, at DA baseline, much closer to the concentration of bound D2Rs ($[D2-DA] \approx 35nM$) than suggested by the different D1 and D2 affinities alone. We further confirmed that this was not due to a specific choice of the dissociation constants in the model, as $[D1-DA]$ and $[D2-DA]$ remained similar over the range of experimentally measured D1R and D2R affinities (Neve and Neve, 1997) (**Fig. 5.1a**). This suggests that $[D1-DA]$ is at most twice as high as $[D2-DA]$ instead of 40 times higher as suggested by the difference in fraction of bound receptors. Therefore, $[D1-DA]$ and $[D2-DA]$ might be better indicators for the signal transmitted to MSNs as the fraction of bound receptors neglects the different receptor type abundances.

Next, we investigated the effect of slow [DA] changes (Grace, 1995; Schultz, 1998; Floresco et al., 2003) by exposing our model to changes in the [DA] baseline. For signalling timescales that are long with respect to the half-life time of the receptors ($t_{slow} >> t_{1/2} \approx 80s$), we used the dissociation constant to calculate the steady state receptor occupancy. We found that for slow changes to a range of [DA] baselines, $[D1-DA]$ and $[D2-DA]$ were also similar (**Fig. 5.1b**). Thus, we conclude that D1R and D2R occupancy reacts similarly to slow, low amplitude [DA] changes because of the different abundances of D1 and D2 receptors. This is contrary to instant kinetics models which suggest that D2Rs are better suited to encode slow or tonic changes in [DA].

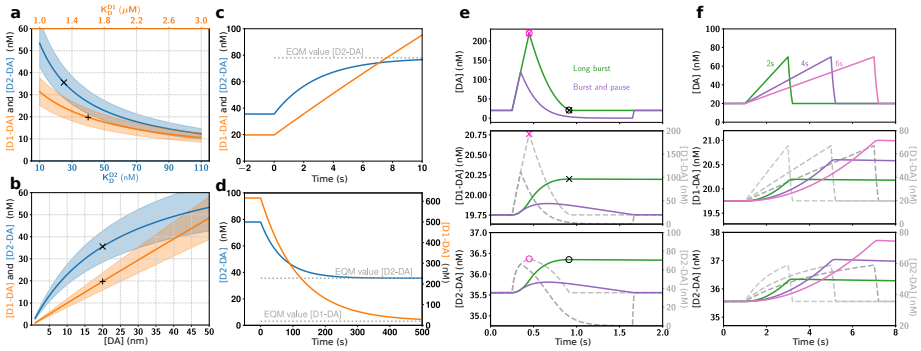

Figure 5.1: Impact of slow kinetics on D1R and D2R binding. **(a, b)** Equilibrium values of absolute concentration of receptors bound to DA vary as a function of receptor affinities (a) and baseline [DA] (b), but are overall similar for D1 and D2 receptors. In (a) baseline [DA] was fixed at 20 nM, and in (b) $K_D^{D1} = 1.6\mu M$ and $K_D^{D2} = 25nM$. '×' and +' indicate the model default parameters. Coloured bands mark the range of values for up to ±20% different receptor abundances. **(c)** For a large step up from $[DA] = 20nM$ to $[DA] = 1\mu M$, and **(d)** a step down from $[DA] = 1\mu M$ to $[DA] = 20nM$, D1 and D2 receptor occupancy approached their new equilibrium (EQM, grey dotted lines) only slowly (i.e. over seconds to minutes). **(e, f)** Effect of different phasic DA signals (top panels) is very different in the slow kinetics model (coloured traces in middle and bottom panels; left scales) compared to the instant kinetics model (dashed grey traces, right scales). The timing of the maximum receptor occupancy ('×' and 'o' for D1 and D2, respectively) coincides for instant kinetics (purple symbols) with the [DA] peak (combined x and o in top panel), while for slow kinetics (black symbols) it coincides with the offset of the [DA] signal instead (combined x and o in top panel).

To study the impact of faster [DA] signals, we measured the step response of the model to a [DA] change from 20nM to $1\mu M$. This is quite a large change compared to phasic DA signals in vivo (Robinson et al., 2001; Cheer et al., 2007; Hamid et al., 2016), which we choose to illustrate that our results are not just due to a small amplitude DA signal. We found that binding to both receptor subtypes increased very slowly. Even for the high affinity D2Rs it took more than $5s$ to reach their new equilibrium (**Fig. 5.1c**). Thus, unlike the instant kinetics model, our model suggests that the D2Rs will not saturate for single reward events, which last overall for up to $\approx 3s$. Note that the non-saturation is independent of the abundance of the receptors and is only determined by the kinetics of the receptors (see **Chapter 5.2**). Due to their slow unbinding, D1Rs and D2Rs also took a long time to return to baseline receptor occupancy after a step down from $[DA] = 1\mu M$ to $[DA] = 20nM$ (**Fig. 5.1d**). Thus, we conclude that with slow kinetics of receptor binding both D1Rs and D2Rs can detect single phasic DA signals and that both remain occupied long after the [DA] has returned to baseline.

Next, we investigated $[D1 - DA]$ and $[D2 - DA]$ for a phasic DA increase (mimicking reward responses; Robinson et al., 2001; Cheer et al., 2007), a phasic DA increase followed by a decrease (mimicking responses to non-reward, salient stimuli; Schultz, 2016), and a prolonged DA ramp (mimicking goal approach; Howe et al., 2013; Hamid et al., 2016). In the instant kinetics model the D1Rs mirrored the [DA] time course, since even at $[DA] = 200nM$ they are far from saturation, whereas the D2Rs showed saturation effects as soon as $[DA] > 2 \cdot K_D^{D2}$, leading to differing D1 and D2 time courses (**Fig. 5.1e, f**). Importantly, in our model with slow kinetics, the time courses of $[D1 - DA]$ and $[D2 - DA]$ were similar for each of the three types of phasic DA signals.

While in our model we assumed slow kinetics based on neurochemical estimates of wildtype DA receptors (Burt et al., 1976; Sano et al., 1979; Maeno, 1982), recent genetically-modified DA receptors, used to probe [DA] changes, have apparent fast kinetics (Sun et al., 2018; Patriarchi et al., 2018). Although their kinetics strongly changed between receptor variants and may not reflect the kinetics of the wildtype receptor, we examined our model also in the context of faster DA kinetics and found that the similarity between $[D1 - DA]$ and $[D2 - DA]$ can be observed even if the actual kinetics were a 100 times faster than assumed in our model (**Fig. 5.2**). Therefore, our results do not depend on the exact kinetics parameters or potential temperature effects, as long as the parameter changes are roughly similar for D1 and D2 receptors. We chose the fastest tested kinetics to be 100 times faster than the measured value, since then the binding rate is in the range of the diffusion limited maximum reaction rate in the Alberty-Hammes-Eigen model (Alberty and Hammes, 1958; Eigen and Hammes, 1963). That means that the diffusion of the DA to the receptor becomes the limiting rate step. So even if the receptor kinetics are faster, the binding could not happen with a higher rate. There are estimates for the diffusion limit an order of magnitude faster (Kuo-Chen and Shou-ping, 1974), however these calculations assume that the enzyme (in our case the receptor) can guide the ligand along its surface to its active zone. This is unlikely to be an applicable description for the D1 and D2 receptors since they are embedded in the cell membrane. The Alberty-Hammes-Eigen model, which assumes that the receptor can only be approached from a half-sphere in space, therefore seems like a better estimator for the diffusion limited reaction rate. Taking into

account different affinity states for D1Rs and D2Rs (Richfield et al., 1989) also preserved the similarity of time courses of D1R and D2R occupancy (**Fig. 5.8**). Finally, pauses in the DA firing following aversive stimuli (Schultz, 2007) that lead to reductions in [DA] (Roitman et al., 2008), also have a similar effect on D1R and D2R occupancy (**Fig. 5.9e**).

Another striking effect of incorporating receptor kinetics was that a phasic increase in [DA] kept the receptors occupied for a long time (**Fig. 5.1e**). However, when a phasic increase was followed by a decrease, $[D1-DA]$ and $[D2-DA]$ quickly returned to baseline. This indicates that burst-pause firing patterns observed in DA cells for aversive or salient non-rewarding signals (Schultz, 2016) can be distinguished from pure burst firing patterns (which only lead to a phasic increase in [DA]) on the level of the MSN DA receptor occupancy. This supports the view that the fast component of the DA firing patterns (Schultz, 2016) is a salience response, and points to the intriguing possibility that the pause following the burst can, at least partly, revoke the receptor-ligand binding induced by the burst (see also **Fig.5.3**). This effect even persists in a sequence of burst and burst-pause events (**Fig. 5.4**). Thereby, the burst-pause firing pattern of DA neurons could effectively signal a reward false-alarm.

The similarity of $[D1-DA]$ and $[D2-DA]$ responses to both slow and fast [DA] changes indicates that the different DA receptors respond similarly independent of the timescale of [DA] changes. To understand why the D1Rs and D2Rs respond similarly, we considered the relevant model parameters in more detail. The binding rate constants of D1Rs and D2Rs differ by a factor of ≈ 60 ($k_{on}^{D1} = 0.0003125nm^{-1}min^{-1}$ and $k_{on}^{D2} = 0.02nm^{-1}min^{-1}$; Burt et al., 1976; Sano et al., 1979; Maeno, 1982; **Chapter 5.2**), suggesting faster D2Rs. However, experimental data suggests that there are ≈ 40 fold more unoccupied D1 receptors ($\approx 1600nM$) than unoccupied D2 receptors ($\approx 40nM$) on MSN membranes in the extracellular space of the rat striatum (Nishikori et al., 1980). Therefore, the absolute binding rate $\frac{d[DX-DA]}{dt}^{+} = k_{on} \cdot [DA] \cdot [DX]$ differs only by a factor of ≈ 1.5 between the D1Rs and D2Rs. That is, the difference in the kinetics of D1Rs and D2Rs is compensated by the different receptor numbers, resulting in nearly indistinguishable aggregate kinetics (**Fig. 5.1e, f**). This is consistent with recent experimental findings that D2R expressing MSNs can detect phasic [DA] signals (Yapo et al., 2017; Marcott et al., 2014).

Incorporating the slow kinetics in the model is crucial for functional considerations of the DA system. Currently, following the instant kinetics model, the amplitude of a DA signal (i.e. peak [DA]) is often considered as a key signal e.g. in the context of reward magnitude or probability (Hamid et al., 2016; Tobler et al., 2005; Morris et al., 2004). However, as DA unbinds slowly (over tens of seconds; **Fig. 5.1d**) and the binding rate changes approximately linearly with [DA], the amount of receptor occupancy primarily depended on the area under the curve of the [DA] signal (**Fig. 5.5**). Therefore, DA ramps, even with a relatively small amplitude (**Fig. 5.1f** and **Fig. 5.9**), were very effective in increasing DA receptor binding. In contrast, for locally very high [DA] (e.g. at corticostriatal synapses during phasic DA cell activity; Grace et al., 2007) the high concentration gradient would only lead to a very short duration of this local DA peak and thereby make it less effective in occupying DA receptors.

The dynamics introduced by the slow kinetics had further effects on the timecourse of DA signalling. With instant kinetics the maximum receptor oc-

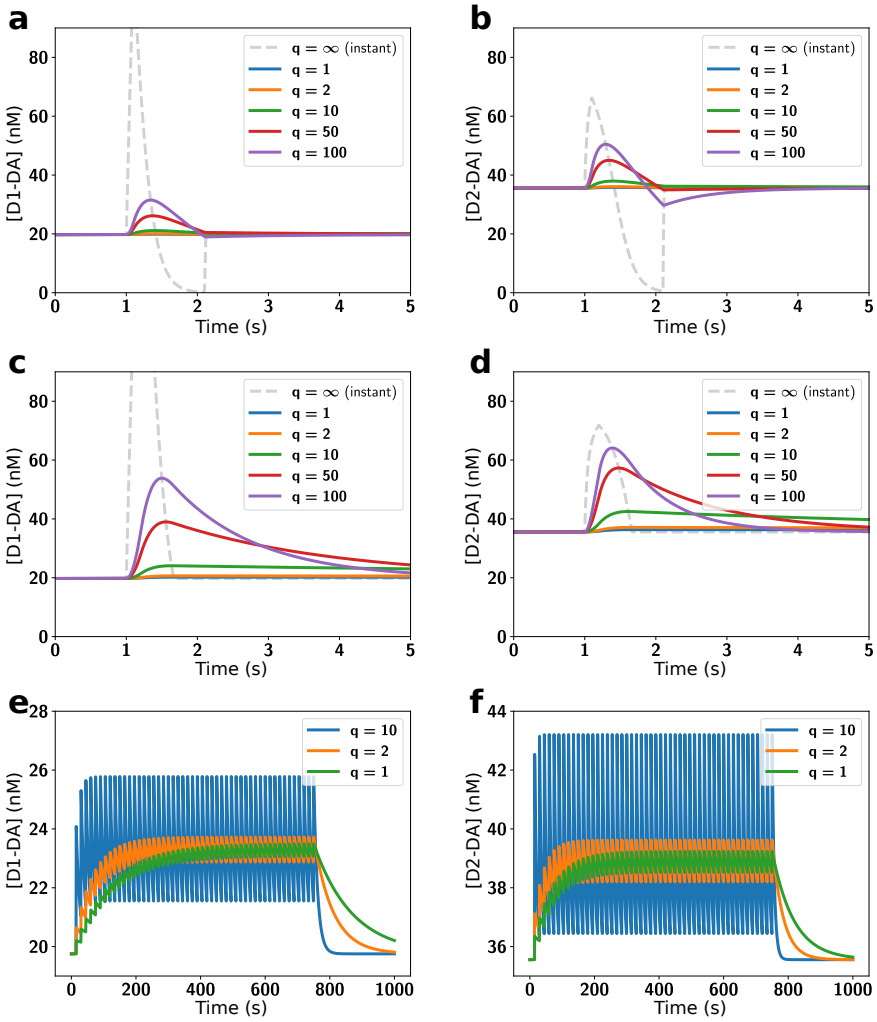

Figure 5.2: Similarities between D1 and D2 responses persist even if kinetics are much faster than our estimate. Fast kinetics were implemented by multiplying k_{on} and k_{off} by q as indicated, keeping K_D constant. Absolute D1R occupancy ([D1-DA]; left column) and D2R occupancy ([D2-DA]; right column) were examined for burst-pause DA signals **(a, b)**, burst-only DA signals **(c, d)**, and the behavioural sequence **(e, f)** (i.e. same simulation scenarios as in Fig. 5.1e and Fig. 5.4). D1Rs and D2Rs reacted very similarly to each other in all [DA] signal scenarios even if their kinetics were up to 100x faster because the difference between the aggregate D1 and D2 binding rates (Eq. 5.5) only differs by a factor of 1.5. Furthermore, the D2Rs do not show visible saturation effects even for $q = 100$. Faster kinetics mostly affected the amplitude of the receptor response and the time it takes to return to baseline receptor occupancy. However, only for $q = 100$ the pauses dropped slightly below baseline receptor occupancy (a, b). On a longer time scale with repetitive DA bursts (e, f) D1Rs and D2Rs integrated the DA bursts over time for $q = 1$ and $q = 2$. This is because the half-time of the receptors were 80 s (for $q = 1$), while the DA burst signal was repeated every 15 s. Thereby, [D1-DA] and [D2-DA] were dominated by the repetition of the signal rather than by the impact of individual DA burst signals. In contrast, for $q = 10$ the change in receptor occupancy was dominated by the single pulses, since the half-life time was 8s, whereby the receptors mostly unbind in between DA pulses.

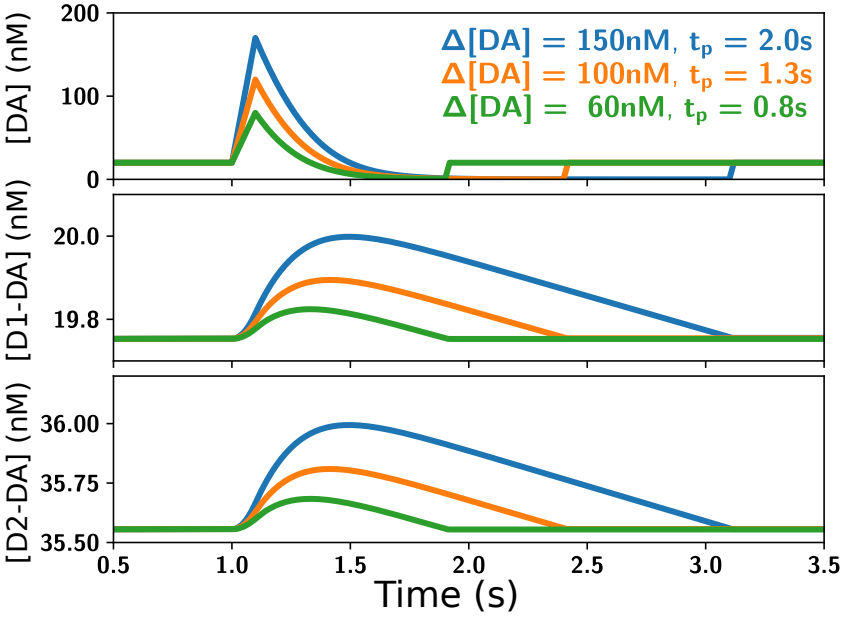

Figure 5.3: Burst-pause DA signals did not lead to increased DA receptor occupancy after the signal, if the duration of the pause was matched to the amplitude of the burst. Panels indicate input DA signal (top) and resulting DA receptor-ligand binding (middle and bottom). The return to baseline after the pulse happened for both D1R and D2R since their aggregate kinetics are similar.

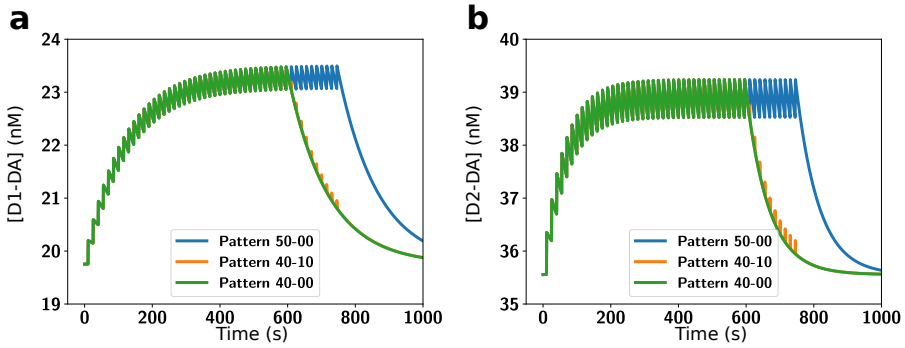

Figure 5.4: Absolute receptor occupancy for D1Rs **(a)** and D2Rs **(b)** following a sequence of 50 events. The sequences consists of 50 rewarding long burst events (blue), 40 long burst and 10 burst-pause events (orange) and 40 long burst events followed by 10 none events (green). A sequence of events lead to an accumulation of occupied receptors, if the pause between long burst events were shorter than $\approx 2 \cdot t_{1/2}$. There was a plateau for the absolute amount of occupied receptor at the level at which the amount of receptors unbinding until the next burst is the same as the amount of receptors getting occupied during a long burst event. Burst-pause events did not lead to an accumulation of occupied receptors over time and were, except during the short bursts, identical to the none events (note the overlapping green and orange curves), in line with a "false alarm" signal over a range of occupancy levels.

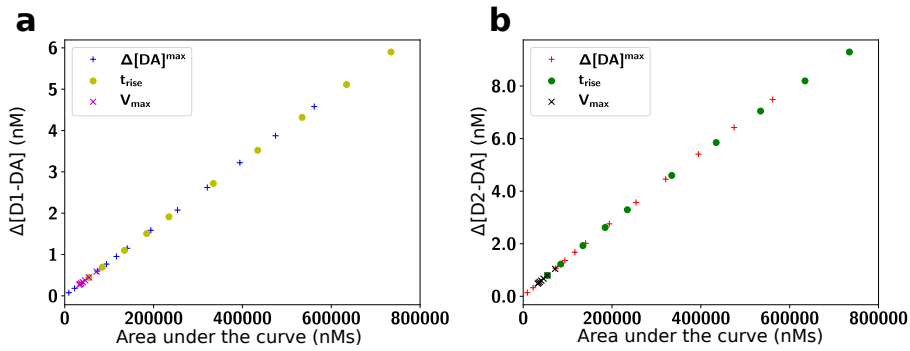

Figure 5.5: In the slow kinetics model the peak change in absolute receptor occupancy of D1Rs **(a)** and D2Rs **(b)** increased linearly with the area under the curve (AUC) of the DA pulses and parameter variations as in **Fig. 5.9a-c** (but with more parameter values). Here $\Delta[DA]^{max}$ marks burst-only DA pulses with varying peak amplitudes (50, 100, 150, 200, 250, 300, 350, 400, 500, 600, 700, 800, 900, 1000 nM), t_{rise} indicates ramping DA signals with with varying rise times (0.2, 0.5, 1.0, 1.5, 2.0, 3.0, 4.0, 5.0, 6.0, 7.0 s) and V_{max} indicates burst-only DA pulses with varying V_{max} (1.0, 1.5, 2.0, 2.5, 3.0, 2.5, 4.0 in $\mu M s^{-1}$). This indicates that D1Rs and D2Rs act as slow integrators of the DA signal and explains why ramps are an effective signal to occupy DA receptors.

cupancy was reached at the peak [DA] (**Fig. 5.1e, f**). By contrast, for slow kinetics the maximum receptor occupancy was reached when [DA] returned to its baseline (**Fig. 5.1e**) because as long as [DA] was higher than the equilibrium value of [D1-DA] and [D2-DA], more receptors continued to become occupied. Therefore for all DA signals, the maximum receptor occupancy was reached towards the end of the pulse (**Fig. 5.1e, f** and **Fig. 5.9**).

Another effect of the slow kinetics was that DA receptors remained occupied long after the DA pulse is over (**Fig. 5.1e, f**). This allowed the integration of DA pulses over minutes (**Fig. 5.7a, b** and **Fig. 5.4**). We investigated potential functional consequences of this integration by exposing the model to a sequence of trials modeling a simple behavioural experiment with stochastic rewards (see **Chapter 5.2**). We found that both D1R and D2R occupancy coded for reward probability (**Fig. 5.7** and **Fig. 5.6**), consistent with functional roles of DA signalling in motivation. However, this does not preclude potential DA roles on shorter time scales, such as the invigoration of movements (Roesch et al., 2009) or fast updates of state value (Hamid et al., 2016), as a sensitive readout mechanism could also detect small increases in [D1-DA] and [D2-DA] (Lamb and Pugh Jr, 1992).

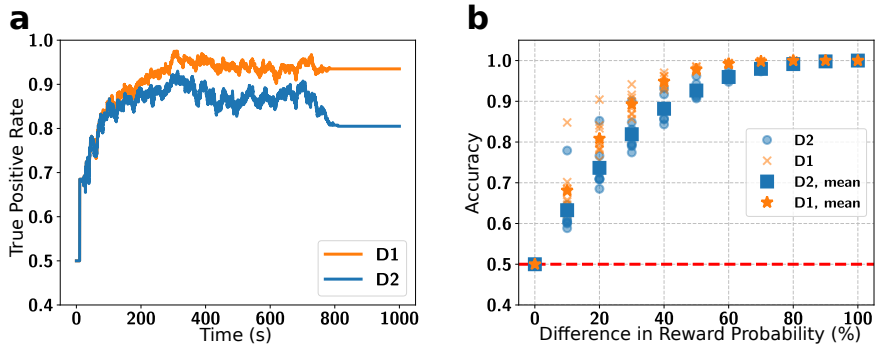

Figure 5.6: **(a)** True positive rates for the classification in a sample session (70% vs 30% reward probability) based on the receptor occupancy (see Methods) of D1 (orange) and D2 (blue) receptors. After a short 'swing-in" the receptors could distinguish between a 70% and a 30% reward rate. **(b)** Accuracy of the classifier for a range of reward probability differences for the D1 (orange) and D2 (blue) receptors (see Methods) for individual sessions and corresponding session averages.

Overall, our slow kinetics model of DA receptor binding casts doubt on several long-held views on DA signalling. Our model indicates that both D1R and D2R systems can detect [DA] changes, independent of the timescale, equally well. Although, D1Rs and D2Rs have opposing effects on the excitability (Flores-Barrera et al., 2011) and strength of cortico-striatal synapse of D1 and D2 type MSNs (Centonze et al., 2001), we challenge the current view that differences in receptor affinity introduce additional asymmetries in D1 and D2 signalling. Instead of listening to different components of the DA signal, D1 and D2 MSNs seem to respond to the same DA input, increasing the differential effect on firing rate response of D1 and D2 MSNs.

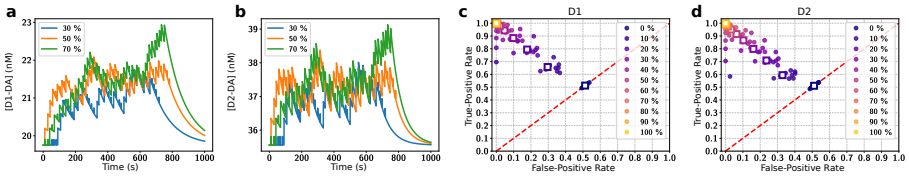

Figure 5.7: Integration of DA signals over minutes in a simulation of a behavioural task. **(a, b)** Timecourse of D1 (a) and D2 (b) receptor occupancy for sequences of 50 trials with a reward probability, as indicated, in each trial. Rewarded trials were modelled with a long DA burst, non-rewarded trials with a burst-pause DA timecourse. **(c, d)** Decoding accuracy of the difference in reward probability based on the D1 (c) and D2 (d) receptor occupancy by a simple classifier. Each data point indicates the decoding accuracy from a simulation scenario with the difference in reward probability indicated by the colour. Single dots correspond to simulations with different absolute reward probabilities. The colour indicates the difference in reward probability (e.g. a 10% difference in purple occurs for 80% vs. 90%, 70% vs. 80%, etc.), and the squares denote the corresponding averages. Red line indicates chance level performance, and a perfect classifier would be at 1.0 true and 0.0 false positive rate. Note that the classification is similar for D1 and D2 receptors, yielding near perfect classification already at 40% reward difference.

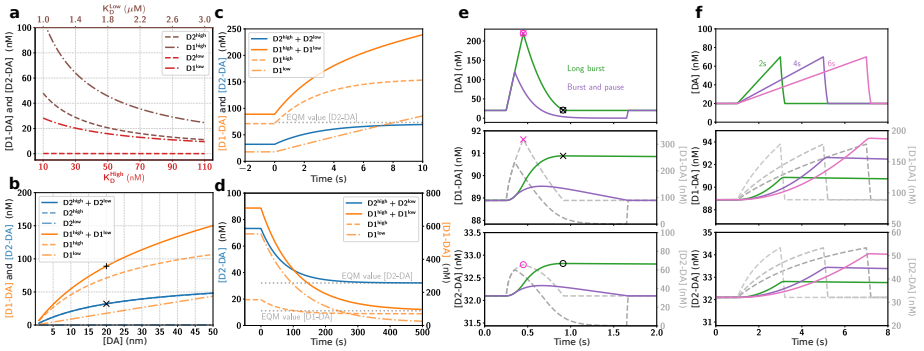

Figure 5.8: Impact of slow kinetics on D1R and D2R binding with 10% of D1R in a high affinity state ($D1^{high}$) and 10% of D2 receptors in a low affinity state ($D2^{low}$) (Richfield et al., 1989). The $D1^{high}$ state was modelled by increasing the on-rate of the D1R but keeping its off-rate constant, creating a receptor identical to the $D2^{high}$ receptor. We choose this model since the high affinity state kinetics of the D1R are currently unknown, and a faster on-rate could potentially have the strongest effect on our conclusions. Correspondingly, we modelled the $D2^{low}$ receptor as a D2R with slower on-rate, which was largely equivalent to simply reducing $[D2^{tot}]$ since the $D2^{low}$ receptors were predominantly unoccupied during baseline DA and bound only sluggishly to DA during phasic signals. The main effect of incorporating the different receptor affinity states was a change in the respective equilibrium values of absolute concentration of receptors bound to DA. **(a)** The receptor occupancy at baseline $[DA] = 20nM$ was dominated by the high affinity states for both receptors, even though only 10% of the D1R were in the high state. As in our default model also D1 receptors were occupied at baseline, enabling them to detect tonic DA signals. **(b)** The amount of bound D1R and D2R stayed within the same order of magnitude over a range of baseline [DA]. '×' and '+' indicate the model default parameters. **(c)** As in the default model, for a large step up from $[DA] = 20nM$ to $[DA] = 1\mu M$, and **(d)** a step down from $[DA] = 1\mu M$ to $[DA] = 20nM$, D1 and D2 receptor occupancy approached their new equilibrium (EQM, grey dotted lines) only slowly (i.e. over seconds to minutes). As the [D1-DA] changes were dominated by the $D1^{high}$ component, they were very similar to the D2R responses. **(e, f)** The effect of different phasic DA signals (top panels) was still very different in the slow kinetics model accounting for affinity states (coloured traces in middle and bottom panels; left scales) compared to the instant kinetics model (dashed grey traces, right scales). As in the default model, the timing of the maximum receptor occupancy ('×' and 'o' for D1 and D2, respectively) coincides for instant kinetics (purple symbols) with the [DA] peak (combined x and o in top panel), while for slow kinetics (black symbols) it coincides with the offset of the [DA] signal instead (combined x and o in top panel). The main difference to the default model is the higher occupancy of the D1R, caused by the $D1^{high}$ component. There is not a two-component unbinding since the $D1^{high}$ and $D1^{low}$ have similar off-rates, but differing on-rates. Overall, also for receptors with two affinity states, DA ramps are very effective in occupying the receptors.

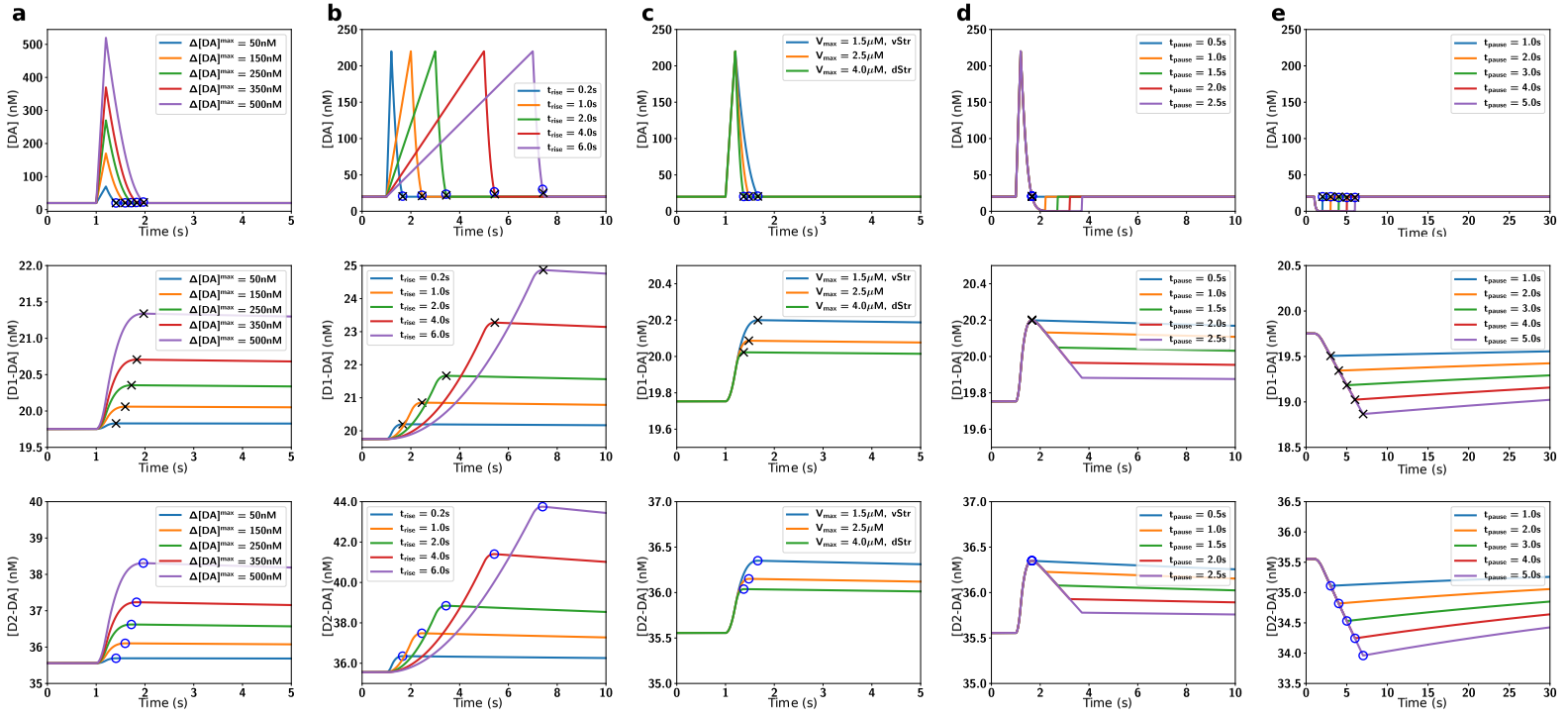

Figure 5.9: Parameter exploration for different DA signals (top row) with the resulting D1 (middle row) and D2 (bottom row) absolute receptor occupancy. The different input DA signals were burst-only with varying amplitude **(a)**, ramp with varying rise time **(b)**, burst-only with varying reuptake **(c)**, burst-pause with varying pause duration **(d)**, and pause-only with varying pause duration **(e)**. Blue circles and black crosses mark the time points of maximum receptor occupancy for D1 and D2, respectively (a-d), and of minimal receptor activation in (e). Note that for both D1 and D2 the time of maximum receptor occupancy was near the end of the DA signal and that D1Rs and D2Rs behaved similarly independent of the specific parameters of the DA pulse.

Chapter 6

Variable DA maps and Unchanging Receptor Maps

This chapter is divided into two parts. The first part treats a set of simulations that were designed to understand the distribution of the instantaneous DA concentration in the striatum. These simulations have no receptor influence, and do not treat receptors. We set out to model DA diffusion in the striatum to investigate if the DA signal in the striatum is fairly homogenous, as often implicitly assumed, or if it has a more complicated structure than that.

The second part treats a set of simulations that was aimed at understanding the distribution of the DA receptor activation in the striatum, and how it relates to the DA maps. We were interested to see if the DA receptor maps are direct copies of the DA maps, or if they show a different temporal or spatial behavior than the DA maps. I will show an analysis of the spatial structure of the DA maps, the activation of receptors, and how these two relate to each other.

6.1 The Spatiotemporal DA Distribution

6.1.1 Simulations: Technical Data

To investigate the structure of the spatiotemporal DA distribution I simulated a model with default parameters (see **Suppl. Table 1**) for $30s$ simulation time. These simulations had a rewarding burst at $t = 15s$ and $t = 22s$ and were performed for a voxel resolution of $h = 1\mu m$ and $h = 2\mu m$, on a cube of 100^3 voxels each, resulting in simulation volumes of $100\mu m$ and $200\mu m$. Temporal resolution was $\Delta t = 1ms$. Furthermore, I started with a model of 100 axons, but I also simulated models with 55 and 10 axons respectively. The simulations with fewer axons use the same axon geometries and spiketrains as the 100 axon models, with some of the axons removed. When removing axons, I made sure that the remaining axons have a similar distribution of spiking patterns (20% high-bursting, 55% irregular, 25% regular) by retaining a similar fraction of axons associated with spiketrains of the fitting type. I also made sure that 70% of the remaining axons participate in the reward bursts. The axon removal was done to simulate Parkinson's Disease (PD) since one of the common clinical signs

of PD is the death of dopaminergic neurons. I simulated 3 realizations of each dataset. However, since there was no qualitative difference between them, most of the data shown is from the first simulation (run-1). For run-1 I also performed simulations with a homogeneous, flat, uptake distribution, the same spiketrains and the same sequence of pseudorandom numbers. This simulation showed the quantitative ($\approx 10\%$) difference we observed in **Section 4.2.2** but otherwise no qualitative differences, so these results are not shown. Furthermore for run-1 a small parameter study for different quantal release sizes $Q = \mathbf{3000}; 6000; 9000$ and release probabilities $p = (0.03; \mathbf{0.06}; 0.09;)$ (bold are the default values) was performed. The simulation with $Q = 9000$ is of special interest, since it is a representation of L-DOPA treatment, which is known to increase quantal sizes (Pothos et al., 1998). One realization of one set of parameters has a runtime of $\approx 36h$ and creates around $\approx 200GB$ of data. In the analysis we focused largely on the $100\mu m$ simulations, results are also valid for the $200\mu m$ cubes (data not shown).

6.1.2 The Spatial and Temporal Distribution of DA is Highly Variable

The DA signal is usually quoted as having a baseline component of around $20 - 30nM$ (Venton et al., 2003; Suaud-Chagny et al., 1992; Borland et al., 2005) that increases by a few $100nM$ (Cheer et al., 2007; Robinson et al., 2001; Day et al., 2007) at a reward burst. In our simulation Averaging the DA concentration over the simulation cube and plotting it for the time before, during and after the reward burst starting at $t = 15s$ (see **Fig. 6.1a, 6.2a, 6.3**) produces the expected result. The DA concentration starts from a baseline concentration of $30nM$ and rises to a peak of $\approx 200nM$ during the reward burst, returning to the baseline after the reward burst.

This description usually evokes a picture of a DA concentration, that is mostly homogeneous in space and time, with the exception of the occasional reward bursts. We even treated in in this way in **Chapter 5**. This picture is analogous to a bathtub that is constantly being filled from a faucet while being drained through a drain. When the drainage rate matches the filling rate, the water surface would be mostly flat and level. However, our simulations indicate that this is not an accurate description of the DA distribution, even during baseline firing. **Fig. 6.1b** shows a volume render of the DA distribution during baseline firing. It is clear that the distribution is not very uniform, even though the average concentration is at $\approx 30nM$. The same can be seen in slices before, and during the burst **Fig. 6.1e, f**. This simulation is not an outlier, we see this behavior in all our simulations, see also **Fig. 6.2c, e** The DA distribution is not a homogeneous monolithic value, but is made up of a large number of single events. More akin to the water-surface of a bathtub constantly pelted with waterbombs, making large splashes on impact. How variable is the DA distribution at a point in time? The coefficient of variation (CV), $CV = \sigma/\mu$, with the standard deviation σ and mean μ, of the DA concentration in space can be used to quantify such a variability.

The signal is highly variable with an average (averaging variances and means) spatial $CV = 4.02;\ 4.07;\ 3.93$ for the $3s$ period before the burst for the three different runs. This changed a little during the burst, $15.0s < t < 15.5s$ where the $CV = 2.27;\ 2.27;\ 2.27$ respectively. The CV during the burst is most likely

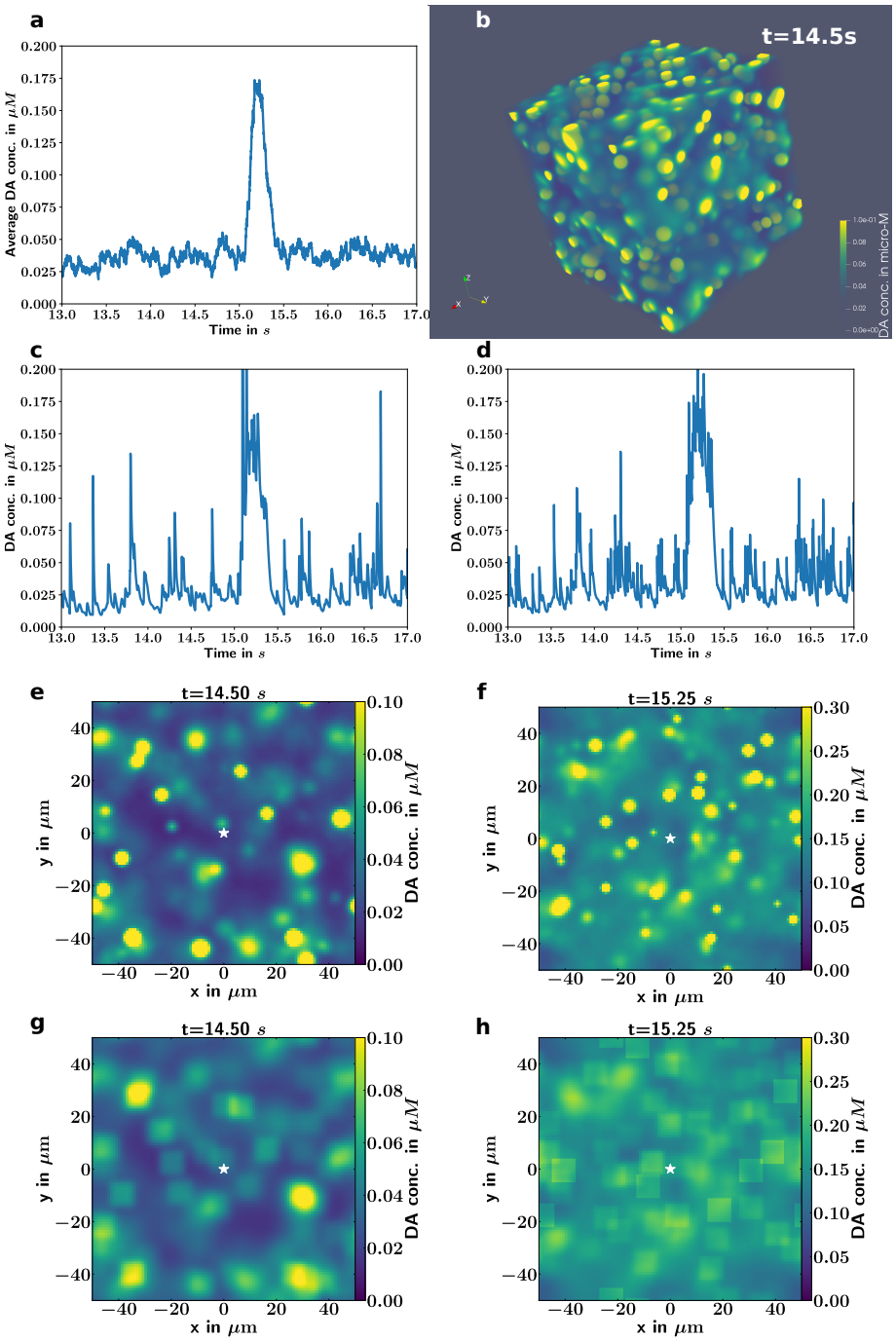

Figure 6.1: DA distribution is very inhomogeneous. Even though the timeline of DA averaged over the simulation cube (a) reproduces measured DA timesignals. The 3D DA distribution (b) is very variable in space. as is timesignal of DA at a a specific location (50,50,50) is highly variable (c), even when averaged over a cubical volume of size $9\mu m$ (d). The spatial distribution of DA in 2D slices of the simulation cube, during baseline firing (e) and during a reward burst (f) is also highly variable. The distribution is characterized by peaks and troughs rather than an average value with small fluctuations. Inhomogeneities can be alleviated, but not removed, when the signal is averaged over a cubical volume of size $9\mu m$. In both the baseline (g) and during burst (h) case.

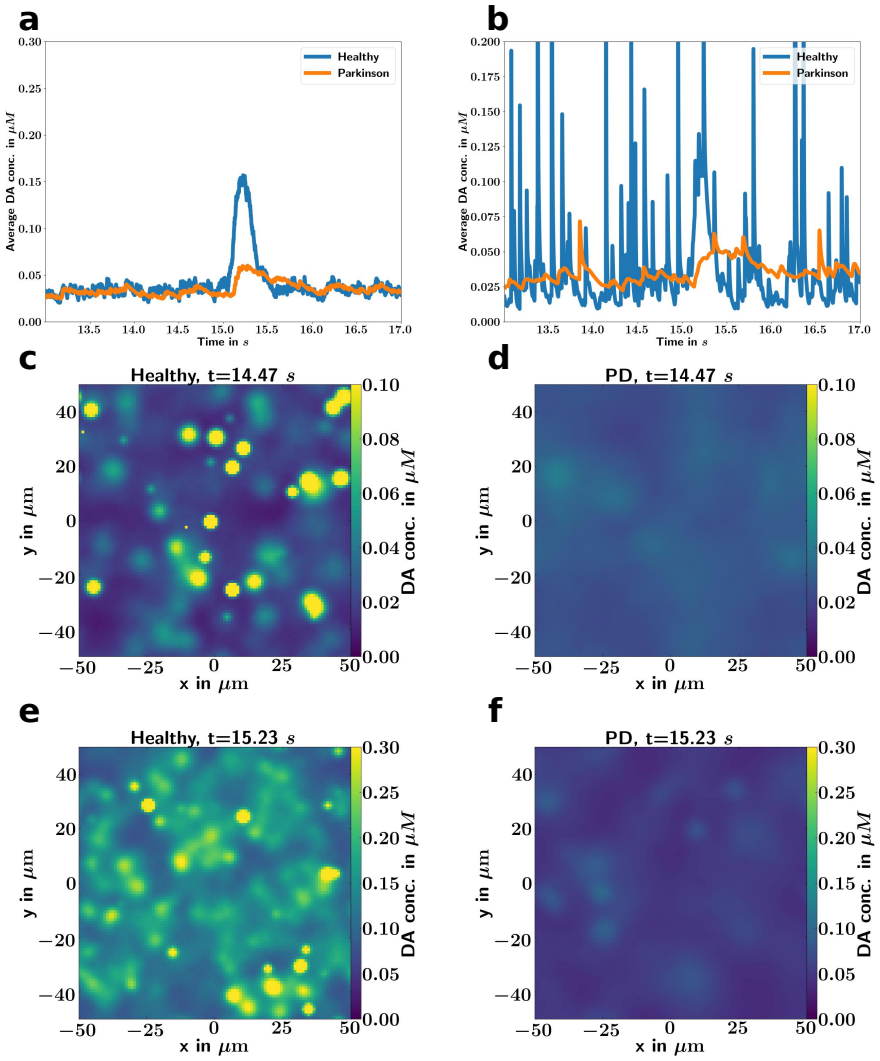

Figure 6.2: The high variability of the DA distribution is space and time is a feature seen in all realizations, as is the reduction of this variability in the PD case. Data shown here is from run-2. The timeline of DA averaged over the simulation cube reproduces measured DA timesignals in the healthy case (blue) (a). The average concentration of DA does not change in the PD case, but during the burst the DA increase is reduced (orange) (a). The healthy single location (50,50,50) timesignal (blue) is highly variable, but in the PD case the timesignal becomes more uniform (orange) (b). The 2D slices in the healthy case show a highly variable DA distribution during baseline (c) and burst (e) firing of the dopaminergic neurons. In the PD case the spatial DA distribution becomes more uniform during both the baseline (d) and burst (f) firing.

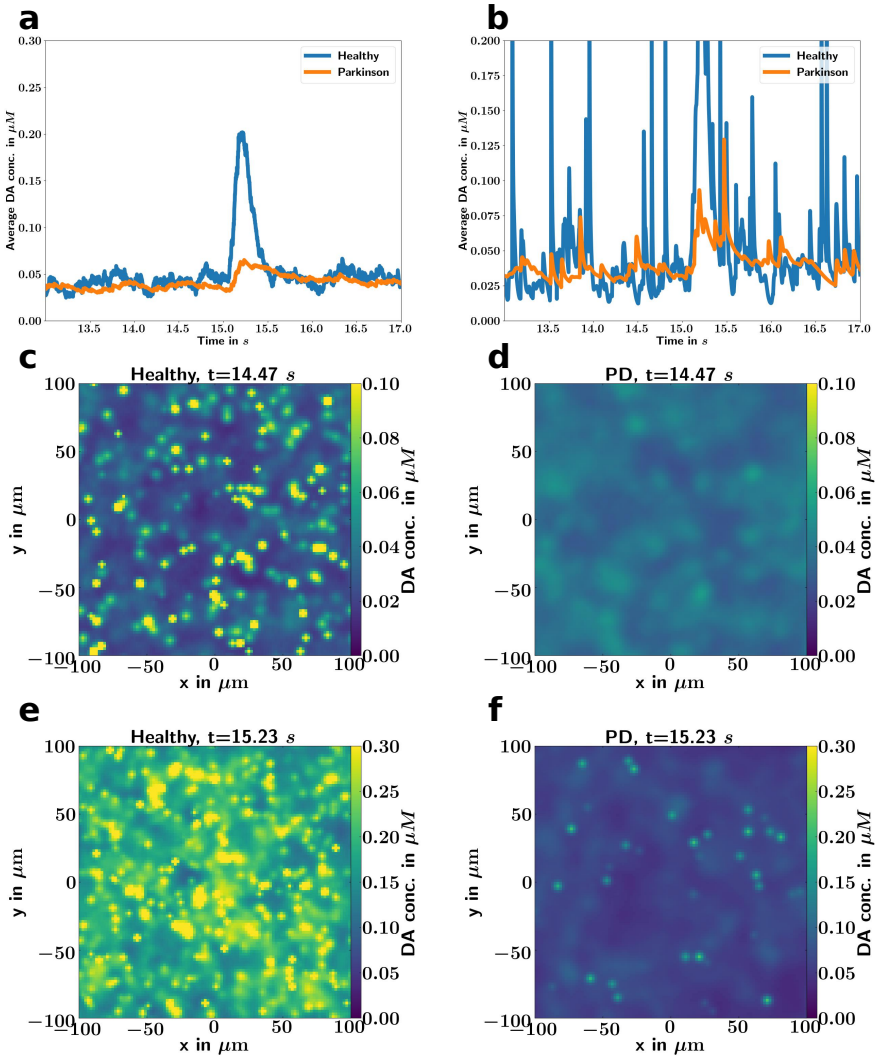

Figure 6.3: The high variability of the DA distribution is space and time is a feature seen in all realizations, as is the reduction of this variability in the PD case. This observation even remains for lower resolution simulations $h = 2\mu m$, covering a larger volume $200\mu m$ as shown here. The timeline of DA averaged over the simulation cube reproduces measured DA timesignals in the healthy case (blue) (a). The average concentration of DA does not change in the PD case, but during the burst the DA increase is reduced (orange) (a). The healthy single location (50,50,50) timesignal (blue) is highly variable, but in the PD case the timesignal becomes more uniform (orange) (b). The 2D slices in the healthy case show a highly variable DA distribution during baseline (c) and burst (e) firing of the dopaminergic neurons. In the PD case the spatial DA distribution becomes more uniform during both the baseline (d) and burst (f) firing.

lower since the mean concentration increases. The spatial distribution of DA is highly variable and can not be compared to a nice and calm bathtub. However, this can be somewhat alleviated by averaging a sub-volume of the DA distribution. As was done for a volume of size $9^3\mu m^3$ and the first run. Each location in the simulation cube was replaced by the average of the surrounding cube motivated by the size of MSN whose diameter is around $d \approx 10\mu m$ and therefore a volume the DA signal might be averaged over. The signal is less variable when looking at this sub-volume averaged signal **Fig. 6.1g, h** with $CV = 0.38$ before and $CV = 0.40$ during the burst, which is not surprising since averages tend to smear out discontinuities. However, the original distribution remains highly variable, and we do not know what weighting MSNs perform on the DA signal, e.g. dendrites could have stronger weights. We will focus on investigating the spatial structure further. The CV analysis was also performed for the simulation in the larger cube **Fig 6.3**, and we found that the CV is lower before $CV = 1.53$ and during $CV = 0.84$ the burst. Again this is likely because the simulation is already averaged over a volume of $2^3\mu m$. The release events in this case are already distributed to the full $2\mu m$ voxel, which reduces the variance of the simulation run. The DA distribution is highly variable, during burst and baseline firing, and can not be adequately described as a homogenous signal in the striatum.

The DA distribution is not only highly variable in space, but also in time. **Fig. 6.1c**, **Fig. 6.2b** and **Fig. 6.3b** show the local DA timeline for the middle $(50, 50, 50)$ of the cube. For these single locations the DA distribution is quite variable in time, due to release events often happening relatively close by. Since these release events are discontinuous, they change the concentration by a large margin in a small timewindow. These are features that look like spikes in the DA timelines. For each run 10 timelines (9 randomly chosen locations and the center) where analyzed. The average CV in time (for each realization) for these runs are $CV = 0.96; 0.79; 0.99$ before and $CV = 1.53; 1.69; 1.60$ during the burst. As another test the first realization was averaged over a cubical volume as described above with the result shown in **Fig. 6.1d**. The timeline stays quite variable even for the sub-volume averaged case ($CV = 0.53$ before and $CV = 0.55$ during burst). For the timewise signal the CV increases during the burst since the number of close by release events increases, making the signal more irregular during the burst. In this case the increase in the mean can not compensate for the increase in variability. The spatiotemporal DA distribution is highly variable in space and time.

6.1.3 Why is the Spatial and Temporal DA Distribution Inhomogeneous?

The DA distribution is inhomogeneous since it is the result of a large number of release events being released while the DA is being taken up by the DAT. Going back to the bathtub analogy, the DA is not supplied by a steady stream but by a sequence of water-bombs. How long is one of these release events visible? Is it reasonable that we see around 30 recent release events (identified as such by a $C_{DA} > 0.1\mu M$) in the baseline firing case (**Fig. 6.1c**, **Fig. 6.2b** and **Fig. 6.3b**)? I was asked this at a conference so I will provide a short answer here. The answer is for the $100\mu m$ cube. For the larger cube some of

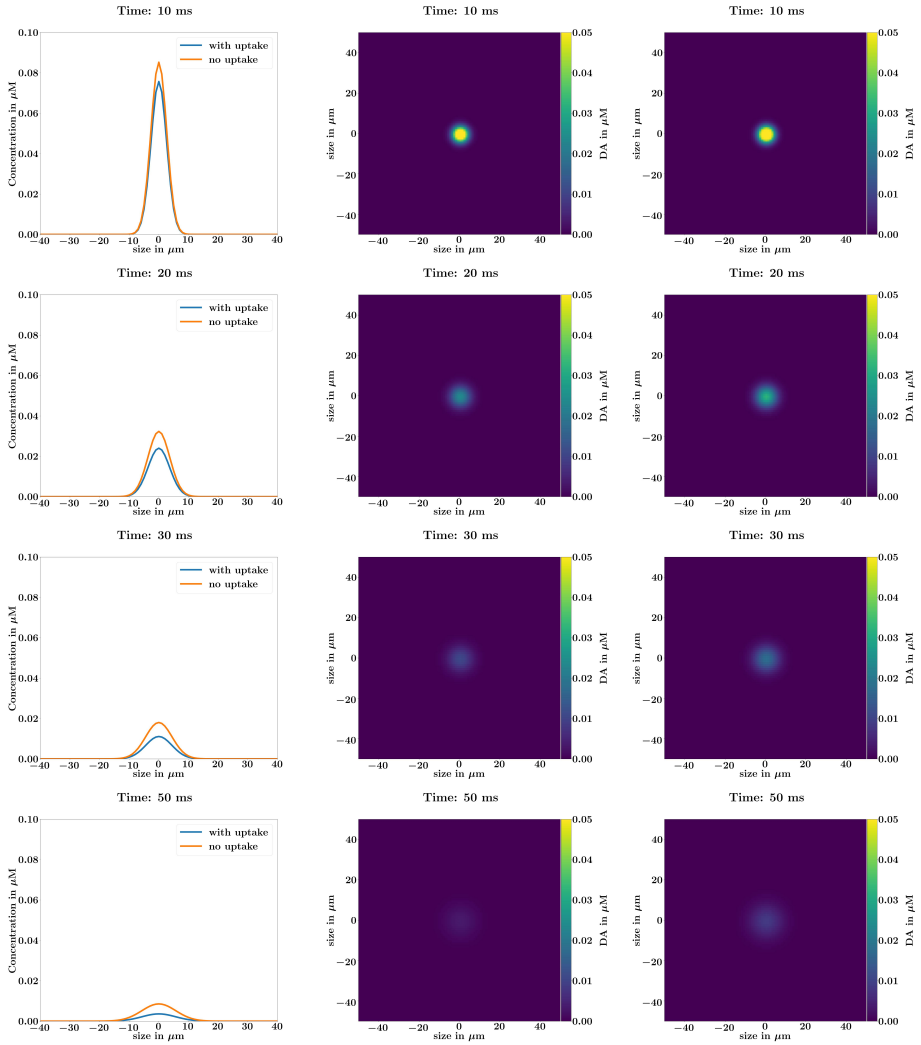

Figure 6.4: A quantal release event initially $< 10ms$ spreads quickly to nearly its full extend. In this beginning phase uptake of DA plays only a minor role. As time progresses the spread of the DA cloud becomes slower and uptake effects become more important. The time until a release events has diffused to approximately baseline values if $\approx 20ms$, independent of uptake one quantal release event has a diameter of $\approx 20\mu m$. Shown are a 1D plot of the DA concentration along the $x = 50, y = 50$ line at different timepoints (left) and 2D slices in the yz-plane for the case with (middle) and without uptake (right).

the arguments have to be scaled accordingly.

Fig. 6.4 shows the comparison of a single release event ($Q = 3000$) with and without uptake simulated for $50ms$. Uptake plays a relatively minor role for the time development in the first $10 - 20ms$. The concentration reduces mainly because the DA diffuses. We see that the released DA does not really spread much farther after the initial expansion to about a diameter of $d = 20\mu m$. Diffusive spreading becomes less and less important with time after the release, due to the mean mean molecule displacement growing with $\sqrt{t}$ (see **Section 2.1**). We can see that after $50ms$ the uptake and no uptake case differ strongly. Since uptake becomes relatively more important since the diffusive spreading becomes slower and slower.

A single release event of $Q = 3000$ stays noticeably above the average concentration of $C_{DA} \approx 30nM$ for around $10ms$ (**Fig. 6.4**). With the diameter of $20\mu m$ found above, it is possible to calculate how many release events should be visible on average in one of the slices shown. The simulation domain is covered by 100 axons. Each axon has an average firing rate of $4Hz$. That means there is a spike every $2.5ms$, since the sum frequency is around $400Hz$. With a release probability of $p = 0.06$ and around 1000 synapses per axon, that means that every $2.5ms$ around 60 release events appear in the simulation cube. Since we estimated the livetime with $10ms$ that means at all times around 200 release events are recognizable as such in the simulation volume of $100\mu m$. Since one release event has a diameter of around $20\mu m$ in a 2D slice one fifth of the release events will be visible. All the release events that overlap with the slice. That means in a 2D slice plot we will see $\approx$ 40 release events. Which is close to what we observe in **Fig. 6.1e** and **Fig. 6.2c**. These release events are the main source of inhomogeneity in the cube. Since where they can be seen the C_{DA} is elevated above baseline, leading to the patchy, inhomogeneous structure.

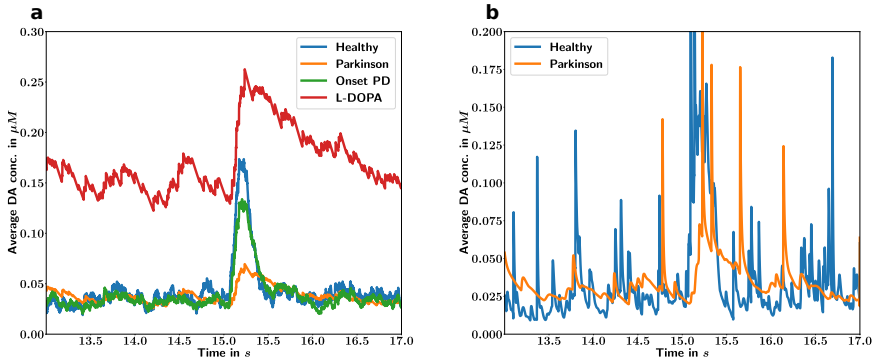

Figure 6.5: The DA concentration timeline averaged over the cube (left) does not show a decreased mean during baseline firing in the PD case (orange) but has a much smaller response to burst firing of dopaminergic neurons than the healthy (blue) case. In the case of L-DOPA medication (red) the average DA concentration increaes in our model, and the increase during bursting is also recovered. The Onset PD case (green) is still very similar to the healthy case. The single location DA concentration (right) is highly variable in time, in the healthy case (blue), but becomes more uniform in the PD case.

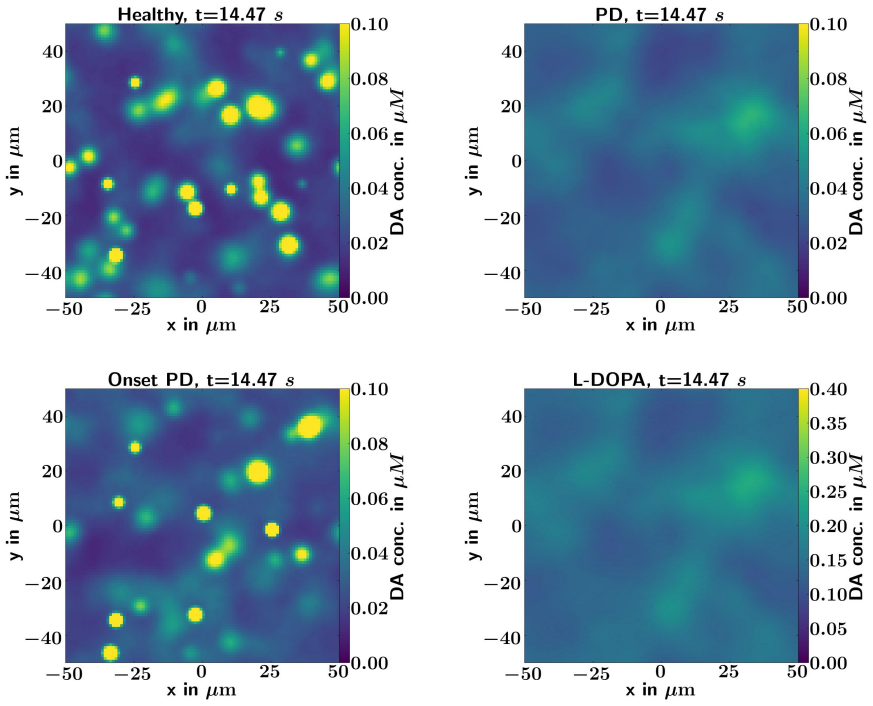

Figure 6.6: The DA concentration distribution is highly variable during baseline firing in the healthy case (a). However during PD, this spatial variation reduces and the DA map becomes more uniform (b). During early onset PD (c) the map is still very similar to the Healthy case but L-DOPA (d) does not recover the variability. Not the different scale on the L-DOPA map due to the higher average concentration in the L-DOPA case.

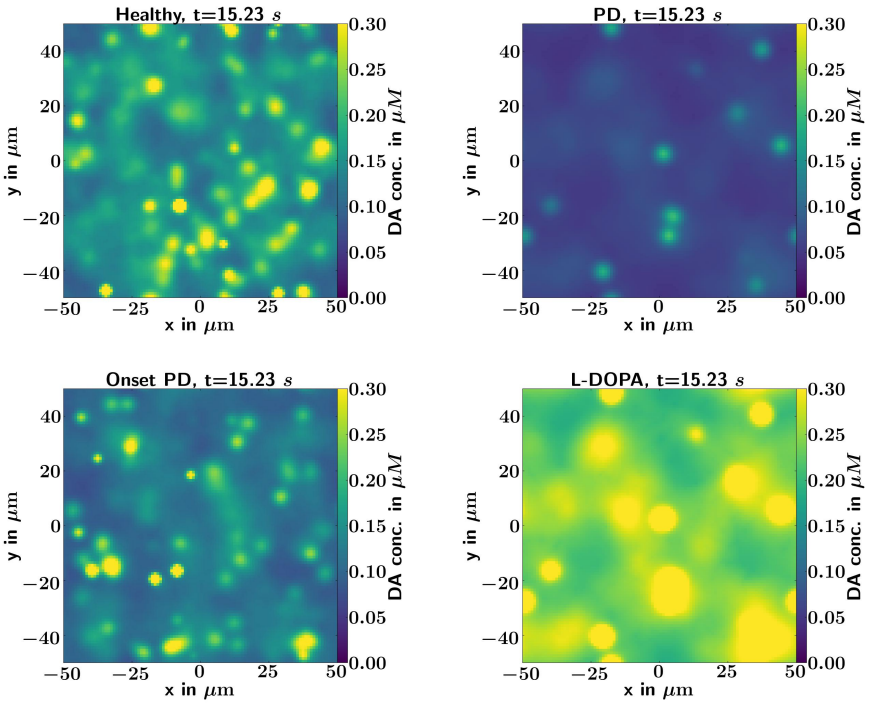

Figure 6.7: The DA concentration distribution is highly variable during reward bursting in the healthy case (a). However during PD, this spatial variation reduces and the DA map becomes more uniform (b). During early onset PD (c) the map is still very similar to the Healthy case but L-DOPA (d) does not recover the variability.

6.1.4 Simulation of PD and Levodopa Treatment

Some of the simulations have a reduced number of axons, simulating Parkinson's Disease (Nr. of axons=10) or early Parkinson's Disease (Nr. of axons=55). One of the simulations has reduced number of axons (Nr. of axons=10) and an increased quantal size $Q = 9000$, this simulation is titled L-DOPA. For the volume averaged timeline in the PD case the average DA concentration does not reduce during baseline firing **Fig. 6.5a, 6.2a, 6.3a**. A reduced number of dopaminergic axons, even by 90% does not lead to a decrease in average DA concentration during baseline firing. This agrees with the findings in Dreyer (2014) and has been experimentally demonstrated in Castaneda et al. (1990). We do find a reduction in burst signaling though. The PD simulation shows a much smaller increase C_{DA} during reward bursts (**Fig. 6.5a, 6.2a, 6.3a**) matching experimental studies Sandberg and Phillips (2009) and other simulations (Dreyer, 2014).

The early Parkinson's case however, leads to only minor changes in the timeline while the L-DOPA case has a generally elevated DA baseline concentration, while having a stronger response to the burst than the PD case. Furthermore, in the L-DOPA case the elevated DA concentration remains much longer than in the healthy case. Why does the baseline DA concentration not reduce when dopaminergic axons are removed? Because dopaminergic axons are also the location of the DAT. That means when dopaminergic axons are removed there are less sources of DA but there is also less DA uptake. This is a homeostatic mechanism where the average DA concentration does not reduce with reduced number of axons. However, in the L-DOPA case, each synapse releases more DA than usual, which overwhelms the now reduced uptake and leads to a higher concentration of DA. It is possible that in a real animal other uptake mechanisms, not modeled in this model, could reduce the increase of the DA tone in the L-DOPA case.

What happens to the DA distribution in the PD case? Before we concluded that the DA signal is highly inhomogenous in the healthy case. However in the Parkinson case, the DA signal becomes a lot less variable in both time, and space. The time-signals for single locations, are a lot less variable than in the healthy case **Fig. 6.5b, 6.2b, 6.3b**, $CV = 0.36; 0.28; 0.47$ before and $CV = 0.44; 0.57; 0.46$ during the burst. There are fewer strong excursions in the DA time-signal, since due to the reduced amount of axons there are a lot less release sites and release events. At single spatial locations, the instantaneous DA concentration is higher than in the healthy case for large sections of time due to the reduced uptake. Generally since there are less release events and less uptake the DA timesignals are less variable. We did not investigate the single location timelines for the L-DOPA and early PD case.

What happens to the spatial distribution? The spatial DA distribution is a lot more homogeneous in the PD case than in the healthy case before $CV = 1.35; 1.48; 1.52$ and during $CV = 1.32; 1.35; 1.40$ bursting **Fig. 6.6** and **Fig. 6.7**. For the PD case more of the locations in space have a DA concentration close to the average concentration than in the healthy case. The variability of the early PD case is reduced slightly $CV = 3.13$ before and $CV = 1.87$ during the burst. However that is hardly noticeable. In the L-DOPA case the average concentration increases, however the spatial distribution stays as invariable as in the PD case $CV = 0.96$ before (**Fig. 6.6**) and $CV = 0.97$ during the burst

(**Fig. 6.7**). The decrease in CV with respect to the PD case is most likely due to the increase in mean concentration (The only difference between the PD simulation and the L-DOPA simulation is the quantal size, all spikes and release events are equal). That means PD also reduces the spatial variability of the DA signal. This reduction in variability is due to a combination of a reduced number of release sites and reduced uptake. Fewer release sites mean fewer release events so there are fewer peaks of DA. Furthermore, there is less uptake in the whole domain, which means there are also fewer areas with very low DA concentration, which means there are also less troughs in the DA concentration. These combined effects make the spatial DA distribution more homogeneous as a whole.

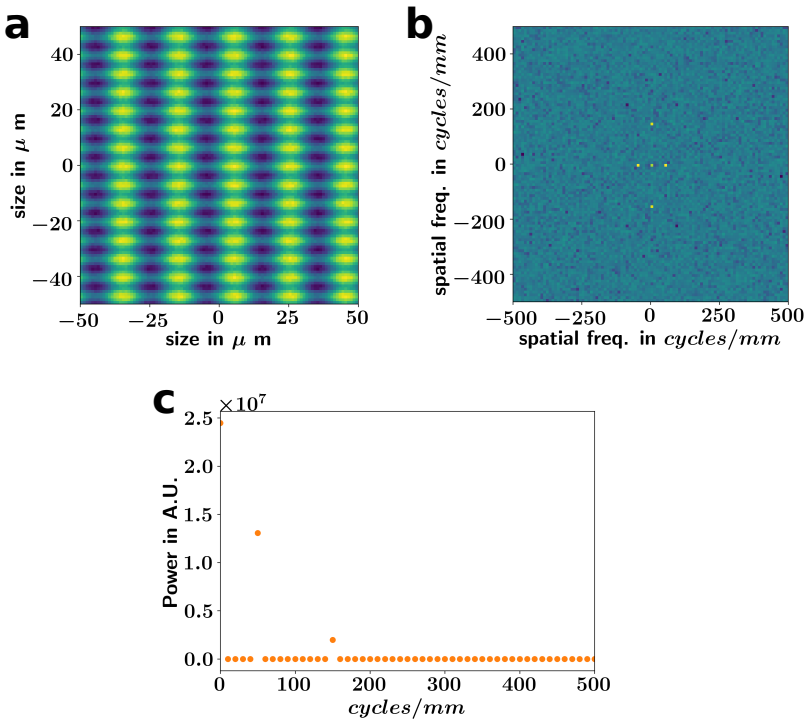

Figure 6.8: The example image with a given oscillation of spatial frequency 150 $cycles/mm$ in the y-direction and 50 $cycles/mm$ in the x direction and some added noise (a) has a very simple 2D spectrum (b). The spectrum is symmetric along the x and y axis, so that the full information is contained in one quadrant of the spectrum. The full spectrum is shown as is convention. Averaging the spectrum by radial frequency distance from the origin produces a 1D spectrum (c) in which the directional information about the frequency of the structures is lost.

6.1.5 Fourier Analysis

To characterise the DA signal in the striatum, I next examined the spatial structure of the DA maps in more detail. This was done using a 3D discrete Fourier

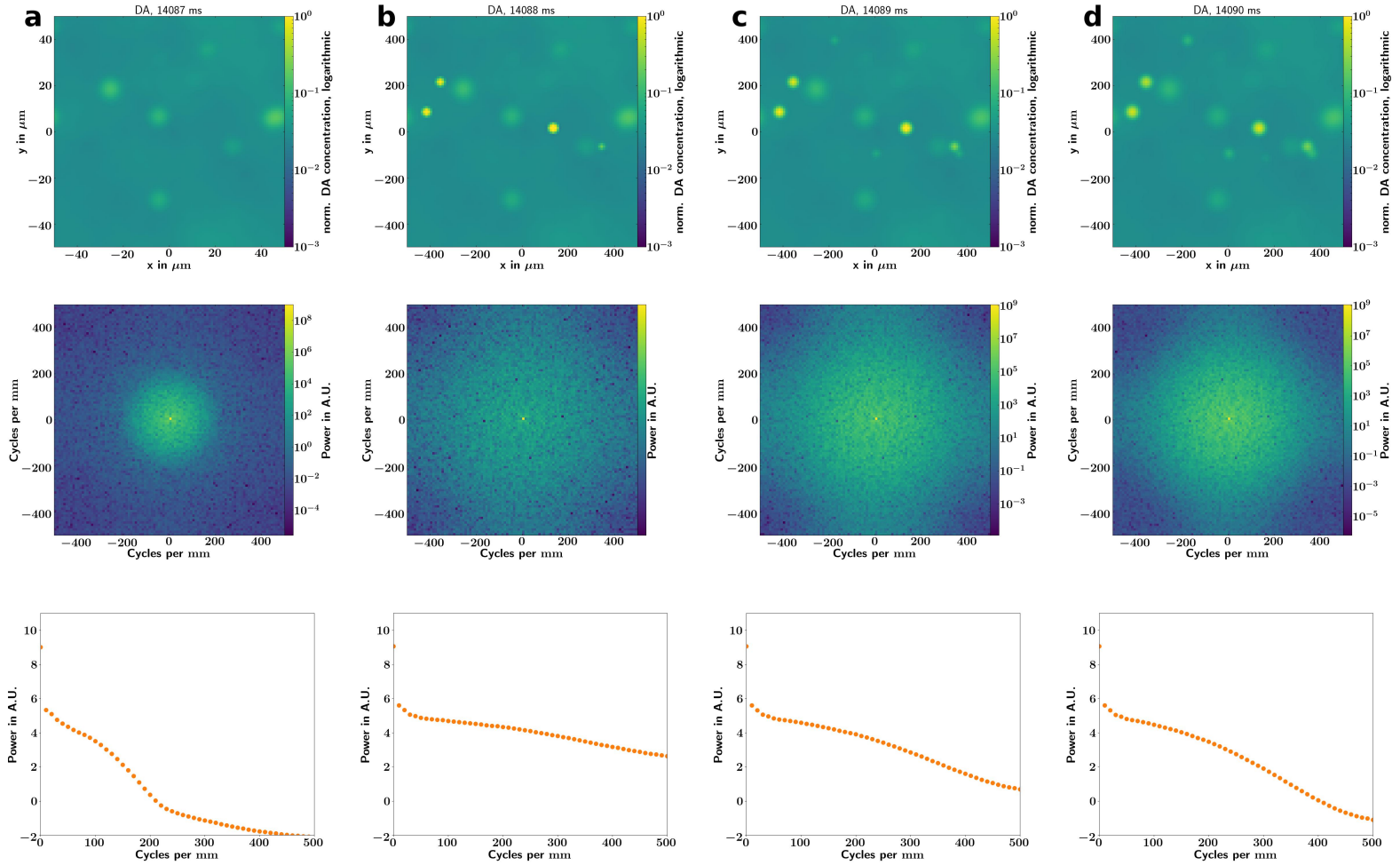

Figure 6.9: The spectrum can vary in time quite strongly. Shown are the DA maps (top), 2D slices of the 3D spectra (middle) and radially averaged spectra (bottom) for 4 consecutive timesteps during baseline firing in the PD case. In the first timestep (a) there are no strong high frequency components, the DA map is quite flat, which is reflected in the spectrum by having only small power in high frequencies. There are some release events, but they have been removed by the filtering. When the DA release appears (b) the spectrum shows the higher frequency components, caused by these release events. However these high frequency components quickly start to decay (c) since the released blobs of dopamine diffuse, spreading them out in space which increases their size and therefore shifts them to lower frequencies. This happens since diffusion damps high frequency components. This continues as time moves on (d), affecting successively lower frequencies since the frequency damping depends on k^2.

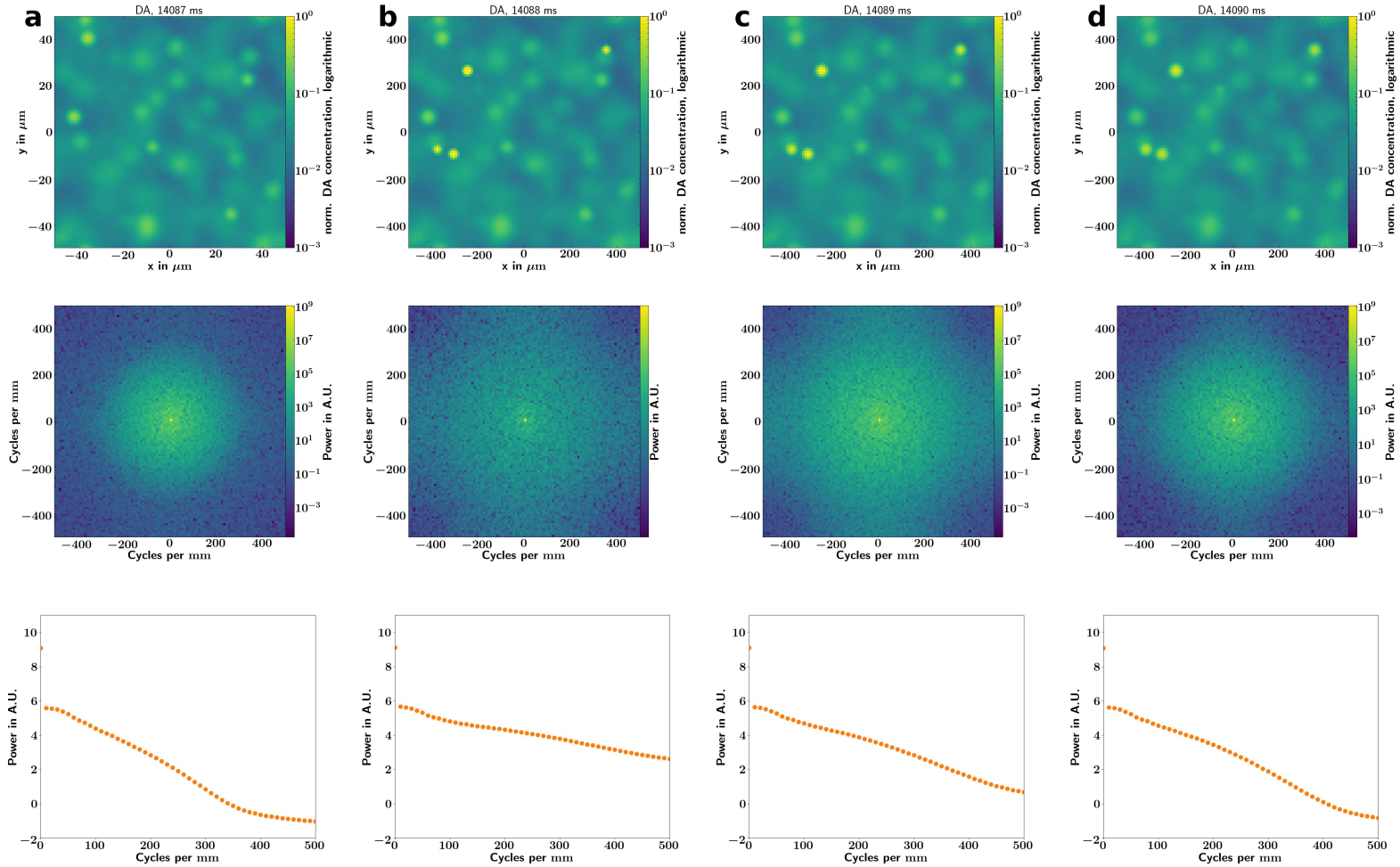

Figure 6.10: The spectrum can vary in time quite strongly. Shown are the DA maps (top), 2D slices of the 3D spectra (middle) and radially averaged spectra (bottom) for 4 consecutive timesteps during baseline firing in the healthy case. In the first timestep (a) high frequency components are somewhat suppressed, but not as strongly as in the PD case since there are smaller structures. The DA map is bumpy which is reflected in the spectrum by having higher power in higher frequency bands than the PD case. There are some release events, but they have been removed by the filtering. When the DA release appears (b) the spectrum shows the higher frequency components, caused by these release events. However these high frequency components quickly start to decay (c) since the released blobs of dopamine diffuse, spreading them out in space which increases their size and therefore shifts them to lower frequencies. This happens since diffusion damps high frequency components. This continues as time moves on (d), affecting successively lower frequencies since the frequency damping depends on k^2.

transformation (DFT) to investigate the spatial power-spectral density (PSD) of the DA maps. The 3D fourier transform of our data, a spatial cube at a given t, will leave us with a 3D spectrum. This spectrum will not have units in a time-wise frequency, e.g. $1/s$, but will give a spatial frequency e.g. $cycles/mm$. The spectrum will not inform us how much power is in an oscillation of a quantity in time, but will inform us about oscillations in space. An oscillation in space can be identified with the size of a given structure e.g. $250 cycles/mm$ is a spatial frequency that corresponds to a structure with the size of a full cycle of $4\mu m$. A toy example, showing an image with an oscillation $150 cycles/mm$ in y direction, $50 cycles/mm$ in x direction (with added noise) can be seen, together with its 2D spectrum in **Fig. 6.8**. The spectrum is symmetric along the x and y axis, however it is convention to show all 4 quadrants. The 2D spectrum still has different directions. The different direction correspond to physical directions. That means an entry on a diagonal would mean that the image contains a spatial component with a spatial frequency $f_{diag} = \sqrt{f_x^2 + f_y^2}$, along the direction of the diagonal. The multidimensional spectrum can be hard to analyze but can be radially averaged which turns it into a 1D spectrum where the frequency f_{1D} corresponds to the average of a quarter annulus around the center with radius f **Fig. 6.8c**. In the toy example, both the x and y component are at the correct position in the 1D spectrum. They don't interact because they are components in directions perpendicular to each other.
This technique was applied to our 3D data. After performing the 3D DFT we were left with a 3D spectrum that contains the spatial frequencies in different directions **Fig. 6.9**. However, since there is no term that creates a systematic asymmetry in our simulations, we would expect the spatial 3D spectrum to be spherically symmetric, an expectation that proves correct **Fig. 6.11**. A systematic asymmetry would mean that structures in one direction would be larger, or have larger amplitude. Since the spectrum is approximately spherically symmetric, we average over directions and get a 1D spectrum (**Fig. 6.11d**) that we can use to investigate the strength of components of different sizes in the DA map. However, a preprocessing step is necessary. Release events have to be removed from the timestep in which they first appear. Their high amplitude makes them act as a stepwise discontinuity which introduces strong components in all frequency bands (this is why we use a numerical method that damps high frequencies). To recover a more meaningful spectrum, release events are median filtered with the points around them for the timestep in which they happen **Fig. 6.12**.

Temporal Fourier Analysis

Synapses releasing DA create a strong high frequency component that subsequently decays, driving the spectrum towards lower frequencies and larger structures **Fig. 6.9** and **Fig. 6.10**. The diffusion equation damps high frequency terms (see **Chapter 3**) driving the spectrum towards lower frequencies.

The PD spectra tend to have less power in the high frequency component than the spectra of the healthy case **Fig. 6.13**. This goes along with our conclusion from above that the spatial distribution of DA in the PD case is a lot less variable than in the healthy case. The power spectrum of the PD is made up of mostly larger structures, whereas the healthy case spectrum contains more

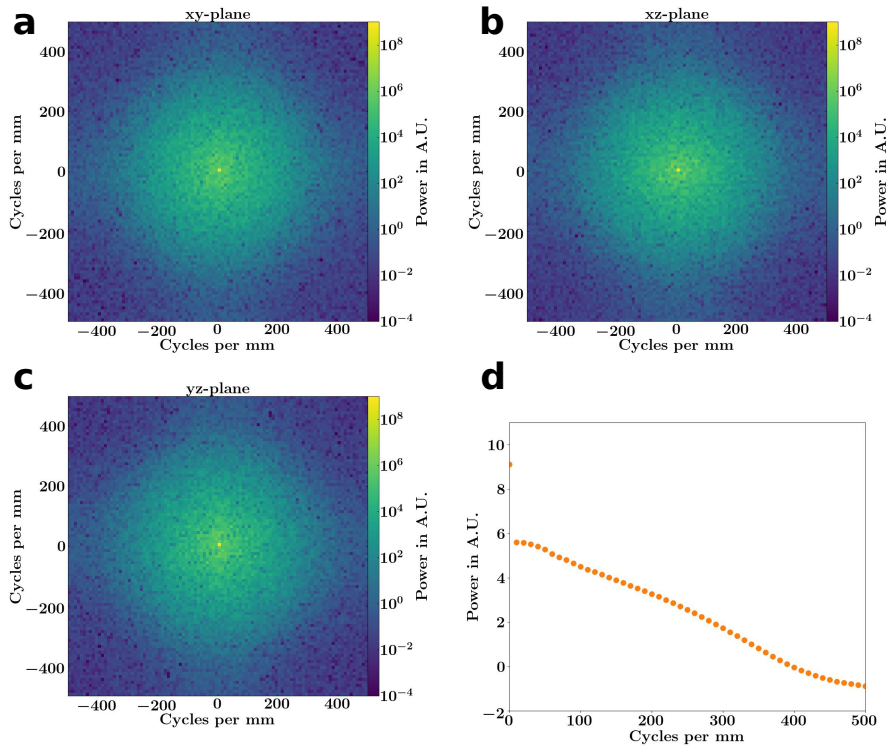

Figure 6.11: The 3D power spectrum for the DA map is approximately spherically symmetric. Shown are representative 2D slices of the healthy system at $t = 14086ms$. The spectrum is symmetric in the xy-plane (a), the xz-plane (b) and the yz-plane. Showing that the system is spherically symmetric. Because of the spherical symmetry we can average all directions and end up with 1D power spectrum (d) without losing important information.

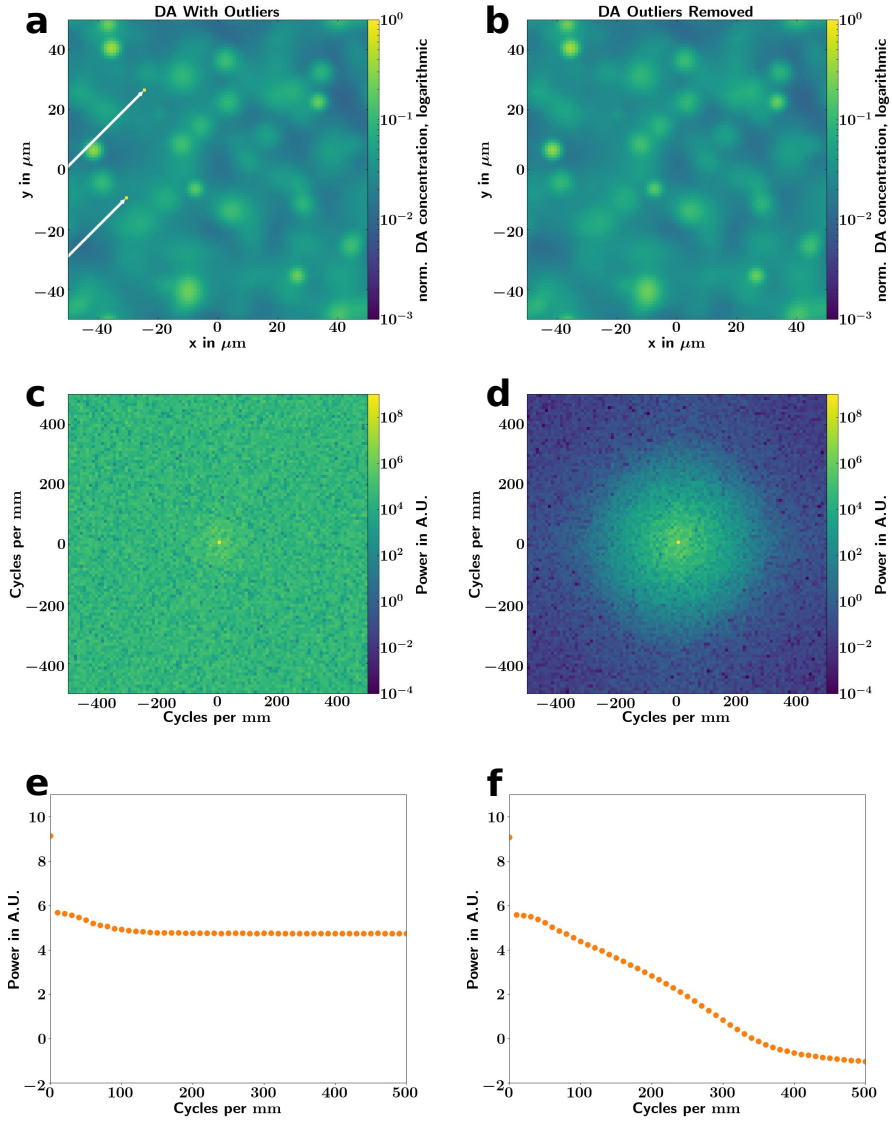

Figure 6.12: To keep our power spectrum free from artifacts caused by very high single voxel values, we have to remove the quantal release events for the timestep when they appear. Single voxels with very high concentrations (a, arrows) cause an artifact in the power spectrum that spreads high over all frequencies (c) and is spherically symmetric, so it also shows up in the radially averaged spectrum (e). When the outlier voxels are removed, by using a median filter on them and their sorrounding (b) the artifact free multidimensional spectrum is recovered (d) whihc also leads to an artifact free radially averaged spectrum (f). The high value voxels are not removed from the simulation, they are just removed for the spectral analysis of the timesteps when they appear.

high frequency i.e. small scale fluctuations. In the healthy case the spectrum has stronger small scale structure. However the one time spectrum is not the final step for this analysis. **Fig. 6.9** and **Fig. 6.10** show that the spectrum can change with time, and even single release events can replenish, for some time, the high frequency components in a DA map. In our simulations we use the same spiketrains for the healthy and PD case, that means it is very unlikely that the PD case has release events at a point in time, when the healthy case has not. However when comparing different realizations looking just at one snapshot can be misleading. To compare PD and healthy case in a systematic way we plot the spectra for a set of times together with the median spectrum. The median spectrum is the spectrum for which half of the spectra at a given frequency have higher power and the other half have lower power. We apply this method to the $1s$ before the burst at $t = 21s$ plotting a spectrum every $5ms$ in **Fig. 6.14** and **Fig. 6.15**.

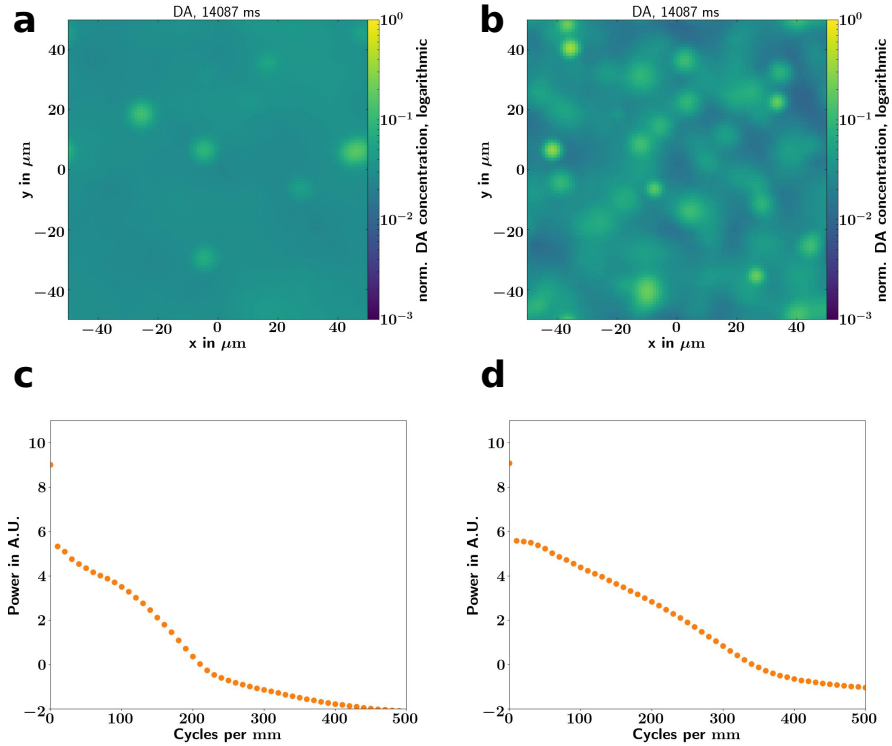

Figure 6.13: In the PD case the DA distribution is more uniform (a) than in the healthy case (b), shown in 2D slices. This is reflected in the power spectra where the PD case has barely any high frequency (small structure) components (c). The spectrum of the healthy case shows more higher frequency components (d) that can also be seen in the DA distribution map.

Our parameter study with different quantal sizes, and release probabilities shows that the spectral shape is not meaningfully changed by either of those parameters, neither in the healthy nor in the PD case (**Fig. 6.14** and **Fig. 6.15**). That means the spatial structure of the DA map is only weakly dependent on release probability and Quantal size. However it is clear that the healthy case

spectra have generally a flatter power spectral distribution. The DA maps for the healthy case have stronger, high frequency components than the PD case. Generally the distribution of spectra in the PD case is wider, that means in time the spatial structure can vary more. However the PD spectra are strongly biased towards lower frequencies **Fig. 6.15**. That means the spatial structure of the PD case is made up of a few large physically large components, whereas the healthy case spectrum has a larger variety of sizes.

Does the power spectrum change during a reward burst? In the rising phase it becomes slightly shifted towards higher frequencies, in the healthy and PD simulations, but afterwards it returns quickly to its pre-burst shape (**Fig. 6.16** and **Fig. 6.17**). Indicating, that the reward burst does not change the structural makeup of the DA map strongly or in a lasting manner.

What do we take from this? Can we explain why the power spectra look as they do? The DA distribution in a healthy striatum is not the result of a gradual release of dopamine. It is the result of a constant bombardment with dopamine release events. The distribution has a fairly consistent structure, because the bombardment is being constantly kept up. The DA release replenishes the spectrum from the high frequency end. Then diffusion lets these high frequency components decay quickly and shifts them towards lower frequencies. That means the High frequency components in the healthy case are the result of continuing release. In the PD disease case the spectrum is shifted towards larger structures. That means that changes in the concentration of DA are more gradual in space. Since they correspond to lower spatial frequencies. The reason why the spectrum for the PD case is shifted to lower frequencies is largely because their is no continuing replenishment of the high frequency components. If DA gets releases it distributes much farther.

Knowing this we can also understand why the L-DOPA increases the DA concentration, but does not recover the spectrum of the healthy system. Even in the L-DOPA case the high frequency components are not constantly replenished like in the healthy case. Diffusion itself biases the system the system towards lower frequencies, even with a larger quantal size. For the beginning PD case, the spectrum is slightly biased towards smaller components, the reduced amount of release events (**Fig. 6.18**) means that the replenishment of the high frequency components is less effective.

6.1.6 Conclusions

The instantanteous DA distribution is highly variable and shows strong components at high spatial frequency that are replenished by continuing release events. When dopaminergic axons die during PD it has an effect on the distribution of DA in the striatum. However this effect is not, as naively expected, a plain decrease in the DA concentration. Rather, during baseline firing, the reduced total frequency of spiking leads to release events happening less frequently, which leads to a DA distribution that is a lot more homogeneous than in the healthy case.

It should also be noted that the Fourier analysis method shown here would

be well suited for comparing our simulation with experimental measurements of the instantaneous DA concentration as is now possible (Patriarchi et al., 2018), since the spectrum is not specific to a single realization. Spectra as shown in **Fig. 6.18** should be a fairly general feature for the same cases (healthy/PD).

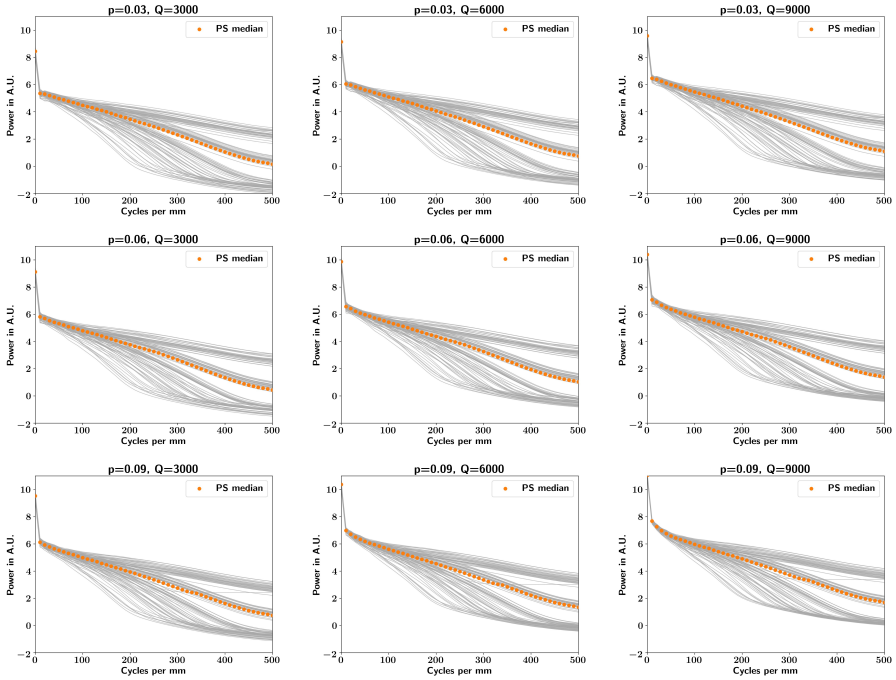

Figure 6.14: The quantal release size and the release probability of synaptic release have no qualitative effect on the power spectrum in the healthy case during baseline firing. Shown are the time spectra every $5ms$ for a second of baseline firing (grey lines) and the median power spectrum (orange) of all the instant spectra. This is shown for simulations with different quantal release sizes $Q = 3000;\ 6000;\ 9000;$ (from left to right) and different release probabilities $p = 0.03;\ 0.06;\ 0.09;$ from top to bottom. The spectra have high frequency components most of the time, half of the spectra show a strong component at the highest measurable frequency, replenished by the frequent spiking release. In the healthy case the DA distribution is very bumpy. The observed banding is probably due to the development of the spectrum in between timesteps.

6.2 DA Receptor Activation Maps

6.2.1 Simulations: Technical Considerations

We also ran simulations where we simulated the DA concentration and the DA receptors. Again we used the default parameters (see **Suppl. Table 1**). We run simulations for 3 different realizations, but will only show the results of one here since there were no qualitative differences. All results presented are with a resolution of $h = 1\mu m$ and a cube size of $100\mu m$, I ran a set larger simulations

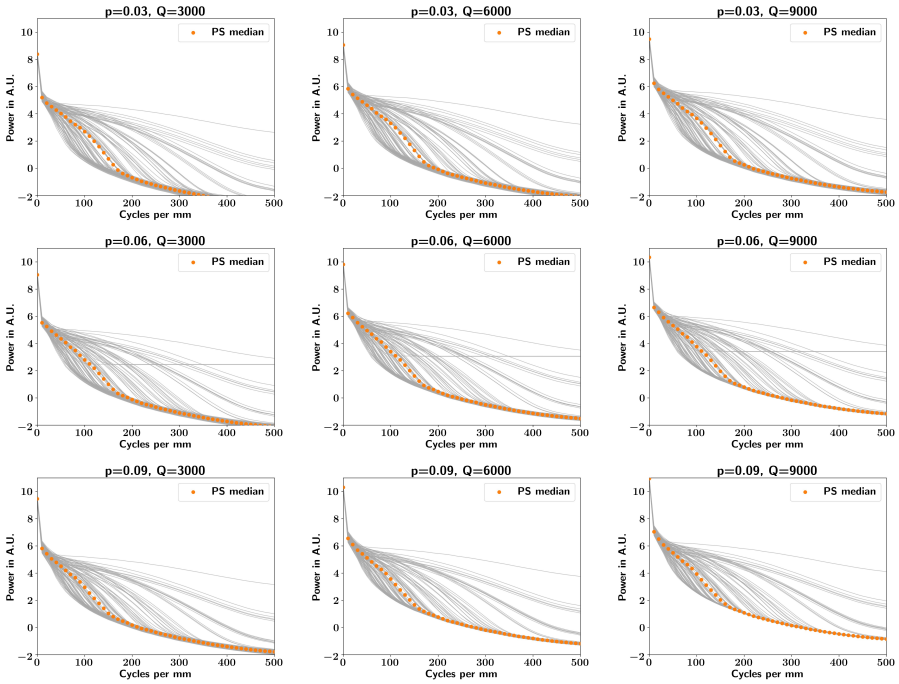

Figure 6.15: The quantal release size and the release probability of synaptic release have no qualitative effect on the power spectrum in the PD case during baseline firing. Shown are the time spectra every $5ms$ for a second of baseline firing (grey lines) and the median power spectrum (orange) of all the instant spectra. This is shown for simulations with different quantal release sizes $Q = 3000;\ 6000;\ 9000$; (from left to right) and different release probabilities $p = 0.03;\ 0.06;\ 0.09$; from top to bottom. Other than in the healthy case the spectra generally lack high frequency ($> 200 cycles/mm$) components since these high frequency components are not replenished by spiking, making the spectrum biased to larger structures, and therefore a more uniform DA map.

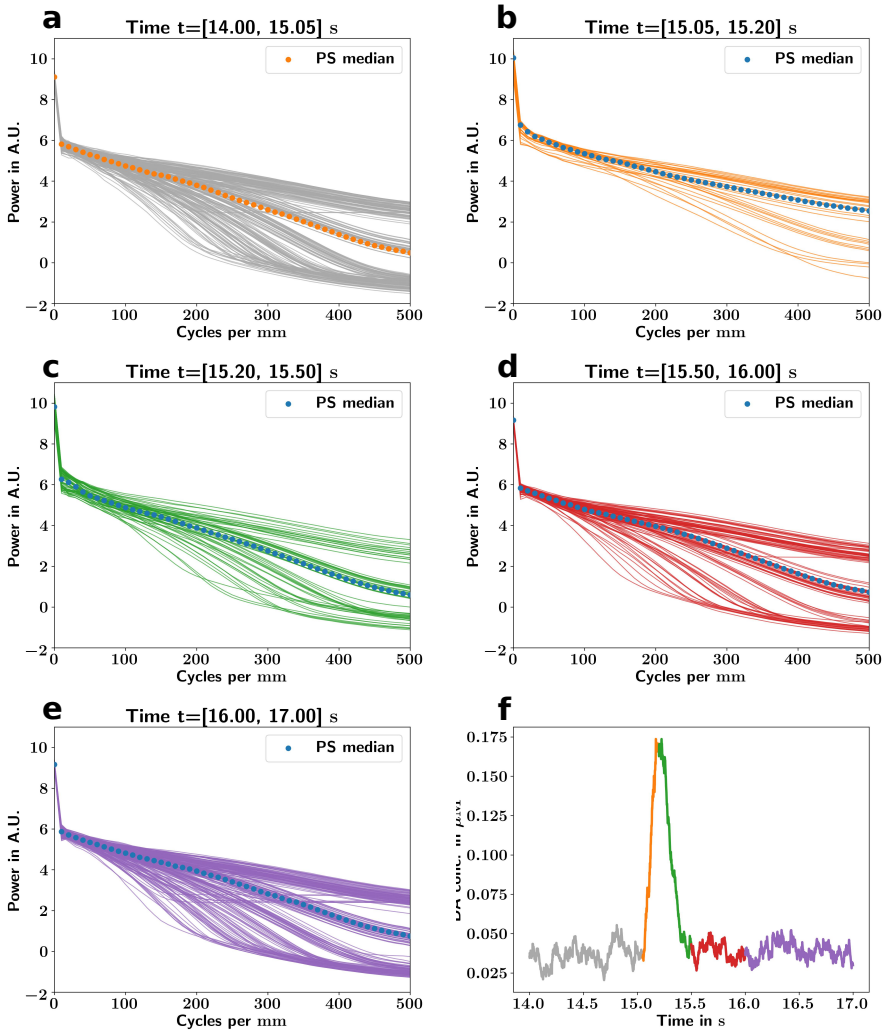

Figure 6.16: During the rewarding burst, in the healthy case, the power spectrum is biased towards smaller structures due to the increased number of spiking release events. Shown are the power spectra every 5 ms in the interval given above each panel, and the median power spectrum in this timeframe (a-e). The average DA concentration in the cube, color coded with the intervals shown in (a-e) is shown in (f). The power spectrum does not change majorly before the burst, or in the phase where the DA declines. During the burst the spectra shows stronger high frequencies components since, during the burst, they are replenished even faster than in during baseline firing.

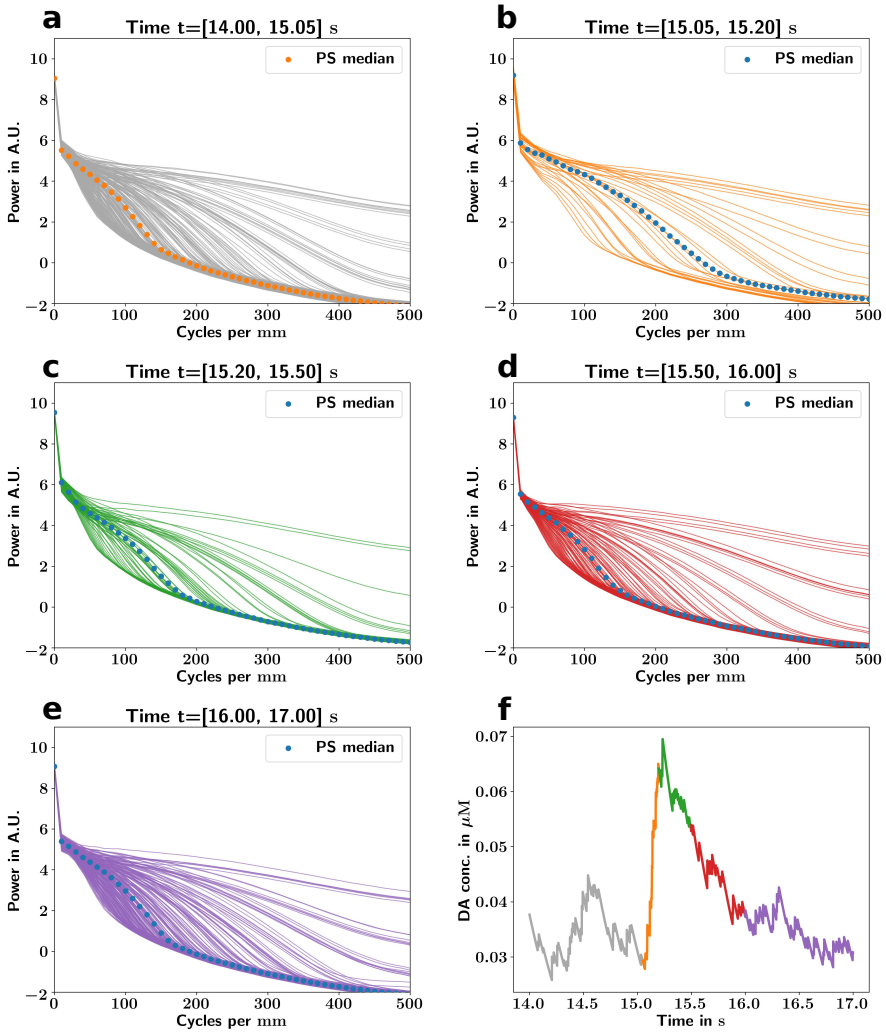

Figure 6.17: During the rewarding burst, in the PD case, the power spectrum shows an increase in high frequency components, however ultimately it does not gain any major high frequency components even during the reward burst. Shown are the power spectra every 5 ms in the interval given above each panel, and the median power spectrum in this timeframe (a-e). The average DA concentration in the cube, color coded with the intervals shown in (a-e) is shown in (f). The power spectrum does not change majorly before the burst, or in the phase where the DA declines. During the burst their is a slight increase in higher frequency components $\approx 250 cycles/mm$ but the DA distribution stays biased towards larger structures even during reward bursts.

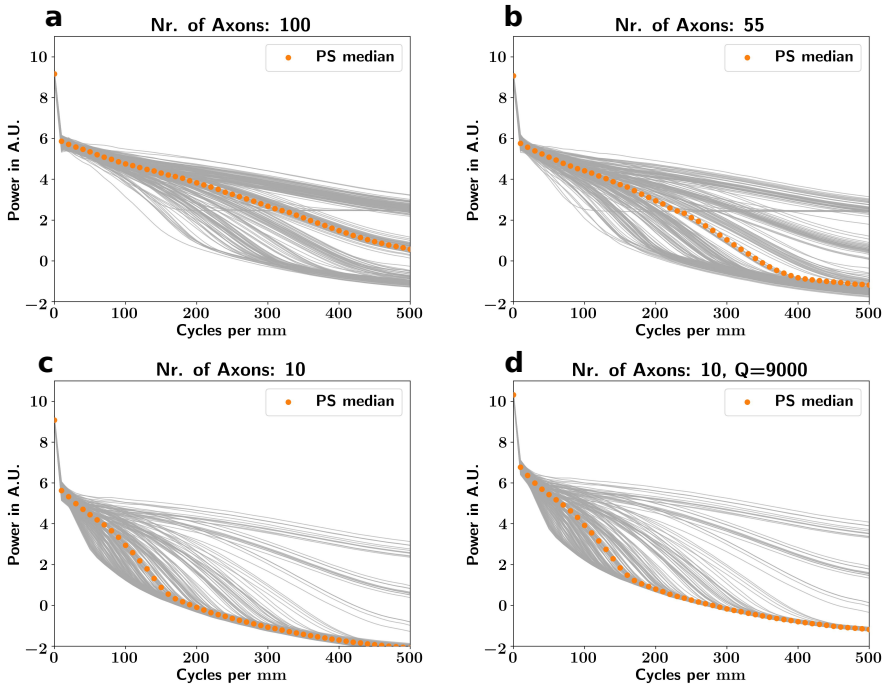

Figure 6.18: The spectrum during baseline firing shows extensive high frequency components in the healthy case (a), which start to be suppressed in early onset PD (b) and are gone in clinical PD (c). The applicaton of L-DOPA does not recover the structure of the DA map (d). Shown are the power spectra every $5ms$ in a 1s period of baseline firing (grey) and the median spectrum (orange).

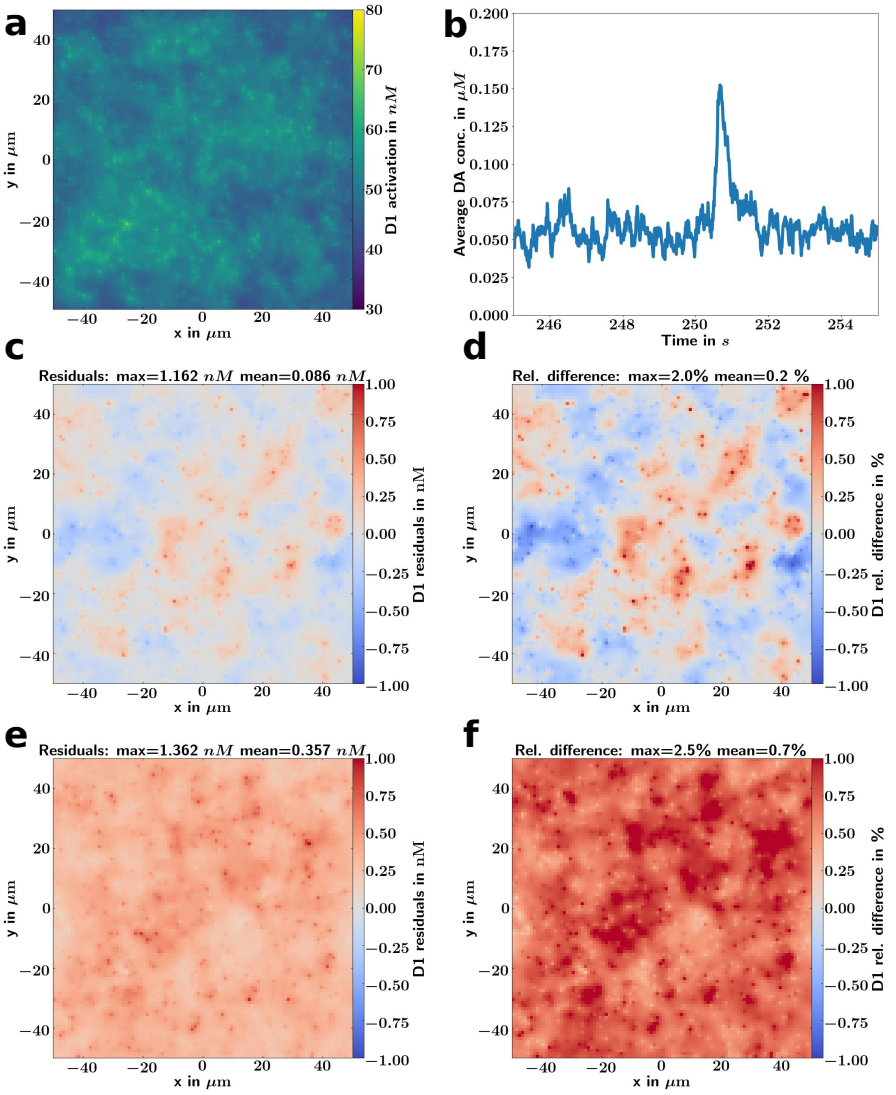

Figure 6.19: The D1 receptors react very slowly to the changes in DA because of their slow kinetics. Shown are the receptor activation map (a) and the cube average DA concentration (b). During the 10s leading up to the burst starting at 250s the absolute differences in the D1 map (c) and the relative differences (d) are quite small. The maximum difference 2%. The difference map between the D1 activation at 252s and 250s, before and after the reward burst, show a small but systematic increase in D1 activation, by up to 2.5%. Generally, even a DA burst changes the D1 activation map only slightly.

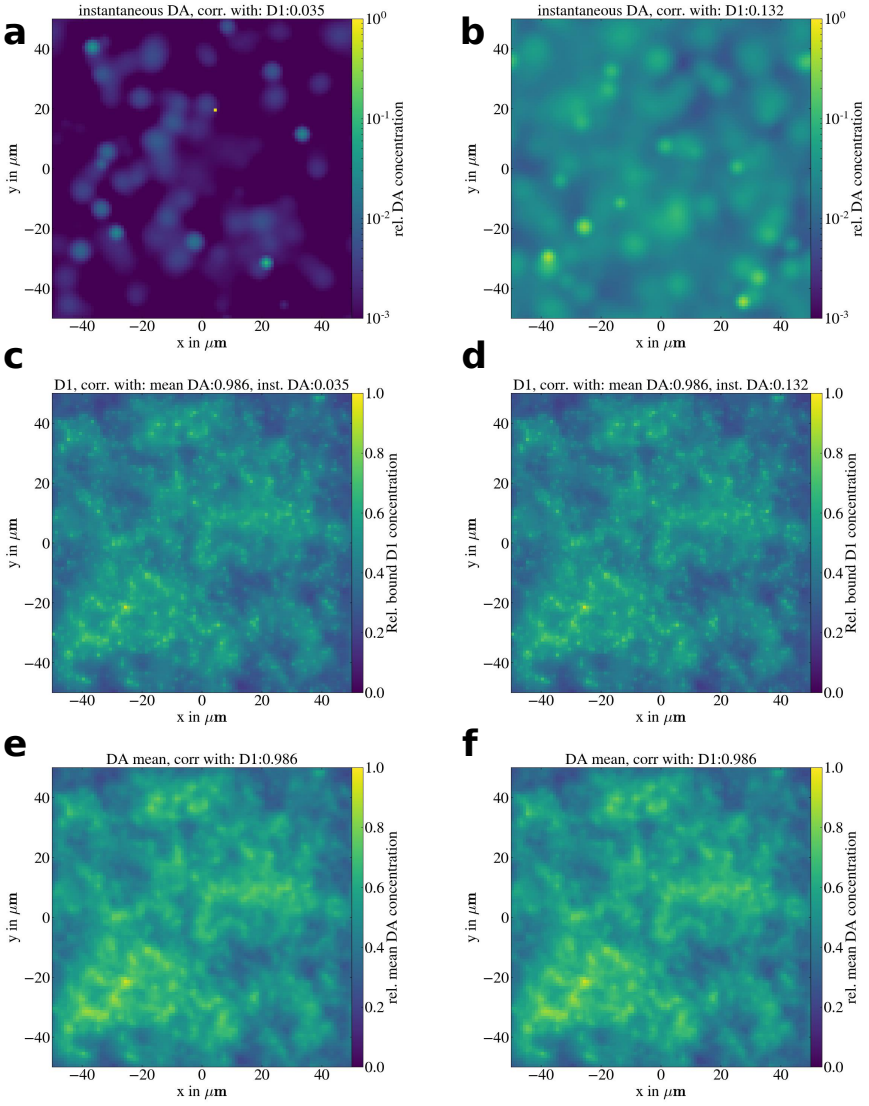

Figure 6.20: The instantaneous DA map is only weakly correlated with the D1 receptor activation map during baseline firing (a). In the rising phase of the burst $t = 250.5s$ the correlation is slightly elevated (b). However the the D1 receptor activation map before (c) and during (d) the reward burst is nearly perfectly correlated with the all-time mean DA concentration map of this simulation, before (e) and during (f) the burst. Due to the slow D1 receptors, the D1 activation maps only change very sluggishly, while the instantaneous DA map is highly variable. All values are normalized to the range $[0 : 1]$.

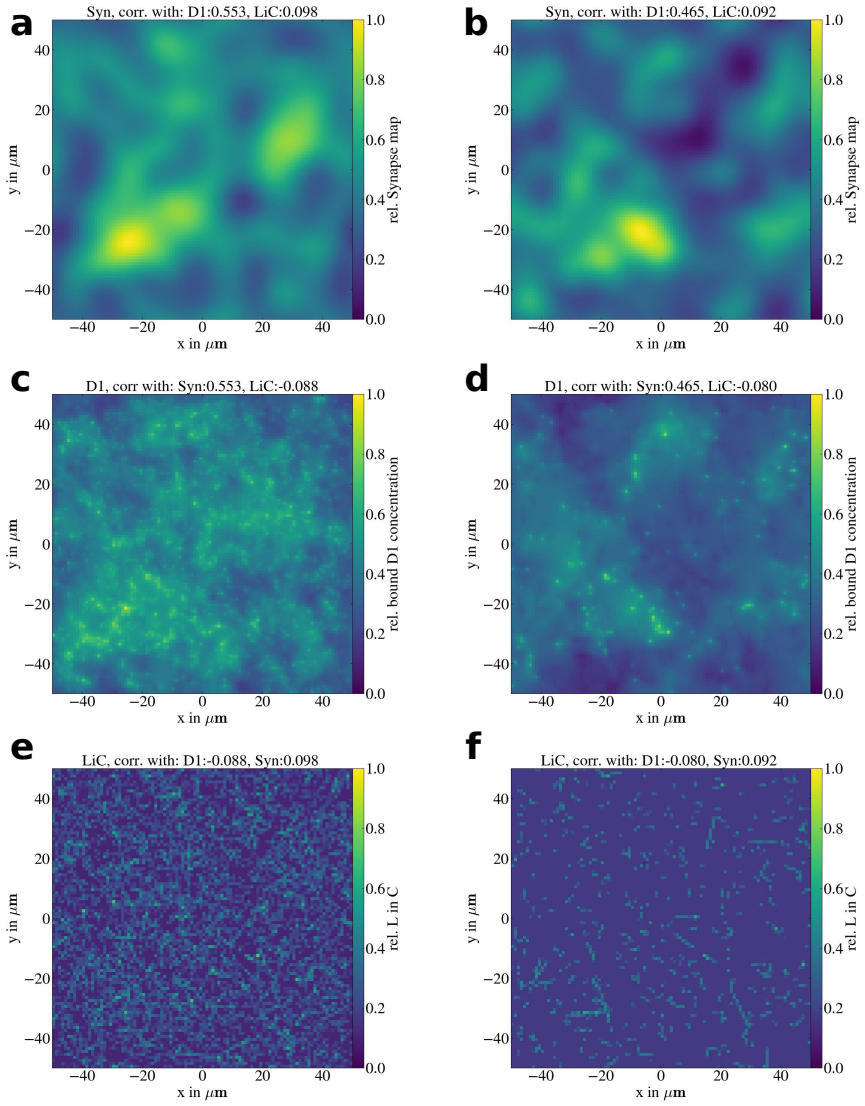

Figure 6.21: The D1 receptor activation is correlated with maps of that try to predict D1 activation from anatomical constraints. Independent if the D1 receptor activation is predicted in a healthy (left) system or a PD case (right). The predicted D1 activation maps derived from synaptic positions (a, b) are strongly correlated with the actual D1 activation maps (c,d). There is also a slight anti-correlation between the Length in voxel (LiC) maps (e,f), a proxy for the strength of inhomogenous uptake, and the D1 activation. More synapses in the vicinity of a given location lead to higher average DA concentration and therefore to higher D1 activation, causing the positive correlation between D1 and the synapse maps. Higher Length in voxel, means stronger uptake which in turn means lower average DA concentration at this location. This in turn leads to lower D1 activation, causing the anti-correlation between D1 and LiC.

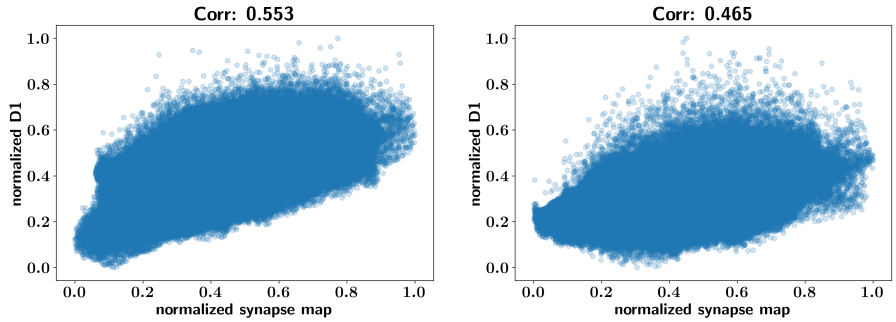

Figure 6.22: The predicted D1 activation maps derived from synaptic locations predict the D1 activation maps well, in the healthy (left) and PD (right) case. There is a linear relationship between the two quantities, shown in scatter plots here.

($h = 2\mu m$), however I did not get to analyzing them yet. The simulations have different simulated runtimes, depending on the chosen receptor kinetics. As mentioned in **Chapter 5** the receptors need at least a multiple of their half life times until they reach an equilibrium state with the surrounding DA concentration. In our simulations this is true for each voxel, since each voxel will have a slightly different DA environment. We can speed this process up by starting the receptors at a value close to the equilibrium of the average DA concentration. However, the receptors will still need some time to get into a state of local equilibrium. That means we have to simulate a swing-in period for each run. The duration of this swing in period will depend mainly on the half-life time of the receptors. For the measured receptor kinetics, as mentioned in **Chapter 5** the half-life time is $\approx 80s$. For our swing in we choose at least 3 half-life times. That means for the slowest receptors we have a swing in time of $240s$, simulated time. Afterwards we let the simulation run for another $60s$ and place a reward burst at $250s$, $260s$, and $270s$ of the total simulation time. Since the receptors develop slowly I only saved the state of the simulation every $10ms$. For the receptors with 10 times faster kinetics (here called $q = 10$ like in **Chapter 5**), I multiplied the on and off rate by $q = 10$ to keep the dissociation constant the same. These simulations require a shorter swing in time, since the receptors are faster. I ran the simulation for $60s$ where the first $40s$ was considered swing in time, I places a burst at $45s$, $50s$ and $55s$. For this simulation the results were also written out every $10ms$. The fast receptor simulations, 100 times faster than the measured values, had a runtime of $30s$ with bursts after $15s$ and $22s$. The simulations with $q = 1$ and $q = 10$ did run with the decoupled DA and receptor method. So there was no feedback of the receptor binding on the the DA distribution. A test with the $q = 1$ simulation showed that the differences were $< 0.01\%$ to the full system. We ran the full model for the $q = 100$ receptors. To get a feel for the impact of receptor binding and unbinding on the instantaneous DA map. The effect is around an order of magnitude weaker than the effect that incorporating non-homogenous uptake has on the DA concentration **Fig. 6.23** (compare to **Fig. 4.15**). In the simulation the maximum error, when comparing the DA concentration with and

without the influence of receptor binding, is below 15% with a mean error of 2%. From that we conclude that even for quite fast receptors, the DA concentration distribution is only weakly effected by the receptor binding and unbinding. It is definitely viable to run the slow receptor simulations, without feedback of receptors on the DA maps.

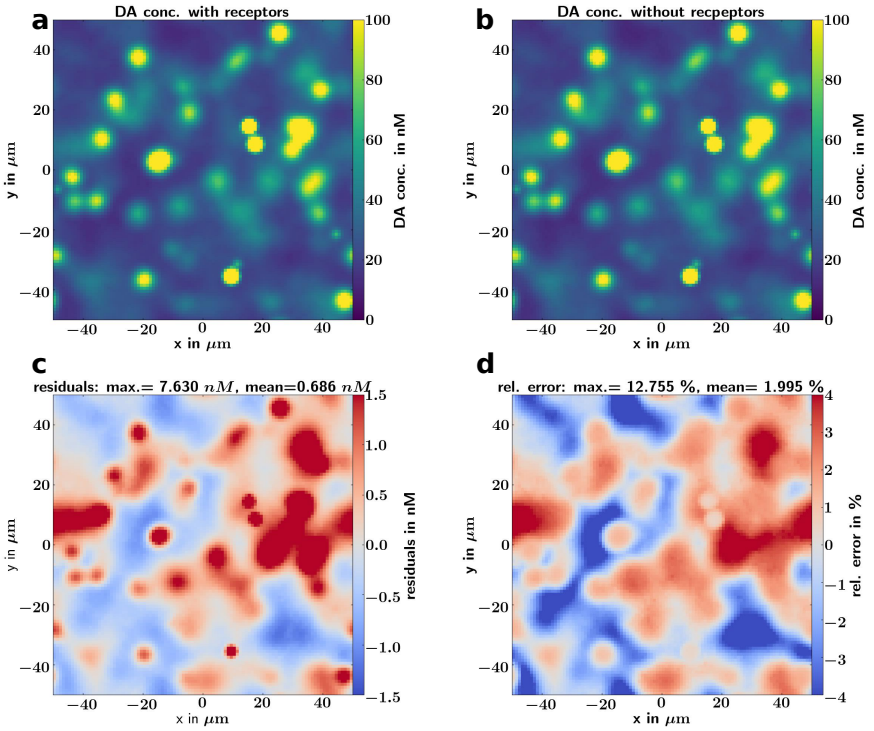

Figure 6.23: The instantaneous DA concentration maps with (a) and without (b) the feedback on the DA due to receptor binding, for receptors that are 100 times faster than default, are fairly similar as shown by the absolute difference map (c) and the relative error map (d) between them. The average error is around 2%, making the receptor feedback, even for $q = 100$ receptors, roughly one order of magnitude less important than the consideration of inhomogeneous uptake. It is a valid course of action to not consider this feedback to save computational time.

Each simulation was run for the healthy system with 100 axons and the PD case with 10 axons. The runtime of these simulations was around $14 days$ for the $q = 1$ case, 3 days for the $q = 10$ case, and $9 days$ for the $q = 100$ case. Where the $q = 1$ case was time-intensive because of the long swing in time, while the $q = 100$ case was time-intensive because the full solver is slower.

6.2.2 Receptor Activation Maps are Correlated with Anatomical Features

The D1 and D2 receptor activation maps are highly correlated in space. Which is not surprising, since in the model they have the same off rate k_{off}. That means that they only differ by a linear scaling factor, as long as none of the two populations are close to saturation. Their correlation coefficient over 20 seconds with two bursts ($245s$ to $265s$) in run-1 for the healthy case was $\rho = 0.9930 \pm 7.7 \cdot 10^{-5}$ and in the PD case $\rho = 0.9935 \pm 2.4 \cdot 10^{-4}$. They are nearly perfectly correlated. For this reason I will only analyze the D1 receptor activation maps in this chapter, since all the finding are also applicable to the D2 receptor activation maps.

In **Chapter 5** we already talked about how the kinetics of the D1 receptors are slow. This remains true even in the case of a constantly changing DA map, with a lot of high frequency components. The DA receptors are very sluggish, and integrate the faster components very slowly. That means the receptor map is very stable in time, **Fig. 6.20** and changes only slowly. Over $10s$ of baseline firing, its maximum change is $\approx 2\%$. During a burst the maximum increase of the receptor activation is $\approx 2.5\%$ while on average the change in a single voxel is closer to 1%. Even though the DA map is highly dynamic, and very variable, the receptors are not. However, the receptor activation map is not flat. There is spatial structure visible that is retained even throughout bursting.

What determines this structure? Is it random, or is it caused by a feature of the DA landscape? The instantaneous DA concentration maps is only weakly correlated with the D1 activation map ($\rho = 0.090 \pm 0.053$ measured over $10s$), however it is nearly perfectly correlated with the running mean DA concentration map $\rho = 0.986$ **Fig. 6.20**. I did not calculate statistics for the mean DA correlation, however the mean DA concentration does barely change with time, and since D1 is also very sluggish they both stay correlated. Why this strong correlation to the time-averaged DA map? The reason is most likely the slowness of the receptors. It is most likely not correlated to the all-time average of the DA map, but to a weighted average over a time-frame of a few half-life times into the past. Since the receptor half life time for the $q = 1$ case is $\approx 80s$ this is likely to be very similar to the all time average for this simulation, since even an activation from the beginning of the simulation $t = 0$ would have only decayed to 12.5% of its starting magnitude at $t = 240s$.

Now we can ask another question, what determines the the values of the time-averaged DA maps? The instantaneous DA map is created by spiking release events, the location of these spiking release events may seem random however, we know that synapses do not change position. Some locations will have a higher average DA-concentration, just because they are closer to more synaptic release sites. However, there is another process that shapes the time-averaged DA map, inhomogeneous uptake.

To investigate if the synaptic placement can be used to predict the receptor activation maps we calculate a predicted DA concentration map from the placement of synapses. We know the placement of synapses in each simulation, however the placement itself is unlikely to be a good descriptor of the mean DA concentration, since most voxels do not have any synapses in them. However, a synapse does not just exert its influence on the voxel it is in buthas a sphere of influence since DA release events spread over a certain distance. What we

want to do is to calculate a predicted receptor activation map from the synapse locations. We do this by placing a kernel, a function that describes the relative importance of a synapse with respect to the distance to this synapse, over each synapse. What is the range and shape of this kernel? To describe the range for the kernel we use the range parameter c, which might have different meaning depending on the kernel. We tried a few, kernel functions but settled on a Gaussian kernel

$$K(r) = e^{\frac{r^2}{2c^2}} \tag{6.1}$$

with a range parameter of $c = 5\mu m$ in the end, since it showed slightly better performance than other kernels. However trying out different kernels showed that the kernel function itself is not too important. We found a strong degree of correlation > 0.4 between the predicted map and the receptor activation for linear maps, where the relative importance declines linearly from $K(0) = 1$ to $K(c) = 0$ and even for flat Kernels

$$K(r) = 1 \rightarrow (r < c);\ 0 \rightarrow (r > c)$$

that essentially count the amount of synapses in a radius c around a voxel. The range parameter itself proofed to be of higher importance. Kernels generally perform well when their sphere of influence has a radius between $5\mu m$ and $15\mu m$, which fits well with the distance that a release event covers **Fig. 6.4**. We also try to see if the map of the length of axon in a (computing) cell (LiC), is correlated with the receptor activation maps. Since it is directly related to the inhomogeneous uptake.

The synaptic maps are highly correlated with the D1 receptor activation maps. The gaussian kernel with range parameter $c = 5$, which gives it a full width at half maximum of $\approx 11\mu m$ has a correlation coefficient of $\rho = 0.553$ **Fig. 6.21**. The synapse map of the flat kernel with range $c = 10$ was also strongly correlated $\rho = 0.485$, as was the linear kernel map with the same range $\rho = 0.536$. We also find a weak anti-correlation between the D1 activation map and the axonal LiC $\rho = -0.088$. That means that the receptor activation maps are highly correlated with the predictive synaptic maps. they are also weakly anti-correlated with the Length of axon in a voxel, which a proxy for the uptake at a given location. There is a strong linear dependency between the D1 receptor maps predicted from the synapse positions and the actual receptor activation maps **Fig. 6.22**. This holds true in the healthy and the PD case, that means that the death of axons does not change the relationship between the synaptic positioning and the receptor activation maps.

So how does this correlation between the synaptic maps and the D1 receptors come to be? Are the synaptic maps correlated with the instantaneous DA concentration? They are, but only slightly **Fig. 6.24**. This is not too surprising since the synaptic maps are not changing in time while the DA maps are highly variable. However, generally the DA concentration is very slightly positively correlated with the synaptic maps in the healthy $\rho = 0.048 \pm 0.040$ and in the PD case $\rho = 0.056 \pm 0.1052$. That means that locations that have a higher influences of synapses get a slightly higher DA concentration than locations with lower influences. These slight influences, can be picked up by the D1 receptors since they integrate over a fairly long time, therefore becoming more

correlated to the synaptic maps. Due to their long integration times the slow D1 receptors are very good sensors for small differences in the average concentration of DA. So even though the Synaptic maps are only very weakly correlated with the instantaneous DA concentration, it is enough to be picked up by the D1 receptors. The same holds true for the slight anti-correlation of the length in voxel with the instantaneous DA concentration **Fig. 6.24** ($\rho = -0.010 \pm 0.010$ for the healthy and $\rho = -0.030 \pm 0.031$). Here the slightly reduced DA concentration also gets picked up by the slowly integrating receptors. That means that anatomical properties are reflected in the activation maps of D1 receptors.

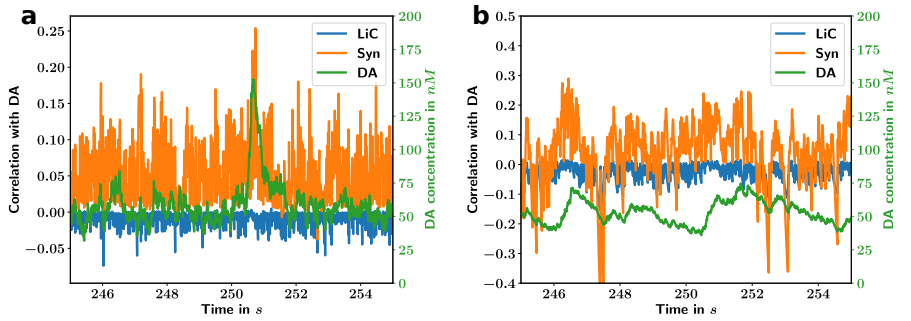

Figure 6.24: The synaptic maps are only weakly correlated with the instantaneous DA concentration (orange). The correlation is weak but fairly consistent in the healthy (left) and PD (right) case. The consistent positive correlation can be integrated by the slow receptors very effectively, leading to the correlation between the synapse map and the D1 activation. In the same vane, the LiC maps are very weakly anti-correlated (blue) with the instantaneous DA concentration, the time integration of the receptors leads to a stronger correlation between LiC and the D1 activation. For comparison the instantaneous DA concentration (green) is also plotted.

Does this only work for slow receptors? No, the correlation with the synaptic and LiC maps persist even for receptor kinetics up to 100 times faster than the measured values **Fig. 6.25**. The correlation stays high for all tested receptor kinetics in a 10 second window **Fig. 6.26**. There is not a lot of dynamic in the $q = 1$ case, so the correlation with the synapse maps is very stable $\rho = 0.553 \pm 0.0008$ The D1 activation is more variable for the faster receptors. The average correlation stays nearly the same for the $q = 10$ receptors ($\rho = 0.551 \pm 0.0060$) and stays elevated even for the $q = 100$ receptors ($\rho = 0.328 \pm 0.0163$ in the 10 second window shown). Furthermore, the anti-correlation with the LiC map also persists for different receptor kinetics, but also stays weaker than the correlation with the synaptic map with $\rho = -0.0880 \pm 0.0002$ in the $q = 1$ case, $\rho = -0.0802 \pm 0.0016$ in the $q = 10$ case and $\rho = -0.0861 \pm 0.0046$ in the $q = 100$ case.

How can this be if the receptors are correlated with the synaptic maps due to their long integration time? It seems, the integration time does not have to be extensively long, for the receptors to pick up on the differences in the average DA concentration map. The slow receptors have a half-life time of $t_{1/2} = 80s$ so

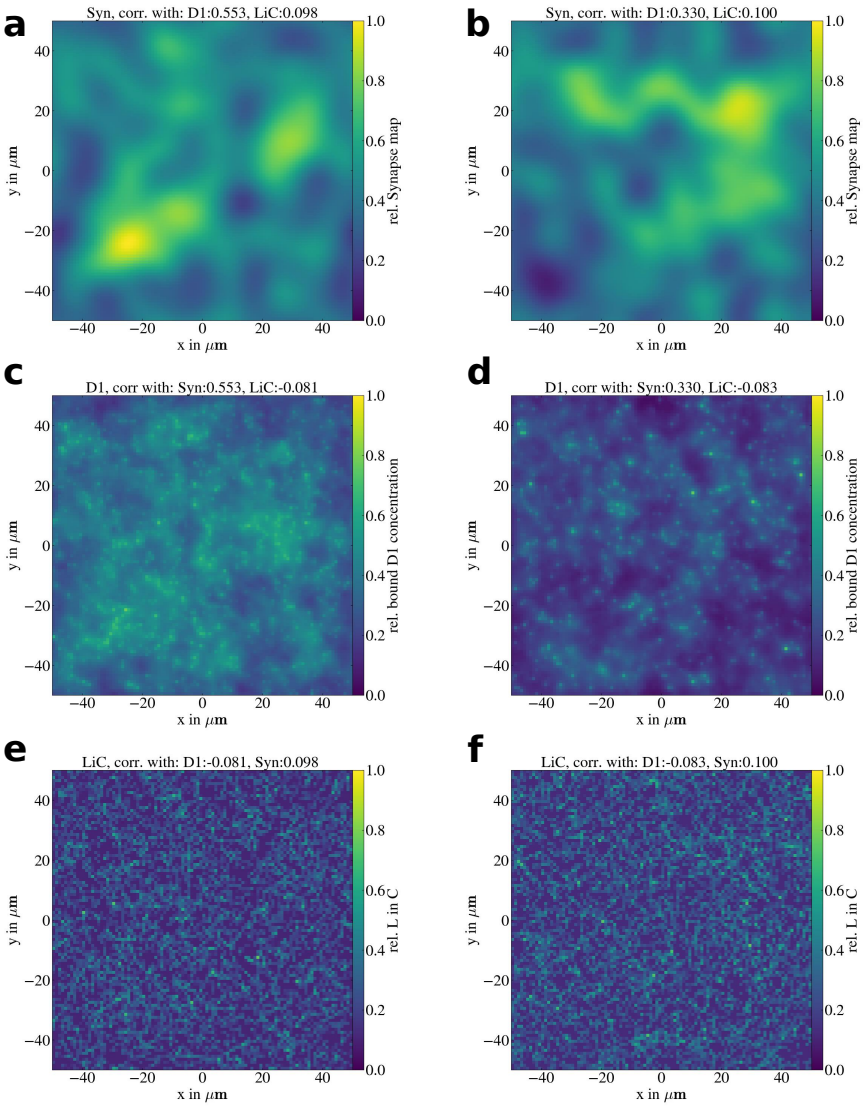

Figure 6.25: The synaptic maps (a,b) still correlate strongly with the D1 maps (c,d), even for 10 times (left) and 100 times (right) faster receptors than in the base model. The correlation of the D1 maps with the LiC maps (e,f) also remains for faster receptors.

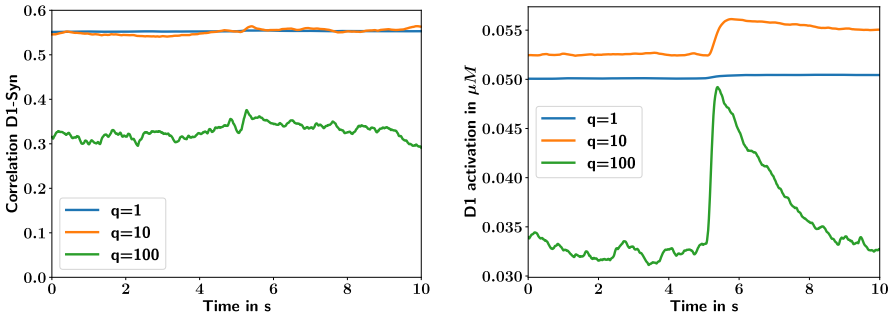

Figure 6.26: The correlation between the synase maps and the D1 activation maps is consistently high, even for receptors q times faster than the default receptors (left). The average amount of D1 activation is less variable for slower receptors. The $q = 10$ and $q = 100$ simulations had an elevated baseline DA, and therefore higher D1 activation. However, even though the D1 activation is more variable for $q = 100$ receptors, they still show a considerable correlation with the synaptic maps.

a signal $240s$ ago still contributes with 12.5% of its value. The integration has a span in time of a least $3t_{1/2}$. However, systematic differences in the average concentration, as caused by the synaptic maps, can already show up for a lot shorter integration times. For receptors with $q = 10$ times faster kinetics, the integration still happens over a timeframe of $\approx 24s$. Which leads to nearly the same correlation to the synaptic map then the $q = 1$ receptor **Fig. 6.25**, and **Fig. 6.26**. Even for the $q = 100$ receptors, that integrate over only $\approx 2.5s$, the correlation with the synaptic map persists. Does this make sense? When we think of of the axonal spiking we know that the average firing rate of the dopaminergic neurons is $4Hz$. That means in the $2.5s$ integration time, each axon will fire around $10spikes$. With a releae probability of $p = 0.06$ that means that each axon fires around $1 - (0.94^{10} \approx 50\%)$ of its synapses at least once. So it is not completely unreasonable that the synapti map can have an imprint on the average DA concentration when integrating over this timeframe. However, the correlation for the faster receptors is lower than for the $q - 1;\ 10;$ receptors. Indicating that this effect will vanish for even faster receptors.

In the end we find that the anatomy, synapses and LiC, can lead to a total correlation with the D1 receptors of up to $\rho = 0.6$ for relatively slow receptors up to $q = 10$, and still correlate with $\rho = 0.4$ to the receptor activation maps of fast receptors. Anatomical properties have a non-negligible influence on the D1 receptor activation maps, even if the D1 receptors are up to 100 times faster than measured.

6.2.3 Conclusion

After analyzing our simulations we are left with two main findings. First, the spatiotemporal DA distribution is highly variable. The DA landscape in space is very inhomogeneous and characterized by the constant bombardment with

release events. Accordingly single location timelines of the DA concentration are also highly variable. However, that changes during PD. The reduction in release events leads to a much flatter, more homogeneous distribution of DA in space, but also for the single location timelines. These very different DA distribution maps during the healthy and PD case are also reflected in the spatial Fourier transforms, where the PD simulations lack the high spatial frequency components of the healthy case.

Second, The DA receptor activation maps are strongly correlated with anatomical factors. Mainly the distribution of synaptic locations, but also the distribution of the inhomogenous uptake. This correlation is caused by the receptors integrating the small systematic DA differences caused by these anatomical factors. However, that does not only work for very slow receptor kinetics, but also for receptor kinetics that are 100 times faster than the measured values. In other words, the receptors do not need to integrate for a very long time to pick up the small systematic differences in the mean DA concentration caused by the anatomical structures. An integration time of $\approx 3s$ is already enough.

Chapter 7

Discussion

I developed a model for DA diffusion in the striatum that is essentially made up of two parts, a solver for the reaction diffusion equations and a generator for synthetic dopaminergic axons. The full model can be found on `https://bitbucket.org/Narur/dope-amine`, in the hope that it can be used by others too. In the course of the development of the diffusion model I also designed a DA receptor activation model that incorporates the slow receptor kinetics of the DA receptors, instead of letting them be infinitely fast.

7.1 Significance of Findings

There has been a 3D diffusion model of DA in the striatum before (Dreyer et al., 2010; Dreyer and Hounsgaard, 2013; Dreyer et al., 2016) however it used a smaller domain $\approx 20\mu m$ and did not explicitly study the tempo-spatial structure of the DA distribution. It incorporates a model of receptor binding, however it uses the instant kinetics model, which makes it quite different from my model.

We designed the model to investigate if the DA signal is monolithic in space. The model predicts that the DA distribution is highly variably in both space and time, differing strongly from the view of commonly used models e.g. for reinforcement learning that essentially implicitly assume that the DA concentration is a flat monolithic signal in the striatum (e.g. Schultz 2007). I show, with the help of Fourier transformations, that the source of this highly variable DA signal is the constant spiking release from the dopaminergic axons. Diffusion does not smooth out these DA maps. Furthermore my model predicts that in the case of PD the spatial DA distribution becomes more homogenous since the quantal release events that make the DA maps very variable become rarer, so that diffusion has the chance to flatten out the map. The treatment with Levodopa does not recover the variability of the healthy DA maps. As predicted by Dreyer (2014) my model also shows passive stabilization in the PD case, the average DA concentration does not reduce during the baseline firing indicating that a reduced DA baseline is not the reason for the motor symptoms of PD. However, the spatio temporal structure of the DA signal changes in the PD case, which could be the starting point for further investigations into how these motor symptoms arise.

A way to experimentally test these predictions of spatially variable DA maps would be to compare the spectra of the model DA maps, with the spectra of measured DA maps with the recently developed method of Patriarchi et al. (2018) and Sun et al. (2018).

When investigating the receptor activation maps, my model differs considerably from the model presented in (Dreyer et al., 2010). This is due to the fact that the receptors in my model have relatively slow kinetics, where in the dreyer model the react essentially instant to changes in DA concentration. An exciting finding of the model is that the calculated receptor activation maps have a spatial structure that are strongly correlated with anatomical factors like synaptic positions and the inhomogenous uptake map, which means that the receptor activation maps have a component that is quite stable in time, since the anatomical factors should not change. This remains true even if the receptors are simulated with kinetics up to 100 times faster than the measured values. This finding is interesting in the light of the identification of spatially compact neuronal clusters, that are stable for days, in the striatum (Barbera et al., 2016). Of course that does not mean that these clusters are necesarrily formed by a mechanism related to spatially varying DA receptor activation. There are models predicting clustering independent of a spatially varying DA receptor map (Humphries et al., 2009). Nevertheless this finding presents a new approach for the formation of these clusters, that might even work in tandem with other clustering approaches.

The model shows that the instantaneous DA concentration does not change qualitatively when incorporating inhomogenous DA uptake. However there are quantitative changes with a mean difference of around 10 % of the instantaneous DA concentration. With the knowledge that the DA receptors, even if they are fairly fast, can and do pick up small changes in the DA concentration I think that inhomogenous uptake should be taken into account for simulations looking at the activation of DA receptors.

The model demonstrated that there is a spatial structure for both the DA and the DA activation maps. Both don't behave as the monolithic signal, independent of spatial location, that is often used for models of learning and motor control. The DA maps themselves are highly variable in space and time, however this variability is smoothed out by the slow kinetics of the dopamine receptors. What these spatial inhomogenities mean for the models of learning and motor control still has to be addressed. However the model presented here could be used as a starting point for these questions. A possible next step to address the effects of the spatial structure of the DA signal would be to combine a spatially resolved neural network simulation of MSNs with our model and directly investigate the effects of the spatiotemporal inhomogenities of DA on the network.

Investigating the spatial structure of the DA signal was not the only goal of my model. I was also trying to test if there are inconsistencies in the understanding of DA signaling. One inconsistency revealed itself when I incorporated the DA receptor activation into the model of DA diffusion. Specifically when I incorporated receptor kinetics for the DA receptors.

I found that when taking into account the kinetics of the DA receptors, which are quite slow, the commonly assumed separation of receptor types for different

temporal DA signals, D1 receptors detect fast high amplitude signals while D2 receptors detect slow small amplitude signals (Dreyer et al., 2010; Surmeier et al., 2007; Grace et al., 2007; Schultz, 2007; Frank and O'Reilly, 2006), breaks down. Hinting that our understanding of the processing of different temporal components of the DA signal is lacking. I showed that even for receptors that have kinetics up to 100 times faster than the measured kinetics the separation of DA signal-type and receptor type does not hold true. It is true that our findings are based on a limited number of, fairly old, experiments (Burt et al., 1976; Sano et al., 1979; Maeno, 1982; Richfield et al., 1989). However the instant kinetics, model essentially argues with no experimental backing and has also never been formally stated, instead it is the result of an implicit assumption. This assumption being that the dissociation constant describes the fractional occupation of the dopamine receptors well. Some recent experiments, using genetically altered DA receptors, cast doubt if the DA receptors are really as slow as assumed in our model (Patriarchi et al., 2018; Sun et al., 2018). However, the kinetics of these genetically modified receptors are unlikely to be the same as a wildtype receptor, since their dissociation constants differ from the wildtype receptor by a factor of ten or more. That means that their kinetics are at least by a factor of $\sqrt{10} \approx 3$ different (assuming, that the on rate is faster and the off rate is slower by the same factor). On top of that the kinetics measured in Sun et al. (2018) still fall within the factor 100 range for which our model predicts a similar response for D1 and D2 receptors independent of the timescale of the signal. Furthermore, it is unlikely that the DA receptors are much faster than 100 times their measured value, since then the would have reaction rates in excess of the estimate for the theoretical maximum for enzymes that are embedded in a membrane (Alberty and Hammes, 1958; Eigen and Hammes, 1963).

Another point to consider with respect to this receptor kinetics dilemma is that, according to our diffusion model, the single location DA concentration time-signal is highly variable even in the baseline firing case. It is unlikely that the strong spike-like increases in DA concentration, in these time signals contain useful information, since the spiking release at the dopaminergic synapses is a stochastic process. That means that the delivery of one spikelike increase, caused by a release event, can not be controlled very precisely by the dopaminergic axon firing the spikes. This is exasperated by the low probability of release on an arriving action potential ($p = 0.06$). In other words, this means that the single-location DA time-signal is very noisy. If the DA receptors are very fast, to the point where the react nearly instantaneous, they would track all of this noise, which would need to be removed by some other process later. It is unlikely that this noise can be removed by spatial averaging, since the spatially averaged DA concentration timeline is still quite noisy **Fig. 6.1**. However, slower receptor kinetics could act as a low-pass filter, removing some of this noise already at the receptor activation stage. Therefore I would argue that it is unlikely that the receptors are nearly instantaneous.

Of course the final goal is to strengthen or dismiss this reasoning with a better estimate of these kinetic parameters. There seems to be a large body of work on the intracellular cascade started by the DA receptors(Lindskog et al., 2006; Nair et al., 2015). However, the beginning step, the kinetics of the binding and unbinding of the DA receptors to DA is not well constrained by experiments. I hope that my work can motivate new measurements of these kinetics to better

constrain the model of DA receptor binding.

7.2 Outlook

The developed model is freely available and will hopefully be used by other researchers to investigate DA and its receptors and their spatiotemporal distribution. There are still exciting avenues of research to be done with the model.

Currently the model is still quite simple, and some straightforward extensions could be incorporated e.g. feedback of D2 autoreceptors on spiking release.

As mentioned above combining the DA diffusion model with neural network models directly could give a better understanding on how the spatiotemporal inhomogenities of the DA distribution influence learning and motor control. Such a combined model would also be useful to follow up on the spatially clustered striatal neurons. Investigating pharmacological manipulations, or the effect of different spiketrain types on the spatiotemporal structure of DA and its receptors are also exciting options for future research. which could be combined with a combined DA diffusion neural network model.

Bibliography

Yves Adam. Highly accurate compact implicit methods and boundary conditions. *Journal of Computational Physics*, 24(1):10–22, 1977.

Robert A Alberty and Gordon G Hammes. Application of the theory of diffusion-controlled reactions to enzyme kinetics. *The Journal of Physical Chemistry*, 62(2):154–159, 1958.

Roger L Albin, Anne B Young, and John B Penney. The functional anatomy of basal ganglia disorders. *Trends in neurosciences*, 12(10):366–375, 1989.

E. Anderson, Z. Bai, C. Bischof, S. Blackford, J. Demmel, J. Dongarra, J. Du Croz, A. Greenbaum, S. Hammarling, A. McKenney, and D. Sorensen. *LAPACK Users' Guide*. Society for Industrial and Applied Mathematics, Philadelphia, PA, third edition, 1999. ISBN 0-89871-447-8 (paperback).

Bengt Andersson, Ronnie Andersson, Love Håkansson, Mikael Mortensen, Rahman Sudiyo, and Berend Van Wachem. *Computational fluid dynamics for engineers*. Cambridge University Press, 2011.

Gordon W Arbuthnott and Jeff Wickens. Space, time and dopamine. *Trends in neurosciences*, 30(2):62–69, 2007.

Christopher W Atcherley, Kevin M Wood, Kate L Parent, Parastoo Hashemi, and Michael L Heien. The coaction of tonic and phasic dopamine dynamics. *Chemical Communications*, 51(12):2235–2238, 2015.

George A Baker, George A Baker Jr, GEORGE A BAKER JR, Peter Graves-Morris, and Susan S Baker. *Padé approximants*, volume 59. Cambridge University Press, 1996.

M Banay-Schwartz, A Kenessey, T DeGuzman, A Lajtha, and M Palkovits. Protein content of various regions of rat brain and adult and aging human brain. *Age*, 15(2):51–54, 1992.

Giovanni Barbera, Bo Liang, Lifeng Zhang, Charles R Gerfen, Eugenio Culurciello, Rong Chen, Yun Li, and Da-Ting Lin. Spatially compact neural clusters in the dorsal striatum encode locomotion relevant information. *Neuron*, 92 (1):202–213, 2016.

Brigitte Berger and Jacques Glowinski. Dopamine uptake in serotoninergic terminals in vitro: a valuable tool for the histochemical differentiation of catecholaminergic and serotoninergic terminals in rat cerebral structures. *Brain research*, 147(1):29–45, 1978.

Brian P Bergstrom and Paul A Garris. 'passive stabilization'of striatal extracellular dopamine across the lesion spectrum encompassing the presymptomatic phase of parkinson's disease: a voltammetric study in the 6-ohda-lesioned rat. *Journal of neurochemistry*, 87(5):1224–1236, 2003.

Joshua D Berke. What does dopamine mean? *Nature neuroscience*, page 1, 2018.

Joshua D Berke and Steven E Hyman. Addiction, dopamine, and the molecular mechanisms of memory. *neuron*, 25(3):515–532, 2000.

Kent C Berridge. The debate over dopamine's role in reward: the case for incentive salience. *Psychopharmacology*, 191(3):391–431, 2007.

Kent C Berridge and Terry E Robinson. What is the role of dopamine in reward: hedonic impact, reward learning, or incentive salience? *Brain research reviews*, 28(3):309–369, 1998.

Tom Binzegger, Rodney J Douglas, and Kevan AC Martin. Axons in cat visual cortex are topologically self-similar. *Cerebral cortex*, 15(2):152–165, 2004.

Anders Björklund and Stephen B Dunnett. Dopamine neuron systems in the brain: an update. *Trends in neurosciences*, 30(5):194–202, 2007.

Laura M Borland, Guoyue Shi, Hua Yang, and Adrian C Michael. Voltammetric study of extracellular dopamine near microdialysis probes acutely implanted in the striatum of the anesthetized rat. *Journal of neuroscience methods*, 146 (2):149–158, 2005.

Gerardine G Botte, James A Ritter, and Ralph E White. Comparison of finite difference and control volume methods for solving differential equations. *Computers & Chemical Engineering*, 24(12):2633–2654, 2000.

I Bronstein et al. Handbook of mathematics. springer, 2004.

David R Burt, Ian Creese, and Solomon H Snyder. Properties of [3h] haloperidol and [3h] dopamine binding associated with dopamine receptors in calf brain membranes. *Molecular pharmacology*, 12(5):800–812, 1976.

Paolo Calabresi, Barbara Picconi, Alessandro Tozzi, Veronica Ghiglieri, and Massimiliano Di Filippo. Direct and indirect pathways of basal ganglia: a critical reappraisal. *Nature neuroscience*, 17(8):1022, 2014.

E Castaneda, Ian Q Whishaw, and Terry E Robinson. Changes in striatal dopamine neurotransmission assessed with microdialysis following recovery from a bilateral 6-ohda lesion: variation as a function of lesion size. *Journal of Neuroscience*, 10(6):1847–1854, 1990.

Diego Centonze, Barbara Picconi, Paolo Gubellini, Giorgio Bernardi, and Paolo Calabresi. Dopaminergic control of synaptic plasticity in the dorsal striatum. *European journal of neuroscience*, 13(6):1071–1077, 2001.

MJ Chang, LC Chow, and WS Chang. Improved alternating-direction implicit method for solving transient three-dimensional heat diffusion problems. *Numerical Heat Transfer, Part B Fundamentals*, 19(1):69–84, 1991.

Jules G Charney, Ragnar Fjörtoft, and J von Neumann. Numerical integration of the barotropic vorticity equation. *Tellus*, 2(4):237–254, 1950.

Joseph F Cheer, Brandon J Aragona, Michael LAV Heien, Andrew T Seipel, Regina M Carelli, and R Mark Wightman. Coordinated accumbal dopamine release and neural activity drive goal-directed behavior. *Neuron*, 54(2):237–244, 2007.

Stephanie J Cragg and Margaret E Rice. Dancing past the dat at a da synapse. *Trends in neurosciences*, 27(5):270–277, 2004.

Stephanie J Cragg, Charles Nicholson, June Kume-Kick, Lian Tao, and Margaret E Rice. Dopamine-mediated volume transmission in midbrain is regulated by distinct extracellular geometry and uptake. *Journal of neurophysiology*, 85(4):1761–1771, 2001.

John Crank and Phyllis Nicolson. A practical method for numerical evaluation of solutions of partial differential equations of the heat-conduction type. In *Mathematical Proceedings of the Cambridge Philosophical Society*, volume 43, pages 50–67. Cambridge University Press, 1947.

Jeremy J Day, Mitchell F Roitman, R Mark Wightman, and Regina M Carelli. Associative learning mediates dynamic shifts in dopamine signaling in the nucleus accumbens. *Nature neuroscience*, 10(8):1020, 2007.

Michelle Day, David Wokosin, Joshua L Plotkin, Xinyoung Tian, and D James Surmeier. Differential excitability and modulation of striatal medium spiny neuron dendrites. *Journal of Neuroscience*, 28(45):11603–11614, 2008.

Gaetano Di Chiara and Valentina Bassareo. Reward system and addiction: what dopamine does and doesn't do. *Current opinion in pharmacology*, 7(1): 69–76, 2007.

GR DiResta, J Lee, N Lau, F Ali, JH Galicich, and E Arbit. Measurement of brain tissue density using pycnometry. In *Brain Edema VIII*, pages 34–36. Springer, 1990.

Jim Douglas. Alternating direction methods for three space variables. *Numerische Mathematik*, 4(1):41–63, 1962.

Jakob K Dreyer. Three mechanisms by which striatal denervation causes breakdown of dopamine signaling. *Journal of Neuroscience*, 34(37):12444–12456, 2014.

Jakob K Dreyer, Kjartan F Herrik, Rune W Berg, and Jørn D Hounsgaard. Influence of phasic and tonic dopamine release on receptor activation. *Journal of Neuroscience*, 30(42):14273–14283, 2010.

Jakob K Dreyer, Caitlin M Vander Weele, Vedran Lovic, and Brandon J Aragona. Functionally distinct dopamine signals in nucleus accumbens core and shell in the freely moving rat. *Journal of Neuroscience*, 36(1):98–112, 2016.

Jakob Kisbye Dreyer and Jørn Hounsgaard. Mathematical model of dopamine autoreceptors and uptake inhibitors and their influence on tonic and phasic dopamine signaling. *Journal of neurophysiology*, 109(1):171–182, 2012.

Jakob Kisbye Dreyer and Jørn Hounsgaard. Mathematical model of dopamine autoreceptors and uptake inhibitors and their influence on tonic and phasic dopamine signaling. *Journal of neurophysiology*, 109(1):171–182, 2013.

Manfred Eigen and Gordon G Hammes. Elementary steps in enzyme reactions (as studied by relaxation spectrometry). *Advances in enzymology and related areas of molecular biology*, 25:1–38, 1963.

Albert Einstein. Über die von der molekularkinetischen theorie der wärme geforderte bewegung von in ruhenden flüssigkeiten suspendierten teilchen. *Annalen der physik*, 322(8):549–560, 1905.

Alexandre Ern and Jean-Luc Guermond. *Theory and practice of finite elements*, volume 159. Springer Science & Business Media, 2013.

Barry J Everitt and Trevor W Robbins. Neural systems of reinforcement for drug addiction: from actions to habits to compulsion. *Nature neuroscience*, 8(11):1481, 2005.

Xin Gui Fang and George Havas. On the worst-case complexity of integer gaussian elimination. In *Proceedings of the 1997 international symposium on Symbolic and algebraic computation*, pages 28–31. ACM, 1997.

Richard P Feynman, Robert B Leighton, and Matthew Sands. The feynman lectures on physics; vol. i. *American Journal of Physics*, 33(9):750–752, 1965.

Adolf Fick. Ueber diffusion. *Annalen der Physik*, 170(1):59–86, 1855.

Edén Flores-Barrera, Bianca J Vizcarra-Chacón, José Bargas, Dagoberto Tapia, and Elvira Galarraga. Dopaminergic modulation of corticostriatal responses in medium spiny projection neurons from direct and indirect pathways. *Frontiers in systems neuroscience*, 5:15, 2011.

Stan B Floresco, Anthony R West, Brian Ash, Holly Moore, and Anthony A Grace. Afferent modulation of dopamine neuron firing differentially regulates tonic and phasic dopamine transmission. *Nature neuroscience*, 6(9):968, 2003.

Michael J Frank and Randall C O'Reilly. A mechanistic account of striatal dopamine function in human cognition: psychopharmacological studies with cabergoline and haloperidol. *Behavioral neuroscience*, 120(3):497, 2006.

Paul A Garris, Edward L Ciolkowski, Paolo Pastore, and R Mark Wightman. Efflux of dopamine from the synaptic cleft in the nucleus accumbens of the rat brain. *Journal of neuroscience*, 14(10):6084–6093, 1994.

Charles R Gerfen and D James Surmeier. Modulation of striatal projection systems by dopamine. *Annual review of neuroscience*, 34:441–466, 2011.

Charles R Gerfen and Charles J Wilson. Chapter ii the basal ganglia. In *Handbook of chemical neuroanatomy*, volume 12, pages 371–468. Elsevier, 1996.

Charles R Gerfen, Thomas M Engber, Lawrence C Mahan, ZVI Susel, Thomas N Chase, FJ Monsma, and David R Sibley. D1 and d2 dopamine receptor-regulated gene expression of striatonigral and striatopallidal neurons. *Science*, 250(4986):1429–1432, 1990.

Anthony A Grace. The tonic/phasic model of dopamine system regulation: its relevance for understanding how stimulant abuse can alter basal ganglia function. *Drug & Alcohol Dependence*, 37(2):111–129, 1995.

Anthony A Grace, Stan B Floresco, Yukiori Goto, and Daniel J Lodge. Regulation of firing of dopaminergic neurons and control of goal-directed behaviors. *Trends in neurosciences*, 30(5):220–227, 2007.

William G Gray and PCY Lee. On the theorems for local volume averaging of multiphase systems. *International Journal of Multiphase Flow*, 3(4):333–340, 1977.

Yuanxian Gu, Wenyuan Liao, and Jianping Zhu. An efficient high-order algorithm for solving systems of 3-d reaction–diffusion equations. *Journal of computational and applied mathematics*, 155(1):1–17, 2003.

Dominik Haddad and Ken Nakamura. Understanding the susceptibility of dopamine neurons to mitochondrial stressors in parkinson's disease. *FEBS letters*, 589(24):3702–3713, 2015.

Arif A Hamid, Jeffrey R Pettibone, Omar S Mabrouk, Vaughn L Hetrick, Robert Schmidt, Caitlin M Vander Weele, Robert T Kennedy, Brandon J Aragona, and Joshua D Berke. Mesolimbic dopamine signals the value of work. *Nature neuroscience*, 19(1):117, 2016.

Steven M Hersch, Brian J Ciliax, Claire-Anne Gutekunst, HD Rees, Craig J Heilman, KK Yung, JP Bolam, E Ince, HONG Yi, and AI Levey. Electron microscopic analysis of d1 and d2 dopamine receptor proteins in the dorsal striatum and their synaptic relationships with motor corticostriatal afferents. *Journal of Neuroscience*, 15(7):5222–5237, 1995.

Steven M Hersch, Hong Yi, Craig J Heilman, Robert H Edwards, and Allan I Levey. Subcellular localization and molecular topology of the dopamine transporter in the striatum and substantia nigra. *Journal of Comparative Neurology*, 388(2):211–227, 1997.

Okihide Hikosaka, Yoriko Takikawa, and Reiko Kawagoe. Role of the basal ganglia in the control of purposive saccadic eye movements. *Physiological reviews*, 80(3):953–978, 2000.

Klaus A Hoffmann and Steve T Chiang. Computational fluid dynamics volume i. *Engineering Education System, Wichita, Kan, USA*, 2000.

Mark W Howe, Patrick L Tierney, Stefan G Sandberg, Paul EM Phillips, and Ann M Graybiel. Prolonged dopamine signalling in striatum signals proximity and value of distant rewards. *Nature*, 500(7464):575–579, 2013.

Mark D Humphries, Ric Wood, and Kevin Gurney. Dopamine-modulated dynamic cell assemblies generated by the gabaergic striatal microcircuit. *Neural Networks*, 22(8):1174–1188, 2009.

BI Hyland, JNJ Reynolds, J Hay, CG Perk, and R Miller. Firing modes of midbrain dopamine cells in the freely moving rat. *Neuroscience*, 114(2):475–492, 2002.

Erica H Jaffe, Alain Marty, Albert Schulte, and Robert H Chow. Extrasynaptic vesicular transmitter release from the somata of substantia nigra neurons in rat midbrain slices. *Journal of Neuroscience*, 18(10):3548–3553, 1998.

KA Jellinger. Recent developments in the pathology of parkinson's disease. In *Ageing and Dementia Current and Future Concepts*, pages 347–384. Springer, 2002.

Derek K Jones and Alexander Leemans. Diffusion tensor imaging. In *Magnetic resonance neuroimaging*, pages 127–144. Springer, 2011.

Eric Jones, Travis Oliphant, Pearu Peterson, et al. SciPy: Open source scientific tools for Python, 2001–. URL `http://www.scipy.org/`. [Online; accessed ¡today¿].

JB Justice Jr. Quantitative microdialysis of neurotransmitters. *Journal of neuroscience methods*, 48(3):263–276, 1993.

Michael J Katz. Axonal branch shapes. *Brain research*, 361(1-2):70–76, 1985a.

MICHAEL J Katz. How straight do axons grow? *Journal of Neuroscience*, 5 (3):589–595, 1985b.

Richard S Kelly and R Mark Wightman. Bevelled carbon-fiber ultramicroelectrodes. *Analytica chimica acta*, 187:79–87, 1986.

Janet M Kemp and Thomas Philip Stroud Powell. The structure of the caudate nucleus of the cat: light and electron microscopy. *Philosophical Transactions of the Royal Society of London. Series B, Biological Sciences*, pages 383–401, 1971.

Chou Kuo-Chen and Jiang Shou-ping. Studies on the rate of diffusioncontrolled reactions of enzymes spatial factor and force field factor. *Scientia Sinica*, 17 (5):664–680, 1974.

TD Lamb and EN Pugh Jr. G-protein cascades: gain and kinetics. *Trends in neurosciences*, 15(8):291–298, 1992.

Hans Petter Langtangen. Finite difference methods for diffusion processes. *University of Oslo*, 2013a.

Hans Petter Langtangen. Truncation error analysis. *Center for Biomedical Computing, Simula Research Laboratory, Department of Informatics, University of Oslo*, 2013b.

Mads Breum Larsen, Mark S Sonders, Ole Valente Mortensen, Gaynor A Larson, Nancy R Zahniser, and Susan G Amara. Dopamine transport by the serotonin transporter: a mechanistically distinct mode of substrate translocation. *Journal of Neuroscience*, 31(17):6605–6615, 2011.

J Douglas Lawson and J Ll Morris. The extrapolation of first order methods for parabolic partial differential equations. i. *SIAM Journal on Numerical Analysis*, 15(6):1212–1224, 1978.

Catherine Le Moine and Bertrand Bloch. D1 and d2 dopamine receptor gene expression in the rat striatum: sensitive crna probes demonstrate prominent segregation of d1 and d2 mrnas in distinct neuronal populations of the dorsal and ventral striatum. *Journal of Comparative Neurology*, 355(3):418–426, 1995.

FK Lehner. On the validity of fick's law for transient diffusion through a porous medium. *Chemical Engineering Science*, 34(6):821–825, 1979.

Knut P Lehre and Niels C Danbolt. The number of glutamate transporter subtype molecules at glutamatergic synapses: chemical and stereological quantification in young adult rat brain. *Journal of Neuroscience*, 18(21):8751–8757, 1998.

Yiming Lei, Hongbin Han, Fan Yuan, Aqeel Javeed, and Yong Zhao. The brain interstitial system: Anatomy, modeling, in vivo measurement, and applications. *Progress in neurobiology*, 157:230–246, 2017.

Wenyuan Liao, Jianping Zhu, and Abdul QM Khaliq. An efficient high-order algorithm for solving systems of reaction-diffusion equations. *Numerical Methods for Partial Differential Equations*, 18(3):340–354, 2002.

Maria Lindskog, MyungSook Kim, Martin A Wikström, Kim T Blackwell, and Jeanette Hellgren Kotaleski. Transient calcium and dopamine increase pka activity and darpp-32 phosphorylation. *PLoS computational biology*, 2(9): e119, 2006.

Changliang Liu, Lauren Kershberg, Jiexin Wang, Shirin Schneeberger, and Pascal S Kaeser. Dopamine secretion is mediated by sparse active zone-like release sites. *Cell*, 172(4):706–718, 2018.

Hiroo Maeno. Dopamine receptors in canine caudate nucleus. *Molecular and cellular biochemistry*, 43(2):65–80, 1982.

Pamela F Marcott, Aphroditi A Mamaligas, and Christopher P Ford. Phasic dopamine release drives rapid activation of striatal d2-receptors. *Neuron*, 84 (1):164–176, 2014.

Wakoto Matsuda, Takahiro Furuta, Kouichi C Nakamura, Hiroyuki Hioki, Fumino Fujiyama, Ryohachi Arai, and Takeshi Kaneko. Single nigrostriatal dopaminergic neurons form widely spread and highly dense axonal arborizations in the neostriatum. *Journal of Neuroscience*, 29(2):444–453, 2009.

P Read Montague, Samuel M McClure, PR Baldwin, Paul EM Phillips, Evgeny A Budygin, Garret D Stuber, Michaux R Kilpatrick, and R Mark Wightman. Dynamic gain control of dopamine delivery in freely moving animals. *Journal of Neuroscience*, 24(7):1754–1759, 2004.

José A Morón, Alicia Brockington, Roy A Wise, Beatriz A Rocha, and Bruce T Hope. Dopamine uptake through the norepinephrine transporter in brain regions with low levels of the dopamine transporter: evidence from knock-out mouse lines. *Journal of Neuroscience*, 22(2):389–395, 2002.

Genela Morris, David Arkadir, Alon Nevet, Eilon Vaadia, and Hagai Bergman. Coincident but distinct messages of midbrain dopamine and striatal tonically active neurons. *Neuron*, 43(1):133–143, 2004.

Anu G Nair, Omar Gutierrez-Arenas, Olivia Eriksson, Pierre Vincent, and Jeanette Hellgren Kotaleski. Sensing positive versus negative reward signals through adenylyl cyclase-coupled gpcrs in direct and indirect pathway striatal medium spiny neurons. *Journal of Neuroscience*, 35(41):14017–14030, 2015.

Alexandra B Nelson and Anatol C Kreitzer. Reassessing models of basal ganglia function and dysfunction. *Annual review of neuroscience*, 37:117–135, 2014.

Kim A Neve and Rachael L Neve. Molecular biology of dopamine receptors. In *The dopamine receptors*, pages 27–76. Springer, 1997.

Ch Nicholson and JM Phillips. Ion diffusion modified by tortuosity and volume fraction in the extracellular microenvironment of the rat cerebellum. *The Journal of Physiology*, 321(1):225–257, 1981.

Charles Nicholson. Interaction between diffusion and michaelis-menten uptake of dopamine after iontophoresis in striatum. *Biophysical journal*, 68(5):1699–1715, 1995.

Charles Nicholson. Diffusion and related transport mechanisms in brain tissue. *Reports on progress in Physics*, 64(7):815, 2001.

Melissa J Nirenberg, Roxanne A Vaughan, George R Uhl, Michael J Kuhar, and Virginia M Pickel. The dopamine transporter is localized to dendritic and axonal plasma membranes of nigrostriatal dopaminergic neurons. *Journal of Neuroscience*, 16(2):436–447, 1996.

Melissa J Nirenberg, June Chan, Alicia Pohorille, Roxanne A Vaughan, George R Uhl, Michael J Kuhar, and Virginia M Pickel. The dopamine transporter: comparative ultrastructure of dopaminergic axons in limbic and motor compartments of the nucleus accumbens. *Journal of Neuroscience*, 17 (18):6899–6907, 1997.

Koji Nishikori, Osamu Noshiro, Kenji Sano, and Hiroo Maeno. Characterization, solubilization, and separation of two distinct dopamine receptors in canine caudate nucleus. *Journal of Biological Chemistry*, 255(22):10909–10915, 1980.

Yael Niv, Nathaniel D Daw, Daphna Joel, and Peter Dayan. Tonic dopamine: opportunity costs and the control of response vigor. *Psychopharmacology*, 191 (3):507–520, 2007.

Wei-Xing Pan, Robert Schmidt, Jeffery R Wickens, and Brian I Hyland. Dopamine cells respond to predicted events during classical conditioning: evidence for eligibility traces in the reward-learning network. *Journal of Neuroscience*, 25(26):6235–6242, 2005.

Wei-Xing Pan, Robert Schmidt, Jeffery R Wickens, and Brian I Hyland. Tripartite mechanism of extinction suggested by dopamine neuron activity and temporal difference model. *Journal of Neuroscience*, 28(39):9619–9631, 2008.

Tommaso Patriarchi, Jounhong Ryan Cho, Katharina Merten, Mark W Howe, Aaron Marley, Wei-Hong Xiong, Robert W Folk, Gerard Joey Broussard, Ruqiang Liang, Min Jee Jang, et al. Ultrafast neuronal imaging of dopamine dynamics with designed genetically encoded sensors. *Science*, page eaat4422, 2018.

Donald W Peaceman and Henry H Rachford, Jr. The numerical solution of parabolic and elliptic differential equations. *Journal of the Society for industrial and Applied Mathematics*, 3(1):28–41, 1955.

Anthony G Phillips, Giada Vacca, and Soyon Ahn. A top-down perspective on dopamine, motivation and memory. *Pharmacology Biochemistry and Behavior*, 90(2):236–249, 2008.

Eleftheria Kyriaki Pissadaki and J Paul Bolam. The energy cost of action potential propagation in dopamine neurons: clues to susceptibility in parkinson's disease. *Frontiers in computational neuroscience*, 7:13, 2013.

Emmanuel N Pothos. Regulation of dopamine quantal size in midbrain and hippocampal neurons. *Behavioural brain research*, 130(1-2):203–207, 2002.

Emmanuel N Pothos, Viviana Davila, and David Sulzer. Presynaptic recording of quanta from midbrain dopamine neurons and modulation of the quantal size. *Journal of Neuroscience*, 18(11):4106–4118, 1998.

Lucıa Prensa and Andre Parent. The nigrostriatal pathway in the rat: a single-axon study of the relationship between dorsal and ventral tier nigral neurons and the striosome/matrix striatal compartments. *Journal of Neuroscience*, 21(18):7247–7260, 2001.

William H Press, Saul A Teukolsky, William T Vetterling, and Brian P Flannery. Numerical recipes in c. *Cambridge University Press*, 1:3, 1988.

Delphine Prou, Wen-Jie Gu, Stéphane Le Crom, Jean-Didier Vincent, Jean Salamero, and Philippe Vernier. Intracellular retention of the two isoforms of the d 2 dopamine receptor promotes endoplasmic reticulum disruption. *Journal of Cell Science*, 114(19):3517–3527, 2001.

Peter Redgrave, Tony J Prescott, and Kevin Gurney. The basal ganglia: a vertebrate solution to the selection problem? *Neuroscience*, 89(4):1009–1023, 1999.

Peter Redgrave, Manuel Rodriguez, Yoland Smith, Maria C Rodriguez-Oroz, Stephane Lehericy, Hagai Bergman, Yves Agid, Mahlon R DeLong, and Jose A Obeso. Goal-directed and habitual control in the basal ganglia: implications for parkinson's disease. *Nature Reviews Neuroscience*, 11(11):760–772, 2010.

Bryan A Reyes, Julie S Pendergast, and Shin Yamazaki. Mammalian peripheral circadian oscillators are temperature compensated. *Journal of biological rhythms*, 23(1):95–98, 2008.

John NJ Reynolds and Jeffery R Wickens. Dopamine-dependent plasticity of corticostriatal synapses. *Neural Networks*, 15(4-6):507–521, 2002.

John NJ Reynolds, Brian I Hyland, and Jeffery R Wickens. A cellular mechanism of reward-related learning. *Nature*, 413(6851):67, 2001.

Margaret E Rice and Stephanie J Cragg. Dopamine spillover after quantal release: rethinking dopamine transmission in the nigrostriatal pathway. *Brain research reviews*, 58(2):303–313, 2008.

Lewis F Richardson, BA J Arthur Gaunt, et al. Viii. the deferred approach to the limit. *Phil. Trans. R. Soc. Lond. A*, 226(636-646):299–361, 1927.

Eric K Richfield, Anne B Young, and John B Penney. Comparative distribution of dopamine d-1 and d-2 receptors in the basal ganglia of turtles, pigeons, rats, cats, and monkeys. *Journal of Comparative Neurology*, 262(3):446–463, 1987.

Eric K Richfield, John B Penney, and Anne B Young. Anatomical and affinity state comparisons between dopamine d 1 and d 2 receptors in the rat central nervous system. *Neuroscience*, 30(3):767–777, 1989.

Donita L Robinson, Paul EM Phillips, Evgeny A Budygin, B Jill Trafton, Paul A Garris, and R Mark Wightman. Sub-second changes in accumbal dopamine during sexual behavior in male rats. *Neuroreport*, 12(11):2549–2552, 2001.

Matthew R Roesch, Teghpal Singh, P Leon Brown, Sylvina E Mullins, and Geoffrey Schoenbaum. Ventral striatal neurons encode the value of the chosen action in rats deciding between differently delayed or sized rewards. *Journal of Neuroscience*, 29(42):13365–13376, 2009.

Mitchell F Roitman, Garret D Stuber, Paul EM Phillips, R Mark Wightman, and Regina M Carelli. Dopamine operates as a subsecond modulator of food seeking. *Journal of Neuroscience*, 24(6):1265–1271, 2004.

Mitchell F Roitman, Robert A Wheeler, R Mark Wightman, and Regina M Carelli. Real-time chemical responses in the nucleus accumbens differentiate rewarding and aversive stimuli. *Nature neuroscience*, 11(12):1376, 2008.

Katherine E Rooney and Lane J Wallace. Computational modeling of extracellular dopamine kinetics suggests low probability of neurotransmitter release. *Synapse*, 69(11):515–525, 2015.

Steven J Ruuth. Implicit-explicit methods for reaction-diffusion problems in pattern formation. *Journal of Mathematical Biology*, 34(2):148–176, 1995.

John D Salamone and Mercè Correa. The mysterious motivational functions of mesolimbic dopamine. *Neuron*, 76(3):470–485, 2012.

Stefan G Sandberg and Paul EM Phillips. Phasic dopaminergic signaling: implications for parkinson's disease. In *Cortico-Subcortical Dynamics in Parkinson's Disease*, pages 37–54. Springer, 2009.

Kenji Sano, Osamu Noshiro, Kimio Katsuda, Koji Nishikori, and Hiroo Maeno. Dopamine receptors and dopamine-sensitive adenylate cyclase in canine caudate nucleus: Characterization and solubilization. *Biochemical pharmacology*, 28(24):3617–3627, 1979.

Wolfram Schultz. Predictive reward signal of dopamine neurons. *Journal of neurophysiology*, 80(1):1–27, 1998.

Wolfram Schultz. Getting formal with dopamine and reward. *Neuron*, 36(2): 241–263, 2002.

Wolfram Schultz. Multiple dopamine functions at different time courses. *Annu. Rev. Neurosci.*, 30:259–288, 2007.

Wolfram Schultz. Dopamine reward prediction-error signalling: a two-component response. *Nature Reviews Neuroscience*, 17(3):183, 2016.

Susan R Sesack, Chiye Aoki, and Virginia M Pickel. Ultrastructural localization of d2 receptor-like immunoreactivity in midbrain dopamine neurons and their striatal targets. *Journal of Neuroscience*, 14(1):88–106, 1994.

Matthew J Simpson and Adam J Ellery. An analytical solution for diffusion and nonlinear uptake of oxygen in a spherical cell. *Applied Mathematical Modelling*, 36(7):3329–3334, 2012.

Yoland Smith and Jeremy Z Kieval. Anatomy of the dopamine system in the basal ganglia. *Trends in neurosciences*, 23:S28–S33, 2000.

Elizabeth E Steinberg, Ronald Keiflin, Josiah R Boivin, Ilana B Witten, Karl Deisseroth, and Patricia H Janak. A causal link between prediction errors, dopamine neurons and learning. *Nature neuroscience*, 16(7):966, 2013.

Arthur N Strahler. Hypsometric (area-altitude) analysis of erosional topography. *Geological Society of America Bulletin*, 63(11):1117–1142, 1952.

MF Suaud-Chagny, K Chergui, G Chouvet, and F Gonon. Relationship between dopamine release in the rat nucleus accumbens and the discharge activity of dopaminergic neurons during local in vivo application of amino acids in the ventral tegmental area. *Neuroscience*, 49(1):63–72, 1992.

Fangmiao Sun, Jianzhi Zeng, Miao Jing, Jingheng Zhou, Jiesi Feng, Scott F Owen, Yichen Luo, Funing Li, Huan Wang, Takashi Yamaguchi, et al. A genetically encoded fluorescent sensor enables rapid and specific detection of dopamine in flies, fish, and mice. *Cell*, 174(2):481–496, 2018.

D James Surmeier, Jun Ding, Michelle Day, Zhongfeng Wang, and Weixing Shen. D1 and d2 dopamine-receptor modulation of striatal glutamatergic signaling in striatal medium spiny neurons. *Trends in neurosciences*, 30(5): 228–235, 2007.

Emilie CJ Syed, Laura L Grima, Peter J Magill, Rafal Bogacz, Peter Brown, and Mark E Walton. Action initiation shapes mesolimbic dopamine encoding of future rewards. *Nature neuroscience*, 19(1):34, 2016.

Eva Syková and Charles Nicholson. Diffusion in brain extracellular space. *Physiological reviews*, 88(4):1277–1340, 2008.

Saul A Teukolsky, Brian P Flannery, WH Press, and WT Vetterling. Numerical recipes in c. *SMR*, 693(1), 1992.

The CGAL Project. *CGAL User and Reference Manual*. CGAL Editorial Board, 4.13 edition, 2018. URL `https://doc.cgal.org/4.13/Manual/packages.html`.

Llewellyn Hilleth Thomas. Elliptic problems in linear difference equations over a network. *Watson Sci. Comput. Lab. Rept., Columbia University, New York*, 1, 1949.

Sarah Threlfell, Tatjana Lalic, Nicola J Platt, Katie A Jennings, Karl Deisseroth, and Stephanie J Cragg. Striatal dopamine release is triggered by synchronized activity in cholinergic interneurons. *Neuron*, 75(1):58–64, 2012.

Philippe N Tobler, Anthony Dickinson, and Wolfram Schultz. Coding of predicted reward omission by dopamine neurons in a conditioned inhibition paradigm. *Journal of Neuroscience*, 23(32):10402–10410, 2003.

Philippe N Tobler, Christopher D Fiorillo, and Wolfram Schultz. Adaptive coding of reward value by dopamine neurons. *Science*, 307(5715):1642–1645, 2005.

Urban Ungerstedt. Stereotaxic mapping of the monoamine pathways in the rat brain. *Acta physiologica scandinavica*, 82(S367):1–48, 1971.

B Jill Venton, Hui Zhang, Paul A Garris, Paul EM Phillips, David Sulzer, and R Mark Wightman. Real-time decoding of dopamine concentration changes in the caudate–putamen during tonic and phasic firing. *Journal of neurochemistry*, 87(5):1284–1295, 2003.

Ronald WH Verwer and Jaap Van Pelt. Topological analysis of binary tree structures when occasional multifurcations occur. *Bulletin of mathematical biology*, 47(2):305, 1985.

Ronald WH Verwer and Jaap Van Pelt. Analysis of binary trees when occasional multifurcations can be considered as aggregates of bifurcations. *Bulletin of mathematical biology*, 52(5):629–641, 1990.

Marian Von Smoluchowski. Zur kinetischen theorie der brownschen molekularbewegung und der suspensionen. *Annalen der physik*, 326(14):756–780, 1906.

Stephen Whitaker. Advances in theory of fluid motion in porous media. *Industrial & engineering chemistry*, 61(12):14–28, 1969.

Stephen Whitaker. A simple geometrical derivation of the spatial averaging theorem. *Chemical engineering education*, 19(1), 1985.

RM Wightman, C Amatorh, RC Engstrom, PD Hale, EW Kristensen, WG Kuhr, and LJ May. Real-time characterization of dopamine overflow and uptake in the rat striatum. *Neuroscience*, 25(2):513–523, 1988.

Cedric Yapo, Anu G Nair, Lorna Clement, Liliana R Castro, Jeanette Hellgren Kotaleski, and Pierre Vincent. Detection of phasic dopamine by d1 and d2 striatal medium spiny neurons. *The Journal of physiology*, 595(24): 7451–7475, 2017.

Appendices

Diffusion Parameters		
Parameter		Source
D_{DA} in $\mu m^2 s^{-1}$	320.0	(Nicholson, 1995)
α	0.2	(Syková and Nicholson, 2008)
$Quantalsize$ in molecules	3000 ± 300	(Pothos et al., 1998)
Release prob. p	0.06	(Dreyer and Hounsgaard, 2012)
V_{max} in $\mu M s^{-1}$	-5.0	(Nicholson, 1995; Wightman et al., 1988)
K_m in nM	0.21	(Nicholson, 1995)
$k_{unspecific}$ in $\mu M s^{-1}$	-0.007	(Cragg et al., 2001)
Δt in ms	1,0	
DA receptor parameters		
Parameter		Source
C_{D1}^{max} in nM	≈ 1600	see Chapter 5
C_{D2}^{max} in nM	≈ 80	see Chapter 5
k_{on}^{D2} in $nm^{-1}min^{-1}$	0.02	(Burt et al., 1976)
k_{off}^{D2} in min^{-1}	0.5	(Burt et al., 1976)
k_{on}^{D1} in $nm^{-1}min^{-1}$	0.0003125	see Chapter 5
k_{off}^{D1} in min^{-1}	0.5	see Chapter 5
Spiketrain parameters		
Parameter		Source
$f_{irregular}$	0.55	(Hyland et al., 2002)
$f_{regular}$	0.25	(Hyland et al., 2002)
$f_{bursting}$	0.2	(Hyland et al., 2002)
$rate_{regular}$ in Hz	4.0 ± 0.8	(Hyland et al., 2002)
$CV_{regular}$	0.35 ± 0.15	(Hyland et al., 2002)
$rate_{irregular}$ in Hz	4.0 ± 0.8	(Hyland et al., 2002)
$k_{irregular}$	3.0	(Hyland et al., 2002)
$rate_{bursting}$ in Hz	4.0 ± 0.8	(Hyland et al., 2002)
$k_{bursting}$	3.0	(Hyland et al., 2002)
$rate_{bursts}$ in Hz	0.82 ± 0.2	(Hyland et al., 2002)
λ	2.7 ± 0.5	(Hyland et al., 2002)
$f_{intraburst}$ in Hz	22.5 ± 5.2	(Hyland et al., 2002)
$max_{eventjitter}$ in ms	100	(Hyland et al., 2002)
f_{reward}	0.7	(Hyland et al., 2002)
Axon generation parameters		
Parameter		Source
$\langle \alpha \rangle$ in degree	70.0	(Katz, 1985a)
$\sigma_{alpha} indegree$	30.0	(Katz, 1985a)
$\langle \epsilon \rangle$ in degree	17.0	(Katz, 1985b)
$\sigma_{epsilon}$ in degree	20.0	(Katz, 1985b)
N_{branch}^{max}	17000	(Matsuda et al., 2009), see Chapter 4
$d_{synapse}$ in μm	7.6	(Arbuthnott and Wickens, 2007)
p_{branch}	0.0192	see Chapter 4
p_{el}	0.9677	see Chapter 4
p_{chdir}	0.1	see Chapter 4

Supplemental Table. 1: Receptor parameters